HZDR-074

FLUID DYNAMICS OF BUBBLY FLOWS

Thomas Ziegenhein

Wissenschaftlich-Technische Berichte
HZDR-074 · ISSN 2191-8708

WISSENSCHAFTLICH-
TECHNISCHE BERICHTE

HZDR
HELMHOLTZ
ZENTRUM DRESDEN
ROSSENDORF

Wissenschaftlich-Technische Berichte
HZDR-074

Thomas Ziegenhein

FLUID DYNAMICS OF BUBBLY FLOWS

HZDR

HELMHOLTZ
ZENTRUM DRESDEN
ROSSENDORF

Druckausgabe: ISSN 2191-8708

Elektronische Ausgabe: ISSN 2191-8716

https://www.hzdr.de/publications/Publ-24297

urn:nbn:de:bsz:d120-qucosa-213581

Die vorliegende Arbeit wurde sowohl als Dissertation an der Fakultät III – Prozesswissenschaften der Technischen Universität Berlin sowie als Wissenschaftlich-Technischer Bericht des Helmholtz-Zentrum Dresden – Rossendorf mit der Berichtsnummer **HZDR-074** veröffentlicht.

2016

Herausgegeben vom

Helmholtz-Zentrum Dresden - Rossendorf

Bautzner Landstraße 400

01328 Dresden

Germany

Fluid dynamics of bubbly flows

vorgelegt von
Dipl.-Ing.
Thomas Ziegenhein
geb. in Jena

von der Fakultät III – Prozesswissenschaften
der Technischen Universität Berlin
zur Erlangung des akademischen Grades

Doktor der Ingenieurwissenschaften
- Dr.-Ing. -

genehmigte Dissertation

Promotionsausschuss:

Vorsitzender: Prof. Dr.-Ing. Felix Ziegler

Gutachter: Prof. Dr.-Ing. Matthias Kraume

Gutachter: Prof. Dr.-Ing. Michael Schlüter

Gutachter: Dr. rer. nat. Dirk Lucas

Tag der wissenschaftlichen Aussprache: 8. Juli 2016

Berlin 2016

“Nur die Idee, die unbegründete Antizipation, der kühne Gedanke ist es, mit dem wir, ihn immer wieder aufs Spiel setzend, die Natur einzufangen versuchen: Wer seine Gedanken der Widerlegung nicht aussetzt, der spielt nicht mit in dem Spiel Wissenschaft”

“Bold ideas, unjustified anticipations, and speculative thought, are our only means for interpreting nature: our only organon, our only instrument, for grasping her. And we must hazard them to win our prize. Those among us who are unwilling to expose their ideas to the hazard of refutation do not take part in the scientific game.”

Karl Popper – Wien, 1934

Acknowledgement

Like probably all doctorate students at the beginning of their studies, I thought in chaotic ways, changed my mind three times a minute and was eager to do everything in a different way than others. Quickly, I learned that scientific progress is a slow progress reasoned on undoubtedly arguments. Nevertheless, I was allowed to keep a bit of the initial chaos, for this I would like to sincerely thank my scientific supervisor Dr. Dirk Lucas. More than once, he was the only one who understands my unconventional ideas and theories so that they could evolve over time. Those lead also to the purpose to build an own experimental facility, which might be uncommon as a member of the theoretical department. For this opportunity, I have to thank him again. In this context, I have to thank the head of the experimental department Prof. Uwe Hampel to tolerate me in his labs as well as the function as head of the project I worked in, the Helmholtz Energy Alliance.

I sincerely thank Prof. Matthias Kraume for accepting me as an external doctorate student as well as for the organization of my PhD at TU-Berlin. In addition, I want to thank Prof. Michael Schlüter for accepting to be a referee for this thesis. I would particularly thank my colleagues at HZDR for the many fruitful discussions, especially Dr. Roland Rzehak, Dr. Sebastian Kriebitzsch, Dr. Eckhard Krepper and Tian Ma.

My gratitude and special thanks go to my friends; they tolerated me without grimness the last three years in which I spend most of the time on my doctorate studies.

Finally yet importantly, I want to thank my father and my mother for supporting and comfort me the last years.

This work was funded by the Helmholtz Association within the frame of the Helmholtz Energy Alliance “Energy Efficient Chemical Multiphase Processes” (HA-E-0004).

Abstract

Bubbly flows can be found in many applications in chemical, biological and power engineering. Reliable simulation tools of such flows that allow the design of new processes and optimization of existing one are therefore highly desirable. CFD-simulations applying the multi-fluid approach are very promising to provide such a design tool for complete facilities. In the multi-fluid approach, however, closure models have to be formulated to model the interaction between the continuous and dispersed phase. Due to the complex nature of bubbly flows, different phenomena have to be taken into account and for every phenomenon different closure models exist. Therefore, reliable predictions of unknown bubbly flows are not yet possible with the multi-fluid approach.

A strategy to overcome this problem is to define a baseline model in which the closure models including the model constants are fixed so that the limitations of the modeling can be evaluated by validating it on different experiments. Afterwards, the shortcomings are identified so that the baseline model can be stepwise improved without losing the validity for the already validated cases. This development of a baseline model is done in the present work by validating the baseline model developed at the Helmholtz-Zentrum Dresden-Rossendorf mainly basing on experimental data for bubbly pipe flows to bubble columns, bubble plumes and airlift reactors that are relevant in chemical and biological engineering applications.

In the present work, a large variety of such setups is used for validation. The buoyancy driven bubbly flows showed thereby a transient behavior on the scale of the facility. Since such large scales are characterized by the geometry of the facility, turbulence models cannot describe them. Therefore, the transient simulation of bubbly flows with two equation models based on the unsteady Reynolds-averaged Navier–Stokes equations is investigated. In combination with the before mentioned baseline model these transient simulations can reproduce many experimental setups without fitting any model. Nevertheless, shortcomings are identified that need to be further investigated to improve the baseline model.

For a validation of models, experiments that describe as far as possible all relevant phenomena of bubbly flows are needed. Since such data are rare in the literature, CFD-grade experiments in an airlift reactor were conducted in the present work. Concepts to measure the bubble size distribution and liquid velocities are developed for this purpose. In particular, the liquid velocity measurements are difficult; a sampling bias that was not yet described in the literature is identified. To overcome this error, a hold processor is developed.

The closure models are usually formulated based on single bubble experiments in simplified conditions. In particular, the lift force was not yet measured in low Morton number systems under turbulent conditions. A new experimental method is developed in the present work to determine the lift force coefficient in such flow conditions without the aid of moving parts so that the lift force can be measured in any chemical system easily.

Zusammenfassung

Die Auslegung und Optimierung von Mehrphasen-Prozessen im Bereich der chemischen und biologischen Verfahrenstechnik sowie der Energietechnik mithilfe von verlässlichen Simulationswerkzeugen ist aufgrund ihrer Vielzahl wünschenswert. Im speziellen für Blasenströmungen sind CFD-Simulationen die auf dem multi-fluid Ansatz basieren sehr vielversprechend um mit Ihrer Hilfe komplette Reaktoren auszulegen. Dabei müssen jedoch Schließungsmodelle formuliert werden, die die Wechselwirkungen zwischen der dispersen und der kontinuierlichen Phase beschreiben. In Blasenströmungen müssen verschieden Phänomene modelliert werden, für die es wiederum verschiedene Schließungsmodelle gibt. Durch diese Komplexität ist es bis jetzt nicht möglich Blasenströmungen die nicht vorher vermessen wurden verlässlich vorherzusagen. Eine Möglichkeit hinzu verlässlichen Modellen ist die Definition eines baseline models in dem alle Modelle und Modellkonstanten festgelegt sind. Durch die Validierung von verschiedenen Experimenten mit solch einem Modellsatz können die Grenzen der Modellierung ausgelotet werden, Defizite erkannt und Schrittweise verbessert werden ohne die Gültigkeit für die bereits bestehenden Anwendungen zu verlieren.

In dieser Arbeit wird das baseline model welches am Helmholtz-Zentrum Dresden-Rossendorf hauptsächlich für Blasenströmungen in Rohren validiert wurde weiterentwickelt, indem es mit einer Vielzahl von Blasensäulen und Schlaufenreaktoren validiert wird, die in der chemischen Industrie und Biotechnologie angewendet werden. Solche dichtegetriebenen Strömungen zeigen charakteristische Strömungsmerkmale in der Größe des Apparates. Solche großen Skalen können im Allgemeinen nicht durch ein Turbulenzmodell abgebildet werden, wodurch die transiente Simulation von Blasenströmungen mit Zweigleichungs-Turbulenzmodellen basierend auf den Reynolds gemittelten Navier-Stokes Gleichungen untersucht wurde. In Kombination mit dem baseline model konnten diese transienten Simulationen die Experimente reproduzieren ohne Modellkonstanten anzupassen. Defizite existieren jedoch, die weiter untersucht werden müssen um das baseline model weiter zu verbessern

Die Anforderungen an die experimentellen Daten bei einer Modellvalidierung sind sehr hoch, so müssen diese soweit möglich jeden relevanten Aspekt von Blasenströmungen beschreiben. Da solche umfassenden Daten in der Literatur selten sind, wurden eigene Experimente für einen Schlaufenreaktor speziell zur CFD-Validierung durchgeführt. In diesem Zusammenhang wurden Messkonzepte entwickelt, um die Blasengrößenverteilung und Flüssiggeschwindigkeit bei hohen Gasgehalten zu bestimmen. Bei der Messung der Flüssiggeschwindigkeit wurde eine Stichprobenverzerrung identifiziert die bis jetzt noch nicht in der Literatur beschrieben wurde. Um diesen Fehler zu beheben, wurde eine hold processor entwickelt.

Die erforderlichen Schließungsmodelle sind im Allgemeinen für Einzelblasenexperimente in vereinfachten Modellsystemen formuliert. Im Besonderen wurde die Lift-Kraft noch nicht in Systemen mit einer niedrigen Morton Zahl und unter turbulenten Bedingungen vermessen. Deshalb ist in dieser Arbeit ein neue Methode beschrieben die es erlaubt die Lift-Kraft in solchen Systemen zu bestimmen, dabei werden, wie üblich, keine beweglichen Teile benutzt wodurch sich diese Methode für eine Vielzahl von chemischen Stoffen eignet.

Contents

List of Figures

List of Tables

Nomenclature[1]

Symbols

A	Area	L^2
C_L	Lift force coefficient	$-$
d	Diameter	L
F	Differentiable function	
F	Force	MLT^{-2}
g	Gravitational acceleration	$L\,T^{-2}$
k	Turbulent kinetic energy	$L^2\,T^{-2}$
M	State function	$-$
$\boldsymbol{n}$	Normal boundary vector	$-$
p, P	Pressure	$M\,L^{-1}T^{-2}$
P_k	Turbulent kinetic energy production term	L^2T^{-3}
S_ϕ	Source term of ϕ	
t	Time	T
u	Horizontal velocity	$L\,T^{-1}$
v	Velocity	$L\,T^{-1}$
v	Vertical velocity	$L\,T^{-1}$
v'	Velocity fluctuation	$L\,T^{-1}$
V	Volume	L^3
V	Averaged velocity	$L\,T^{-1}$
$\boldsymbol{x}$	Position vector	$-$
X	Lagrangian coordinates	$-$

Greek and other symbols

α	Void fraction	$-$
$\mathcal{C}_T$	Count trajectories	$-$
$\mathfrak{g}$	Body forces	$L\,T^{-2}$
δ	Interface thickness	L
Δ	Difference of two values	$-$
ϵ	Turbulence dissipation rate	L^2T^{-3}
μ	Viscosity	$M\,L^{-1}T^{-1}$
∂_t	Partial derivative with respect to the variable t	T^{-1}
ρ	Density	$M\,L^{-3}$
$\mathfrak{I}$	Efflux	
∇	Nabla operator	$-$
$\mathfrak{R}$	Non-convective flux	
σ	Surface tension	$M\,T^{-2}$
τ	Characteristic time scale	T
$\mathbb{T}$	Particle/micro bubble track	$-$
Φ	Field variable	$-$

[1] Only symbols that are used more than once are given

Indices

b	Boundary
B	Bubble; spherical equivalent bubble diameter
D	Drag
BIT	Bubble induced turbulence
F	Fluid flow
G or g	Gas phase
$Major$	Maximum axis of a bubble
$Minor$	Maximum axis perpendicular to the major axis
P	Particle
L, l or $Liq.$	Liquid phase
rel	Relative velocity

Dimensionless numbers

C_D – Drag force coefficient	$\frac{2F_D}{\rho v_{rel}^2 A}$
Eo – Eötvös number	$\frac{\Delta\rho g d^2}{\sigma}$
Fr – Froude number	$\frac{v_{rel}}{g d_B}$
Mo – Morton number	$\frac{g\mu^4\Delta\rho}{\rho^2\sigma^3}$
Re – Reynolds number	$\frac{\rho v_{rel} d_B}{\mu}$
St – Stokes number	$\frac{\tau_{Particle}}{\tau_{Flow}}$
We – Weber number	$\frac{\rho v_{rel}^2 d_B}{\sigma}$

1 Introduction

1.1 Subject and motivation

Bubbly flows are well known and encounter in everyday life from refreshing drinks to cooking. Beyond those trivial applications, aerated flows are a fundamental principle in biological, chemical, energy and metallurgy engineering. In energy engineering, bubbles are produced in heat exchangers, evaporators or cooling systems. In biological and chemical engineering, in contrast, gas is supplied in a liquid for process intensification due to a large interface and enhanced mixing. No matter how the bubbles originate, a great interest exists to fully understand bubbly flows and predict their behavior with suitable models and simulations.

Despite the high interest in modeling bubbly flows, a distinct lack of understanding of such exists. This lack is due to the complex interface formed by the bubble. Even fundamental hydrodynamic characteristics like the bubble size are very challenging to measure and to model. Paired with the broad usage of bubbly flows, a better understanding has a great potential to increase the efficiency and energy saving for applications in nearly all fields of process engineering.

In the last years, new measuring techniques were developed for bubbly flows. In particular, the measurement of the gas phase structure with impedance measuring techniques (da Silva 2008) or computer tomography (Hampel et al. 2012) is available. Moreover, liquid velocity measuring techniques that are used in single phase flows are adopted and the capability to measure at higher gas load is increased, e.g. as shown by Hosokawa & Tomiyama (2013) with the laser Doppler anemometry.

In addition to new measuring techniques, the ability to perform simulations of bubbly flows with a complete resolved interface has been developed in the last years. From simulating single bubbles at lower Reynolds numbers (Tryggvason et al. 2006) up to several bubbles at higher Reynolds numbers (Roghair et al. 2013) the possibilities are steadily increasing thanks to more powerful computer systems. Besides, innovative methods of interface capturing like the combination of the level set and front tracking method (Maric et al. 2015) increase the possibilities of resolved simulations.

Without doubt, not every chemical reactor or heat exchanger can be examined with a computer tomography technique and not every single bubble of a bubble column can be simulated with a detailed resolved interface. Nevertheless, this new methods allow a deep insight to hydrodynamics of bubbly flows that are used to develop and improve models for simulation methods which are capable to simulate bubbly flows in complete vessels or pipes. The simplest methods are zero dimensional based on an integral balance equation of the complete system.

Since it is often needed to see local effects, methods are formulated in between a resolved surface simulation and the integral balance formulation. One of these methods is the Euler-Euler method that is based on the phase averaged Navier-Stokes equations formulated for the continuous and dispersed phase (Ishii & Hibiki 2006). In this process, the interface information is lost due to the averaging so that the interaction between the continuous and dispersed phase has to be modeled. With this method, three-dimensional simulations of large facilities are possible with locally resolved hydrodynamics. Using

reliable models that are based on a deep understanding of bubbly flows, promising results were obtained with this method in the recent years.

Despite the efforts being made in the last years to improve the models for the Euler-Euler method by validating a great model variety, no consensus for modelling could be found, especially in the area of chemical engineering (Tabib et al. 2008) (Masood & Delgado 2014). However, based on long-term validation of pipe flows in the area of nuclear safety engineering (Lucas et al. 2007a) (Frank et al. 2008) (Rzehak & Krepper 2013a) a baseline model has been suggested for bubbly flows (Rzehak & Krepper 2013b).

In such a baseline model, all well-known effects of bubbly flows are included and the model parameters are fixed. The baseline model is improved by simulating a broad range of experiments under different conditions with the fixed models. From such simulations, shortcomings are identified and the models are strategically improved with specifically dedicated experiments. Moreover, the baseline model is validated in a certain range of usage so that a prediction of bubbly flows is possible within an assessable error. This knowledge is essential for the process design of bubbly flows in all fields.

The superior aim of the present work is to improve the understanding of the hydrodynamics in bubbly flows towards predictable simulations in all fields. In particular, to adopt and extend the recently suggested baseline model for the Euler-Euler method to the applications beyond nuclear safety. Besides widespread CFD simulations of bubble columns, new measuring techniques and concepts were developed as well as experiments were executed particular for CFD validation.

1.2 Modelling bubbly flows

To understand complex bubbly flows, the motion of single bubbles is investigated, which is in general strongly affected by their shape. In simple quiescent fluids the shape can be determined by knowing the Reynolds number, which is the ratio between inertial and viscous forces

$$Re = \frac{\rho_l v_{rel} d_B}{\mu_l} \quad , \tag{1-1}$$

and the Eötvös/Bond number, which is the ratio between gravitational and surface tension forces

$$Eo = \frac{\Delta\rho g d_B^2}{\sigma} \quad . \tag{1-2}$$

Besides the material values density ρ, dynamic viscosity μ and surface tension σ, the bubble size and the slip/relative velocity v_{rel} between gas and liquid phase and the bubble diameter d_B is of importance. With these parameters the shape of bubbles can be estimated as demonstrated by Grace et al. (1976) proposing the Grace Diagram shown in Figure 1-1. Moreover, the rising velocity, which is equal to the relative velocity in quiescent fluids, can be estimated by calculating the Morton number

$$Mo = \frac{g\mu_l^4 \Delta\rho}{\rho_l^2 \sigma^3} \quad , \tag{1-3}$$

which is denoted as M in the Grace diagram.

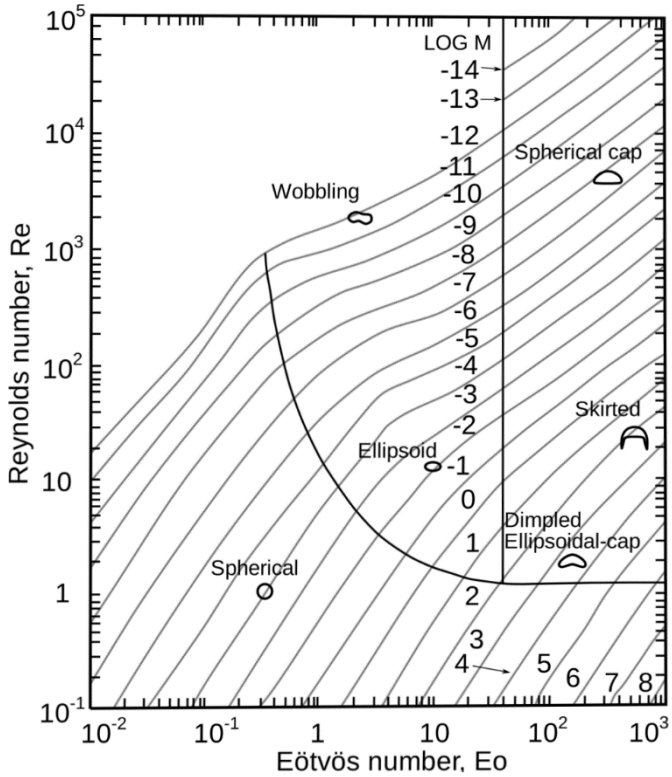

Figure 1-1 Grace Diagram (Grace et al. 1976) for bubble shapes and bubble rise velocity. The Morton number is denoted as 'M' in the diagram.

Since the Morton number is only a function of the material properties of both phases, the rising velocity is determined by knowing the bubble diameter and the materials. In the present work, air in deionized water is used in general, which has a Morton number of around $2.63 \cdot 10^{-11}$. Thus, the wobbling regime is very large ranging from $Eo = 0.25$ up to $Eo = 40$ or from a bubble diameter of 1.4 mm up to 17 mm, respectively.

In Figure 1-2 bubbles in a range from 2.2 mm up to 9.8 mm with different Eötvös numbers in air/water are shown, which is the size range investigated in the present work. In addition, a bubble in air/water with 2 ppm of Triton X-100 is shown. In this case, the bubble has a significantly different shape compared to the corresponding bubble in water, but with an almost equal Morton number (Surface tension measured in steady state conditions). The rising bubble has a slip velocity so that the impurity concentration on the surface is not homogeneous distributed. This leads to the Marangoni convection, which is not covered by the Grace Diagram. Such effects might be important in almost all bubbly flows in which chemical reactions take place since a multi-material composite is often present. The low integral concentration of 2 ppm illustrates that even small impurity concentrations lead to large effects and the great complexity of bubbly flows in technical use. Such complex impurity effects, however, are beyond the scope of this work since the hydrodynamics of clean air/water systems are still not well understood. Nevertheless, the findings are often compared to fully contaminated systems in which the bubble behavior is similar for different impurities due to a very high concentration of such.

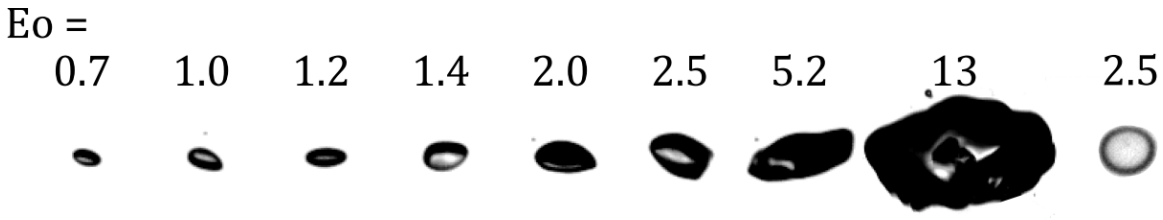

Figure 1-2 Bubbles for different Eötvös Numbers in air/water except the right bubble is in air/(water + 2ppm Triton X-100) at Morton number of $2.63 \cdot 10^{-11}$.

Although all bubbles in Figure 1-2 are in the wobbling regime distinct differences are observed. For lower Eötvös numbers the surface is smooth and the shape is elliptical, with increasing Eötvös number, the surface is disturbed and the shape becomes more random. These differences lead to different interactions of the bubble with the surrounding fluid. Usually, these interactions are modelled as forces that effect the bubble as well as the surrounding fluid according to the third Newton's law of motion.

The best-examined bubble force might be the drag force of a single bubble rising in a stagnant liquid. For example, important work on this topic was done by Haberman & Morton (1953) in the 50's; however, still new findings are made to the drag force like the dependency of the drag coefficient to the initial bubble shape (Tomiyama 2004). Without doubt, the drag is not the only effect but it is often stated as the most important one. In the present work, a variety of forces is used in order to model the complex bubble motion in technical use.

In moving fluids, also the turbulence is of importance. The turbulence is in general affected by the presence of a bubble, which has to be modeled as well. From single-phase flow different approaches regarding turbulence modeling exists that are also used for bubbly flows. In general, these approaches can be described by their capability to resolve different scales of fluid motion. In technical use, large apparatuses have to be modeled so that turbulence structures are almost completely modeled and barely resolved by the approach. In contrast, fundamental flow behavior is studied with methods that fully resolve the turbulence so that no modelling is needed. In the same way, approaches of modeling bubbles can be described by their capability to resolve the interface of the gas bubbles. Methods for technical use do not resolve the interface due to its complexity; methods used for model development fully resolve the interface. The first one need the just mentioned forces, the later one do not need any modeling of the bubble motion (for very simple problems). Naturally, the turbulence model and interface handling have to be consistent.

Simulations in which all time and length scales are resolved are called direct numerical simulations (DNS). Indeed, DNS of bubbly flows are not fully resolving all scales, for example, the coalescence of bubbles depends on a film rupture between the bubbles that is in the range of nanometers. Such small scales are beyond the possibilities and the present scope of DNS for bubbly flows, a discussion about this issue is for example given by Tryggvason et al. (2013).

Nevertheless, DNS in the field of bubbly flows is a very active field; probably the most investigated phenomenon is the drag of bubbles in an infinite fluid. The drag is correctly reproduced by DNS up to high Reynolds numbers and large bubbles (Dijkhuizen et al. 2010a). Thus, the methods to capture the deformable interface are at a high level, which

is also indicated by the simulations of Tripathi et al. (2015) proposing a new kind of break up mechanism at low Morton numbers from DNS simulations. Moreover, the lift force of bubbles in a shear field is a frequently topic of DNS. Whereas the calculation of the correct drag is a challenging task, dealing with the lift force is a more complicated problem since the bubble shape interacts with a shear field and the bubble wake. Therefore, a highly unsteady problem over a wide range of time and length scales occurs so that only studies were published containing just a small amount of bubbles and simulations (Rabha & Buwa 2009) (Zhongchuna et al. 2014). However, Dijkhuizen et al. (2010b) performed in a limited range of Reynolds numbers a large amount of DNS regarding the lift force and compared it to own experimental results. Important effects could be reproduced with the DNS but also deviations to their own experimental data arise, especially simulations in fluids with impurities. Besides the problem of bubbles in an infinite fluid, also the interaction of bubbles with a wall is recently investigated with DNS (Sugioka & Tsukada 2015).

DNS provide also room for simplifications so that DNS were realized for turbulent bubble laden flows in channels with the assumption of rigid spheres (Santarelli & Fröhlich 2012), small bubbles (Bolotnov et al. 2011) or in small deformation regimes (Dabiri et al. 2013) (Murai et al. 2001). Summarizing, DNS can provide essential data for single bubble phenomena up to turbulent flows with few bubbles. The recent methods can be used for assistance in modelling of physical effects. These simulations are still limited to low Reynolds numbers and/or only few simulations with few bubbles so that a statistical reliable validation is difficult.

A next step towards simulations at higher Reynolds numbers and increasing amount of bubbles is the Euler-Lagrange method. The bubbles are treated as point sources, thus the interface information are no longer directly available so that the interaction of the bubble and the fluid has to be modelled. The interactions are formulated as forces as described above. Besides the drag force, effects like the lagging boundary development in turbulent conditions (Basset force) up to bubble clustering effects are modeled. In addition, since the bubbles are in general larger than the smallest turbulence length scale a specific turbulence modelling is necessary. For this purpose, the most common methods are the large eddy simulations (LES) (bin Mohd Akbar et al. 2012) (Jain et al. 2013) and the unsteady Reynolds averaged Navier Stokes equations (URANS) (Muñoz-Cobo et al. 2012) (Besbes et al. 2015). Despite the simplification that bubbles are treated as points without interface, every bubble is tracked separately in order to track bubble-bubble and bubble-wall collisions as well. For some applications, bubbles can be merged to parcels to reduce the numerical effort. The knowledge of the collisions is used for a detailed modelling of the effects that arise from such, e.g. coalescence and break-up (Lau et al. 2014) (Gruber et al. 2013) (Jain et al. 2014).

In the Euler-Lagrange formulation, for every bubble a complete set of motion equations has to be solved, which are expensive calculations. Furthermore, a mapping from the Lagrange formulation of the bubbles to the Eulerian formulations of the fluid and vice versa must be implemented (Kitagawa et al. 2001). Obviously, the maximum possible bubble size is somehow restricted to the mesh size of the Eulerian fluid grid; else, the assumption of a point source is no longer valid. The grid size, however, is connected to the flow situation so that it is not freely selectable. Recently, methods that combine a resolved interface for large bubbles and the point source formulation for smaller bubbles

in the Lagrangian formulation are developed (Hua 2015). Nevertheless, bubbles exist that are too small for a resolved interface treatment but are too large for the Lagrangian formulation. To overcome this, Badreddine et al. (2015) proposed a new method to treat bubbles in this transition, which gives reasonable results for simple test cases.

Overall, the Euler-Lagrange method is a powerful and often used tool for simulating bubbly flows. Moreover, this field is a very active area of research proposing new ways of simulations and methods. Every bubble has to be tracked separately, which is for technical apparatuses usually far beyond the computational possibilities.

A higher level of modeling is the treatment of both phases as interpenetrating continua in the Eulerian formulation. The dispersed gas phase is averaged in space and/or time with the purpose to dissolve the interface of the bubbles so that a continuum formulation is obtained. Without knowing anything about the interface structure, every bubble-liquid, bubble-wall and bubble-bubble interaction has to be modeled. Nevertheless, simulations in which every effect is seen locally, depending on the used models, for very large apparatuses are possible. This approach is called Euler-Euler formulation and is the objective of the present work. A detailed introduction is given in the following sections.

In contrast to the Lagrangian approach, the Eulerian description has no limits regarding the bubble size to cell size ratio. However, the modeling of very large bubbles, which might be already treated as gas structures, in the Eulerian framework is difficult especially looking at the turbulence modeling. For this problem, also promising attempts were made to combine resolved and unresolved bubbly flow modeling, e.g. the generalized two-phase flow (GENTOP) concept as described by Hänsch et al. (2012). Such large bubbles that have to be resolved, however, are not in the focus of the present work.

The highest levels of modeling are the integral based methods that model parts of an apparatus, a complete apparatus or a complete process module. The models are normally designed for one existing process so that they are less applicable to others. Usually, the hydrodynamics are given as an input and specific values or the yield is calculated in a limited input range. Such methods are typically used in practice of process engineering.

The advantage of CFD methods compared to integral methods is obvious; the CFD methods are general so that they can be used for every process configuration. In general, CFD methods are used if local effects, e.g. complex geometrics, are important for the total process. Such problems are called multiscale problems since small scales influence the large scale and vice versa. Bubbly flows are such multiscale problems, even if the reactor geometry is simple. Usually, the flow on every scale in bubbly flows is significantly influenced by the bubbles. The local bubble concentration and size are in return determined by the local flow parameters. Thus, the hydrodynamics in bubbly flows cannot be modeled in general with simple zero or one-dimensional approaches. Moreover, complex flow situations including heat and mass transport underline the need of CFD for bubbly flows. Apart from interest in its own right, the hydrodynamic studies from the present work are a good starting point for the investigation of such complex situations including heat and mass transport.

2 Simulation Methods

2.1 Computational fluid dynamics

The formulation of conservative equations is the basic concept of fluid dynamics and so the basic concept of computational fluid dynamics (CFD). In these fields, a separation between material or Lagrangian coordinates and spatial or Eulerian coordinates is used. At first, the Reynolds transport theorem used for the Lagrange perspective as a generalization of the Leibniz's rule for differentiation of integrals is derived. Afterwards, the finite volume method is explained as an Eulerian perspective.

2.1.1 Material balance equations – Reynolds transport theorem

The Leibniz's rule gives information how to derivate an integral with the limits of integration as a function of the variable to derivate. Let be $f(t,x)$ a sufficient smooth function that the partial derivate of $f(t,x)$, $\partial_t f(t,x)$ and $f(t,x)$ exists and is continuous in t and x, then the Leibniz's rule reads

$$\frac{d}{dt}\left(\int_{a(t)}^{b(t)} f(t,x)dx\right) = \int_{a(t)}^{b(t)} \partial_t f(t,x)dx + f\big(t,b(t)\big)\frac{db(t)}{dt} - f\big(t,a(t)\big)\frac{da(t)}{dt}. \qquad (2\text{-}1)$$

This rule can be also used for a three dimensional volume $V(t)$ that is changing over time. This formulation is called the Reynolds transport theorem:

$$\frac{d}{dt}\left(\int_{V(t)} \Phi(t,\boldsymbol{x})dV\right) = \int_{V(t)} \partial_t \Phi(t,\boldsymbol{x})dV + \oint_{\partial V(t)} \Phi(t,\boldsymbol{x})\boldsymbol{v_b}\cdot\boldsymbol{n}dA\,. \qquad (2\text{-}2)$$

The boundary of the volume $V(t)$ is written as $\partial V(t)$, the velocity of the boundary is written as $\boldsymbol{v_b}$. As can be seen, the Reynolds transport theorem gives no information about the surrounding flow field or matter of the surrounding volume. On the right hand side, the first term is the change of the field variable Φ over time itself, whereas the second term is the change of the field variable Φ caused by a movement of the boundary.

The material or Lagrangian coordinates are a way of defining the volume used in the Reynolds transport theorem so that the volume consists always the same continuum-matter, particles or other matters depending on the problem. In consequence, if the volume is located in a velocity field the boundary velocity $\boldsymbol{v_b}$ in Equation (2-2) is the same velocity as the instantaneous velocity at the boundary of the volume when the volume is defined as a material volume.

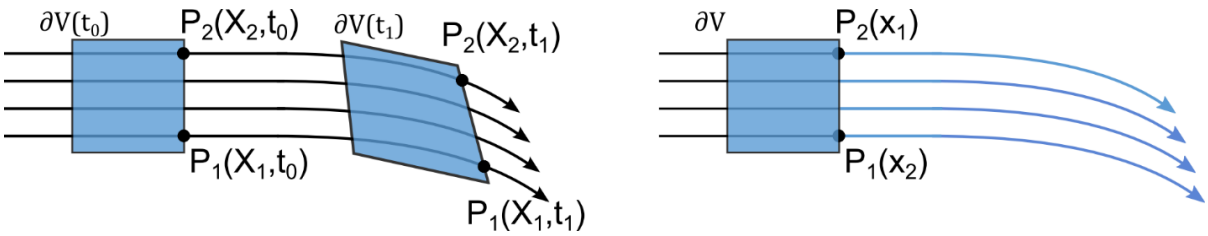

Figure 2-1 The difference between material and spatial perspective. Left a material control volume with always the same material; right a fixed control volume with the streaklines in blue.

In Figure 2-1 the material and spatial perspective is sketched, the blue material volume in the left picture is shown at two different times, t_0 and t_1, and is moving with the flow field. Exemplary, two points are highlighted in Lagrangian coordinates X. Following them over time, the pathlines, which are in a steady flow equal to the streamlines and streaklines, are obtained. Since a flow field is continuous, the position x of every point in the material control volume can be calculated by knowing the flow field itself, the starting point X (which are called Lagrangian coordinates) and the time t. Consequently, a transformation to the spatial coordinates x, which are the coordinates connected to the matter inside the volume, can be given as

$$x = \theta(X, t). \tag{2-3}$$

Defining the volume in the spatial perspective the volume is not depending on the matter inside the volume. A volume in spatial coordinates for a fixed coordinate system is illustrated In Figure 2-1 on the right hand side. If the matter that passes the spatial volume is tracked, the streaklines are obtained. Obviously, if the considered volume is not connected to matter inside the volume the boundary velocity $\boldsymbol{v_b}$ in Equation (2-1) is not the same as the velocity of the flow field. In the case that the volume is fixed in the used reference coordinate system, the boundary velocity $\boldsymbol{v_b}$ is zero and the second term in Equation (2-1) vanishes.

Using the Stokes' theorem, the surface integral on the right hand side of Equation (2-2) can be written as the divergence of $\Phi(t, \boldsymbol{x})\boldsymbol{v_b}$ inside the control volume so that a conservative balance equation can be formulated:

$$\frac{d}{dt}\left(\int_{V(t)} \Phi(t, \boldsymbol{x}) dV\right) = \int_{V(t)} \partial_t \Phi(t, \boldsymbol{x}) + \boldsymbol{\nabla}(\Phi(t, \boldsymbol{x})\boldsymbol{v_b})\, dV = RHS\,. \tag{2-4}$$

The right hand side (RHS) contains the efflux $\mathfrak{J}$ of the volume V and a source term S_Φ inside the volume

$$RHS = -\oint_{\partial V(t)} \mathfrak{J} \cdot \boldsymbol{n}\, dA + \int_{V(t)} S_\Phi\, dV = \int_{V(t)} -\boldsymbol{\nabla}\mathfrak{J} + S_\Phi\, dV \tag{2-5}$$

Additionally, in Equation (2-5) Stokes' theorem is used to rewrite the surface integral. Using the material perspective, the efflux is not containing any convective flux since the volume $V(t)$ is defined in a way that all matter stay inside the volume. Therefore, the efflux is containing in general transfer effects like the viscosity in the momentum equation when the material perspective is used.

In the following of this work, the Lagrangian formulation/material perspective is used for a dispersed phase like solid or gaseous particles (if they are resolved). Moreover, the particles in such problems are simplified to points, so the efflux can be treated as source terms and no surface deformation occur. The continuous phase (including an averaged dispersed phase) is formulated in the Eulerian formulation/spatial perspective treated by the finite volume method as discussed in the next section.

2.1.2 General balance equation, Navier-Stokes equation and finite volumes

A general balance equation can also be formulated from the Reynolds transport theorem; however, it is common to formulate a general balance equation from a differential form

as will be shortly shown in this section. The common way to formulate this form is from the Eulerian perspective that is straightforward towards the finite volume method (FVM). The later obtained results might not be exactly calculated with the methods shown here since complicated solution methods for the FVM exists in commercial CFD codes which to explain and review is beyond the scope of this work.

The general balance equation can be derived with an infinitesimal volume in Cartesian coordinates as shown in Figure 2-2 without losing generality. in Figure 2-2 the flux around an infinitesimal volume is shown, which summed up over all elements gives

$$\begin{aligned}\left(e_x\mathfrak{J} - e_x\mathfrak{J} + \frac{\partial \mathfrak{J}}{\partial x}dx\right)dydz + \left(e_y\mathfrak{J} - e_y\mathfrak{J} + \frac{\partial \mathfrak{J}}{\partial y}dy\right)dxdz \\ + \left(e_z\mathfrak{J} - e_z\mathfrak{J} + \frac{\partial \mathfrak{J}}{\partial z}dz\right)dxdy = \left(\frac{\partial \mathfrak{J}}{\partial x} + \frac{\partial \mathfrak{J}}{\partial y} + \frac{\partial \mathfrak{J}}{\partial z}\right)dV \\ = (\nabla \cdot \mathfrak{J})dV\end{aligned} \tag{2-6}$$

The unit vectors are written as $e_{x,y,z}$, the product of the unit vector with the flux $\mathfrak{J}$ is the flux in the direction of the unit vector. The flux $\mathfrak{J}$ is defined per area; therefore, the flux is multiplied with the infinitesimal front surface of the volume. The expression can be simplified by sum up the flux in every direction and take out the equal amount of the in and out flow terms. It remains the effective flux $\nabla \cdot \mathfrak{J}$ per volume.

In contrast to the material perspective, the efflux contains in the spatial perspective also the convective part. Thus, the flux can be split up to $\mathfrak{J} = \rho\phi\boldsymbol{v} + \mathfrak{N}$ with $\rho\phi\boldsymbol{v}$ the convective flux and $\mathfrak{N}$ the non-convective flux. Besides the change of the efflux, the properties inside the volume can change because of processes inside the volume itself, this processes can be written as source terms S_ϕ. Since no other processes than flux through the boundaries or internal processes can change the properties inside the volume, a general balance equation in arbitrary coordinates can be formulated

$$\frac{\partial \rho\phi}{\partial t} = -\boldsymbol{\nabla} \cdot (\rho\phi\boldsymbol{v} + \mathfrak{N}) + S_\phi \;\Leftrightarrow\; \frac{\partial \rho\phi}{\partial t} + \boldsymbol{\nabla} \cdot (\rho\phi\boldsymbol{v}) = -\boldsymbol{\nabla} \cdot (\mathfrak{N}) + S_\phi\,. \tag{2-7}$$

The mass balance equation is obtained by setting $\phi = 1$. Furthermore, there is no source of mass and no non-convective transport of mass, thus $\mathfrak{N} = 0 = S_\phi$. The well-known continuity equation is obtained

$$\frac{\partial \rho\phi}{\partial t} + \boldsymbol{\nabla} \cdot (\rho\phi\boldsymbol{v}) = 0\,. \tag{2-8}$$

The conservation of momentum can be expressed by setting $\phi = \boldsymbol{v}$, $\mathfrak{N} = -p\boldsymbol{I} + \boldsymbol{T}$ and $S_\phi = \rho\mathfrak{g}$. The transport term is the sum of the scalar pressure multiplied with the unit tensor $\boldsymbol{I}$ and the viscous stress tensor. The viscous stress tensor can be very complex depending on the used fluid. In the present work, however, mainly water is used and the viscous stress tensor can be simplified to $\boldsymbol{T} = \frac{1}{2}\left((\nabla\boldsymbol{v}) + (\nabla\boldsymbol{v})^T\right)$. The displacement in a fluid is the velocity so the distortion gradient is equal to the Jacobian matrix of the velocity $\nabla\boldsymbol{v}$. The viscous stress tensor is a linearization of the Green-Lagrange deformation tensor $E = \frac{1}{2}\left((\nabla\boldsymbol{v} + \boldsymbol{I})(\nabla\boldsymbol{v} + \boldsymbol{I})^T - \boldsymbol{I}\right) = \frac{1}{2}(\nabla\boldsymbol{v} + (\nabla\boldsymbol{v})^{\boldsymbol{T}} + (\nabla\boldsymbol{v})^{\boldsymbol{T}}\nabla\boldsymbol{v})$, the product of the Jacobian matrix with its transposed is taken as zero and the viscous stress

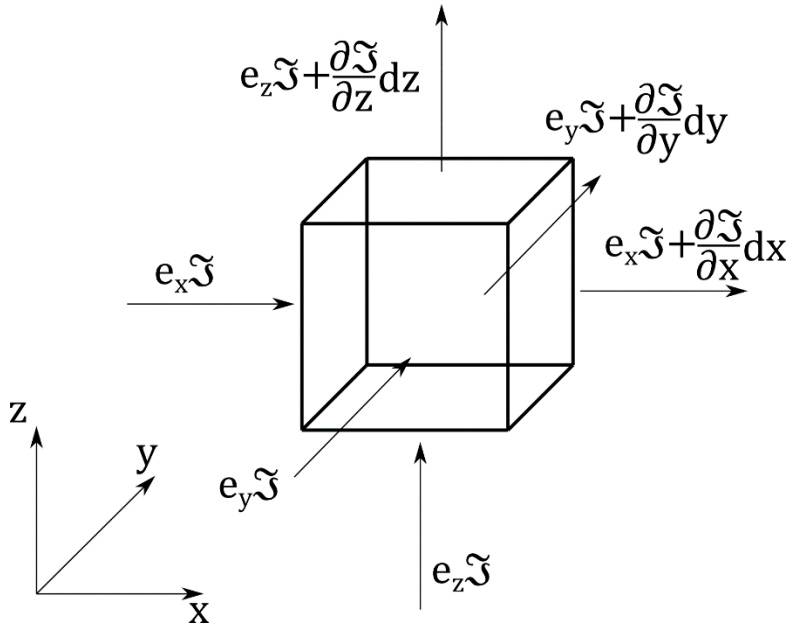

Figure 2-2 Flux around an infinite volume

tensor is obtained $\boldsymbol{T} = t_{ij} = \frac{1}{2}\left(\frac{\partial v_i}{x_j} + \frac{\partial v_j}{x_i}\right)$. With $\mathfrak{g}$ called the body forces as momentum source term the momentum conservation can be written as

$$\frac{\partial \rho \boldsymbol{v}}{\partial t} + \boldsymbol{\nabla}(\rho \boldsymbol{v}\boldsymbol{v}) = -\boldsymbol{\nabla} \cdot p + \boldsymbol{\nabla} \cdot \boldsymbol{T} + \rho \mathfrak{g} \,. \tag{2-9}$$

In the same way the energy conservation and species conservation equations can be obtained, which is not shown at this point.

The Navier-Stokes equations are the summarization of the mass, momentum and energy conservation equations. In general, no analytic solution exists on complex computational domains and the problem has to be solved numerically. For this purpose different numerical methods exist, the most widely-know methods are the finite element method (FEM) and the finite volume method (FVM). Using the latter one, the computational domain is split up in many well-defined finite volumes.

The finite volumes that are in sum the finite computational domain are generated in a way that every surface of a finite volume has contact to another finite volume or the boundary of the domain and that no gaps are present. Therefore, the volumes are discretizing the computational domain and called mesh or grid in total and grid cell in particular. Around the grid cell, a balance equation equal to the balance equation around an infinite volume can be formulated. In general, the integral formulation of Equation (2-7) is more advantageous for this purpose

$$\int_{GC} \frac{\partial \rho \phi}{\partial t} dV + \oint_{\partial GC} \rho \phi \boldsymbol{v} \cdot n d\boldsymbol{A} = -\oint_{\partial GC} \mathfrak{N} \cdot n d\boldsymbol{A} + \int_{GC} S_\phi dV \,. \tag{2-10}$$

This equation is solved for every grid cell. Furthermore, since the sum of all grid cells is equal to the domain the general integral balance equation is obtained by summation of all grid cells. Therefore, the finite volume method is fulfilling the general balance equation for the domain automatically, which is a benefit of this method.

The values of a problem during a simulation, however, are only known at discrete points that are usually located in the centroid of the grid cells. Thus, the Integrals have to be approximated somehow. The surface integrals are commonly approximated with the Gaussian quadrature rule, the simplest one is to take the integral average multiplied with one. The integral average is often taken as the value in the centroid of the grid cell surface, which is correct if the problem is linear. This approximation is of second order, nevertheless, the value in the centroid of the surface is not known since only the values in the volume centroid are known. Consequently, the value in the surface centroid has to be interpolated which can be done by just using the next known value in the direction of the flow (upwind scheme – first order) or by interpolating linear between the neighboring grid cell (central difference scheme – second order). The volume integral is approximated similar, the value at the volume centroid is multiplied with the volume of the grid cell, which is correct for linear problems. The approximation and interpolation schemes can be more complex if the problem requires a complex treatment (Ferziger & Peric 2002).

Summarizing, the material/Lagrangian and spatial/Eulerian perspective and the corresponding balance equations for mass and momentum were introduced. Furthermore, with the finite volume method a numerical method was shown, which is able to solve these balance equations on a computational domain. The presented methods can also be applied to multiphase problems; these methods, however, are only valid whether one phase or only the interface itself is inside the considered volume. In the next section, a way is shown how these methods are formulated for multiphase problems without these limitations.

2.2 Eulerian averaging, two-fluid model and closure problem

In the following section the two fluid method for formulating a balance equation for a volume with both phases inside is introduced. The main idea is to average the quantities of both phases weighted with the volume fraction. The averaging can be done over time at one point as it is shown in this section or by averaging over a volume; in both cases the same equations are obtained. As a result, balance equations for every phase are obtained that are coupled with interphase exchange terms. The cost of the averaging is the loss of the interface information, which has to be modeled and put into the interphase exchange terms. The advantage of the lost interface is that the simulation methods are simplified and multiphase problems with a very large interface size can be simulated.

In the following, a simplification is done by assuming that the interface cannot store mass or momentum. The consequence of the first assumption is that the interface is in an equilibrium; the consequence of the second one is that the interface tension is not minded in the balance equation. A more precise treatment of the interface can be obtained by formulating the so-called jump conditions over the interface as discussed for example by Aris (1962) or Delhaye (1974). In the present work, however, the above simplifications are sufficient. In the following, a very short derivation of the two-fluid formulations is given by using the averaging in time method based on the work of Ishii & Hibiki (2006). The purpose is to give an idea of the two-fluid method and to introduce the notations used in this work, a complete derivation can be found in literature.

At first, the state functions are defined which distinguish between the phases and the interface. If a problem with two phases is given, two state functions and one interface function is needed

$$M_k(x,t) = \begin{cases} 1 & \text{if the } k^{th} - \text{phase is present at point x at time t} \\ 0 & \text{else} \end{cases}$$
$$M_S(x,t) = \begin{cases} 1 & \text{if the interface is present at point x at time t} \\ 0 & \text{else} \end{cases} . \tag{2-11}$$

A general differentiable function inside the phases is written as F; the multiplication with the state function is written as F_k. The thickness of the interface δ is assumed to vanish, which is written as $\lim \delta \to 0$.

With the assumption of a vanishing interface thickness the Eulerian time average of the function F is defined as

$$\bar{F}(x,t) \equiv \lim_{\delta \to 0} \frac{1}{\Delta\tau} \int_{[\Delta\tau]_T} F(x,\tau) d\tau \ . \tag{2-12}$$

With τ the averaging time, $\Delta\tau$ the average interval and $[\Delta\tau]_T$ the time interval without the surface, which is the same as $[\Delta\tau]$ with an assumed zero boundary thickness. Using this averaging the local void fraction of the k^{th}-phase can be defined

$$\alpha_k \equiv \overline{M_k}(x,t) \, . \tag{2-13}$$

Further, the mean value of the general function F of the k^{th}-phase $\overline{F_k}$ is calculated to

$$\overline{F_k} = \overline{F M_k} \, . \tag{2-14}$$

Since the integral is a linear function, the averaged values are also linear

$$\bar{F} = \sum_k \overline{F_k} \ ; \ 1 = \sum_k \overline{M_k} = \sum_k \alpha_k \, . \tag{2-15}$$

Therefore, the local void fraction can also be interpreted as a probability of seeing the k^{th}-phase at the place x to the time t.

Besides the averaged values over the total time interval $\bar{F}$, the averaged values of only the k^{th}-phase are also of interest which are called phase average

$$\overline{\overline{F_k}} \equiv \frac{\overline{M_k F_k}}{\overline{M_k}} = \frac{\overline{F_k}}{\alpha_k} \, . \tag{2-16}$$

The phase-averaged values are obtained by weighting the Eulerian averaged values with the state function. In particular, the phase average values are not depending on the quantity of the phase since it is divided by this. Finally, the mass weighted averaged values are needed since the conserved quantities are extensive values

$$\widehat{\phi_k} \equiv \frac{\overline{\rho_k \phi_k}}{\overline{\rho_k}} = \frac{\overline{\overline{\rho_k \phi_k}}}{\overline{\overline{\rho_k}}} \, . \tag{2-17}$$

Since the mass is conservative itself, the mass averaged quantities are additive and from the definition of the mass weighted mean values follows

$$\overline{\rho\phi} = \sum_k \overline{\rho_k \phi_k} \,. \tag{2-18}$$

Summarizing, a relation can be written between mixture properties and phase averaged properties

$$\hat{\phi} = \frac{\sum_k \alpha_k \overline{\overline{\rho_k}}\,\widehat{\phi_k}}{\sum_k \alpha_k \overline{\overline{\rho_k}}} = \frac{\sum_k \overline{\rho_k}\,\widehat{\phi_k}}{\sum_k \overline{\rho_k}} \,. \tag{2-19}$$

With the above shown averaging methods, the balance equations for multiphase problems can be formulated. Nevertheless, a lot work has to be done to formulate the differentiation and all fluxes for the averaged values correctly, this is referred to the literature at this point, e.g. as is found in the book of Ishii & Hibiki (2006). The mass conservation for the k^{th}-phase can be written after averaging as

$$\frac{\partial \alpha_k \overline{\overline{\rho_k}}}{\partial t} + \boldsymbol{\nabla} \cdot (\alpha_k \overline{\overline{\rho_k}}\,\widehat{\boldsymbol{v_k}}) = \Gamma_k \,. \tag{2-20}$$

The mass exchange term between the phases is written as Γ_k; the sum of all mass exchange terms is zero because it is assumed that the interface cannot store mass. Moreover, the momentum balance equation can be formulated as

$$\begin{aligned} \frac{\partial \alpha_k \overline{\overline{\rho_k}}\,\widehat{\boldsymbol{v_k}}}{\partial t} + \boldsymbol{\nabla} \cdot (\alpha_k \overline{\overline{\rho_k}}\,\widehat{\boldsymbol{v_k}}\widehat{\boldsymbol{v_k}}) \\ = -\boldsymbol{\nabla} \cdot (\alpha_k \overline{\overline{p_k}}) + \boldsymbol{\nabla} \cdot \left[\alpha_k \left(\overline{\overline{T_k}} + \mathfrak{C}_k^T\right)\right] + \alpha_k \overline{\overline{\rho_k}}\,\widehat{\boldsymbol{g_k}} + S_{\boldsymbol{k}} \,. \end{aligned} \tag{2-21}$$

The averaged viscous stress tensor of the k^{th}-phase $\overline{\overline{T_k}}$ can be obtained by phase averaging the velocities. Additionally, an interfacial turbulent flux tensor $\mathfrak{C}_k^T$ is obtained due to the averaging. Moreover, the interfacial momentum exchange term $S_{\boldsymbol{k}}$ occurs with the side condition

$$\sum_k \mathrm{S}_k = S_S = 0 \,. \tag{2-22}$$

The sum of all interfacial exchange terms is zero because it is assumed that the interface cannot store momentum. The interfacial momentum exchange term connects the phases; all interface information that is lost due to the averaging process must be covered in this term. If for example the interfacial exchange were zero, the phases would barely 'see' each other and would just exists side by side.

The correct formulation of the interfacial exchange term is called closure problem and is one topic of the present work. The exchange is in general formulated as force per volume, which is called closure models, and contains for example the drag force between the phases. The forces in the exchange term can describe complex phenomena like the interaction of the wake structure behind bubbles and the bubble itself. In the next section, the closure models are formulated and reviewed shortly.

Summarizing, the two-fluid model is introduced and the average balance equations for the phases are given. Because of the averaging a probability function α_k, which is the local void fraction, is obtained that quantifies the probability if the k^{th}-phase can be seen

at a point x and time t. Therefore, the phases literally exists side by side, which is reflected by formulating balance equations for every phase in the same space and time. The connection of the phases is done by coupling terms, which have to be modelled explicitly since the interface information is lost due to the averaging.

2.3 Closure models and multiple bubble velocity classes

In the following section, the above-described closure models without the turbulence closures are described. In the present work, the drag, lift, turbulent dispersion, virtual mass and wall force might be the most important. Noteworthy, a boundary layer that is not in the steady state, which is modeled as so-called history force, affects all these forces. Such effects are usually not taken into account because the other forces are measured in more or less stagnant fluids under steady state conditions. The drag and lift force are described in detail in the following sections, the others briefly in the following.

The turbulent dispersion force describes the effect of the turbulent fluctuations of the liquid velocity on the bubbles. Burns et al. (2004) derived by Favre averaging the drag force an explicit expression, namely

$$F_{Disp} = \frac{3}{4} C_D \frac{\alpha_G}{d_B} |\vec{v}_G - \vec{v}_L| \frac{\mu_L^{turb}}{\sigma_{TD}} \left(\frac{1}{\alpha_L} + \frac{1}{\alpha_G} \right) \nabla \alpha_G \,. \tag{2-23}$$

In analogy to molecular diffusion, σ_{TD} is referred to as a Schmidt number. In principle, it should be possible to obtain its value from single bubble experiments by evaluating the statistics of bubble trajectories in well-characterized turbulent flows but to the authors knowledge this has not been done yet. A value of $\sigma_{TD} = 0.9$ is typically used.

A bubble translating next to a wall in an otherwise quiescent liquid experiences a lift force. This wall lift force, often simply referred to as wall force, has the general form

$$F_{Wall} = \frac{2}{d_B} C_W \rho_L \alpha_G |\vec{v}_G - \vec{v}_L|^2 \, \hat{y} \,, \tag{2-24}$$

in which $\hat{y}$ is the unit normal perpendicular to the wall pointing into the fluid. The dimensionless wall force coefficient C_W depends on the distance to the wall y; the coefficient is expected to be positive so that the bubble is driven away from the wall. Based on the observation of single bubble trajectories in simple shear flow of glycerol water solutions Tomiyama et al. (1995) and later Hosokawa et al. (2002) concluded the functional dependence

$$C_W(y) = f(Eo) \left(\frac{d_B}{2y} \right)^2 , \tag{2-25}$$

where in the limit of small Morton number (Hosokawa et al. 2002)

$$f(Eo) = 0.0217 Eo \,. \tag{2-26}$$

The experimental conditions on which Eq. (2-26) is based are $2.2 \leq Eo \leq 22$ and $-2.5 \leq \log_{10} Mo \leq -6.0$ which is still different from the water–air system with $Mo = 2.63 \cdot 10^{-11}$. A recent comparison of this and other distance-dependencies that have been proposed (Rzehak et al. 2012) has nonetheless shown that good predictions could be obtained for a set of data on vertical pipe flow of air bubbles in water.

The virtual mass is the inertia of the surrounding fluid that has to be taken into account when a bubble or particle is accelerated relative to the surrounding continuous phase

$$F_{VM} = C_{VM}\alpha_G\rho_G\left(\frac{D\vec{u}_G}{Dt} - \frac{D\vec{u}_L}{Dt}\right), \tag{2-27}$$

where D/Dt denotes the substantial derivative. The coefficient C_{VM} is simply set to 0.5 as suggested by Mougin and Magnaudet (2002).

2.3.1 Drag force

Bodies within a fluid that are moving with a relative velocity greater zero experience a drag force counteracting to the motion in the opposite direction of the velocity. The drag force F_D is a function of the density ρ, viscosity μ, the velocity v and a length scale of the object. Regarding to the Buckingham Π-Theorem (Buckingham 1914) two dimensional groups can be formed from this 5 variables, which are taken as the Reynolds number and the drag coefficient

$$C_D \equiv \frac{F_D}{0.5\rho v^2 A}\ . \tag{2-28}$$

The surface A is a reference area, which is here defined as the projected area of the sphere equivalent volume of the bubble (Haberman & Morton 1953).

Indeed, the drag coefficient is the sum of the frictional drag coefficient and the pressure drag coefficient. The corresponding frictional force and pressure drag force are obtained by integrating the shear stress over the surface and the pressure over the surface, respectively. For completely laminar flow situations, the drag force is dominated by the frictional force since the inertial forces are small compared to the viscous forces as indicated by a particle Reynolds number far below one. Here, a theoretical solution of the drag force is possible that is called the Stokes law; for rigid spheres, the drag coefficient is calculated to $24/Re$. For bubbles it can be shown that the drag coefficient is $16/Re$ (Hadamard 1911) which is only the 2/3 of the rigid sphere since the bubble surface is not rigid. However, through pollution and the resulting Marangoni convection towards the bubble cap, the drag force is nearly the same as for the rigid sphere (Lakshmanan & Ehrhard 2010).

Looking at bubbles, the drag force is equal to the buoyancy force if the bubble rises with a constant velocity in a quiescent fluid. Thus, determining the drag coefficient is reduced to determine the terminal velocity of the bubble. Based on a dimensional analysis by Schmidt (1934) using the Π-Theorem and further work by Rosenberg (1950), the bubble motion was described using the Reynolds number, the drag coefficient and the Morton number. The Morton number is a combination of the Froude (Fr - ratio of inertia to body force), Reynolds (ratio of inertia to viscous force) and Weber number (We - ratio of inertia to surface forces). Based on this Haberman & Morton (1953) described based on a large preceding experimental work of others the bubble motion for various liquids.

In the following years, several theoretical and experimental work was done regarding the bubble motion, which is for example summarized by (Loth 2008). The drag coefficient, however, is often formulated as a function of the Reynolds and Eötvös number (ratio of surface tension to body forces) in which empirical and semi-empirical

formulations exists. Normally, three different conditions are distinguished, spherical bubbles, distorted bubbles and cap bubbles with a blending function between them as for example used by Ishii & Zuber (1979)

$$C_{D,Sphere} = \frac{24}{\mathrm{Re}}(1 + 0.1\mathrm{Re}^{0.75}) \ ,$$

$$C_{D,Distorted} = \frac{2}{3}\mathrm{Eo}^{0.5} \ , \tag{2-29}$$

$$C_{D,Cap} = \frac{8}{3} \ ,$$

$$C_D = \left(\max\left(C_{D,Sphere}, \min\left(C_{D,Distordted}, C_{D,Cap}\right)\right)\right) \ .$$

This drag law is among others measured for polluted air/water systems; differences occur for pure systems as shown by Tomiyama et al. (1998).

Another approach of describing the drag coefficient is done by Bozzano and Dente (2001) by the multiplication of a friction factor f to a deformation factor $(a/r)^2$ – a is the major axis and r the equivalent spherical radius – obtained from a minimization of the total energy

$$f = \frac{48}{\mathrm{Re}}\left(\frac{1 + 12\mathrm{Mo}^{1/3}}{1 + 36\mathrm{Mo}^{1/3}}\right) + 0.9\frac{\mathrm{Eo}^{3/2}}{1.4\left(1 + 30\mathrm{Mo}^{1/6}\right) + \mathrm{Eo}^{\frac{3}{2}}} \ ,$$

$$\left(\frac{a}{r}\right)^2 \cong \frac{10\left(1 + 1.3\ \mathrm{Mo}^{1/6}\right) + 3.1\mathrm{Eo}}{10\left(1 + 1.3\ \mathrm{Mo}^{1/6}\right) + \mathrm{Eo}} \ , \tag{2-30}$$

$$C_D = f \cdot \left(\frac{a}{r}\right)^2 .$$

The discussed drag laws are compared in Figure 2-3; clearly, the differences between the drag laws for pure systems and the contaminated systems are seen. For the CFD simulations in the present work the drag law of Ishii and Zuber (1979) will be used. The drag force formulate in frame of the two fluid averaging as explained in Section 2.2 reads

$$F_{Drag} = \frac{3}{4d_B}C_D\rho_l\alpha_G|\vec{u}_G - \vec{u}_L|(\vec{u}_G - \vec{u}_L) \ . \tag{2-31}$$

The gas velocity is denoted with $\vec{u}_G$ and the liquid velocity with $\vec{u}_L$.

For tracking mini bubbles in the sections below, the drag law of Bozzano and Dente (2001) will be used since the experimental data for this drag law are validated also for smaller bubbles.

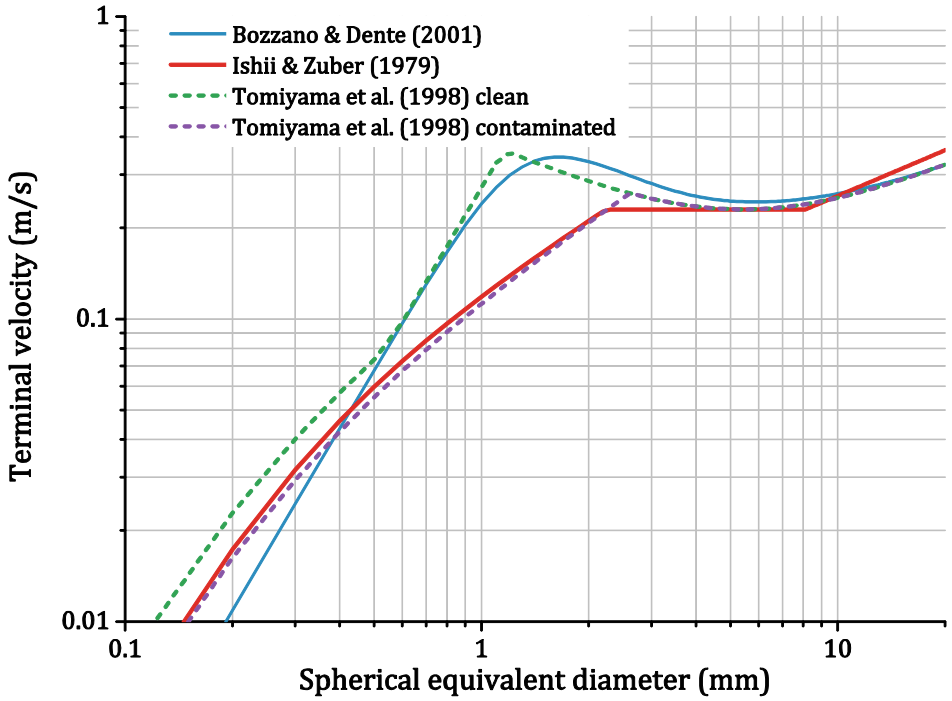

Figure 2-3 Terminal velocity obtained with different drag laws in air/water systems

2.3.2 Lift force

The lift force is usually a force acting mainly perpendicular to the main flow direction. In contrast to the well-known aerodynamic lift force the lift force on particles and bubbles is fundamental different. The lift on very small rigid particles due to the shear lift force and particle rotation was described by Saffmann (1965) for very low particle and vorticity Reynolds numbers. Nonetheless, larger bubbles also experience a lift force even in complex flow situations as shown for example by Serizawa et al. (1975) by measuring a wall peak in bubbly pipe flows. The lift force on bubbles is described by a shear induced formulation (Zun 1980) based on the formulation for rigid spherical particles (Lawler 1971):

$$F_{Lift} = -C_L \rho_L (\vec{u}_G - \vec{u}_L) \times rot(\vec{u}_L) \ . \tag{2-32}$$

The lift force coefficient is denoted with C_L, the liquid velocity with $\vec{u}_L$, the gas velocity with $\vec{u}_G$, the liquid density with ρ_L. Various work was done calculating the lift force for inviscid fluids at small shear rates (Auton 1987) and extending the work by Saffmann (Mei & Klausner 1994) (Legendre & Magnaudet 1997) for viscid fluids $Re_P \to 0$ and finite shear rates. It was found that at very low particle and vorticity Reynolds numbers the lift force is $(2/3)^2$ of the lift force of a rigid sphere (Legendre & Magnaudet 1997). Based on an extensive study on spherical non-deformable bubbles based on DNS calculations by Legendre & Magnaudet (1998) two regimes can be identified, the viscid dominant regime with $Re_P \to 0$ and the inertia dominated $Re_P \to \infty$ describing two different physical effects. At low Reynolds numbers, the effect is dominated by the rapid diffusion of the vorticity generated by the presence of the bubble and its asymmetrical transportation by the far flow field. At high Reynolds numbers, the vorticity of the undisturbed flow is asymmetrical distorted due to the presence of the bubble. In between, the effects get very

complicated and are depending on the shear rate (Legendre & Magnaudet 1998). From the theoretical and numerical work, the lift coefficient was found to be 0.5 for higher particle Reynolds number; however, some experimental work, for example by Zun (1980) or Lance & de Bertodano (1994), suppose a lift force coefficient between 0.2 and 0.3. Furthermore, the lift force is also influenced by the contamination of the water and even a change of sign appear due to contamination was observed (Fukuta et al. 2008).

The complexity is increased when the bubbles get larger and the assumption of spherical bubbles is not valid or the shear stress is that high that the bubbles are deformed. For larger bubbles, the lift force is changed fundamentally as experimentally shown by Kariyasaki (1987). Kariyasaki used a rotating belt in a channel and supplied gas bubbles of different sizes; they observed that the lift force changes the sign for larger bubbles. This change of sign could also be shown in DNS simulations (Ervin & Tryggvason 1997) (Bothe et al. 2006). Two fundamental effects describing the lift force for larger bubbles might be identified. First, the non-spherical shape which is theoretically examined using a fixed ellipsoid for low shear rates and inviscid fluids by Naciri (1992), which is later studied by Adoua et al. (2009) using DNS calculations over a wide range of Reynolds numbers and shear rates. The lift force for this fixed ellipsoid is significantly influenced by the Reynolds number, shear rates and the aspect ratio of the ellipsoid. Increasing the aspect ratio for specific shear rates and Reynolds numbers, the lift force changes its sign caused by the vorticity generated at the ellipsoid surface. Besides the change of sign, it could be shown experimentally by Tomiyama et al. (1999) (2002) for high Morton numbers and low Reynolds numbers that the lift force coefficient might not be influenced by the shear rate. Thus, the lift force might be dominated by the deformation of the bubble surface by the shear flow and the produced vortexes at the bubble surface itself. The empirical correlation for the lift coefficient by Tomiyama et al. (2002) reads

$$C_L = \begin{cases} \min[0.288\tanh(0.121\mathrm{Re}), f(\mathrm{Eo}_\perp)], & \mathrm{Eo}_\perp < 4 \\ f(Eo_\perp), & 4 \le \mathrm{Eo}_\perp < 10.7 \\ -0.28 & \mathrm{Eo}_\perp \ge 10.7 \end{cases}, \tag{2-33}$$

with

$$f(Eo_\perp) = 0.00105Eo_\perp^3 - 0.0159Eo_\perp^2 - 0.0204Eo_\perp + 0.474\,. \tag{2-34}$$

The modified Eötvös number $Eo_\perp$ is calculated with the maximum horizontal diameter $d_\perp$; usually the empirical formulation by Wellek et al. (1966) is used

$$d_\perp = d_B \sqrt[3]{1 + 0.163\mathrm{Eo}^{0.757}}\,. \tag{2-35}$$

The lift coefficient in air-water systems is drawn in Figure 2-4 to emphasis the change of the sign, which is here at around 5.83 mm for the sphere equivalent diameter. The measurements of Tomiyama et al. (2002) stopped at a modified Eötvös number $Eo_\perp$ of around 10.7 because larger bubbles were not stable, the constant value of -0.28 for larger bubbles is usually assumed. Indeed, the lift coefficients obtained by Bothe et al. (2006)

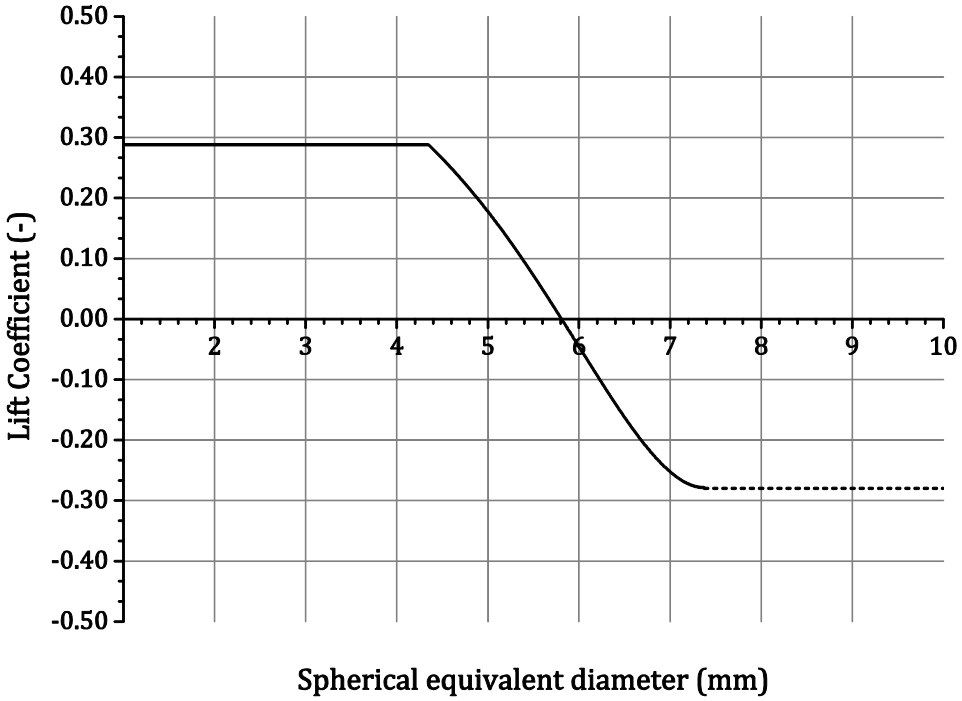

Figure 2-4 Lift coefficient correlation of Tomiyama et al. (2002) for air-water systems. The dashed line indicates the not measured region.

and Rabha & Buwa (2009) using DNS and VOF, respectively, indicate that the lift coefficient decreases further with larger bubble size.

In the past, no experiments were published in which the lift force coefficient was successfully measured in low Morton number systems like air/water. Kulkarni (2008), however, determined indirect the lift force coefficient in an air/water bubble column. The results are in the same area as the results measured by Tomiyama et al. (2002) but the lift coefficients differ also over the column diameter and show a different behavior for larger bubbles. Also, Lucas & Tomiyama (2011) investigated a large data obtained from bubbly flows in pipes and could confirm that the sign of the lift force in water changes at around 5.8 mm as the Tomiyama lift coefficient correlation predicts.

In the following CFD studies, the lift coefficient correlation of Tomiyama et al. (2002) is used.

2.3.3 Multiple bubble classes

In practice, a distribution of different bubble sizes is present. The distribution has to be covered since the behavior of the bubbles depends on their size. For example, small bubbles have a positive lift force coefficient and large bubbles a negative. Thus, at least two different velocity fields for the gas phase covering the bubbles below 5.83 mm (zero of the Tomiyama lift force coefficient) and above are needed.

Nevertheless, for some cases this separation is not sufficient, for example in the downcomer of an airlift reactor the bubble sizes are separated due to the different drag force acting on them. This is discussed in detail in Section 7.3. Moreover, if coalescence and break up effects are significant the bubble distribution must be discretized by bubble classes (Krepper et al. 2008) or represented by a characteristic function (e.g. quadrature method of moments) besides the modeling with different velocity fields. This topic is

discussed e.g. by Jay Sanyal et al. (2005). In the present work the bubble sizes are assumed fixed, the bubble size distribution is modeled with different gas phases having their own velocity fields.

It should be noted, that for all forces the same bubble diameter is used, even when a distinct distribution of the bubble size is present. Looking at the different non-linear bubble force models this is not correct. In fact, every closure model needs its own bubble size due to their non-linearity. Nevertheless, this is not a common practice, since the bubble size distributions are normally not known, so that it will not used in the present work also.

2.4 Turbulence modeling

Turbulence is a comprehensive phenomenon occurring in nearly all engineering applications and, therefore, is an important effect in bubbly flows. Turbulence is the apparently three-dimensional random fluid motion in space and time. In the following section, the very basics of turbulence modelling are given which are needed to understand the discussions in this work. The Einstein notation is used in this section for this purpose. For further information, an introduction to turbulence can be found in the books of Pope (2000) and Tennekes & Lumley (1972).

The momentum equation with constant density ρ as given in Section 2.1.2 in Cartesian coordinates using the Einstein notation reads

$$\rho\left[\frac{\partial v_i}{\partial t}+v_j\frac{\partial v_i}{\partial x_j}\right]=-\frac{\partial p}{\partial x_i}+\frac{\partial s_{ij}}{\partial x_j}. \tag{2-36}$$

With s_{ij} the viscous stress tensor as defined also in Section 2.1.2.

To investigate the velocity fluctuations, the velocity v is decomposed into a mean value and a fluctuation value, which is called Reynolds decomposition

$$v_i=V_i+v_i'. \tag{2-37}$$

The instantaneous velocity v_i is the summation of the mean velocity V_i and the fluctuation v_i'. The mean value is determined by using the ensemble average of v_i, which is denoted in the following with $\langle\cdot\rangle$. This decomposition is done for all values in Equation (2-36). Inserting the decomposition in Equation (2-36) the ensemble average of this equation reads

$$\rho\left[\frac{\partial V_i}{\partial t}+V_j\frac{\partial V_i}{\partial x_j}\right]=-\frac{\partial p}{\partial x_i}+\frac{\partial \mathrm{S}_{ij}}{\partial x_j}-\rho\left\langle v_j'\frac{\partial v_j'}{\partial x_j}\right\rangle. \tag{2-38}$$

Adding the divergence of the velocity on the right hand side of Equation (2-38) and zero to the left hand side, which is possible since the divergence of the velocity is zero for incompressible flows, results in

$$\rho\left[\frac{\partial V_i}{\partial t}+V_j\frac{\partial V_i}{\partial x_j}\right]=-\frac{\partial p}{\partial x_i}+\frac{\partial}{\partial x_j}\left[S_{ij}-\rho\langle v_i'v_j'\rangle\right]. \tag{2-39}$$

The term $\rho\langle v_i'v_j'\rangle$ is called the Reynolds stress tensor τ_{ij}, which arises out of the non-linearity of the momentum conservation equation.

Normally, by solving the momentum equation numerically always a discretization in space and time is used that is larger than the smallest velocity fluctuation scales unless a direct numerical simulation is performed. Therefore, the Reynolds stress tensor has to be modelled using the values from the mean flow leading to the closure problem of turbulence.

A frequently used concept is the Boussinesq approximation introducing an eddy viscosity μ_t

$$\rho\langle v_i' v_j'\rangle = 2\mu_T S_{ij} - \rho\langle v_i' v_i'\rangle\,\delta_{ij}. \tag{2-40}$$

The Reynolds stress tensor is formulated by using the mean strain rate tensor S_{ij} as defined above. The second term is needed since the trace of S_{ij} is zero. Thus, the problem is reformulated by modelling the eddy viscosity and the trace of the Reynolds stress tensor.

2.4.1 Reynolds Averaged Navier Stokes (RANS) equations

Different approaches were developed in the last century to model the Reynolds stress tensor; the most often used in engineering problems are the two equations models. Two equation models are based on the postulation of Prandtl (1961) using the square root of the turbulent kinetic energy k as the characteristic mixing velocity for the eddy viscosity

$$k = \frac{1}{2}\langle v_i' v_i'\rangle\,. \tag{2-41}$$

A transport equation for k can be formulated by formulating the fluctuation transport equation. Afterwards, subtracting the momentum conservation formulated with the Reynolds decomposing with the mean averaged transport equation, Equation (2-38), and multiply it with the fluctuation itself (Wilcox 1994)

$$\rho\left[\frac{\partial k}{\partial t} + V_j\frac{\partial k}{\partial x_j}\right] = \frac{\partial}{\partial x_i}\left[-\langle p v_i'\rangle\delta_{ij} - \frac{1}{2}\langle v_i' v_i' v_j'\rangle + \mu\frac{\partial k}{\partial x_j}\right] - \tau_{ij}\frac{\partial V_i}{\partial x_j} - \epsilon\rho\,. \tag{2-42}$$

The left hand side of Equation (2-42) describes the change of k due to convection and inner processes. The three terms in the brackets on the right hand side describe the pressure diffusion, the turbulent transport and the molecular diffusion of k, respectively, which are summarized by defining a quantity σ_k (Wilcox 1994)

$$-\langle p v_i'\rangle - \frac{1}{2}\langle v_i' v_i' v_j'\rangle + \mu\frac{\partial k}{\partial x_j} = \left(\frac{\mu_T}{\sigma_k} + \mu\right)\frac{\partial k}{\partial x_j}\,. \tag{2-43}$$

The next term on the right hand side of Equation (2-42) is the production term of k due to the shear of the mean flow, which is therefore often named shear-induced turbulence $-P_k$. Finally, the last term is the sink term of the turbulent kinetic energy named turbulence dissipation rate ϵ

$$\epsilon \equiv \nu\left\langle\frac{\partial v_i'}{\partial x_j}\frac{\partial v_i'}{\partial x_j}\right\rangle \sim \frac{k^{\frac{3}{2}}}{l}\,. \tag{2-44}$$

From a dimensional analysis, the turbulence dissipation might be described by the turbulent kinetic energy and a length scale, which can be taken as the mixing length scale (Wilcox 1994). Summarizing, the k-equation is written as

$$\rho\left[\frac{\partial k}{\partial t}+V_j\frac{\partial k}{\partial x_j}\right]=\frac{\partial}{\partial x_i}\left[-\left(\frac{\mu_T}{\sigma_k}+\mu\right)\frac{\partial k}{\partial x_j}\right]+P_k-\epsilon\rho\,. \tag{2-45}$$

Thus, an equation for the turbulent kinetic energy is obtained that is used for the characteristic mixing velocity to estimate the eddy viscosity. Nonetheless, a mixing length scale is needed to describe the eddy viscosity and, additionally, is needed to model the turbulence dissipation rate ϵ since the dissipation rate is not accessible with mean values by definition.

For the length scale modelling with a two-equation model, two approaches are frequently used: Formulating a transport equation for the dissipation per unit turbulent kinetic energy ω or formulating a transport equation for the dissipation rate ϵ. The transport equation for the latter one reads (Jones & Launder 1972)

$$\rho\left[\frac{\partial \rho\epsilon}{\partial t}+V_j\frac{\partial \rho\epsilon}{\partial x_j}\right]=\frac{\partial}{\partial x_i}\left[-\left(\frac{\mu_T}{\sigma_\epsilon}+\mu\right)\frac{\partial \epsilon}{\partial x_j}\right]+C_{1\epsilon}\frac{\epsilon}{k}P_k+C_{2\epsilon}\rho\frac{\epsilon^2}{k}\,. \tag{2-46}$$

For further studies a model distinguishing near wall and free turbulence by blending between the $k-\omega$ and $k-\epsilon$ model called SST $k-\omega$ model by Menter et al. (2003) is used with

$$\rho\left[\frac{\partial \rho\omega}{\partial t}+V_j\frac{\partial \rho\omega}{\partial x_j}\right]=\frac{\partial}{\partial x_i}\left[-\left(\frac{\mu_T}{\sigma_\omega}+\mu\right)\frac{\partial \omega}{\partial x_j}\right]+P_\omega-Y_\omega+D_\omega\,. \tag{2-47}$$

The production term P_ω and dissipation term Y_ω are more complicated than for the k or ϵ equation as described by Menter et al. (2003). A derivation for these values is not shown at this point. The term D_ω arises due to the blending between the model formulations.

2.4.2 Unsteady RANS equations

As described above, the length and time scales of turbulence are in general very small. By the use of an extra eddy viscosity, these very small scales are modeled (or filtered as discussed in the next section). Thus, just a coarse mesh is needed to resolve the remaining scales. The RANS equations need only a relative coarse mesh compared to other methods, which is a great advantage in technical use.

Nevertheless, turbulence is a complex phenomenon and depends on the local geometry/local flow. Furthermore, the usage of a total kinetic turbulent kinetic energy k in the transport equation implies the assumption of isotropic turbulence, which is often not given. Anisotropic turbulence phenomena, however, occur often on the larger scales whereas the assumption of isotropic turbulence phenomena is good for the smaller scales. Thus, the small scales might be described with general models while the larger scales should be resolved. Therefore, an improvement is reached by calculating the large-scale fluctuations directly while the smaller scales are modeled. For this purpose, the RANS equations are solved transient while the small scales are modeled by the same equations as for the steady state case. This method is often called unsteady RANS (URANS) or very large eddy simulation (VLES). Often, the relatively simple and fast URANS calculations are even treated with stationary boundary conditions to study for

example vortex shedding at bluff bodies, which gives reasonable predictions as discussed by Spalart (2000).

With the URANS approach, the fluctuations of the velocity are decomposed in resolved and unresolved parts. For comparison with experiments, both fluctuation parts have to be considered to get the total fluctuation. In general, for transient simulations the total time-averaged kinetic energy is simply equal to the sum of the squared averaged velocity and the average of the squared fluctuations:

$$\frac{1}{2}\rho\,\overline{vv} = \frac{1}{2}\rho(\bar{v}\bar{v} + \overline{v'v'}) \quad . \tag{2-48}$$

Analog to above, $\bar{v}$ is the average over time and v' is the fluctuation around the average. The modeled and resolved fluctuation that are obtained in the URANS approach can be written as the sum of these two components

$$v' = \widetilde{v'} + v'' \quad , \tag{2-49}$$

where $\widetilde{v'}$ denotes the resolved fluctuation and v'' the modeled fluctuation. Using this summation the turbulent kinetic energy for the velocity component v can be written as

$$\overline{v'v'} = \overline{\widetilde{v'}\widetilde{v'} + \widetilde{v''v''}} \quad . \tag{2-50}$$

The modeled fluctuation $\widetilde{v''v''}$ is described by the above defined k_{mod} transport equation. Since only the total modeled turbulent kinetic energy is known, $\widetilde{v''v''}$ is calculated by

$$\widetilde{v''v''} = \frac{2}{3}k_{mod} \quad . \tag{2-51}$$

Whereas the resolved part is obtained from the transient simulation. The normal component of the Reynolds stress tensor is therefore

$$\overline{v'v'} = \overline{\widetilde{v'}\widetilde{v'}} + \frac{2}{3}\overline{k_{mod}} \quad . \tag{2-52}$$

2.4.3 Large Eddy Simulations

Large eddy simulations (LES) are similar to URANS simulations, but the small scales are specifically filtered using filter functions. The filtering of the small scales for LES is done by a convolution of the value with a filter function. Different filter functions exist for different purposes. The selection of the scales is regulated by varying the size of the filter functions, which is often called filter length. The advantage of this selection is that the small scales can be specifically modelled. Normally, the small scales are only needed for the dissipation of the turbulent kinetic energy, so a simple model can be used.

By filtering the Navier-Stokes equations, the filtered Navier Stokes equations and an unresolved part are obtained, similar to the URANS equations. Differences to the URANS equations occur since the filters usually used in LES have not the same properties as the RANS models. Nevertheless, also the filter functions have to fulfill specific requirements (Lesieur et al. 2005) and cannot be chosen arbitrary. The filtered Navier Stokes equations can be discretized using for example the finite volume (FV) method and can be solved

using the standard procedures with consideration of the properties of the filtering process.

Usually, the filter is connected to the used discretization, e.g. on a rectangular mesh using the FV method the Navier-Stokes equations are naturally filtered with the shape of a box filter. Therefore, the models for the small scales are connected to the local grid size. Consequently, with this procedure a mesh independent solution is usually not achieved.

The unresolved scale is usually called sub-grid-scale (SGS) and has to be modeled. Often, the SGS are modeled using the Boussinesq-approximation so that a turbulent viscosity is modeled. For this purpose, different model approaches exists, ranging from algebraic models up to two equation or Reynolds-stress models. A common model is the algebraic Smagorinsky model using the filter width Δ and the rate of strain tensor $\underline{\boldsymbol{S}}$

$$\nu_t = (C_S\Delta)^2\left|\underline{\boldsymbol{S}}\right| \ . \tag{2-53}$$

The prefactor C_S depends on the actual flow conditions; a constant value between 0.1 and 0.24 is usually taken.

Modelling the turbulence of bubbly flows is not trivial with the LES approach and an active topic of research. Often, an additional turbulent viscosity is added to the modeled turbulent viscosity obtained from the SGS modelling. Among others, the modelling of the bubble-induced turbulence using an additional turbulent viscosity is discussed in the next section.

2.4.4 Turbulence in Bubbly flows

The turbulence in bubbly flows is not very well investigated compared to the turbulence in single-phase flows. The presence of bubbles can either increase or suppress the turbulence (Serizawa & Kataoka 1990). The wake of the bubbles, for example, usually leads to an increase in turbulence. In addition, the turbulence interaction of bubbles and their wake structures with the surrounding turbulence might be very complicated, up to now no reliable models exists. Moreover, the gas phase distribution in the reactor due to the turbulent dispersion of the bubbles and the gas phase structure due to break up and coalescence processes is influenced by the turbulence. The gas phase distribution and bubble size in return influence the turbulence; the interaction of the turbulence with the bubbles is in general depending on the bubble size/length as well as the turbulence length scale, which are both more or less continuously distributed and both often not known. Since the turbulence of such complex bubbly flows are not understood no straight forward theory exists, as for single-phase flows. Thus, a discussion of this topic is beyond the scope of this section and is referred to the literature (Kataoka & Serizawa 1989) (de Bertodano et al. 1994) (Risso et al. 2008) (Riboux et al. 2010). Nevertheless, in the following some frequently used modeling approaches are shown, which are also used for CFD simulations.

In practice, the turbulence in bubbly flows is modeled by the superposition of the single-phase flow (SP) with a bubbly flow (B). One approach is the assumption that the eddy viscosity is superimposed

$$\mu_T = \mu_{T,SP} + \mu_{T,B} \ . \tag{2-54}$$

An early semi-empirical model is the well-known Sato model (Sato et al. 1981) that reads in the formulation of the two fluid model

$$\mu_{T,B} = 0.6\rho\alpha d_p|\boldsymbol{v}_G - \boldsymbol{v}_L| \ . \tag{2-55}$$

Originally, this model was developed for pipe flows with a zero equation turbulence model. Nevertheless, using two equation turbulence models derived for single phase flows and just adding the additionally viscosity afterwards good results are obtained in pipe flows (Krepper et al. 2005) and bubble columns (Tabib et al. 2008). In addition, the separation of the turbulent viscosities is also a useful method to investigate the turbulence in bubbly flows (Hosokawa & Tomiyama 2004). These models are useful for the sub grid scale modeling in large eddy simulations (Ma et al. 2015) and for Reynolds stress models (Masood et al. 2014).

Despite the usefulness of such viscosity superposition, the turbulent kinetic energy is usually underpredicted, especially in combination with one or more equation models. The only contribution to the turbulent kinetic energy production is to the shear induced production P_k in Equation (2-45)

$$P_k = \tau_{ij}\frac{\partial V_i}{x_j} = \mu_t\left(2S_{ij}S_{ji}\right) = \left(\mu_{T,SP} + \mu_{T,B}\right)\left(2S_{ij}S_{ji}\right) \ , \tag{2-56}$$

with S_{ij} the mean strain rate tensor. It is imaginable that this contribution is not enough if wake effects significantly contribute to the turbulent kinetic energy. This underprediction is significant if further effects in bubbly flows depending on the kinetic energy are modeled, in particular the break up and coalescence effects.

Another approach is the superposition of the production terms P in Equations (2-45) to (2-47) with a bubble induced turbulence (BIT) term. The production of the turbulent kinetic energy then reads

$$P_k = \mu_t\left(2S_{ij}S_{ji}\right) + P_{k,BIT} \ . \tag{2-57}$$

The production term $P_{k,BIT}$ is usually taken as the energy transferred to the surrounding liquid due to the slip velocity

$$P_{k,BIT} = C_{k,BIT}F_{Drag}|\boldsymbol{v}_G - \boldsymbol{v}_L| \ . \tag{2-58}$$

The prefactor $C_{k,BIT}$ is normally taken to one, which is also used in the following.

Formulating the production terms of the energy dissipation and dissipation rate the similar heuristic is used as for single-phase flows (Rzehak & Krepper 2013a), e.g.

$$P_{\epsilon,BIT} = C_{\epsilon,BIT}\ \frac{P_{k,BIT}}{\tau} \ . \tag{2-59}$$

The production term is formulated by dividing the production of the turbulent kinetic energy by a time scale τ with a prefactor $C_{\epsilon,BIT}$. Using a dimensional analysis the time scale can be formulated on four different ways as shown in Table 2-1.

Author	$1/\tau$	$C_{\epsilon,BIT}$
Morel (1997)	$\left(\frac{\epsilon}{d_B^2}\right)^{1/3}$	1
Troshko & Hassan (2001)	$\frac{\lvert \boldsymbol{v}_G - \boldsymbol{v}_L \rvert}{d_B}$	0.45
Politano et al. (2003)	$\frac{\epsilon}{k}$	1.93
Rzehak & Krepper (2012)	$\frac{\sqrt{k}}{d_B}$	1

Table 2-1 Different formulations of the time scale of the turbulence dissipation production

All the models in Table 2-1 are formulated and/or validated for different pipe flows. The latter one formulated by Rzehak & Krepper (2012) is taken for the simulations in bubble columns.

2.5 Baseline concept for simulating bubbly flows

CFD simulations of dispersed bubbly flow on the scale of technical equipment are feasible within the above-discussed Eulerian two-fluid framework of interpenetrating continua. By the use of suitable closure models describing the physics on the scale of individual bubbles or groups thereof. A large number of numerical work exists, in each of those largely a different set of closure relations is compared to a different set of experimental data. However, the used models are often explicitly picked and adjusted to fit the actual experimental data. Therefore, a reasonable agreement for a specific case is reached but a reliable predictive modeling is not given. Predictive simulation, however, requires a model that works without any adjustments within the targeted domain of applicability.

As a step towards this goal, the HZDR CFD group attempted to collect the best available description for all aspects known to be relevant for adiabatic bubbly flows to a baseline model. This attempt was predominantly focused on pipe flows with external pressure gradients. In the present work, the performance of this baseline in bubbly flows, which are driven by the bubbles, in particular bubble columns, is investigated and extended.

Aspects requiring closure for adiabatic bubbly flows that have to be fixed in the baseline model are the exchange of momentum between liquid and gas phases, the effects of the dispersed bubbles on the turbulence of the liquid carrier phase and processes of bubble coalescence and breakup that determine the distribution of bubble sizes. Those closure models require a reliable validation, preferably by the use of experiments, which are dedicated to one specific problem over a large range of boundary conditions. Since such experimental data not exist, also because the closure models are strongly coupled, the complex validation problem has to be simplified. A reasonable simplification is to confine on problems with a fixed bubble size distribution as discussed above. In this way the sub-models for bubble forces and bubble-induced turbulence can be validated independently of bubble coalescence and breakup processes. The validation of this

partial problem is done by the use of experimental data from the literature as well as experimental data that was produced in the framework of the present work.

Besides a set of closure models, which are summarized in Table 2-2, other aspects of simulating bubbly flows have to be determined. Up to now, these aspects are not fixed in the current baseline model version; in the present work, however, they are held constant. In particular, the URANS formulation with the SST turbulence model (Menter et al. 2003) is used to resolve the large-scale structures, which often occur in bubbly driven flow, including a reasonable convergence criterion. Moreover, a slip condition for the gas phase and a no-slip condition for the liquid phase are used at the walls. The surface that normally occurs in bubbly driven flows is modeled with a degassing boundary with a variable pressure on it (Ansys 2013). Here the pressure remains variable over the top of the column, which might be interpreted as different surface heights at different positions due to the flow, for other scalar quantities of the dispersed phase a constant gradient is imposed. Thus, effects of a free surface such as waves or foaming is not considered. The gas inlet is modeled by the use of mass flow through surfaces in the range of the generated bubble sizes. Accordingly, the initial gas velocity is taken to the ratio of the gas volume flow rate to the corresponding inlet area. Therefore, the initial velocity of the gas phase in the experiments, which range from zero for single bubble formation to large velocities for aerating with gas jets, is not directly modeled because the terminal bubble velocity is usually reached after one or two cells (Sokolichin et al. 2004). Furthermore, no experimental data with significant gas jets are used in the present work.

In addition, it is attended to use a simple mesh consisting of rectangular volume cells of the same size, only for the simulations of an airlift reactor in Section 7.3 the size of the rectangular volume cells differs over the calculation domain due to the complex geometry. The size of the volume cells was determined for every validation case in a mesh study separately containing at least three different meshes, which is shown once in Section 4. A cells size of 5 mm was usually found to be sufficient. For the spatial discretization a high-resolution scheme is used (Ansys 2013). For the transient discretization, a second-order backward Euler scheme is used.

Drag force	Ishii and Zuber (1979)
Lift force	Tomiyama et al. (2002)
Wall force	Hosokawa et al. (2002)
Virtual mass	$C_{VM} = 0.5$
Turbulent dispersion	Favre Averaging (Burns et al. 2004)

Table 2-2 Closure models in the baseline model.

Apart from interest in its own right, results obtained for the momentum exchange restricted problem also provide a good starting point for the investigation of more complex situations including heat and mass transport, phase change and chemical reactions in bubbly flows.

3 Experimental Methods

3.1 Experimental facility

The used experimental facility, which was build up during the present work, is a rectangular Plexiglas® bubble column shown in Figure 3-1. The cross sectional area is 250×50 mm^2 large. The total height is 1000 mm. The liquid level is set depending on the application. The ground plate is made of 10 mm thick stainless steel and up to 18 needles can be placed in the threaded holes shown in the right side of Figure 3-1. The holes are displaced to each other. The bubble column is placed in a frame of profiles as shown in Figure 3-2.

The sparger consists of single needles pressed in a bracket with an inner radius of 3 mm and are screwed in the ground plate. The deburred needles are cut flatly and various sizes of them were used in the experiments. The gas volume flow rate is regulated by up to two mass flow controllers from Omega Engineering.

For a proper design of the experiments, the bubble sizes generated by different needles were determined with the methods described in Section 3.2. In Figure 3-3 the spherical equivalent diameter of the projected area with its standard deviation over the volume flow rate per needle is shown. In addition, the bubbles are wobbling during the ascent. This wobbling is artificial because the bubble size is evaluated from the projected area; the resulting artificial standard deviation is shown in Figure 3-4. The shown wobbling standard deviation is the arithmetic average of the standard deviations determined along the bubble tracks.

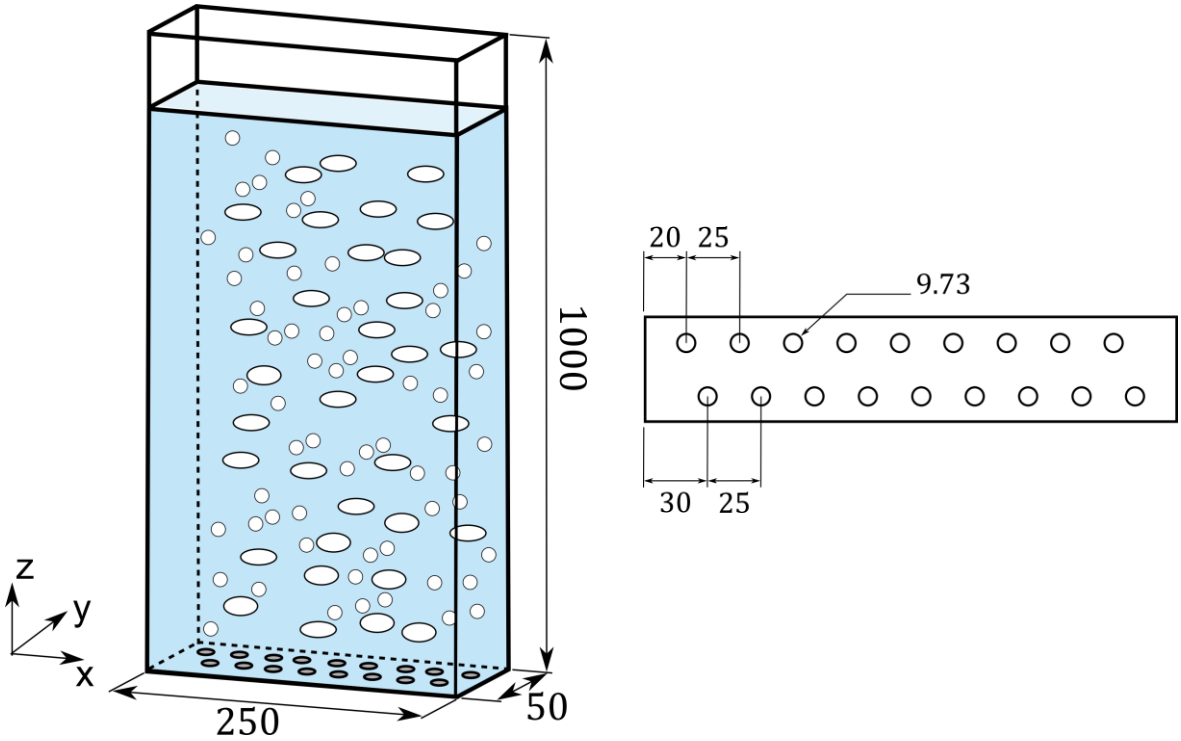

Figure 3-1 Sketch of the experimental setup and the ground plate with (right) (metrics in mm).

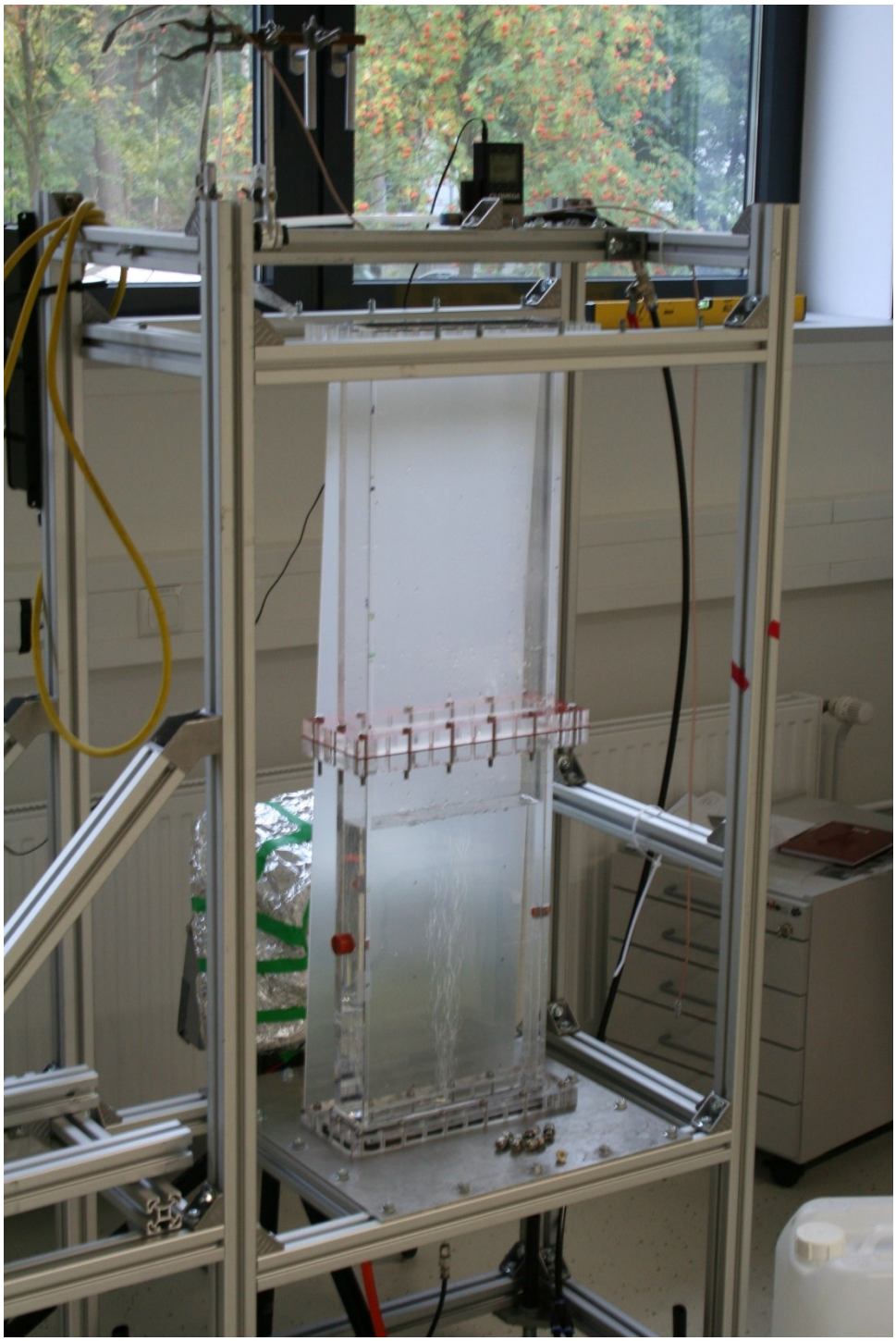

Figure 3-2 Photograph of the experimental setup

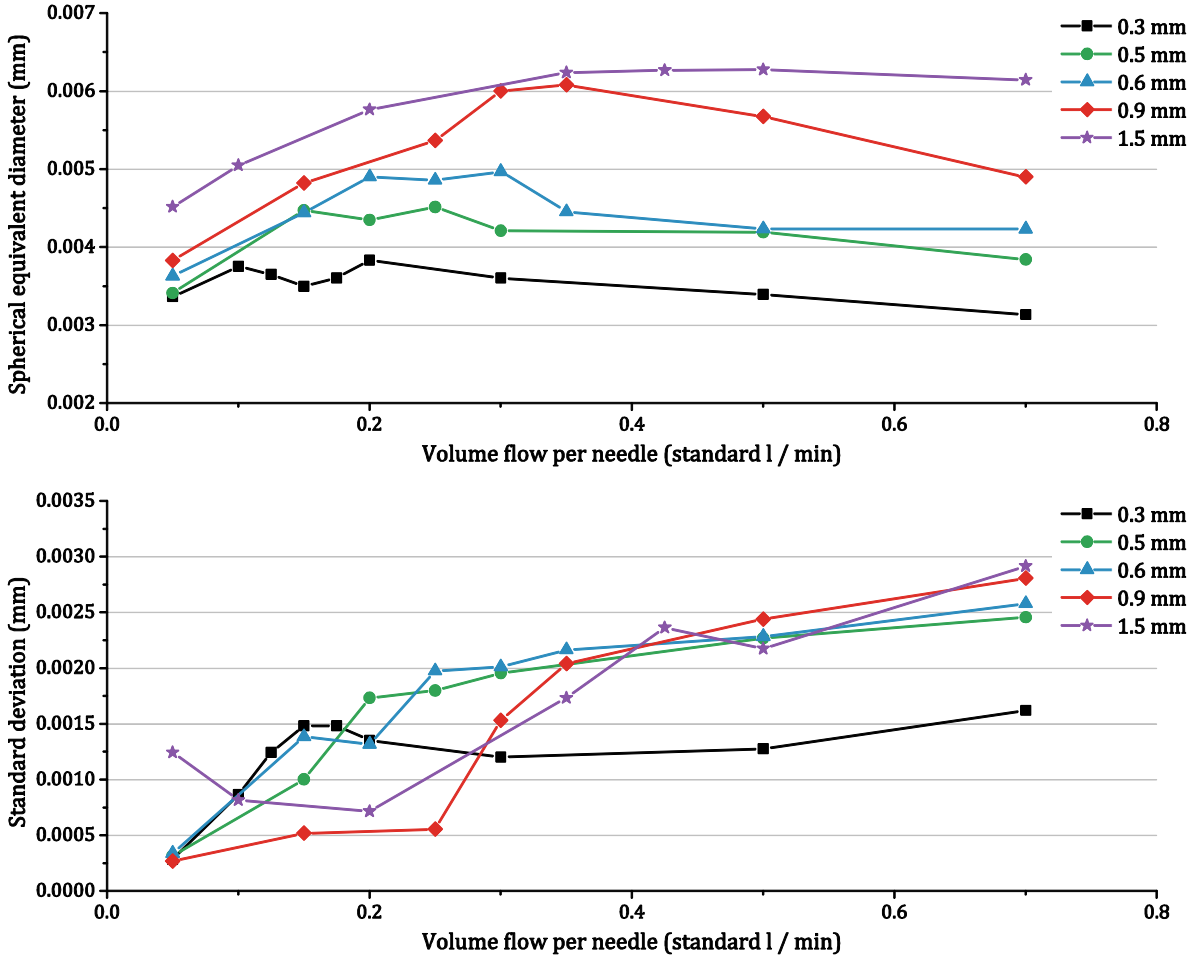

Figure 3-3 Size of the bubbles (top) and the standard deviation of the size (bottom) over the volume flow rate for different needle sizes.

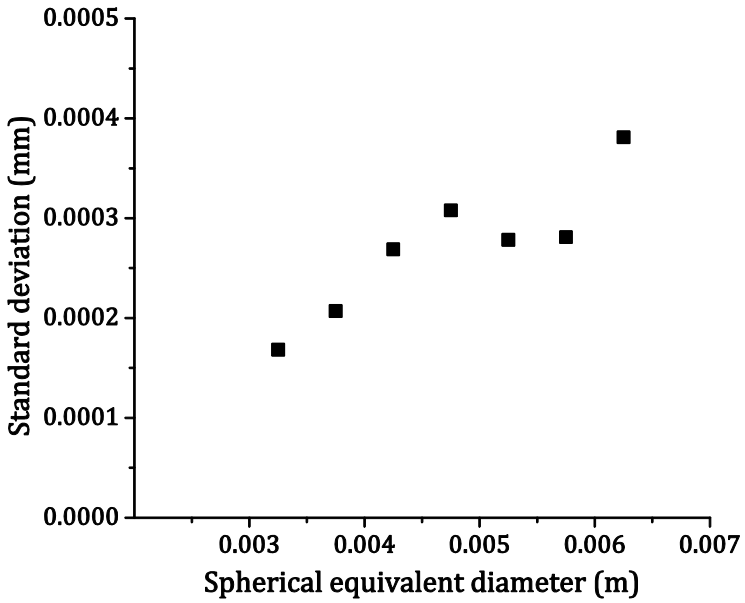

Figure 3-4 Wobbling uncertainty

3.2 Bubble size

Determining the bubble size distribution in bubbly flows is essential since all closure models discussed above depend on them. Digital image analysis of bubbly flows is often used in order to determine the bubble size distribution, which is described e.g. by Bröder & Sommerfeld (2007) or Lau et al. (2013). Although the identification of objects from photographs is a well-known technique, the reliable identification of bubbles from images is still very challenging. The nature of bubbly flows, in particular bubble clusters that consists of many overlapping bubbles, is very complex so that a reliable identification of bubbles is problematic. Therefore, bubbles in complex bubbly flows are normally identified by hand (e.g. by Mohd Akbar et al. (2012)).

In the following, the used and developed digital image analysis methods in the present work are described, ranging from automatized single bubble identification to methods of handling bubbles in dense clusters. In the first part, the determination of single bubbles with an edge detector is described; further, the basic principles of bubble detection are introduced. In the second part, an algorithm is developed to evaluate whether a bubble is overlaid by another bubble or not. Using this algorithm, bubble sizes can be automatically determined for very low void fractions and/or narrow bubble size distributions. Finally, a method is developed to pick bubbles by hand in dense clusters with the aid of the previous developed methods.

After the bubbles are identified, a representative bubble size has to be determined. For this purpose, two reasonable assumptions exist, first the circular equivalent diameter of the projected area and second the spherical equivalent diameter of the solid of rotation of the projected area. Since the closure models are formulated by using the spherical equivalent diameter of the bubble volume (Haberman & Morton 1953) (Tomiyama et al. 2002) the latter one might be a reasonable choice.

The solid of rotation is calculated by half rotating the left and the right half of the bubble that is split by the rotation center as demonstrated in Figure 3-5. The red point marks the rotation center of the bubble. The boundary ($\Omega_1 + \Omega_2$) and the projected Area ($A_1 + A_2$) of the bubble is separated by the rotation symmetry (dashed line). The left and right half of the bubble have an own centroid (blue and black point, respectively) with a distance to the rotation symmetry of Δx_1 and Δx_2, respectively.

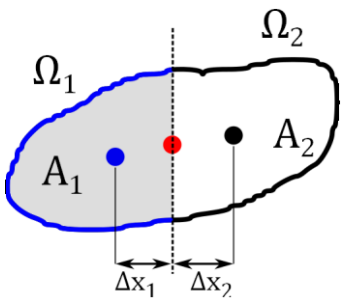

Figure 3-5 Calculation of the solid of rotation of a bubble.

Using the second Guldinus theorem and further assuming $A_1 = A_2$, the volume is calculated by

$$V_{Rotation} = \pi(\mathrm{A}_1 \Delta x_1 + A_2 \Delta x_2) = \pi \frac{A_{projected}}{2} (\Delta x_1 + \Delta x_2)\,. \tag{3-1}$$

With the spherical equivalent diameter of this volume, the density functions (DF) are calculated. For this purpose, the determined bubbles are separated in bubble size classes $d_i - {}^{\Delta d_i}/_2 \leq d_b < d_i + {}^{\Delta d_i}/_2$. The discretized density functions are then calculated by

$$DF_i = \frac{f_i}{\sum_i f_i} \frac{1}{\Delta d_i}\,, \qquad f_i = \sum\nolimits_{d_i - {}^{\Delta d_i}/_2 \leq d_b < d_i + {}^{\Delta d_i}/_2} f(d_b)\ \ , \tag{3-2}$$

With f the characteristic function. The number density function is calculated by using $f(d_b) = 1$, the area density function by $f(d_b) = \pi d_b^2$ and the volume density function by $f(d_b) = \pi/6\ d_b^3$. The expected value (E) is calculated by

$$E_f = \sum_i f_i d_i \Delta d_i\ \ . \tag{3-3}$$

For example, the Sauter diameter is the expected value of the area density function. This diameter is in the following given as bubble diameter, if not explicitly said otherwise.

3.2.1 Single bubbles

In this section, the procedure to determine single bubbles is explained, as for example shown in Figure 3-6. All algorithms are based on a modified Canny edge detector (Canny 1986). The basic algorithm is shortly introduced and results are shown. The mathematically description of every step is not given at this point since it is standard knowledge and can be found in the literature (Petrou & Petrou 2010) (Parker 2010). All images were recorded with a backlight technique with diffusors between the light source and the bubble column.

As a first step the images are generally preprocessed, particularly the images are cut, rotated, the contrast is corrected and modified to the needs of the edge detecting algorithms. The contrast is corrected by renormalizing the white and black pixels at the end of the histogram and elongating the grey scale histogram to fit the complete grey scale. For a higher edge detecting quality, a Median and a Gaussian Filter is used. Besides, the pixel size and the reference point are determined with calibration grids on the experimental facility to identify later the size and position of the bubbles.

The used edge-detecting algorithm can be separated in the steps: Two dimensional derivation, edge thinning and edge selection. The two dimensional derivation is obtained by a convolution using the Sobel operator. The edges are thinned to one pixel by taking the pixel that is at the minimum of the absolute value function of the two dimensional derivation along the normal direction of the bubble surface. The normal direction of the surface is calculated from the arctangent function of the derivation in vertical and horizontal direction. The normal direction is discretized to 45-degree angels corresponding to the pixel discretization of the image. Afterwards, a hysteresis with two thresholds is used for the edge selection so that three categories are obtained, below the first (edge is deleted), in the middle of the first and second (weak edge) and above the second threshold (strong edge). Afterwards, if a weak edge is direct or indirect over other weak edges connected to a strong edge, the weak edge becomes a strong edge; else, the weak edge is deleted. The output of this double threshold is shown in Figure 3-6.

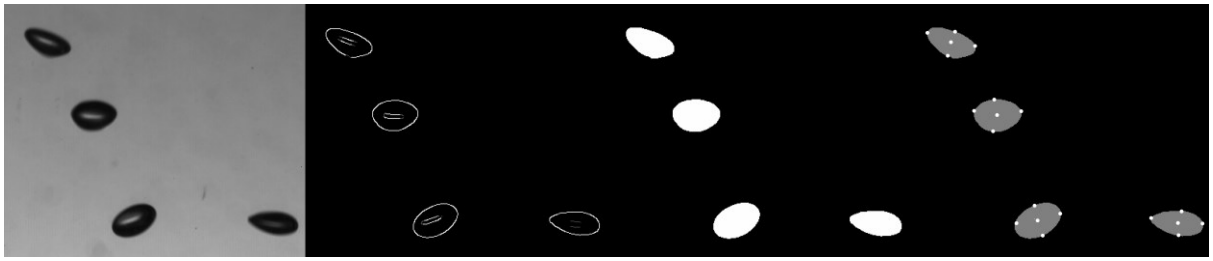

Figure 3-6 Main steps for bubble size determination of single bubbles, left to the right: Original image; Edges with weak (grey) and strong edges (white); filled structures; result with major and minor axis and area centroid (white dots).

After the edges are detected, the bubbles have to be identified as such. At First, the edges are closed by a simple dilatation and erosion step. Next, the inside and outside of every bubble have to be defined. For this purpose, the detected edges are marked as white and the rest as black. Afterwards, the obtained image is as often dilated until all the image is covered by white. Then, the previous dilation step is considered and evaluated if a black pixel exists that have in the original (preprocessed) image a grey value of 127 or larger. If so, this pixel is stated as a point in the surrounding and the surrounding is obtained by getting the connected black pixels from the image obtained from the edge detecting. If there is no black pixel that has a value greater than 127 in the original (preprocessed) image, the next previous dilatation step is considered and so on. This algorithm is very stable and gives in almost all cases a very good result. The definition of the surrounding of the bubbles is very important since the bubbles have also structures inside as can be seen in Figure 3-6. Moreover, for complex problems like the particle tracking in bubbly flows described below the definition of the surrounding is problematic since most of the image is covered by very big bubbles or bubble clusters. Here, the described algorithm also works very well. After the surrounding of the single bubbles is defined, the bubbles are separated by nature and can be identified easily. Clearly, if bubbles are overlapping an extra step for separation is necessary. Finally, the projected areas of the bubbles are obtained and the bubble sizes are calculated as described above.

The limit of the shown algorithm is when two bubbles are touching. Nevertheless, the algorithm already shows good results for a single needle sparger as shown in Figure 3-7.

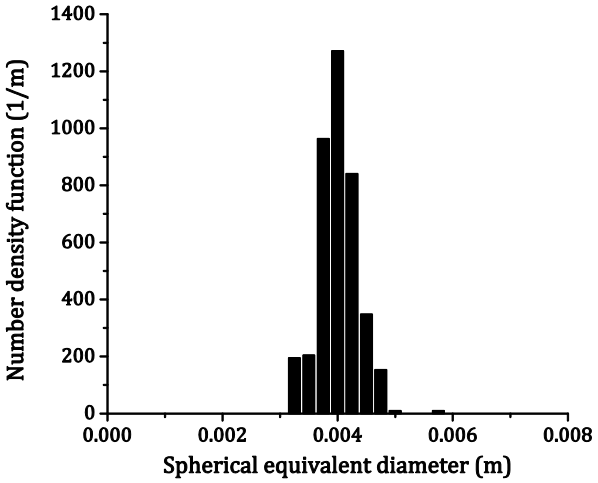

Figure 3-7 Bubble size measurement for a 0.6 mm inner diameter single needle sparger with 0.05 l/min gas volume flow rate.

3.2.2 Systems with very low void fraction or narrow bubble size distributions

In the following section, an algorithm is developed to determine whether a bubble is overlaid by other bubbles or not. Identifying bubbles that are overlaid by other bubbles is simple, but identifying whether a bubble is in front or not is more difficult as well as the reconstruction of the bubble(s) in the back. Up to now, no reliable and/or efficient methods exist for this purpose. Thus, only the non-overlaid bubbles are used to determine the bubble size distribution, segmentation of the overlaid bubbles is not conducted.

Determining the bubble size distribution from the non-overlaid bubbles only, imposes the assumption that all bubbles have the same probability to be overlaid, else a wrong result is obtained. This assumption is only appropriate if the bubble size distribution is narrow.

The algorithm for the automated evaluation of the recordings is demonstrated in Figure 3-8. At first, the raw picture is segmented by the use of an adaptive threshold to divide the black surrounding of the bubble and the translucent inside. The adaptive threshold is determined for every pixel by averaging over a 25 × 25 pixel area; usually this value is subtracted by 5 grey values afterwards. After the adaptive threshold is applied, the bubbles that have a translucent inside are identified by a simple divide and conquer algorithm.

The centroid of the translucent inside is used as bubble position. Furthermore, if an object appears completely black without a white inside, the use of the adaptive threshold is repeated for this single object with a threshold determined with reduced averaging area size. This leads to a better segmentation of the previously under-segmented completely dark object.

Next, the result of the above-described edge-detecting algorithm is combined with the result of the segmentation; if inside a closed edge more than two bubbles are found, the area inside the edge is treated as overlaid bubbles. Finally, the bubble size distribution is determined with the non-overlaid bubbles as shown in Figure 3-8.

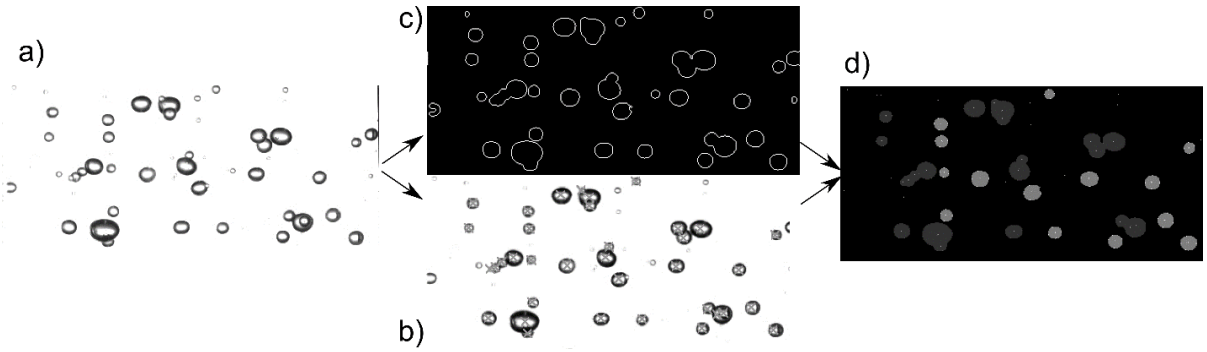

Figure 3-8: Automated detection of overlaid bubbles. a) Input with corrected contrast b) segmented bubbles with positions (grey crosses) c) edge detection algorithm d) cutting out the overlaid bubbles (dark grey). Only bubbles larger than 1.5 mm are treated.

This algorithm is used to identify bubbles in single needle experiments at higher gas volume flow rates. Moreover, the algorithm is used in the downcomer of the later discussed airlift reactor; a determined volume density function is shown in Figure 3-9. Among others, this determined volume density function was compared to a

comprehensive evaluating of the bubble size by hand using the algorithm described in the next section; as a result, an underprediction of 5 % was found. In general, this algorithm gives very good results in bubbly flows containing small bubbles with a narrow bubble size distribution and low gas void fraction.

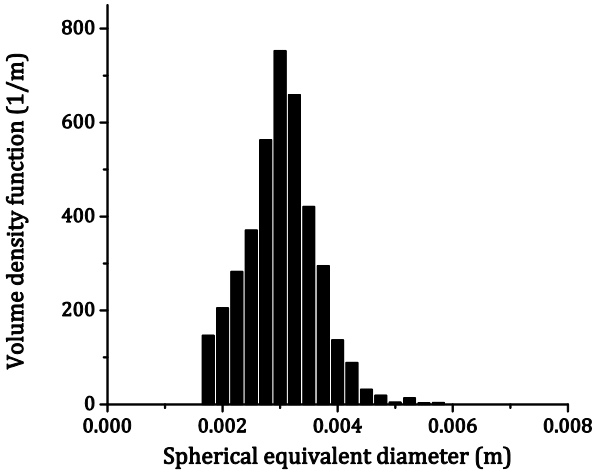

Figure 3-9 Volume density function in the downcomer of an airlift reactor shown in Section 7, the shown volume density function is obtained in the downcomer for case 6 between y = 0.2 m and y = 0.3 m.

3.2.3 Systems with higher void fractions and wide bubble size distributions

In general, wide bubble size distributions as well as bubble clusters are found in bubbly flows. No method or algorithm is published that can determine reliable bubble sizes in such flows. The level reached are methods that are trying to reconstruct overlaid bubble structures from single pictures (Bröder & Sommerfeld 2007) (Lau et al. 2013). Such reconstruction methods are very limited and can only be used in flow situations with simple shapes like spherical or ellipsoid. In real flow problems, larger bubbles have an arbitrary shape as demonstrated in Figure 3-10. Even at the lowest flow rate of 3 l/min with an integral hold up of around 2% bubble clusters occur and an automated reconstruction of the overlaid bubbles might be not possible.

Figure 3-10 Bubbly flow for different volume flow rates, left, 3 l/min, right, 7 l/min. The used sparger setup is discussed in Section 3.4.

In this context, a semi-automated algorithm is developed. The main idea is to follow a bubble cluster over a certain time until all bubbles of the cluster were clearly seen, a maximum time is exceeded or the cluster moves out of the observation area. The bubble identification in general is again done by an edge-detecting algorithm based on the Canny edge detector (Canny 1986). Despite a certain amount of automation, the used algorithms need the input of a user for proper separation of complex clusters.

In Figure 3-11 the results for a bubble cluster recorded over ten frames are shown. The projected area of the bubbles at frame zero, five and ten is determined refereed to frame zero. The used edge-detecting algorithm suggests shapes of bubbles, the user has to pick bubbles and/or separate them from others. In principal, the result is equal to a handpicked bubble size distribution. Although the bubble clusters are followed over time not all bubbles from the cluster could be evaluated; the bubble in the left corner of frame zero is moving behind the larger bubbles the whole time. From experience, such bubbles are relatively seldom and are neglected.

Depending on the distribution of the bubble sizes, 1000 to 4000 identified bubbles were found to represent sufficiently narrow and broad bubble size distributions, respectively. The repeatability of the method was tested for different flow conditions by evaluating the same flow conditions three times, in all cases almost equal bubble size distributions were obtained. The reliability of the method cannot be evaluated by comparing the obtained bubble size distributions with other methods from the literature since no valid methods exist. To get a feeling for the reliability, setups in which no coalescence and break up is expected (relatively low gas hold but a broad bubble size distribution and using salt as coalescence inhibitor) were evaluated at two different heights. A narrow sparger setup was used in order to obtain a bubble plume at the lower height and a more or less homogenized bubby flow at the higher. Almost the same results at both heights were obtained as demonstrated in Figure 3-12. Thus, it is reasonable to assume that the shown method is reliable and robust for complex bubbly flows.

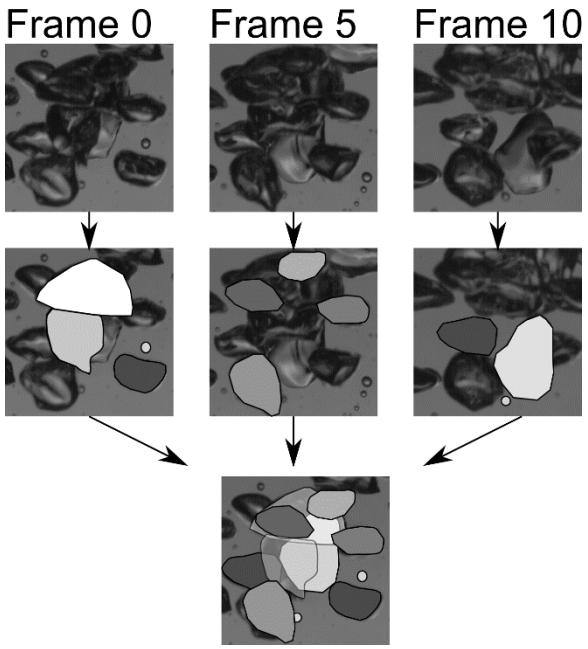

Figure 3-11 Determination of the bubble sizes in bubble clusters by following the cluster over ten frames with 200 frames per second recording speed.

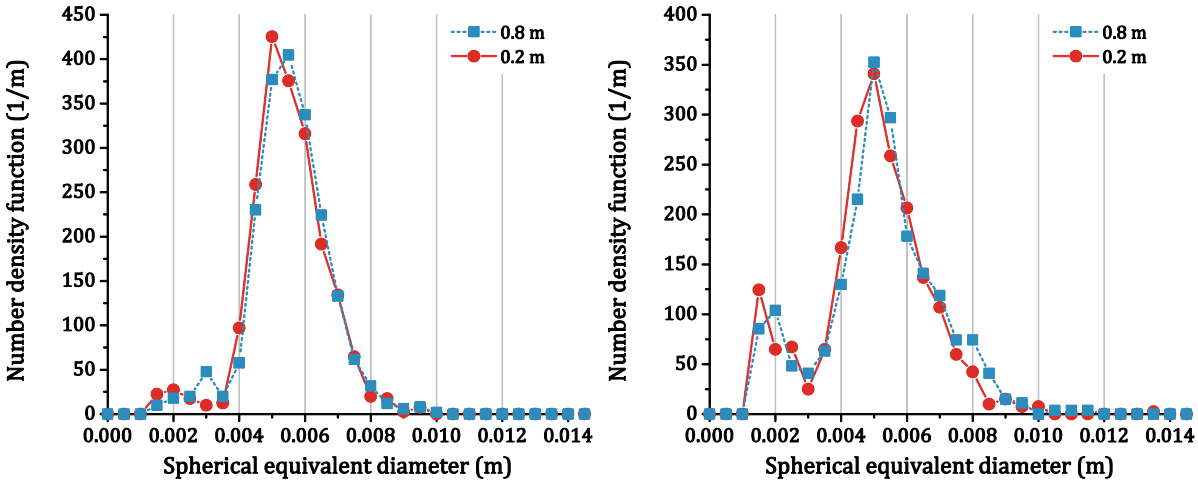

Figure 3-12 Bubble size distribution determined at two different heights and two different volume flow rates; left, 2.2 l/min, right, 3.4 l/min. The sparger consists of four needles with 1.5 mm and four needles with 0.6 mm inner diameter.

3.3 Void fraction

3.3.1 Needle probe

The volume fraction is measured by the use of a conductivity needle probe. The performance is discussed in several studies, e.g. by Le Corre et al. (2001) or by Manera et al. (2009). In the present work, a single needle probe that is described by Da Silva et al. (2007) and Schleicher et al. (2008) is used. The probe lance is assembled movable at the top of the reactor.

A needle probe is an invasive method and not usable if the probe lance disturbs the flow. Depending on the bubble size, the bubbles need a distinct relative velocity to the probe to get reliable information. For example, in the downcomer of the later discussed airlift reactor the bubbles are small and have a slow relative velocity to the needle so that a needle probe is not useable.

3.3.2 2D-Videometry

For very small void fractions, the void fraction is determined with videometry. For this purpose, the method for the bubble size measurement given in Section 3.2.2 and shown in Figure 3-8 is used. The divide and conquer algorithm that identifies the bubbles from the segmented pictures gives the count of all bubbles including the overlaid bubbles. From the non-overlaid bubbles, the volume of the solid of revolution obtained by revolving of the projected area is calculated. The average of these volumes is assumed representative for the bubbly flow so that the total gas volume is calculated by multiplying the total bubble count (including overlaid bubbles) with the averaged bubble volume (excluding the overlaid bubbles). Performing this method in different areas of the downcomer the two-dimensional void fraction distribution along the downcomer is obtained. This void fraction is a volume-averaged value over the cross section of the downcomer and a certain height.

Using the above-described manual bubble-picking algorithm, the results of the automated void fraction algorithm are compared to an extensive evaluation by hand. As a result, an underprediction of 15 % was found for the case with the highest void fraction

and broadest bubble size distribution evaluated with the automated method. This error is mainly caused by an underprediction of the large bubbles since they have a higher probability to be overlaid by smaller bubbles, which leads to a smaller determined averaged bubble volume. For lower void fractions and narrower bubble size distributions, the error was found to be smaller.

3.4 Liquid velocity, turbulence & Sampling bias in bubbly flows

In the following section the particle tracking velocimetry (PTV) using naturally occurring micro bubbles and the particle image velocimetry (PIV) using fluorescence particles are described. The results of the determined velocity, turbulent kinetic energy and fluctuation distribution with both methods are compared and discussed.

In single-phase flow, added tracer particles do not disturb the flow; in multiphase flows, however, these particles often tend to accumulate at the interfaces and could affect the flow. In addition, tracer particles contaminate the facility in general, which might disturb chemical as well as biological processes. Besides, the seeding of particles can be problematic, for example in oceanographic applications. To overcome such problems naturally occurring micro bubbles can be used as tracer particles.

Tracking micro bubbles so that the velocity of the continuous phase can be determined is not extensively investigated yet. Nevertheless, some applications can be found in literature, e.g. in breaking waves (Ryu et al. 2005), behind propellers bubbles (Graff et al. 2008), around dolphins (Fish et al. 2014) or in horizontal channels (Murai et al. 2006). Noteworthy, micro bubbles can also be explicitly generated for particle tracking as for example shown by Ishikawa et al. (2009).

In the present work, particle-tracking velocimetry with micro bubbles (BTV) in bubbly flows is investigated. In a rectangular tabletop bubble column, the results obtained by tracking micro bubbles in the range of 100-300 µm are compared to PIV measurements. For BTV a volume illumination is used so that high gas void fractions can be investigated. A two dimensional measuring plane is obtained by using a narrow depth of field in combination with an edge filter technique.

Using PTV and PIV the view on the measuring plane is hindered in general because of passing bubbles. This leads to a sampling bias that has a significant effect on the measurements. This effect is described in the present work; further, a method is developed to overcome the bias.

The sampling bias in general is a well-known phenomenon for many applications. For example, in single-phase flow it is described for the usage of LDA (Hoesel & Rodi 1977) (Edwards 1987). Based on that, the sampling bias for bubbly flows by the use of LDA was described recently by Hosokawa & Tomiyama (2013). Nonetheless, a sampling bias in multiphase flow is not restricted to LDA measurements, it might occurs for all measuring techniques that are affected by the phases.

3.4.1 Particle Image velocimetry in bubbly flows

Particle image velocimetry in bubbly flows is a well-known method and is frequently used since the late nineties of the last century (Oakley et al. 1997). The fundamental principle is to illuminate tracer particles with a laser once or multiple times; the velocity is determined by the particle displacement.

In multiphase flow, the problem arises to distinguish between the phases. The bubbles are usually masked from the images (Brücker 2000) (Deen et al. 2002) for this

purpose. An early method that is described by Jakobsen et al. (1996) uses edge detecting algorithm to identify the brighter illuminated bubbles, which is also used recently by Pang & Wei (2013). Later, the use of fluorescence particles imprinted with Rhodamine is used (Lindken et al. 1999). Rhodamine is fluorescenting in the yellow to red spectra whereas the lasers used for PIV often emitting green light. A color filter for green light is used in order to reduce reflections coming from the bubbles. The fluorescence particles, however, tend to accumulated at the bubble surfaces and the bubbles are still present in the recording.

Noteworthy, besides cutting the bubbles out, the phases can be distinguished by different displacement peaks (Delnoij et al. 2000). Another method is the shadowgraph technique which is described e.g. by Lindken & Merzkirch (2002) and is frequently used in bubbly flows (Fujiwara et al. 2004) (Bröder & Sommerfeld 2007) (Sathe et al. 2010) (Deen et al. 2001). The bubbly flow is illuminated with an additional light source so that only bubbles by a second camera or in an extra pulse are recorded. The resulting complex experimental setup is a disadvantage of those techniques. For that reason, fluorescence particles are used in combination with digital image analysis in order to identify the bubbles in the same recording with the PIV particles.

The flow is seeded with 20-50 µm PMMA particles imprinted with Rhodamine from microParticles GmbH in Berlin. The particles are illuminated by a two dimensional laser light sheet from the side. A double-pulsed laser is used with a difference of 1/2500 s between the pulses, the double pulse is generated every 1/10 s. Every pulse is recorded separately by one high-speed camera.

The recorded pictures are separated in rectangular interrogation areas, which are 2 mm large and are overlapping 50%. The commercial software Davis 8.2.1 is used for this purpose. Hence, the PIV methods are not explicitly discussed at this point, a detailed explanation of those can be found in various books, e.g. in the book of Raffel (2007). For the phase discrimination, the complete interrogation areas that touch a bubble or a shadow are excluded. Thus, the bubbles and shadows have to be identified from the recordings.

A median filter is used in order to eliminate the tracer particles from the image (Lindken et al. 1999), which is demonstrated in Figure 3-13. After the median filter is applied (2), two thresholds are used. First, a low threshold value is applied to get more or less closed bubble boundaries (3); many structures remain that do not belong to bubbles. Second, a high threshold value is used to get only the bubbles (4). The obtained bubbles are not complete, but almost all structures belong reliable to bubbles. The pictures obtained from both thresholds are segmented and combined. If an object from (4) touches an object from (3), this object (from (3)) is taken as a bubble. The bubble structures are colored black in (5). Finally, the identified bubbles are dilated and eroded to close possible disrupted boundaries (6). The artificial coalescence that is seen in (6) is not adverse because possibly overexposed areas are identified as well.

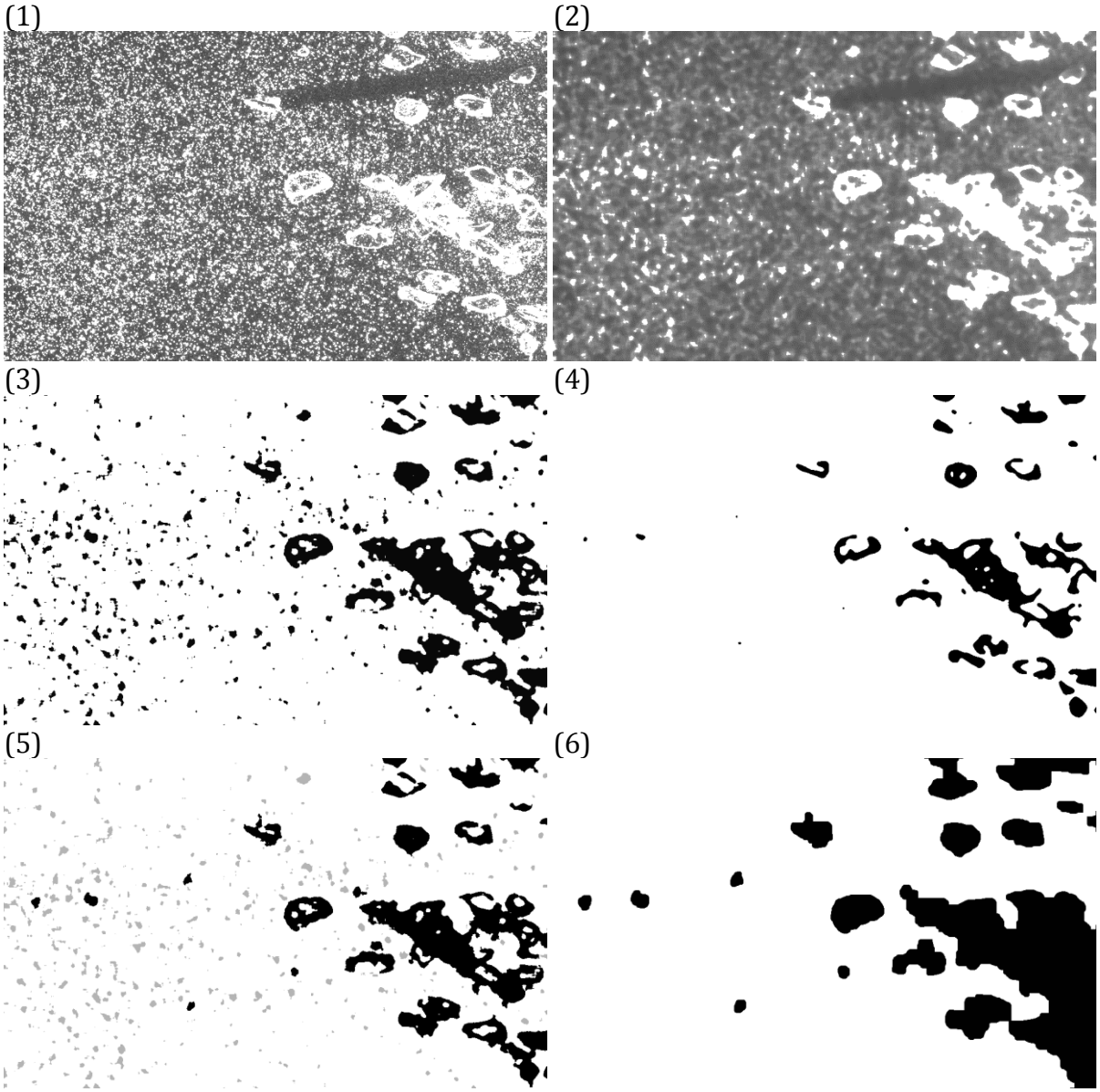

Figure 3-13 Algorithm for determining the bubbles in the PIV image for case 3 **(1)**: The obtained image from the PIV camera. **(2)**: Applying a median filter on **(1)**. **(3)**: Results obtained from a low threshold on **(2)**. **(4)**: Results obtained from a high threshold on **(2)**. **(5):** Hysteresis of the low and high threshold value results **(6)**: Closing the boundaries and filling the structures.

The laser that illuminates the particles is coming from the left in Figure 3-13 **(1)** so that the bubble located in the sheet produce a shadow in which no particles are seen. Therefore, such shadows have to be cut out as well. The same procedure as described for the bubbles is used for this purpose. The result of the bubble and shadow detecting is shown in Figure 3-14. In the top right corner the shadow is not detected (marked red in b)) because the reflections of the other bubbles re-illuminate it, which is representative for a distinct problem using PIV in multiphase flow in general; the light is reflected arbitrary at the bubble surface. Such reflections lead to a scattering of the accurate produced laser sheet. Consequently, particles might be seen that are not in the quasi two-dimensional measuring area originally generated by the laser sheet.

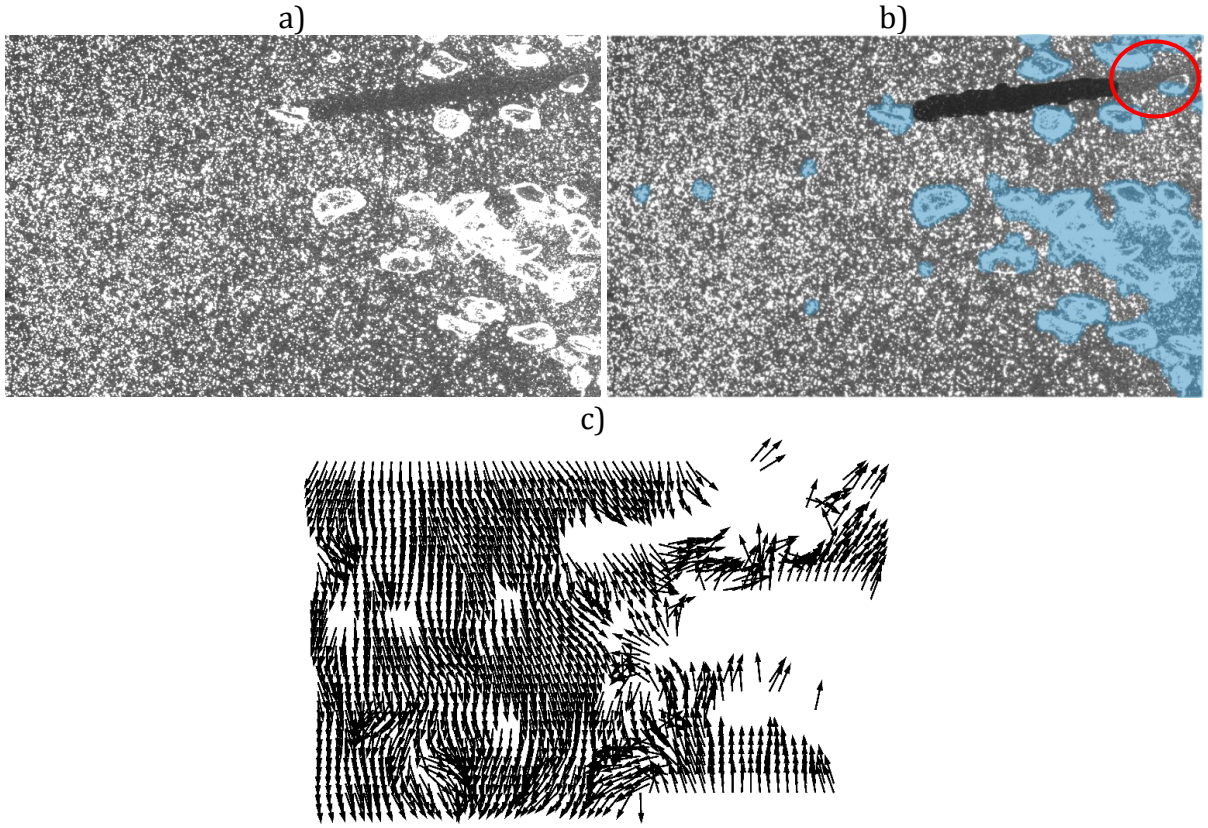

Figure 3-14 Masking the bubbles and shadows. a) The original PIV image; b) the bubble masks (blue) and shadow mask (black); c) obtained velocity vectors.

Despite fluorescenting particles are used, nearly all bubbles in the bubble column are seen. Bubbles that are not in the laser sheet are illuminated by the scattered light from the bubbles in it and other reflections. These bubbles are seen bright in the recorded pictures and are cut out by the post processing. The out of plane bubbles can be identified in Figure 3-14 by the missing shadow behind them (light comes from left).

Therefore, the velocity information in general behind or before a bubble (related to the view of the recording camera) in the bubble column is not measureable, besides, the bubbles between the laser sheet and the camera naturally block the view in general. This behavior leads to a sampling bias discussed below.

3.4.2 Particle tracking velocimetry with micro bubbles in bubbly flows

In contrast to the frequent use of PIV, PTV is rarely used in bubbly flows and only few examples are found in literature. However, PTV is an often-used technique in single-phase flows (Dimotakis et al. 1981). In the present work, micro bubbles as tracking particles are used (Bubble tracking velocimetry – BTV).

In contrast to PIV, a volume illumination is used so that the experimental set-up is simplified and higher gas volume fractions can be realized. A camera setup with a narrow depth of field in combination with an edge filter is used in order to obtain a two dimensional measuring plane. The technique is demonstrated in Figure 3-15. The field of maximum sharpness is situated between the fourth and the fifth object from the left. The blurring is increasing with increasing distance to the field of maximum sharpness. The edge-detecting algorithm (Canny 1986) is applied on the a); the normalized edge strength is shown along the red-white dotted line in picture b). Here, only the edges of the squares are of interest, so the borders of the objects are excluded from the diagram in order to

a)

b)

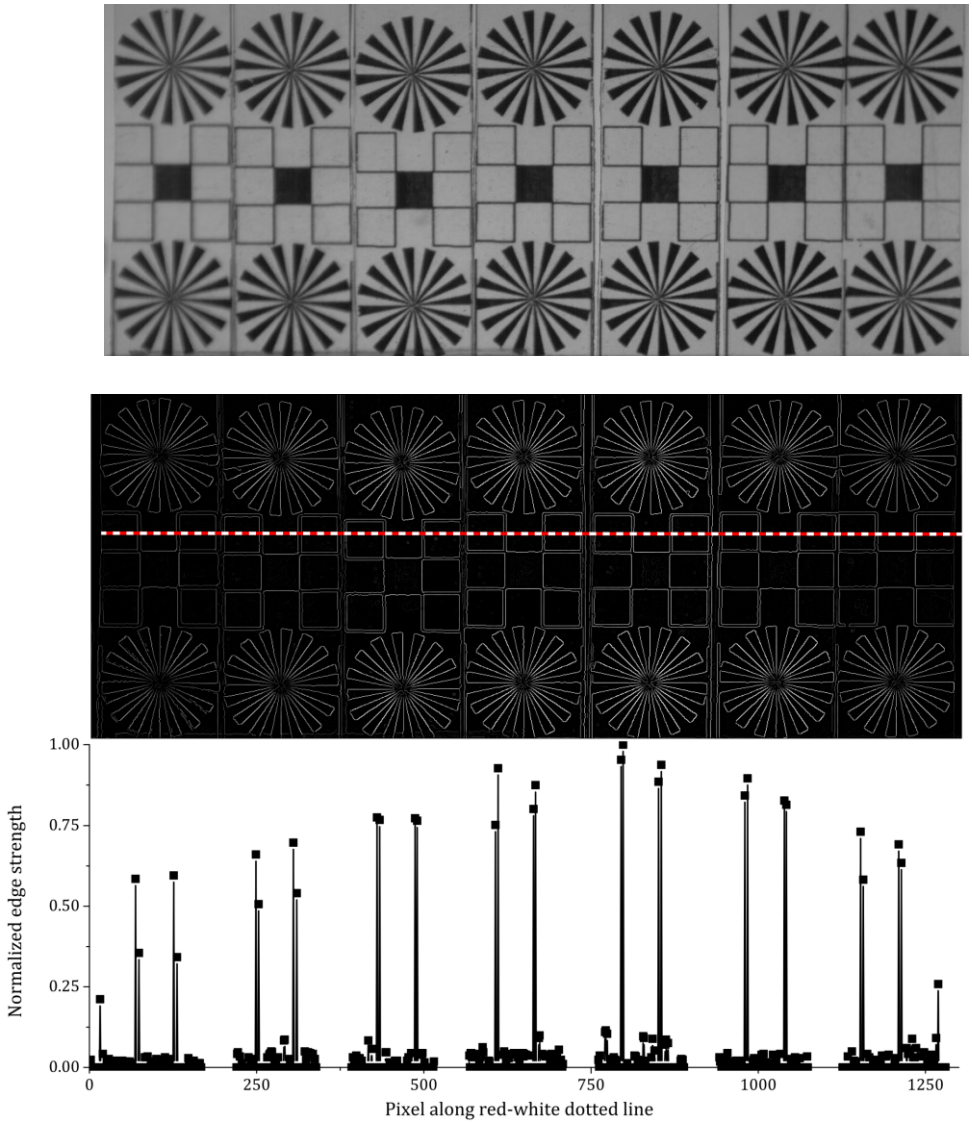

Figure 3-15 Determining the depth of field by filtering the edge strength. The distance in depth between the test prints is 1 mm. a) Original picture, b) edge strength in grey shades and as graph along the red-white dotted line.

constitute the method clearly. A hysteresis on the edge strength is applied so that the blurred edges are excluded. For the shown example, the hysteresis would cut out all edges with an edge strength below 0.8.

With a similar test set-up, the depth of field was calibrated to 2 mm; the results of this calibration are shown in Figure 3-16. The lowest measurable depth of field with the present setup is 2 mm because the test object displacement in depth is 1 mm similar to that shown in Figure 3-15. In practice, a resolution of 21 Px/mm with a normalized edge filter of 0.75 gives good results so that a sufficient large area of view is still seen. These settings will be used for the measurements in this work. The method applied to bubbly flows is demonstrated in Figure 3-17. The marked bubbles, which are in the maximum field of sharpness, are used for tracking.

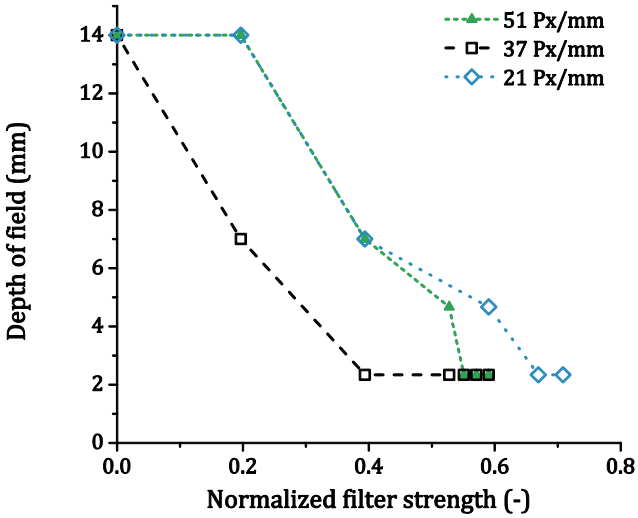

Figure 3-16 Determination of the depth of field depending on the edge filter for three different resolutions.

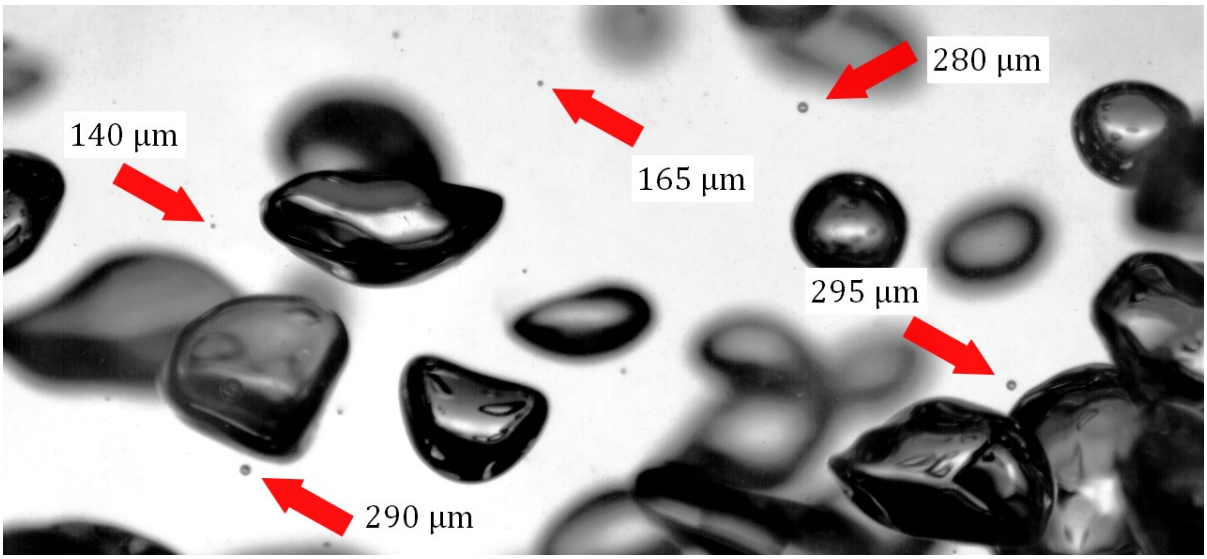

Figure 3-17 Bubbles that are used for tracking in the field of maximum sharpness.

After the micro bubbles are identified, the weighted averaged position of the pixels that belongs to the micro bubble is calculated in order to calculate the bubble position

$$\boldsymbol{x}_P = \frac{1}{\sum_j \omega_j} \sum_j \omega_j \boldsymbol{x}_j \quad . \tag{3-4}$$

With $\boldsymbol{x}_P$ the resulting positon vector, $\boldsymbol{x}_j$ the position vector of the j^{th}-pixel, ω_j the scalar weight function of the j^{th}-pixel and j the pixel index over all pixels assigned to the micro bubble. In general, the mass weighted centroid is the correct position for particle tracking. Since this information is often not accessible, other methods are required as discussed by Feng et al. (2007) and by Saunter (2010). Here, the position is determined by calculating the centroid of the projected area ($\omega_j = 1 \; \forall j$), which is reliable since the micro bubbles are spherical and have a sharp boundary.

After the positions are determined in all pictures that belong to a burst, the particle tracks have to be determined. In principal, this problem can be formulated to define similarity conditions that group positions to one track. For problems with a very high particle concentration, this can be a challenging task and is still an active discussion in literature. For the present setup, however, the concentration of the micro bubbles is low; hence, the nearest particle in the next image is used to connect the particles to a track:

$$\mathbb{T}_\mathrm{i} = \{\mathbf{x}_{\mathrm{P,k}}(\mathrm{t}), \mathbf{x}_{\mathrm{P,j}}(\mathrm{t}+\Delta\mathrm{t}) \in \text{ith Burst} \big| \|\mathbf{x}_{\mathrm{P,k}}(\mathrm{t}) - \mathbf{x}_{\mathrm{P,j}}(\mathrm{t}+\Delta\mathrm{t})\| < \mathrm{d} \\ \cap \forall \mathbf{x}_\mathrm{p}(\mathrm{t}+\Delta\mathrm{t}): \|\mathbf{x}_{\mathrm{P,k}}(\mathrm{t}) - \mathbf{x}_\mathrm{P}(\mathrm{t}+\Delta\mathrm{t})\| \leq \|\mathbf{x}_{\mathrm{P,k}}(\mathrm{t}) - \mathbf{x}_{\mathrm{P,j}}(\mathrm{t}+\Delta\mathrm{t})\|\}. \tag{3-5}$$

The micro bubble positions $\mathbf{x}_{\mathrm{P,k}}(\mathrm{t}), \mathbf{x}_{\mathrm{P,j}}(t+\Delta t)$ in a burst of pictures are in the set $\mathbb{T}_i$ if the distance between $\mathbf{x}_{\mathrm{P,k}}(\mathrm{t})$ and $\mathbf{x}_{\mathrm{P,j}}(t+\Delta t)$ is smaller than d and $\mathbf{x}_{\mathrm{P,j}}(t+\Delta t)$ is the nearest position at time $t+\Delta t$ compared to $\mathbf{x}_{\mathrm{P,k}}(\mathrm{t})$; the set $\mathbb{T}_i$ is called the i^{th}- track. From experience, the distance d is chosen to be equivalent to a velocity of 1.5 m/s divided by the measuring frequency for the discussed bubble column experiments. The set formulated in Equation (3-5) is only meaningful if two or more micro bubbles are not crossing each other during the recording. This does almost not exist because the recording frequency is high so that the micro bubble displacement is low.

In Figure 3-18 an example of the BTV method in a 60 mm wide channel is shown. Two pictures are taken consecutively with a recording frequency of 1000 Hz. In general, it is assumed that the micro bubbles move linear, hence the velocity of the i^{th}-track is calculated by the displacement multiplied with the recording frequency:

$$\boldsymbol{v_{P,i}}(\bar{t}_i, \overline{\boldsymbol{x}}_\boldsymbol{i}) = \frac{1}{\Delta t}\left(\boldsymbol{x_{P,i}}(t_i+\Delta t) - \boldsymbol{x_{P,i}}(t_i)\right), \qquad \boldsymbol{x}_{P,i} \in \mathbb{T}_i\,. \tag{3-6}$$

With $\boldsymbol{v_{P,i}}$ the velocity vector of the i^{th}-track, $\bar{t}_i$ and $\overline{\boldsymbol{x}}_\boldsymbol{i}$ the time and position of the calculated velocity vector, respectively. Since the movement is assumed linear, the position $\overline{\boldsymbol{x}}_i$ of the velocity vector is calculated by

$$\overline{\boldsymbol{x}}_i = \boldsymbol{x_{P,i}}(t_i) + \frac{1}{2}\left(\boldsymbol{x_{P,i}}(t_i+\Delta t) - \boldsymbol{x_{P,i}}(t_i)\right);\ \bar{t}_i = t_i + \frac{1}{2}(\Delta t), \qquad \boldsymbol{x}_{P,i} \in \mathbb{T}_i\,. \tag{3-7}$$

The time $\bar{t}_i$ of the velocity vector $\boldsymbol{v_{P,i}}$ is taken as the time in between the frames.

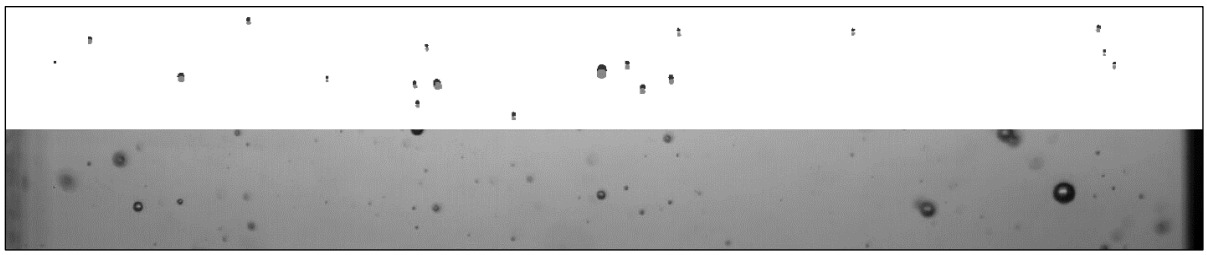

Figure 3-18 Particle tracking using mini bubbles below 500 µm diameter in a 60 mm wide chanel. Bottom: The original picture at $\mathrm{t} = \mathrm{t}_1$; top: The selected particles at $\mathrm{t} = \mathrm{t}_1$ and $\mathrm{t} = \mathrm{t}_1 + \Delta\mathrm{t}$ labeld with different grey tones, $\Delta\mathrm{t} = 1/1000$ s.

The demand of linear movement of the micro bubbles leads to a high recording frequency. On the contrary, a high recording frequency leads to very small displacements if the particles have a small velocity. The pictures are recorded in discrete pixels so that the pixel-discretization error becomes significant for very small displacements. In order to obtain sufficient displacements, the particles are usually tracked at least four times by a pulsed camera every 1/1600 s; if the micro bubble does not move its own radius from one picture to another, the next picture will be taken. The first and the last picture are used if a bubble does not move its own radius during the four-recorded frames.

It should be noted that the time interval between two pictures becomes important if the particles are strongly accelerated in this time. This problem is also reduced by recording several images in one burst of several pictures because the recording frequency is increased; this topic is discussed for example by Feng et al. (2011).

In general, the naturally occurring micro bubbles are used as tracking particles so that the size of them cannot be controlled. Micro bubbles in the range of 100 – 300 µm exist in large numbers in the investigated bubbly flows. Such are large compared to tracer particles usually used for velocity measurements, but the micro bubbles are distinctly lighter than such tracers are. The micro bubbles, however, have a terminal velocity that has to be taken into account.

The *St*okes number (St) gives information about if particles are capable to follow all turbulent scales of the flow and, therefore, if the determined particle velocities give reliable information about the flow. The Stokes number is equal to the ratio between the characteristic time scale of the particle and the flow

$$St \equiv \frac{\tau_P}{\tau_F} \quad . \tag{3-8}$$

For velocity measurements very small, buoyancy neutral tracer particles are used that fulfill $St \ll 1$. If the Stokes number is around one or even larger, important deviations occur from the perfect flow following behavior. For particles with a greater density than the continuous phase and a Stokes number around one the particles are accumulating in region with high strain (Maxey 1987), which can be quantified with the second invariant of the strain tensor $\frac{\partial u_i}{\partial x_j}\frac{\partial u_j}{\partial x_i}$ (Squires 1990). It could be shown that larger particles than the Kolmogorov length with a density similar to the flow show a similar behavior as heavier particles smaller than the Kolmogorov length (Xu & Bodenschatz 2008) (Bourgoin et al. 2011). The wake effects of the larger particles and the Faxen correction of the added mass becomes important, as dicussed for example by (Calzavarini et al. 2011). More recently, the behavior of micro bubbles is studied in turbulence with Stokes numbers below one (Mercado et al. 2012), for 75 µm bubbles with a Stokes number around one (Volk et al. 2008) and above (Prakash 2013). In comparison to heavy particles, bubbles show a different behaviour; however, compared to tracer particles also a different behavior and clustering effects depending on the turbulence structure occur. Therefore, it can be assumed that such clustering effects also occur in bubbly flows when the micro bubbles are used for particle tracking. This is important because if the micro bubbles, for example, tend to accumulate in the wake region of the larger bubbles, this regions might be overrated in the averaging process, hypothetically. This topic, however, is not yet investigated and the effect of the wake and turbulence structure in bubbly flows on the

accumulation of micro bubbles are speculative, hence these possible effects are neglected at this point but should be keept in mind.

The characteristic time scale of complex bubbly flows is not known so that the Stokes number cannot be used at this point. To get an idea, however, the results obtained with different micro bubble sizes are compared below. Moreover, the characteristic time scale is used in order to compare the micro bubbles with tracers used in similar experiments, which is shown in Table 3-1. The characteristic time scale, which is the time constant of the exponential decay of the particle velocity due to drag, is calculated by taking the virtual mass into account (Calzavarini et al. 2008) to

$$\tau_P = \frac{1}{12}\frac{d_P^2}{\nu}\frac{2\rho_P + \rho_F}{3\rho_f} \quad . \tag{3-9}$$

In general, the time scale of the used micro bubbles is comparable to other methods. Their time scale is in the range of the PIV particles used by Deen et al. (2001). LDA particles, however, have a distinctly smaller time scale whereas the polystyrene particles used for Computer-Automated Radioactive Particle Tracking (Luo & Al-Dahhan 2008) have a significantly larger time scale.

Reference	Time scale τ_P	Particles	Method
Present work	100 µm: 0.3 ms 200 µm: 1.1 ms 300 µm: 2.5 ms	Bubbles d_P: 100-300 µm	Particle tracking
Deen et al. (2001)	0.21 ms	PMMA particles d_P: 50 µm	PIV
Julia et al. (2007)	0.03 ms	Hole glass particles d_P: 20 µm	LDA
Luo & Al-Dahhan (2008)	53 ms	PS particles d_P: 800 µm	Computer-Automated Radioactive Particle Tracking (CARPT)

Table 3-1 Characteristic particle time scale for different measurement techniques in bubbly flows

In contrast to buoyancy neutral tracer particles, the density of the micro bubbles is smaller than the density of the liquid. The rising velocity has to be subtracted from the measured velocity. The rising velocity is calculated by using the drag law by Bozzano & Dente (2001).

3.4.3 Sampling Bias in bubbly flows

A sampling bias occurs if a not representative sample, in which some values are less likely included than others, is picked. If the liquid velocity is measured with BTV or PIV in bubbly flows, such a not representative sample is picked. Bubbles that are passing the field of view hinder the view on the measuring plane. However, these large bubbles drive

the flow so that higher velocities occur just when many of these bubbles are in the field of view. Since these velocities are less likely measured because the large bubbles hinder the view, a sampling bias occurs. It should be noted, that the sampling bias is not caused by the bubbles inside the measuring plane, but by the bubbles out of it.

The sampling bias is demonstrated in Figure 3-19. Clearly, the count of the velocity information is low when the vertical velocity is high and vice versa. The above-described behavior leads to this negative correlation. Other mechanisms might be identified that cause a sampling bias, for example the re-illumination of the shadows by the other bubbles for the PIV measurements or the micro bubble generation by the system for the BTV measurements. The hindered view on the measuring plane due to the passing bubbles, however, seems to be the most significant for the present setup.

Due to the sampling bias, the calculation of the correct averaged velocity is not trivial. The ensemble average is usually used to calculate the averaged velocity

$$\overline{\boldsymbol{v}}_P = \langle \boldsymbol{v}_P \rangle = \frac{1}{\sum_i 1} \sum_i \boldsymbol{v}_{P,i}\left(\boldsymbol{x}_{P,i}, t_i\right) \quad , \tag{3-10}$$

with $\boldsymbol{v}_{P,i}\left(\boldsymbol{x}_{P,i}, t_i\right)$ the particle velocity. When the non-random picked sample is used, an error occurs using the ensemble average. This might be quantified with the correlation coefficient

$$\rho(\overline{\boldsymbol{v}}_P, \mathcal{C}_T) = \frac{Cov(\overline{\boldsymbol{v}}_P, \mathcal{C}_T)}{\sigma(\overline{\boldsymbol{v}}_P)\sigma(\mathcal{C}_T)} \quad , \tag{3-11}$$

with $Cov(\overline{\boldsymbol{v}}_P, \mathcal{C}_T)$ the covariance between the averaged velocity $\overline{\boldsymbol{v}}_P$ and the count of the trajectories $\mathcal{C}_T$ that are used to calculate this averaged velocity

$$Cov(\overline{\boldsymbol{v}}_P, \mathcal{C}_T) = \langle \left(\overline{\boldsymbol{v}}_P - \langle \overline{\boldsymbol{v}}_P \rangle\right) \cdot \left(\mathcal{C}_T - \langle \mathcal{C}_T \rangle\right) \rangle \quad . \tag{3-12}$$

In PTV methods, the averaged velocity $\overline{\boldsymbol{v}}_P$ is the average of the particle velocities in a certain measuring area so that $\mathcal{C}_T$ is the count of trajectories in this measuring area. The correlation coefficients of the examples in Figure 3-19 are both around -0.4.

To overcome the sampling bias various methods exist. If the flow contains enough particles and the velocity is only desired at one specific point, a windowed ensemble average over time $\overline{\boldsymbol{v}}_{P,i}$ will provide reasonable results

$$\overline{\boldsymbol{v}}_{P,i} = \langle \boldsymbol{v}_{P,i} \rangle_{\Delta t} = \frac{1}{\mathcal{C}_{T_{\Delta t}}} \sum_{t_i - \frac{\Delta t}{2} \le t_i < t_i + \frac{\Delta t}{2}} \boldsymbol{v}_P(\boldsymbol{x}_P, t_i) \quad , \tag{3-13}$$

with $\mathcal{C}_{T_{\Delta t}}$ the count of trajectories in the time window Δt. The averaged velocity over the total time is then calculated by

$$\overline{\boldsymbol{v}}_P = \overline{\left(\overline{\boldsymbol{v}}_{P,i}\right)} = \langle \langle \boldsymbol{v}_{P,i} \rangle_{\Delta t} \rangle = \frac{1}{\sum_i 1} \sum_i \langle \boldsymbol{v}_{P,i} \rangle_{\Delta t} \quad . \tag{3-14}$$

As a consequence, the covariance between $\overline{\boldsymbol{v}}_{P,i}$ and the count of the windowed averages $\mathcal{C}_{\Delta t} = 1$ is zero because $1 - \langle 1 \rangle = 0$ and, thus, also the correlation coefficient. This averaging is also used in single-phase flow problems using (LDA) (Edwards 1987) (Murai et al. 2001) and is called hold processor.

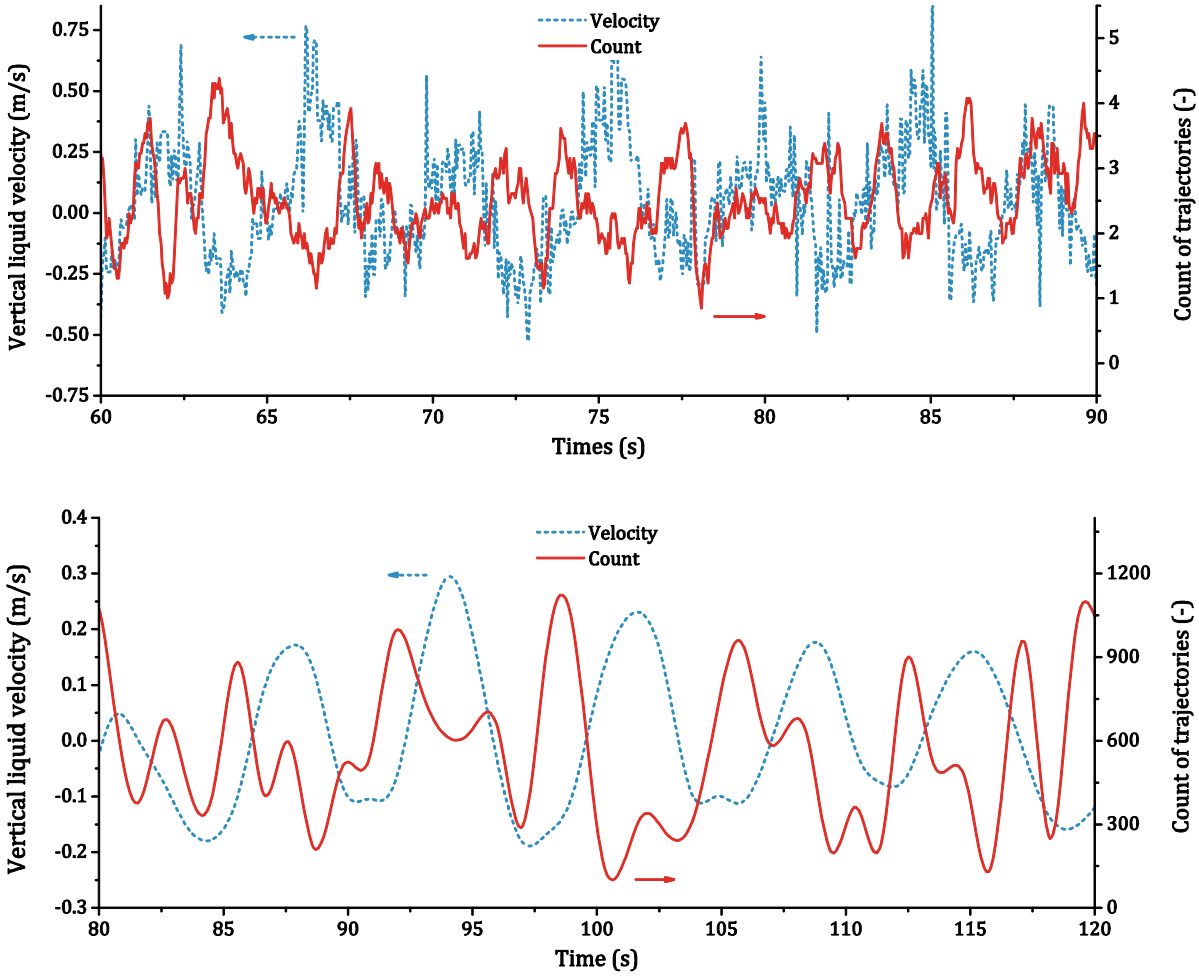

Figure 3-19 Sampling bias in bubbly flows using BTV (top) and PIV (bottom). The tracked vertical velocity (dashed blue line) and the count of the determined trajectories (continuous red line) are smoothed with a moving average to represent the sampling bias clearly.

The length of the time interval Δt is problematic; if a too long or too short interval is used, the same sampling bias will be obtained. The problem is solved by using a variable time interval depending on the distribution of the velocity information over the measuring area.

In fact, the velocity information is not distributed equally over the measuring area for the used setups. More bubbles that hinder the field of view are found in the center so that the count of the velocity information near the wall is twice as high as in the center. Therefore, simple hold-processors that wait in time until certain amounts of trajectories in one area/at one point are sampled are not meaningful. Therefore, the measuring area is discretized in grid cells and the hold processor waits the time Δt_i (hold time) until all grid cells are filled with at least one velocity information. Afterwards, the velocity information is averaged over the time Δt_i inside the grid cells. Thus, one value in each grid cell is obtained afterwards. The averaging over the grid cell is a windowed averaging in space. After the complete measuring time, these averaged values are arithmetic averaged. In the following, this hold processor in space and time is written as $\langle v_{P,j} \rangle_{\Delta t_i}$. This procedure can be formulated as

$$\langle v_P \rangle_{\Delta t_i}(\boldsymbol{x}_j) = \frac{1}{\mathcal{C}_{T\,\Delta t_i}(\boldsymbol{x}_j)} \sum_{t_i - \frac{\Delta t_i}{2} \le t_i < t_i + \frac{\Delta t_i}{2}} \boldsymbol{v}_P(\boldsymbol{x}_P, t_i) \quad , x_P^k \in \left(x_j^k - d^k, x_j^k + d^k\right] \ ,$$

(3-15)

with $\boldsymbol{x}_j$ the centroid of the j^{th}-grid cell and $\mathcal{C}_{T\,\Delta t_i}(\boldsymbol{x}_j)$ the count of the trajectories collected over Δt_i in the j^{th}-grid. For the present setups, the grid cells are quadratic so that $x_P^k \in \left(x_j^k - d^k, x_j^k + d^k\right]$ for the k^{th}-coordinate. The algorithm is illustrated in Figure 3-20.

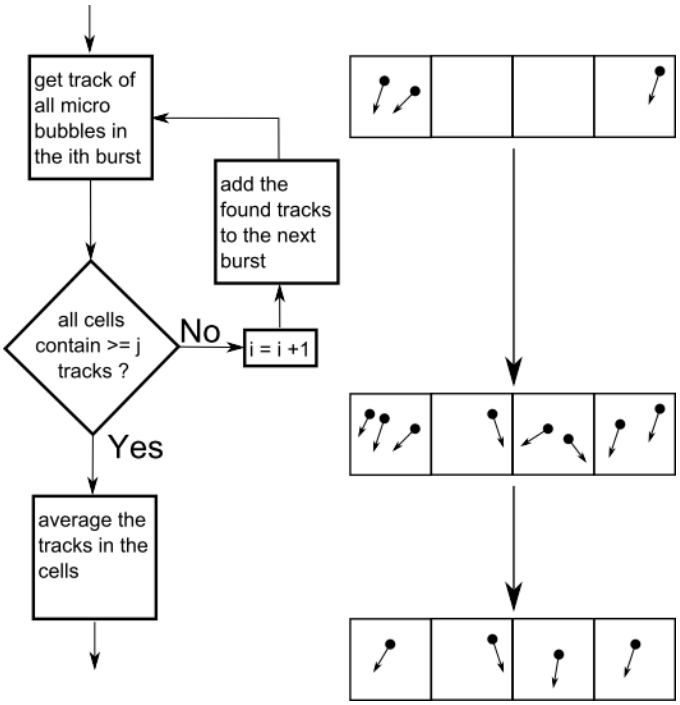

Figure 3-20 The algorithm for the hold processor in space and time with an example on an Eulerian grid with illustrated velocity vectors.

Using this hold processor, the sampling bias is overcome. For investigation a test function with an analytic solution can be defined, for example

$$y_j(x_i) = \sin\left(\left(\frac{\mathbb{G}\left(n(i)\right)_j}{\sqrt{s}} + \frac{\mathrm{x_i}}{\pi}\right) \cdot \pi\right) + d, \qquad x_i = x_{i-1}\mathrm{sgn}\left(\sin\left((\Delta x \cdot i)\pi\right)\right) \cdot \Delta x \ .$$

(3-16)

The function described by Equation (3-16) is a discretized sinus function. The Gaussian distribution function $\mathbb{G}\left(n(i)\right)_j$ provides $n(i)$ points between 0 and 1. The sinus function is meandering in time by shifting the x-axis; the time is denoted with i. The amount of discretization points $n(i)$ is randomly distributed over time. The meandering Gaussian distribution simulates a problem similar to the one shown in Figure 3-19 with a positive correlation coefficient between sampling count (represented by the Gaussian

distribution) and the measuring value (the sinus function value y) . The correct average in continuous space over the steps i of this test function is simply $y(\langle x_i \rangle) = \sin(X\pi + \langle x_i \rangle) + d$ (X is the x-axis).

The above defined hold processor $\langle v_{P,j} \rangle_{\Delta t_i}$ can be studied by the use of this easy test function nicely. For example, using $\Delta x = 0.1$ and $d = 0.5$ the sinus function is meandering in $0.1/\pi$ steps around 0.5 with $x_i \in [-0.5, 0.5]$. Using $s = 50$, the normalized averaged results obtained with the hold processor, the simple ensemble averaging and the analytical solution are shown in Figure 3-21. Obviously, the hold processor can represent the averaged function. The ensemble average method, in contrast, cannot represent it.

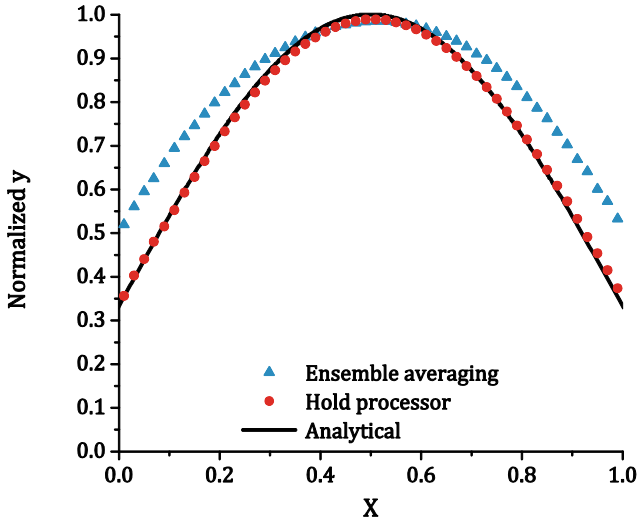

Figure 3-21 Comparison of the hold processor with the simple ensemble averaging used on the analytical test function.

If the time step is too large or the hold processor have to wait too long, the result will tend to the simple ensemble-averaged result. The best results will be obtained if no waiting time is needed so that only the information is windowed averaged in space due to the grid definition; if the grid cells are too large, the sampling bias persists inside them. Naturally, if no sampling bias occurs and enough velocity information is available, the hold processor is equal to the ensemble average.

Turbulence parameters have to be formulated correctly when the hold processor is used. For example, the turbulent kinetic energy k is defined as

$$k(t) = \frac{1}{2}\left(v_x' v_x' + v_y' v_y' + v_z' v_z'\right) . \tag{3-17}$$

With v_k' the fluctuation in the k^{th}-direction

$$v_k'(t) = v_k(t) - \langle v_k \rangle . \tag{3-18}$$

The hold processor must not be simply used on the turbulent kinetic energy or the fluctuation. The fluctuation in the j^{th}-cell in the k^{th}-direction have to be written as

$$v_{j,k}'(t) = v_{j,k}(t) - \bar{v}_{j,k} = v_{j,k}(t) - \langle v_{j,k} \rangle_{\Delta t_i} . \tag{3-19}$$

Moreover, the fluctuation must not be simply averaged over the hold time because the fluctuations with different sign would compensate each other. Consequently, the square

of the fluctuation is averaged with the hold processor, hence the turbulent kinetic energy at the discrete time t_i in the j^{th}-cell is calculated by

$$k_j(t_i) = \frac{1}{2}\left(\langle v'_{j,x}v'_{j,x}\rangle_{\Delta t_i} + \langle v'_{j,y}v'_{j,y}\rangle_{\Delta t_i} + \langle v'_{j,z}v'_{j,z}\rangle_{\Delta t_i}\right) . \quad (3\text{-}20)$$

The same treatment is needed for all statistic variables.

3.4.4 Results

The bubble column that is described in Section 3.1 is used. The liquid velocities and turbulence parameters were determined at the centerline 0.2 m above the ground plate as shown in Figure 3-22. The sparger that is installed level with the ground plate consists of eight needles with an inner diameter of 1.5 mm.

Six different volume flow rates, which are given in Table 3-2, are investigated. The volume flow rate was measured and controlled with a mass flow controller. 0.375 liter per minute per needle was the smallest possible volume flow rate whereas 20 liter per minute in total was the highest possible with used mass flow controllers.

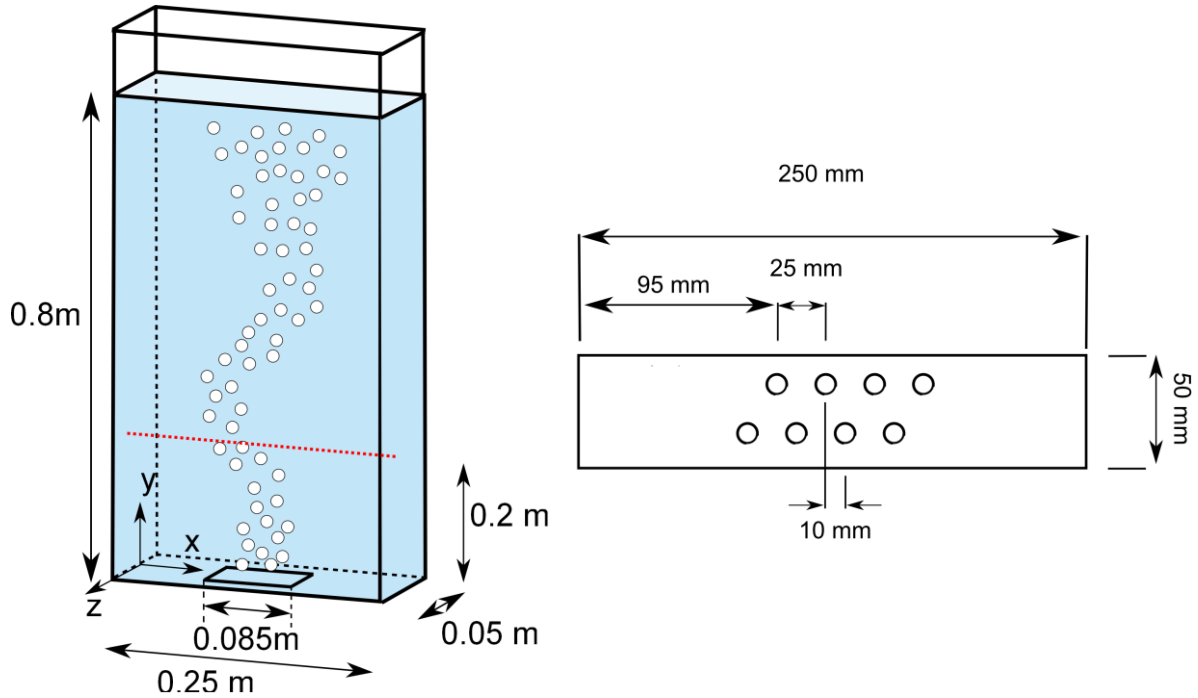

Figure 3-22 Experimental setup used for the liquid velocity experiments. Left a sketch of the facility, the measuring line is dotted red, the axis indicate the origin; right the ground plate of the bubble column with the holes for the used needle sparger.

Case Number	Volume flow rate [liter/min]	Flow per needle [liter/min]
3	3	0.375
4	4	0.5
5	5	0.625
7	7	0.875
13	13	1.625
20	20	2.5

Table 3-2 The different gas volume flow rates used for the experiments, the values are refereed to standard conditions.

3.4.4.1 Micro bubble tracking velocimetry

The micro bubbles were tracked by the use of a Redlake motion pro high-speed camera and a Sigma macro objective with a focal length of 300 mm. Since a distinct magnification was needed, only a quarter of the bubble column could be recorded so that two different measurements had to be executed in order to get a velocity profile over half of the bubble column. Moreover, the different volume flow rates were measured for one window consecutively to reduce the measuring effort. Nevertheless, no significant mismatch at the overlapping regions was observed as demonstrated in Figure 3-23. Therefore, this error is negligible and the overlapping regions are simply averaged.

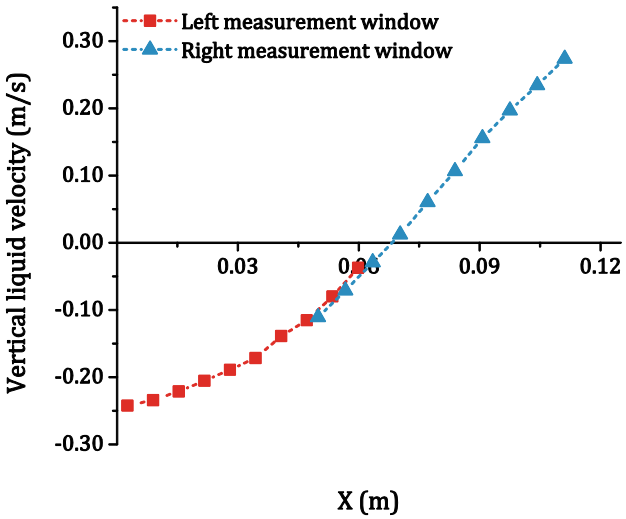

Figure 3-23 Left and the right measuring window of the left half of the column for case 13.

Micro bubble size

The size of the micro bubbles that are used for particle tracking is not uniform and different at different positions. Bubble size distributions at two positions are demonstrated in Figure 3-24. Near the wall, the count of smaller bubbles is higher than towards the center. Hypothetically, if the smaller bubbles follow the flow better than the larger bubbles, locally different turbulence parameters are obtained. Therefore, it is essential to track bubbles in a range of size in which the capability to follow the flow is the same. Moreover, the general capability of the micro bubbles to follow the liquid flow fields is of interest to assess possible errors due to the larger size and smaller density of them compared to, for example, LDA or PIV particles.

The results that are obtained by using different micro bubble sizes are compared to each other for case 13 in Figure 3-25. They are discretized in five different groups. For every group the liquid velocity and fluctuation is determined.

The vertical liquid velocity is similar for all bubble groups except for the group of 400-500 µm micro bubbles; near the wall, the results are lower than the others are. Tracking larger micro bubbles, however, must not imply a larger vertical velocity due to the higher terminal velocity because the liquid velocity is corrected with this. The results that are obtained by using all bubbles (bubble group 150-500 µm) is not equal to the average of the results over all sub bubble groups because all results are obtained by using the hold processor. In addition, the quantity of the tracked micro bubbles in the different bubble

groups is not the same, but the quantity of the smallest group is sufficient to produce a plausible result.

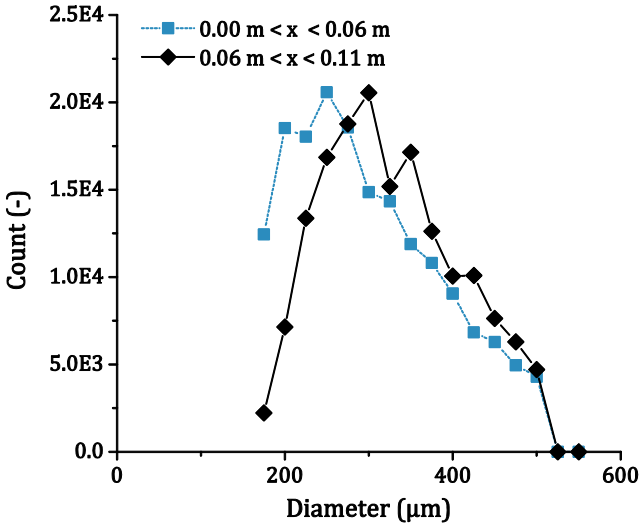

Figure 3-24 Count of the tracked micro bubbles for case 13 at the wall and towards the center; the center is at x = 0.125 m.

The normal Reynolds stress tensor component v′v′(v is the vertical velocity) might indicate a different ability to follow the flow for the different bubble sizes. Looking at b) in Figure 3-25 a clear trend is seen. In the center v′v′ is decreasing with increasing bubble size. The results obtained with the bubble groups ranging from 150 to 250 µm and from 200 to 300 µm, however, are almost equal.

In addition, the probability density function (PDF) of the fluctuations is shown in c) and d); the larger and smaller micro bubbles have the same behavior in general. The PDF of the larger bubbles, however, are smoother than the functions of the smaller bubbles, although the quantity of the smaller size group is larger; particularly in picture c), the smaller size group contains 7 600 tracks whereas the larger bubble size group only 6 300 tracks. Despite this, the PDFs of the small bubbles and the large bubbles are similar, especially at the shoulders.

Overall, the results obtained using larger micro bubbles are different compared to the results using smaller micro bubbles. The trend of decreasing Reynolds stress tensor component v′v′ with increasing size might indicate a worse capability to follow the flow of these. However, the PDFs of the small and large bubbles are similar at high fluctuations. A definite conclusion cannot be drawn since the characteristic time scale of the fluid flow is unknown. Nevertheless, the results that are obtained using bubbles between 150 and 300 µm are similar for the present setup so that this bubble group is used for further investigations. Noteworthy, the good agreement between the PIV results and the bubble tracking results, which is later discussed, might confirm that the chosen bubble size group is reasonable.

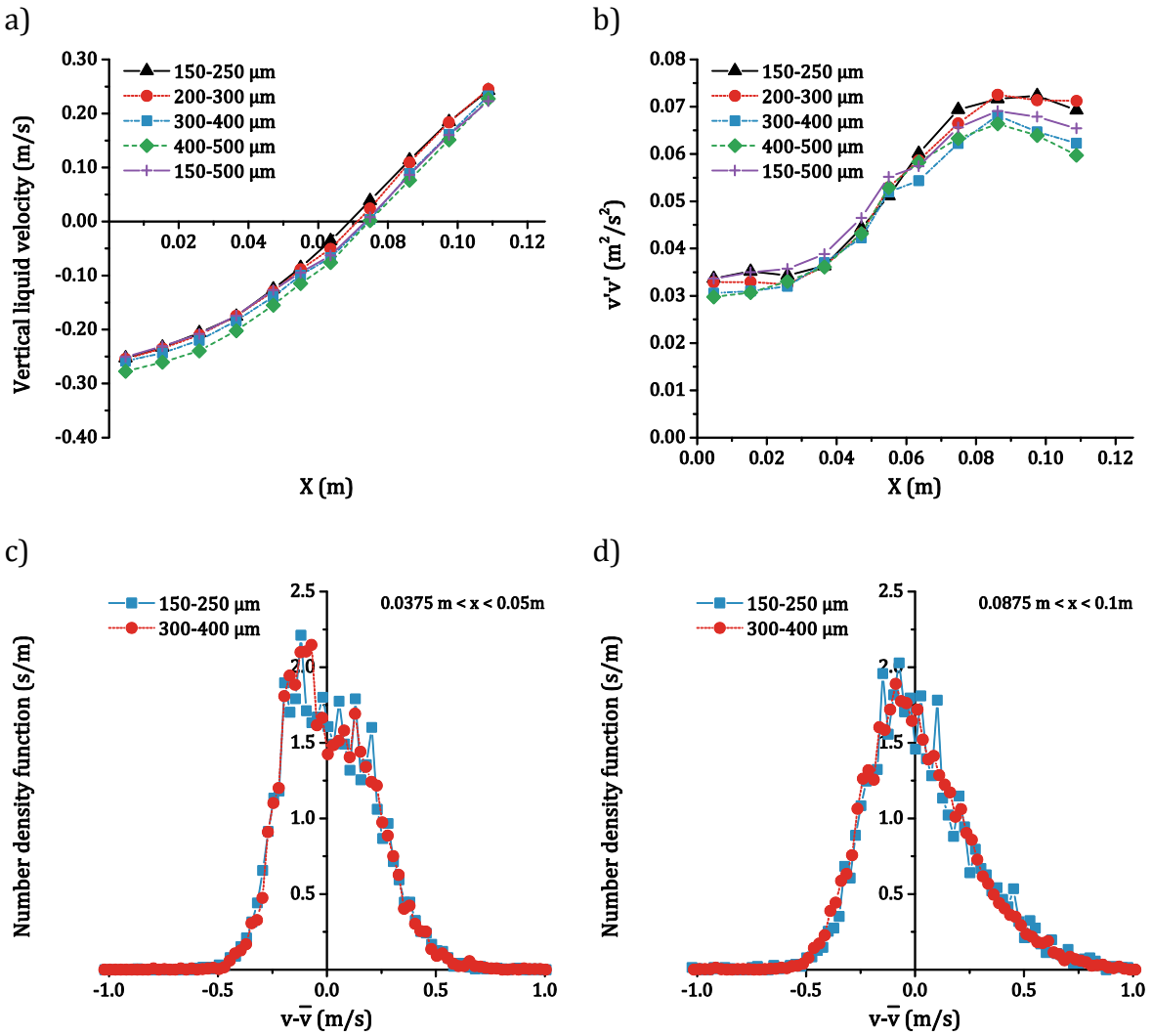

Figure 3-25 Comparing the results obtained by tracking different bubble sizes. a) The vertical liquid velocity v for the different bubble sizes, b) the normal Reynolds stress tensor component v′v′, c) the fluctuation probability function in 0.0375 m < x < 0.05 m for two bubble groups, b) the fluctuation probability function in 0.0875 m < x < 0.1 m for two bubble groups.

Influence of the different volume flow rates

The results for all cases that are obtained with the BTV technique are shown in Figure 3-26. The progression of the vertical liquid velocity with increasing the gas volume flow rates is reasonable.

As expected, the normal Reynolds stress tensor components $v'v'$ and $u'u'$ are increasing with increasing gas volume flow rates (u is the horizontal velocity). The graphs of $v'v'$ show a distinct peak between the wall and the center for all volume flow rates. In contrast, $u'u'$ is permanently increasing towards the center. This behavior is also described in other work using similar experimental setups (Mudde et al. 1997) (Simiano et al. 2006). Since the flow regime is changing, $v'v'$ and $u'u'$ obtained for case 20 are distinctly higher than these for the other flow rates are. In case 20 all bubble sizes are pulled downwards in the recirculation zone so that the bubble column is completely filled with bubbles; whereas in case 13 bubble clusters are pulled downward occasionally and

in case 7 only few bubbles. The possible outlier in the $u'u'$ graph obtained for case 20 at around x = 0.055 m is discussed below.

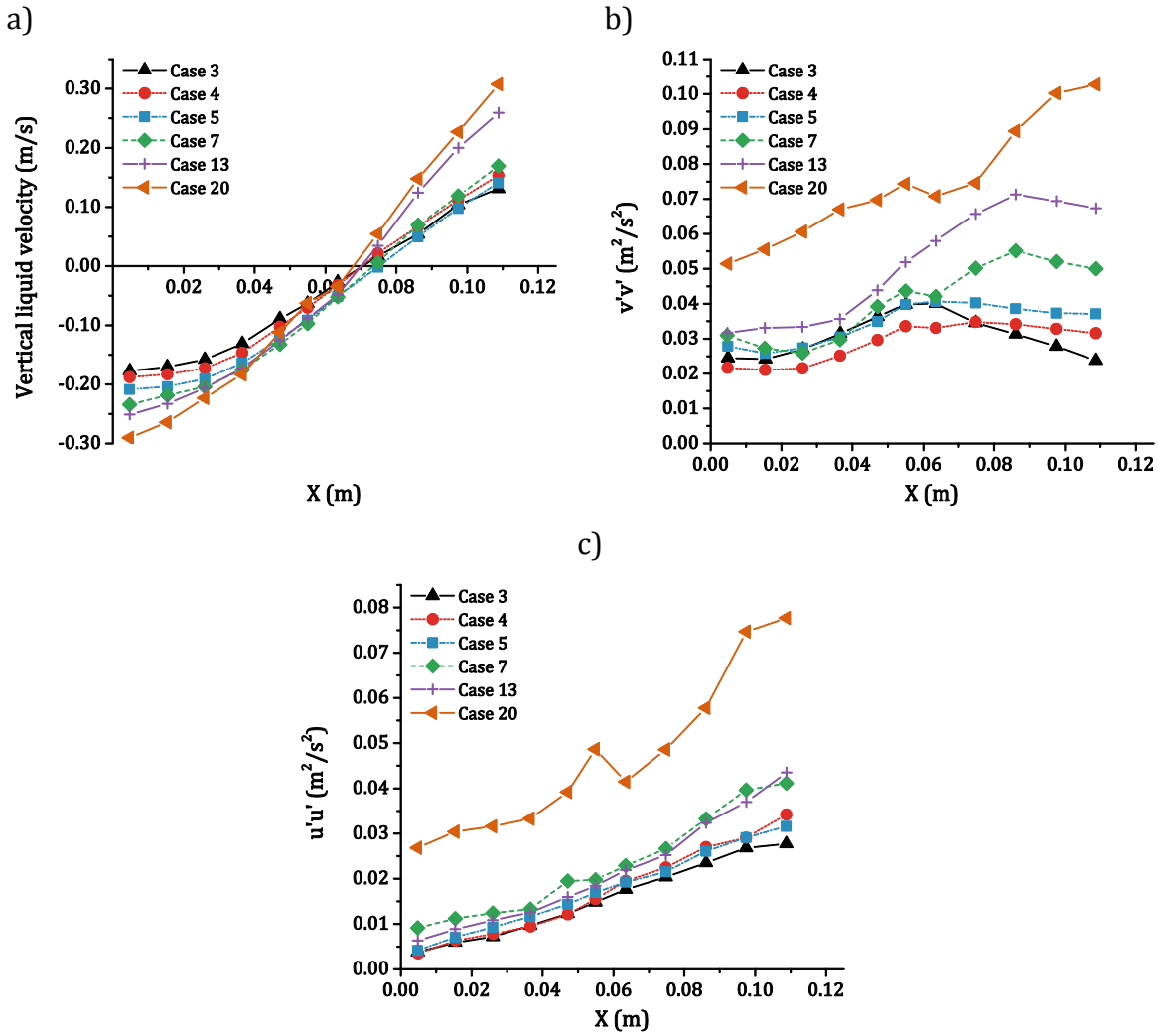

Figure 3-26 Results of the BTV for all cases. a) Vertical liquid velocity v b) normal Reynolds stress component v′v′ c) normal Reynolds stress u′u′ (u is the horizontal liquid velocity).

3.4.4.2 Comparison with PIV

Influence of the sampling bias

The influence of the sampling bias on the PIV results is demonstrated for three different volume flow rates in Figure 3-27. The measuring area is discretized in twelve areas, the hold processor waits until all areas contain at least one velocity information as discussed above. Looking at the liquid velocity, the sampling bias leads to a flat velocity profile for all flow rates. The underprediction in the center is due to the bubbles which drive the flow and ,parallel, hinder the view on the measuring plane, therefore, the velocity information which contains the higher velocities are underrated. A large negative vertical velocity at the wall might be connected to a larger count of bubbles that are pulled downward so that these bubbles might block the view on the measuring plane, which leads to an underrating of the large negative velocities.

The normal component of the Reynolds stress tensor $v'v'$ is affected by the sampling bias in the same way as the liquid velocity. Towards the center, the $v'v'$ values are

underpredicted for all volume flow rates; the underprediction increases with increasing the volume flow rate. Surprisingly, the sampling bias has no effect near the wall in contrast to the liquid velocity. Similar to $v'v'$ the cross component $u'v'$ of the Reynolds stress tensor is affected by the sampling bias, although the effect is smaller in the center.

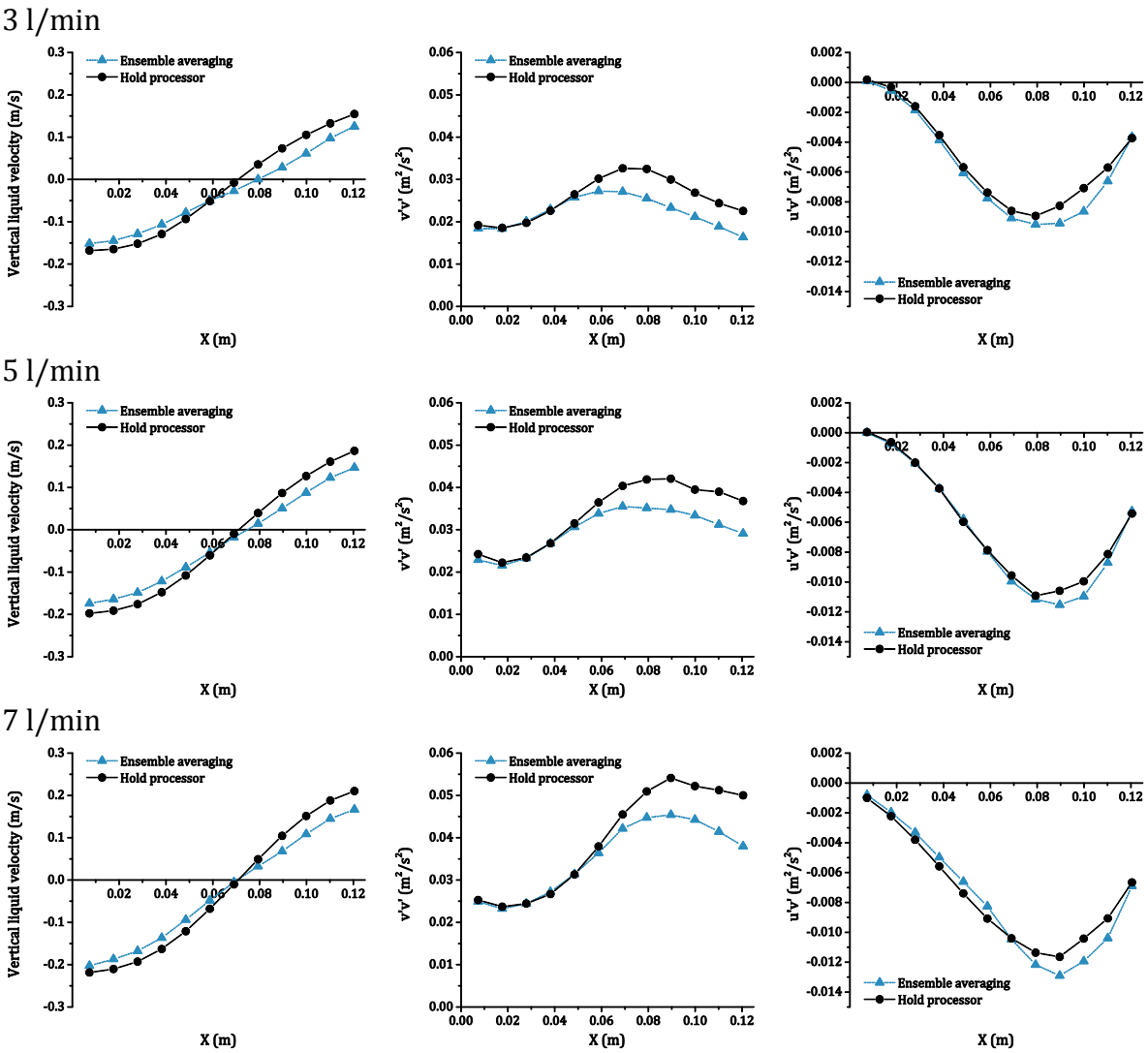

Figure 3-27 The influence of the sampling bias on the PIV results for different volume flow rates.

The influence on the BTV results is not as strong as on the PIV results as shown in Figure 3-28; the influence is weak near the wall for the liquid velocity. Towards the center, however, the influence is significant. The same trend is seen for the $v'v'$ graph. Looking at the $u'v'$ graph the influence is compared to the PIV results minor.

Although PIV and BTV are influenced differently by the sampling bias, the results obtained with the hold processor are similar. For the other volume flow rates, the agreement between PIV and BTV is very good as well, which is discussed below. Thus, the hold processor might be reasonable and both, BTV and PIV, can represent the liquid velocity fields.

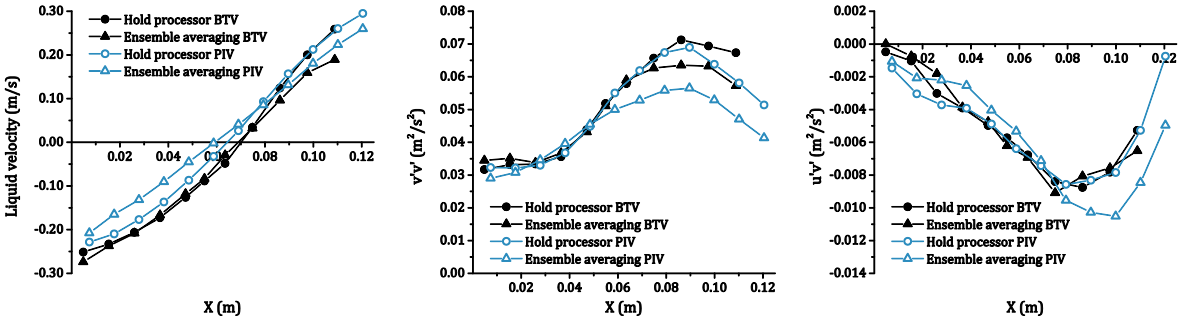

Figure 3-28 The influence of the sampling bias on the BTV results compared to the PIV results for case 13.

Comparison for different volume flow rates

The results that are obtained with PIV are compared to those with BTV; for the PIV measurements 10 minutes were recorded per case whereas for the BTV measurements 3.75 minutes were recorded. All results are obtained by the use of the hold processor.

The PDFs of v′ for case 13, which are shown in Figure 3-29, are in good agreement. At zero fluctuations near the wall between 0.0375 m < x < 0.05 m, however, the results are slightly different but difficult to compare since the BTV graph is too noisy here. Nevertheless, the peak at around -0.12 $^{m}/_{s}$ is clearly represented by both measuring techniques. The PDFs of the fluctuation towards the center at 0.0875 m < x < 0.1 m are almost perfectly matching.

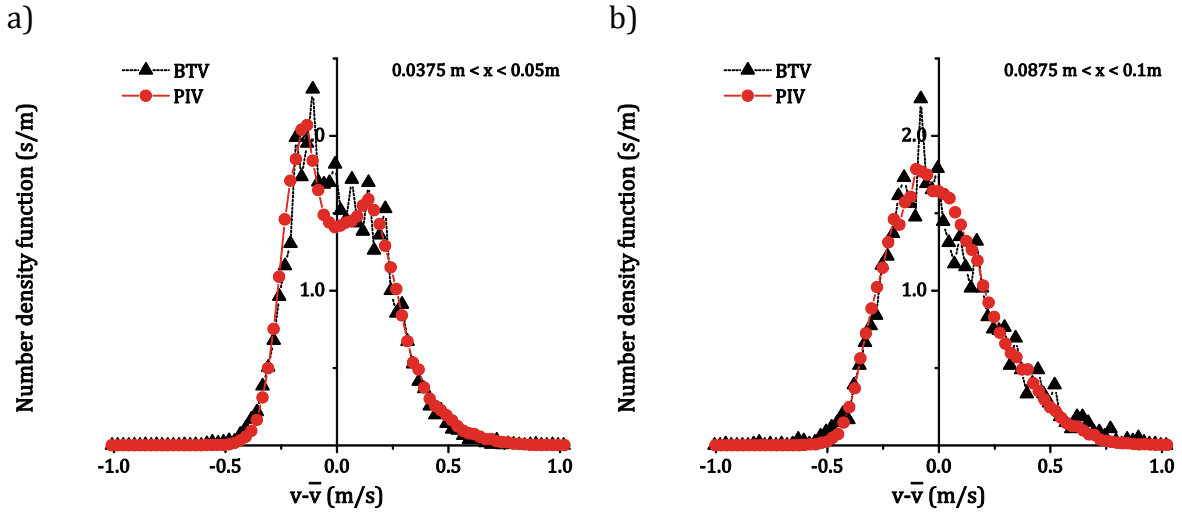

Figure 3-29 The probability density function of the upward liquid velocity fluctuations obtained with PIV and BTV for case 13. a) Near the wall between 0.0375 m < x < 0.05 m, b) towards the center between 0.0875 m < x < 0.1 m.

The time averaged liquid velocity profiles that are obtained with PIV and BTV and shown in Figure 3-30 are perfectly matching until case 13. Despite a relatively high gas void fraction for case 13 and 20, still a good result is obtained with PIV.

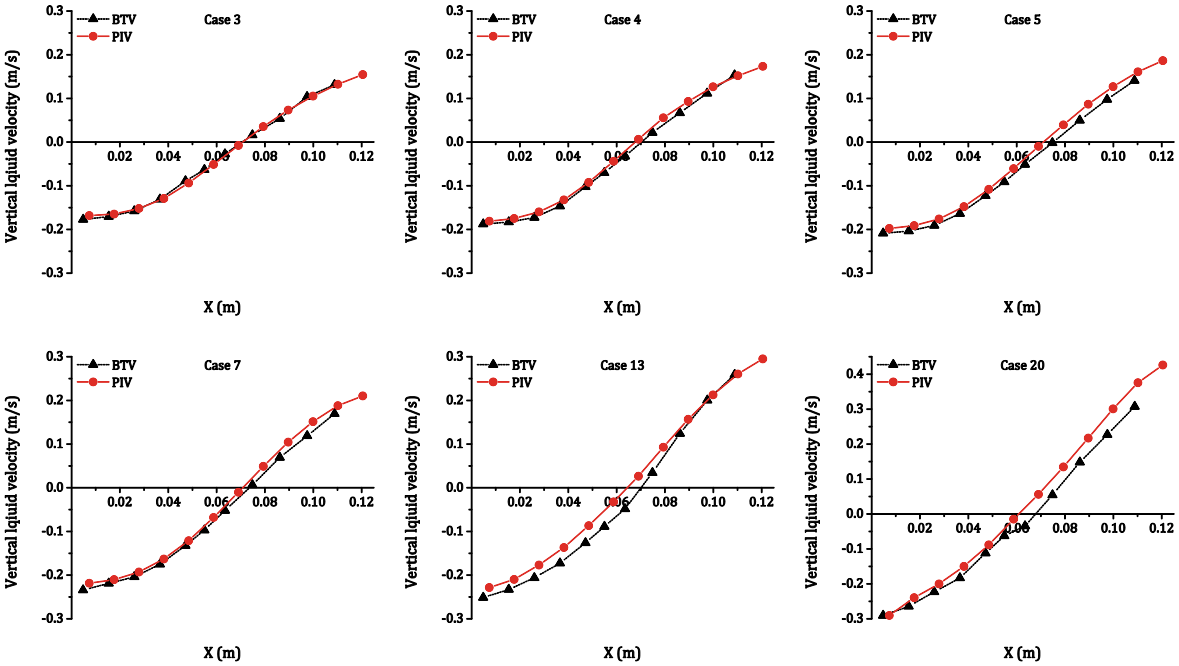

Figure 3-30 The vertical liquid velocity obtained with PIV with BTV for different gas volume flow rates.

The results for $v'v'$ and $u'u'$, which are shown in Figure 3-31 a), are similar up to case 20. Some deviations occur, for case 3 the peak of the $v'v'$ graph obtained with BTV is closer to the wall than the peak obtained with PIV. In fact, the amount of the naturally occurring micro bubbles is very small for this case because of the small gas volume flow rate. In combination with the small void fraction in general, the PIV technique might be advantageous for case 3. For case 4 and case 5, however, the obtained Reynolds stresses are very similar.

Looking at $v'v'$ for case 7 and $u'u'$ for case 20, possible outliers at around 0.055 m occur. These outliers are situated at the connection between the left and the right measurement window. The two needed separate measurements to get a half profile as discussed above, in combination that the bubble plume sometimes tends to prefer one side of the bubble column so that it is swinging not symmetrical for a distinct time, might be the reasons for this possible outlier. For the PIV measurements, in contrast, a larger measuring time was used and the complete measuring area was recorded at once so that such problems not arose.

The first distinct differences between the PIV and BTV measurements occur for case 13. In the center, the normal Reynolds stresses $v'v'$ that are obtained with PIV are smaller. The higher gas volume fraction might distort the PIV measurements, the bubble clusters that are pulled downward at the walls block the laser assembled at the side of the bubble column. In comparison, since the amount of micro bubbles is increasing with increasing volume flow rate the BTV measurements are easier to evaluate for case 13. In addition, the volume illumination is not as strong disturbed by the higher gas void fraction as the PIV laser. Nevertheless, the results are still in good agreement as also discussed above by using the PDFs of the fluctuation shown in Figure 3-29.

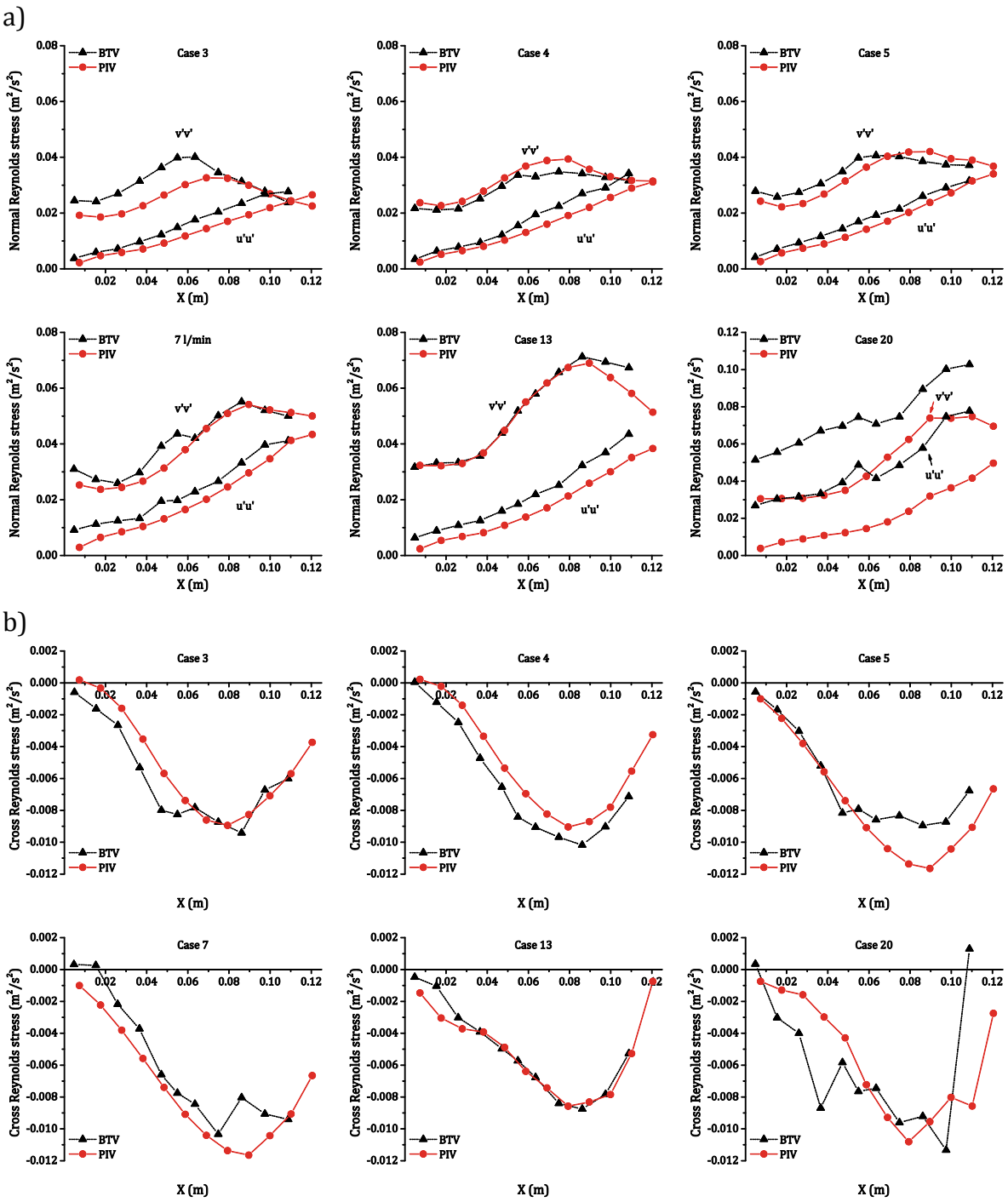

Figure 3-31 Reynolds stress components obtained by using PIV and BTV. a) Normal Reynolds stress components v′v′ and u′u′ (u is the horizontal liquid velocity), b) cross Reynolds stress component u′v′.

A mismatch between both methods is obtained for case 20; here all sizes of bubbles are pulled downward by the circulating flow so that the light sheet of the PIV laser is barely available. In contrast, the BTV measurements are still good manageable because of the volume illumination. Although the agreement is good for the time-averaged velocity, the normal Reynolds stresses obtained with PIV are strongly under predicted. These normal Reynolds stresses are in the range of the results obtained for case 13, which is not reasonable. As expected, the results for case 20 obtained with BTV are higher than

the results for case 13. Therefore, for case 20 the BTV results are more reasonable than the PIV results.

The results for the cross Reynolds stress component $u'v'$ are shown in Figure 3-31 b). The agreement between both measuring techniques is acceptable. However, the shorter measuring time in combination with a relatively small amount of micro bubbles might lead to an insufficient statistic in the BTV measurements, especially for case 3. Surprisingly, for case 13 the graphs are matching almost perfectly.

3.4.5 Conclusions

The particle tracking velocimetry using micro bubbles (BTV) is investigated. Micro bubbles in the range of 100-300 µm that naturally occur in bubbly flows are used to determine the liquid velocity and basic turbulence parameters. The particle relaxation time of the micro bubbles is comparable to other measurement techniques used in multiphase flows. Also from the results obtained with different micro bubble sizes and from the comparison with PIV measurements these micro bubbles are capable to represent the flow for the present setup. The liquid velocity, two normal and a cross Reynolds stress tensor component obtained with BTV are compared to PIV measurements, very good agreement is obtained.

Moreover, the use of a volume illumination in bubbly flows is described. Bubbles in a quasi-two dimensional plane are identified with an edge filter provided by a camera setup with a narrow depth of field. This measurement assembly is very simple so that measurements in difficult environments like in pilot plants or submerged oceanic multiphase flows problems are simpler feasible. In addition, high void fraction (in the present measurements over 15 % gas holdup) measurements up in a narrow test section are easily possible.

The sampling bias caused by the presence of bubbles was described. It was found that indifferent whether BTV or PIV is used a distinct sampling bias occurs. In general, the sampling bias is important for all measuring techniques affected by the dispersed phase. This effect might be quantified by calculating the correlation coefficient of the measured value and the sample. For PIV and BTV measurements, the measured value is the velocity and the sample was chosen to the count of the velocity information.

The described sampling bias is overcome by using a multidimensional hold processor defined in the present work. This derived hold processor, which was also tested with analytical test functions, gave reasonable results. It was found that the BTV and PIV measurements were affected by the hold processor differently. The results obtained with the hold processor for PIV and BTV, however, were similar; further, both measurements are only in accordance by using the hold processor. Therefore, the quality of the velocity measurements in bubbly flows using PIV and PTV/BTV can be improved with this method.

4 Eulerian bubbly flow simulations with the URANS equations

In the following the method for simulating bubbly flows in the present work is developed. As described above, the recent baseline model concept developed mainly for pipe flows should be adopted and studied for gravity driven flows. For this purpose, the URANS solution method described in Section 2.4.2 is used to cover the influence of large-scale turbulence (Mudde 2005) in such flows. Such large-scale phenomenon occurs due to an uneven aeration (Juliá et al. 2007) or in heterogeneous flow regimes (Lucas et al. 2007b).

A proper turbulence modeling including large-scale structures in dispersed multiphase flows is essential for a correct prediction of the momentum exchange between the phases. Especially for bubbly flows the break-up and coalescence processes, which are responsible for the bubble size distribution, are dominated by turbulence (Liao & Lucas 2009). Since all modeled forces depend on the bubble size, the importance of a reliable turbulence prediction is underlined. In bubble columns the large scale structures are also very important for mixing in technical apparatuses, as described for example by Joshi et al. (2002). Mixing might be underpredicted if these large-scale fluctuations are suppressed by a steady solution method.

In contrast to the consistently stated conclusion, e.g. by (Tabib et al. 2008) or (Masood et al. 2014), it is shown that the virtual mass force is not negligible in bubbly flows with distinct large-scale turbulence structures. In addition, with the aid of a developed convergence criteria it is shown that a solution time, time step length and mesh size independent solution for the bubbly flow URANS simulations exists.

4.1 Modelling, setup and convergence criteria

As an experimental reference, the results of Mohd Akbar et al. (2012) are used. The experiments were executed in a rectangular water/air bubble column at ambient conditions. The ground plate is a rectangle of 240 × 72 mm and the water level is at 700 mm. The inlet is realized through needles at the bottom. Measurements were performed for two superficial velocities, 3 mm/s and 13 mm/s, the integral void fraction for both conditions is below 10%. The measurement plane is 500 mm above the inlet. A sketch of the experimental setup is shown in Figure 4-1.

The measured quantities are the liquid velocity, gas volume fraction and the turbulence intensity in the upward direction. Additionally, the bubble size distributions at the inlet and at the measurement plane were measured. The bubble size distributions are reproduced in Figure 4-2.

In contrast to the case with 3 mm/s superficial velocity, which is treated as monodisperse using 4.3 mm as bubble size, for the case with 13 mm/s superficial velocity a distinct amount of bubbles is above and below 5.83 mm. Therefore, two bubble classes with its own velocity field as described in Section 2.3.3 are used. In particular, the first bubble class has a bubble diameter of 5.3 mm, the second 6.3 mm. The inlet gas volume flow is split up to 63 % and 37 %, respectively. As indicated in Figure 4-2 coalescence and break-up processes are not dominant for the present setup, thus these processes are neglected.

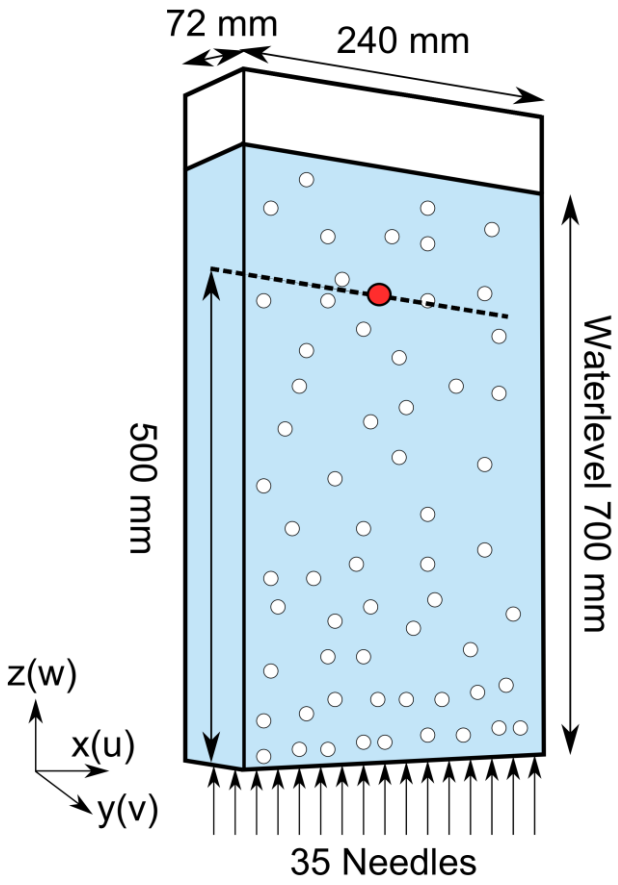

Figure 4-1 Experimental setup

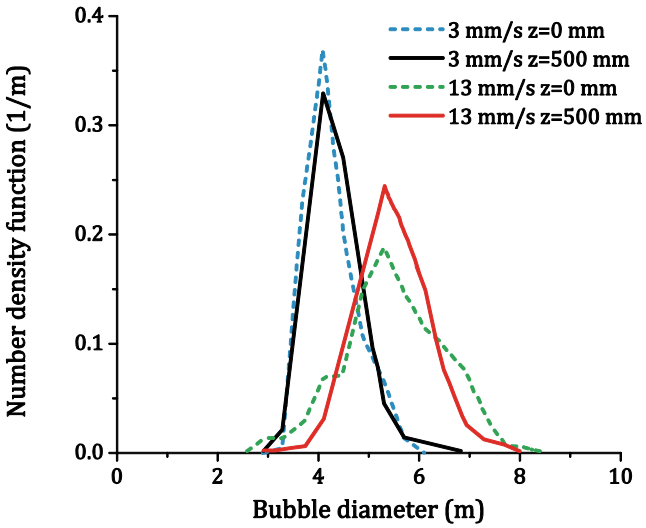

Figure 4-2 Number density function of the bubble diameter in the experiment of Mohd Akbar et al. (2012)

The rectangular bubble column is discretized in structured rectangular volumes. The size of the volumes is determined after a mesh study, which is shown below. The inlet is defined as surfaces at the bottom of the domain, representing the experimental needle setup. The surface that represents one needle is rectangular with an edge length of 4 × 4 mm. The gas volume flow is divided equally over all needles.

To determine whether the results are independent of the total simulation time a convergence criterion is needed. Often a fixed total simulation time is taken as a convergence criterion. If this fixed simulation time is reached, the simulation is defined as convergent. This simple method makes the assumption that a convergent state exists and that this state is reliably reached after the defined time. Therefore, this method is insufficient to investigate the convergence behavior of a simulation. In addition, this method is insufficient if it is unknown if the convergence is reliably reached after this time. Therefore, another convergence criterion is needed for the present investigations.

The convergence criterion is defined in a way that averages $\bar{f}$ taken over the simulation time T of a function f do not change significantly anymore when T is increased. The average over a finite time ζ is defined as

$$\bar{f}(\zeta) = \frac{1}{\zeta}\int_0^{\zeta} f(t)dt\,. \tag{4-1}$$

In particular, the averages $\bar{f}$ tend to be a constant asymptote as ζ is increased. A reasonable convergence criterion can be defined by analyzing the distance between $\bar{f}(\zeta)$ and this constant asymptote.

Nevertheless, the constant asymptote that $\bar{f}(\zeta)$ is tending to is not known. However, if $\bar{f}(\zeta)$ is tending to be a constant asymptote, the values of $\bar{f}(\zeta)$ will change less with increasing ζ. For example, the difference between $\bar{f}(T-\Delta\zeta)$ and $\bar{f}(\zeta)$ tends to zero with increasing simulation time T. If the difference between all values of $\bar{f}$ in the interval between $T-\Delta\zeta$ and T is evaluated, a trustworthy convergence criterion is obtained. The effort of this procedure is reduced by comparing each value of $\bar{f}$ in this interval to an average of $\bar{f}$ over this interval. This is expressed mathematically by requiring that

$$\left|\frac{1}{\Delta\zeta}\int_{T-\Delta\zeta}^{T}\bar{f}(\zeta)d\zeta - \bar{f}(\zeta)\right| \leq \epsilon;\quad T-\Delta\zeta \leq \zeta \leq T\,. \tag{4-2}$$

As function f the upward liquid velocity is chosen. Based on experience, $\Delta\zeta = 150s$ and ϵ to half of the experimental uncertainty (1.5% of the experimental value) is chosen to obtain a good approximation without consuming excessive CPU-time. The convergence criterion is evaluated at two points, x_1 and x_2, which are chosen symmetric. Therefore, a criterion evaluating the symmetry of the obtained result can be defined

$$\left|\bar{f}(x_1,\zeta) - \bar{f}(x_2,\zeta)\right| \leq 2\epsilon;\quad T-\Delta\zeta \leq \zeta \leq T\,. \tag{4-3}$$

This criterion is meaningful because the setup is symmetrical and a symmetric result is expected. It will be used in the further discussion.

4.2 Mesh and time step study

To obtain a mesh independent solution an intensive mesh study was performed. An extract of this study for the case with a superficial velocity of 13 mm/s is shown in Figure 4-3. All simulations are converged using the defined convergence criterion. Four meshes are presented:

- an isotropic mesh with 4 mm edge length of each cell, which contains around 200 000 cells,
- two anisotropic meshes, one with an edge length of 3 mm in depth and vertical direction and 4 mm in the width direction, which contains around 300 000 cells and the other with an edge length of 5 mm in depth and vertical direction and 4 mm in the width direction which contains around 140 000 cells,
- a dilation in stream wise direction with 10 mm edge length in the vertical direction and 4 mm edge length in depth and width direction with 80 000 cells.

The mesh study is conducted by investigating the gas volume fraction, the upward liquid velocity and the root mean square of the normal component of the Reynolds stress tensor $RMS(w'w')$. Comparing the obtained values for the gas volume fraction and the upward liquid velocity even the coarse grid with 80 000 cells gives similar results as the finest mesh with 300 000 cells. The resolved turbulence intensity is a little bit different, but a clear trend with mesh size is not observable.

The $RMS(w'w')$ diagram consists of three curves that correspond to the URANS modeling discussed in Section 2.4.2. The curve marked with 'resolved' corresponds to the resolved part of the Reynolds stress component $\widetilde{w'}\widetilde{w'}$, the curve marked with 'unresolved' to the modeled component $\overline{\widetilde{w''}\widetilde{w''}} = 2/3\,\overline{k_{mod}}$ and the curve marked with 'total' to the total component $\overline{w'w'}$. The unresolved curve is the result that would be obtained if a stationary simulation would be performed. Further, the resolved curve represents the amount, which is added through the transient simulation. The total curve represents the $RMS(w'w')$ as it is obtained in the experiment.

The differences in the $RMS(w'w')$ graphs occur close to the wall. Using the isotropic and the finest mesh, two peaks are noticeable at the walls. Using the two coarser meshes, these wall peaks are less pronounced. With the coarsest mesh, a slightly higher value overall is obtained. Nevertheless, deviations are quantitatively small.

Summarizing, the solution is mesh-independent already for the isotropic mesh; hence, this is used for the further calculations. It should be noted that a mesh study is only possible if the solution is independent of the time step and vice versa. This circumstance was considered and the mesh study was performed with sufficiently minor steps, which is discussed in the following.

To find conditions under which the solution becomes independent of the time step a study is performed for 13 mm/s superficial velocity. Since it turns out that the time step is connected with the virtual mass force, both model variations including the virtual mass force and not including the virtual mass force are investigated. The difference between both model setups is discussed in detail in the next section.

To characterize the discretization of the problem in time and space the Courant–Friedrichs–Lewy number (CFL number, $CFL = |u|(|\Delta x|/\Delta t)$) is used. Because the velocity is a function of position and time so is the CFL number. To get a characteristic value, the root mean square of all CFL numbers in the computational domain is calculated. Further, the maximum and minimum $RMS(CFL)$ numbers over time are given.

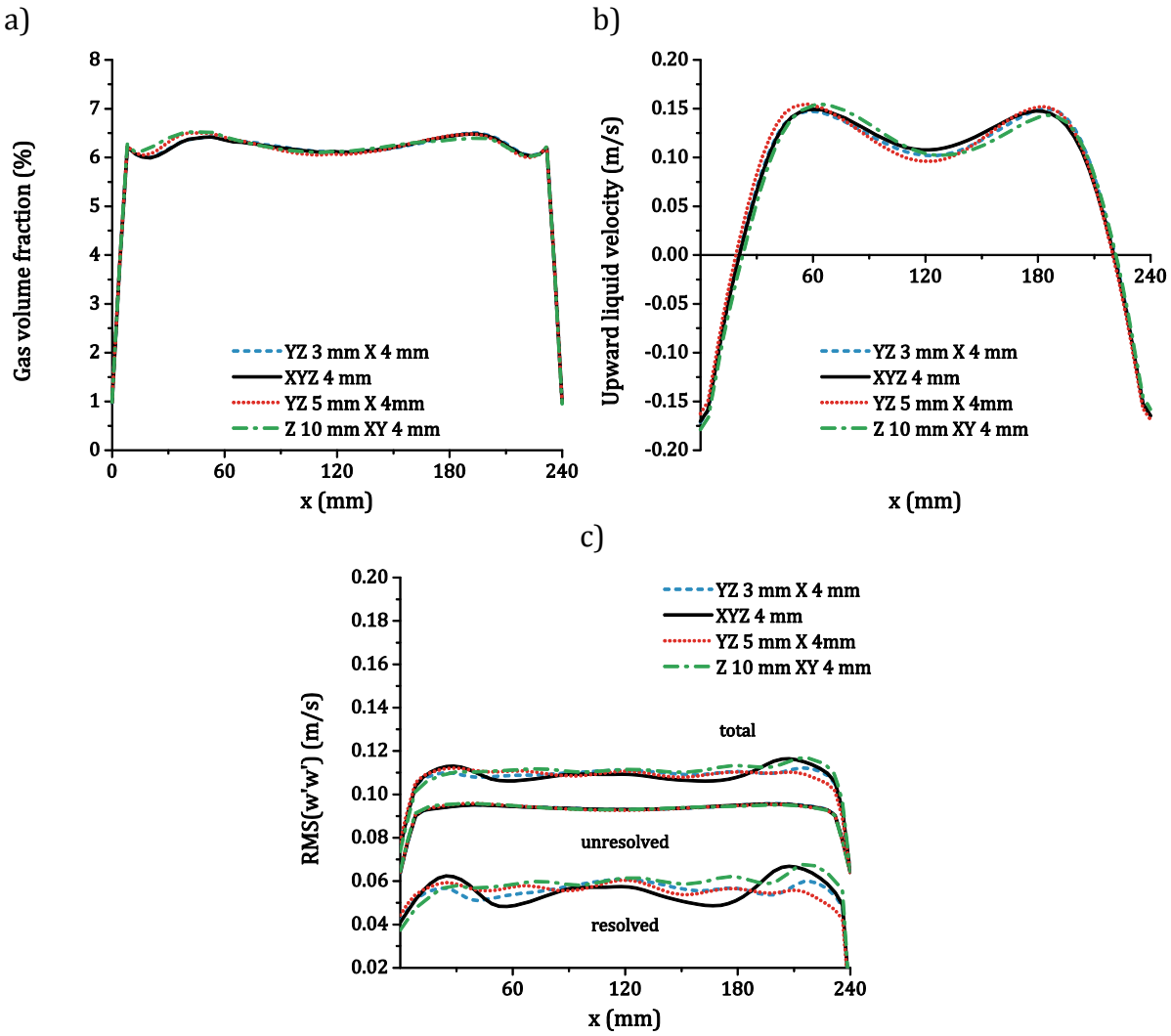

Figure 4-3 Mesh study for four different meshes.

4.3 Influence of the virtual mass force

The time step study with the virtual mass force was performed in the range of $RMS(CFL) = 0.8$ up to $RMS(CFL) = 2.6$. The results are shown in Figure 4-4 for the 13 mm/s case. For both simulations the convergence and symmetry criteria are reached.

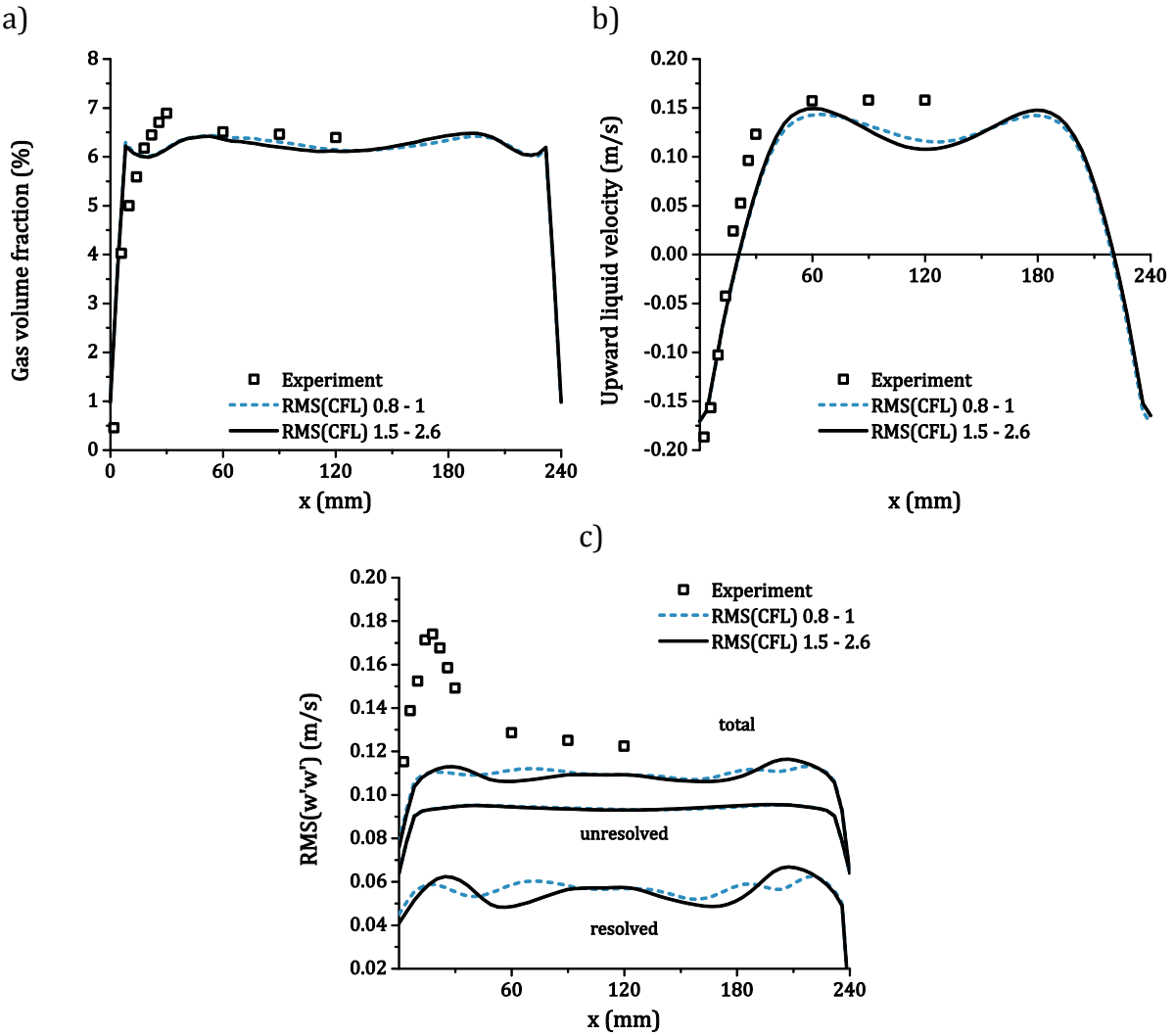

Figure 4-4 Time step study for different CFL numbers using the virtual mass force for the 13 mm/s case

Comparing the gas volume fraction and the liquid velocity profile for both time steps good accordance is reached. The volume fraction profile is nearly the same for both time steps. The liquid velocity profile differs a little bit for the different time steps. The resolved upward turbulence profiles for the different time steps are slightly different, the peak near the wall being slightly higher for the larger value of $RMS(CFL)$. The unresolved turbulence profiles are equal for both time steps. Since the unresolved contribution constitutes a major part of the total turbulence intensity, the curves for this quantity are in good agreement as well.

In conclusion, when the virtual mass force is included, the solution becomes independent of the time step for $RMS(CFL) \lesssim 2.6$.

The time step study without using the virtual mass force was performed in the range of $RMS(CFL) = 0.6$ up to $RMS(CFL) = 8$. In Figure 4-5 selected results of the time step

study are shown. All simulations are convergent using the convergence criterion defined in Section 4.1.

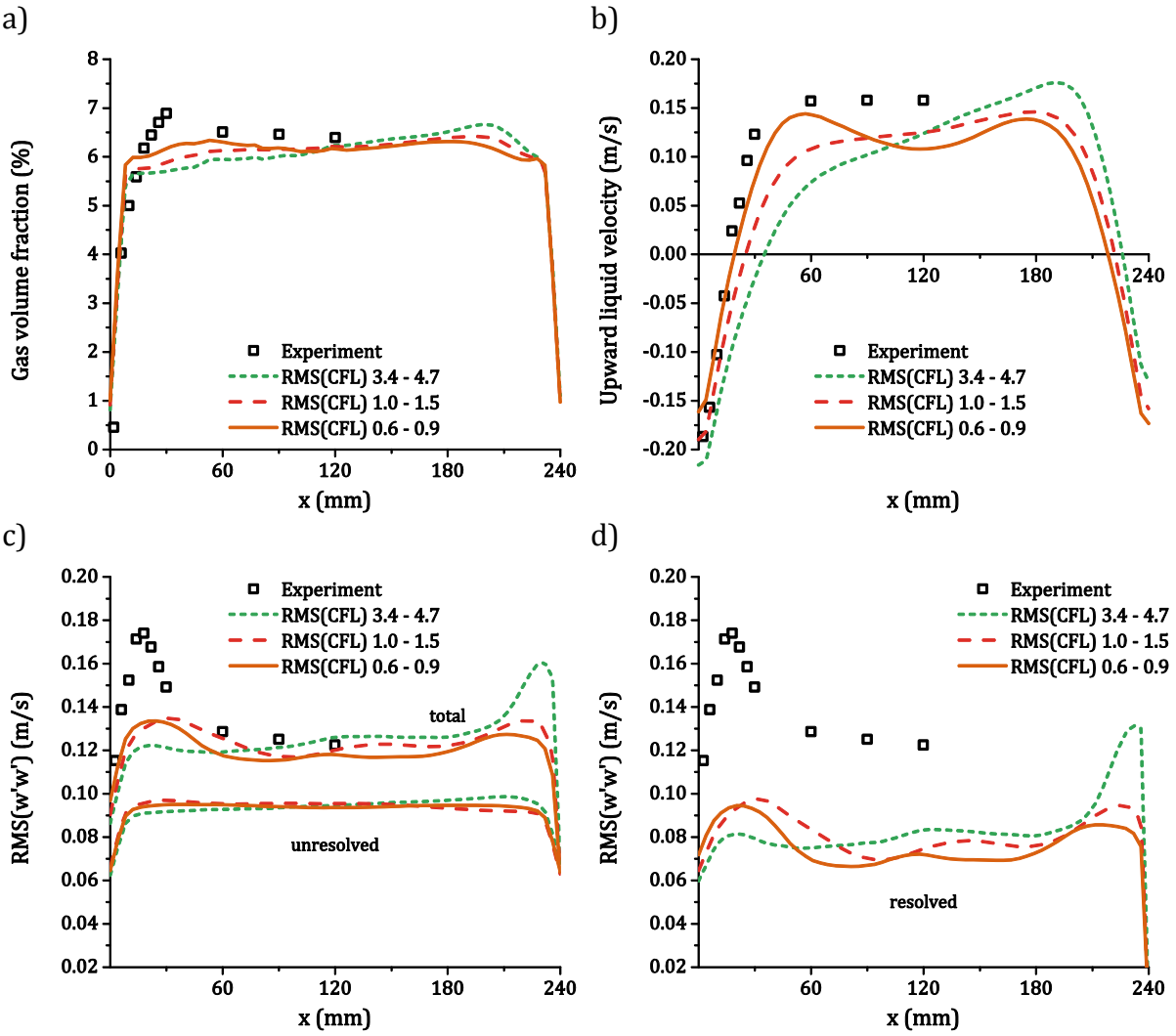

Figure 4-5 Time study for different $RMS(CFL)$-numbers without using the virtual mass force for the 13 mm/s case

Comparing the gas volume fraction, the upward liquid velocity and $RMS(w'w')$ significant differences can be seen. In particular, the simulations using $RMS(CFL)$ above 1 do not fulfill the expected symmetry according to the criterion given in Section 4.1. In contrast, the simulation using $RMS(CFL)$ below 1 does fulfill this criterion. Also, in contrast to the simulations using $RMS(CFL)$ above 1 the simulation using $RMS(CFL)$ below 1 gives two peaks in all three quantities. Comparing the simulation using $RMS(CFL)$ below 1 with the simulations including the virtual mass force in Figure 4-4, very small differences are seen.

In conclusion, when the virtual mass force is neglected, a solution that is independent of the time step is achieved if the condition $RMS(CFL) < 1$ is satisfied.

Besides the discussed influence on a reliable CFL number, the virtual mass force influences also the other values. In Figure 4-6 the results of the simulations with and without virtual mass force are shown for both superficial velocities 13 mm/s and 3 mm/s. For 3 mm/s superficial velocity the results obtained with and without virtual mass force

are the same. This is different for 13 mm/s superficial velocity. Therefore, the following discussion is only related to the 13 mm/s case.

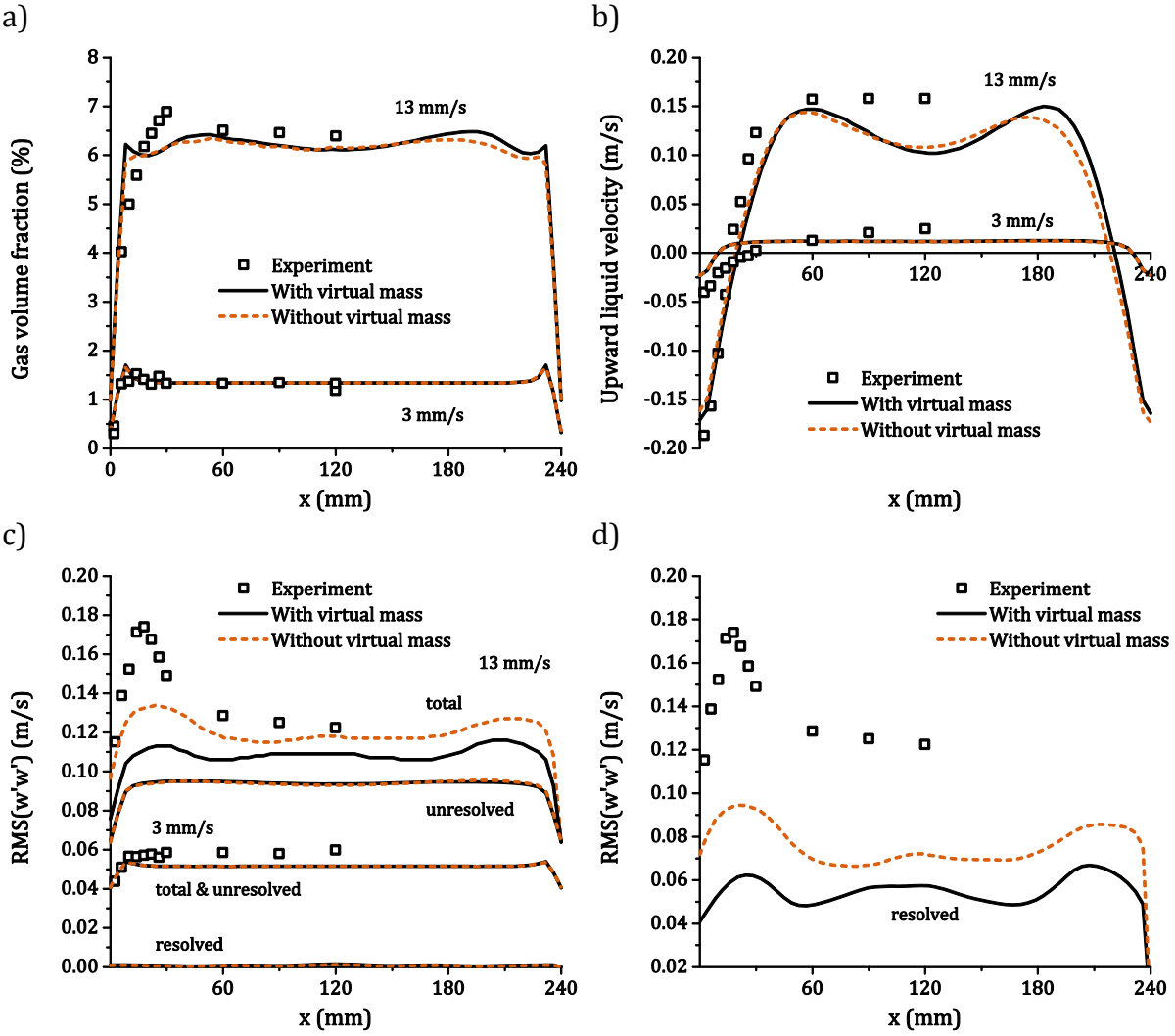

Figure 4-6 Comparison between using the virtual mass force and not using the virtual mass force for a superficial velocity of 13 mm/s and 3 mm/s. The curves for using the virtual mass force and not using the virtual mass force for the 3 mm/s case are on the top of each other.

Looking at the liquid velocity profiles for the case with 13 m/s superficial velocity, no differences between the model variants with and without virtual mass force are seen. Distinct peaks at each side can be observed in the profiles. At the same positions as in the liquid velocity profile, broad maxima can be observed in the gas volume fraction profile for both model variants. In addition, if the model variant including the virtual mass force is used, the gas volume fraction profile will exhibit sharp peaks almost at the wall. In contrast, if the model variant neglecting the virtual mass force is used, these sharp peaks will nearly vanish.

The broad maxima near the center in the gas volume fraction profile can be explained by the stability criterion of Lucas et al. (2005), which is derived analytically from the force balance, depending on the volume fraction of big and small bubbles. This stability criterion is based on the change of sign in the lift force coefficient and is, therefore,

connected to the gradient of the liquid velocity. By solving separate momentum equations for big and small bubbles this effect is also taken into account in the present simulations. Since the liquid velocity gradient and the volume fractions of big and small bubbles depend on the local position, the stability criterion of Lucas et al. (2005) has to be evaluated locally.

In the lower section of the column, the big and small bubbles are not separated. Due to the wall shear stress and the resulting liquid velocity gradient, the big and small bubbles separate with increasing height. The big bubbles move to the center, the small bubbles move to the wall. Consequently, the local concentration of the big bubbles rises from the wall towards the center of the column. Further, away from the wall the lateral movement of the big bubbles is slowed down, because of the decreasing liquid velocity gradient. As a result, the big bubbles accumulate and the local void fraction of the big bubbles increases at the same point. Due to buoyancy, this is accompanied by an increase of the local liquid velocity. If the stability criterion described in Lucas et al. (2005) is exceeded, a distinct liquid velocity peak will be formed at this point. Once this has happened the large bubbles cannot move further towards the center because of the negative lift coefficient. This means that steady profiles with peaks in the liquid velocity and gas fraction are established.

The near wall peak in the gas fraction graphs is also caused by the described separation of small and big bubbles. The small bubbles move to the wall due to the liquid velocity gradient; however, near the wall the wall force push the bubbles away from the wall. The bubbles accumulate where both forces have the same quantity and, consequently, a wall peak occurs.

Figure 4-6 also shows the upward $RMS(w'w')$ values. Here, for the case with 13 mm/s superficial velocity also peaks near the wall can be observed. These peaks are not at the same position as the peaks in the liquid velocity profile and might be less affected by the separation of big and small bubbles. The near wall peaks in the $RMS(w'w')$ profile are nearly at the point where the liquid velocity passes through the zero line, which is the point of the highest liquid velocity gradient. In addition, the resolved $RMS(w'w')$ profile is higher in general for the simulation without using the virtual mass force. Therefore, by using the virtual mass force a damping of the liquid velocity fluctuations is introduced.

Overall, neglecting the virtual mass force leads to different results for the case with 13 mm/s superficial velocity. The gas volume fraction profile is quantitatively almost the same for both model variants. However, not using the virtual mass force the near wall peak in the gas volume fraction profile nearly vanishes. The resolved $RMS(w'w')$ profiles have the same shape, but quantitatively the resolved $RMS(w'w')$ is higher if the virtual mass force is neglected. While the gas volume fraction and the upward turbulence profiles are different, the liquid velocity profile is nearly the same for both model variants. In contrast to the case with 13 mm/s superficial velocity, all profiles obtained for the 3 mm/s superficial velocity are the same. The equality might be explained by the fact that the resolved upward turbulence intensity at the measurement plane is nearly zero. Consequently, nearly no fluctuation is resolved and the acceleration is nearly zero. As a result, the virtual mass force is nearly zero.

4.4 Influence of the bubble induced turbulence

The influence of the bubble induced turbulence (BIT) model on the URANS simulations is discussed in this section. For this purpose, the bubble induced turbulence (BIT) modeling used in the baseline model with source terms (Rzehak & Krepper 2013a), with an additional viscosity (Sato et al. 1981), both described in Section 2.4.4 and a model neglecting the bubble induced turbulence are compared.

The results for 13 mm/s superficial velocity are shown in Figure 4-7. The gas hold up is quantitatively very similar for all considered models, but the sharp near wall peak is pronounced only for turbulence modeling with source terms. The liquid velocity using the Sato model and using the no BIT model is lower than the experiments and the profile obtained with the baseline model. Qualitatively the different model approaches show the same behavior. However, using the Sato model and using the no BIT model both peaks in the liquid velocity profile are shifted towards the center and are smaller.

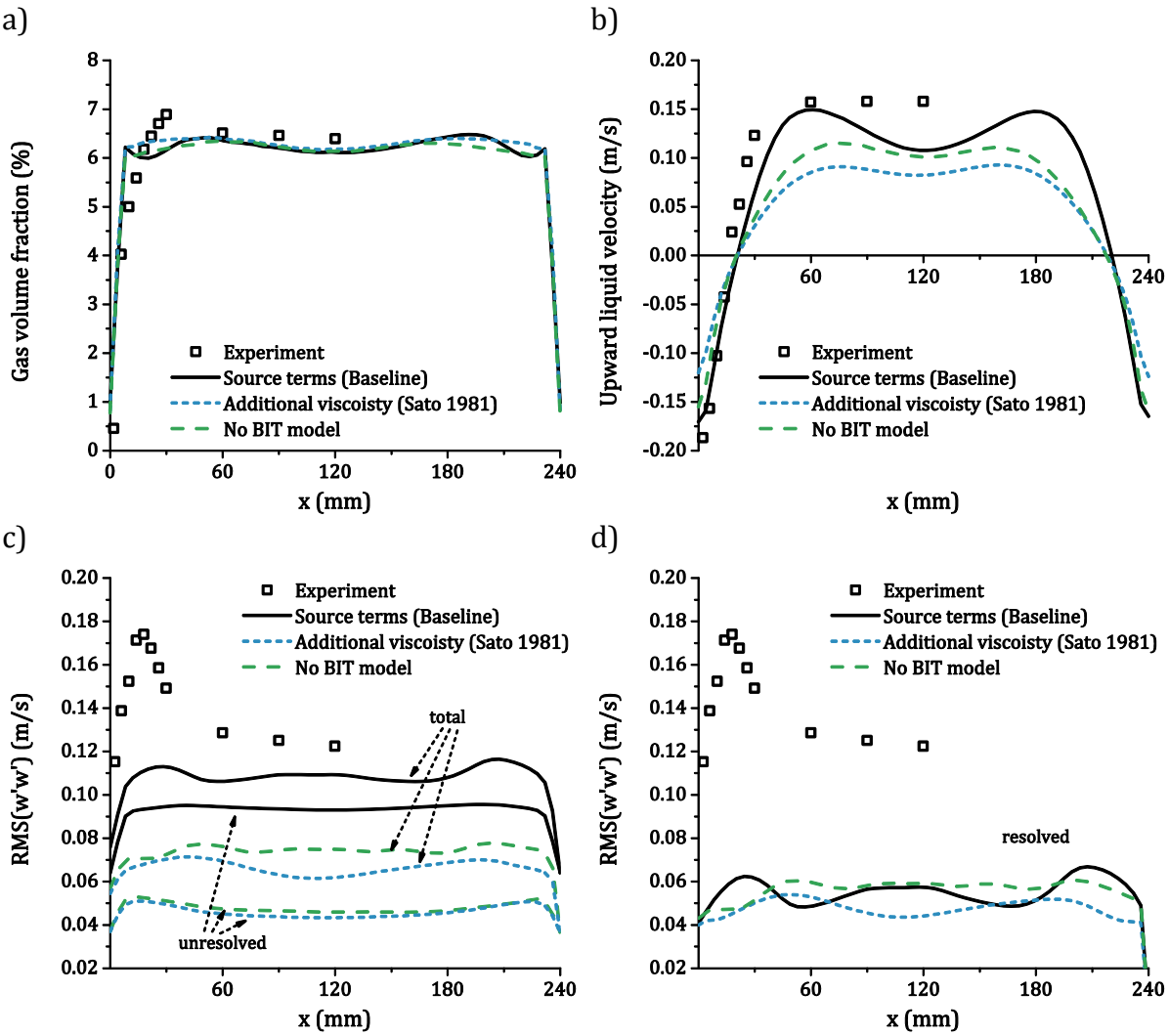

Figure 4-7 Comparison of different bubble induced turbulence modeling approaches for 13 mm/s superficial velocity.

Remarkably, the quantity of the resolved turbulence intensity is very similar for all used BIT models. Concerning the shape of the profiles, the peaks are shifted to the center and are smaller for the models not using the source terms. The total $RMS(w'w')$ values

are underpredicted by all models but significantly closer to the data for the models with source terms. Differences between the Sato model and neglecting BIT are small in comparison.

The differences between the different approaches to BIT modeling can be explained by considering the turbulent viscosity, which is shown in Figure 4-8. As the resolved $RMS(w'w')$ values are comparable for all models, only the unresolved part of the turbulent viscosity is shown. It can be seen from Figure 4-8 that for the BIT modeling using source terms the turbulent viscosity is the lowest. This is caused by a higher turbulence dissipation rate (not shown). Looking only at the turbulent kinetic energy that is the highest for the modeling using source terms, the opposite effect on the turbulence viscosity may have been expected. The reason for the behavior observed in the simulations must be sought in the bubble induced source term of the turbulence dissipation rate.

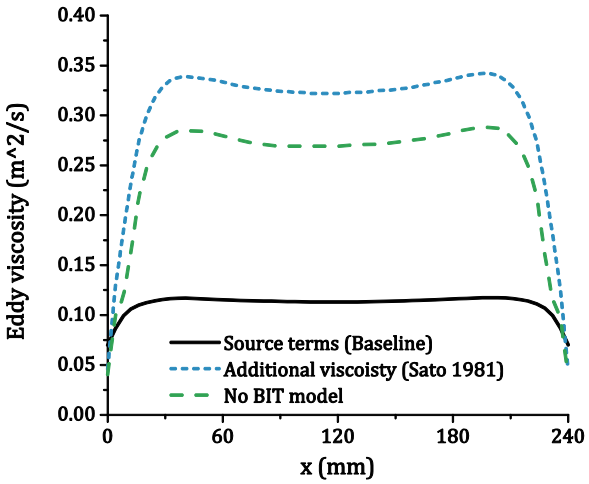

Figure 4-8 Unresolved turbulent viscosity for different modeling approaches for 13 mm/s superficial velocity.

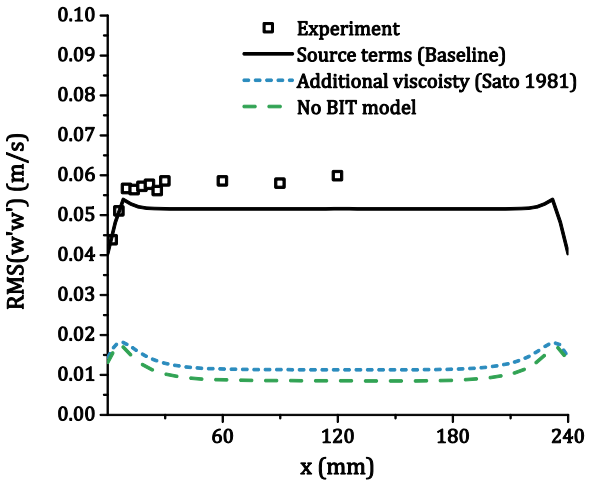

Figure 4-9 Comparison of the total upward turbulence intensity for different bubble induced turbulence modeling approaches for 3 mm/s superficial velocity.

Further, as expected, the turbulent viscosity using a BIT model with additional viscosity is the highest. Using the no BIT model the level of the turbulent viscosity is between the other approaches.

The higher turbulent viscosity obtained with the Sato model and using the no BIT model is causing a reduced amplitude in the lower liquid velocity profile compared to the BIT modeling with source terms, as shown in Figure 4-7. In particular, using the Sato model and using the no BIT model the liquid velocity gradient near the wall is smaller compared to the experiment and the BIT modeling with source terms. Consequently, the instability caused by the separation by the big and small bubbles, as discussed above, is also shifted to the center. Therefore, the observed velocity peaks using the Sato model and using the no BIT model observed in Figure 4-7 are shifted to the center.

Another effect of the higher turbulent viscosity that is obtained with the Sato model and using the no BIT model is a higher turbulent dispersion of the bubbles. As described in Section 2.3, the turbulent dispersion force is proportional to the turbulent viscosity and to the gradient of the gas volume fraction. It acts towards a uniform distribution of

gas. As a result, the peaks in the gas volume fraction profiles shown in Figure 4-7 are flatter when using the Sato model or using the no BIT model compared to the BIT modeling with source terms. Consequently, the liquid velocity peak is also flatten when using the Sato model or using the no BIT model. In particular, the near wall peak of the small bubbles that can be observed for the BIT modeling with source terms in Figure 4-7 nearly vanishes when using the Sato model or using no BIT model.

For the case with 3 mm /s superficial velocity, the liquid velocity and the gas volume fraction profiles obtained by using the different BIT model approaches are nearly the same. Therefore, only the total $RMS(w'w')$ values are discussed in the following. The results are shown in Figure 4-9.

It can be seen from Figure 4-9 that the $RMS(w'w')$ values are quite well predicted by the BIT modeling with source terms. In contrast, using the Sato model or using the no BIT model they are considerably underpredicted. This is the same trend seen for the case with 13 mm/s superficial velocity.

Summarizing, the best prediction of $RMS(w'w')$ is obtained by the turbulence modeling with source terms, using the baseline model. The position of the peak in the $RMS(w'w')$ graphs for 13 mm/s superficial velocity is well reproduced. Using the Sato model or the no BIT model $RMS(w'w')$ is considerably underpredicted compared to the experimental data. Furthermore, there is no peak in the $RMS(w'w')$ graphs for 13 mm/s superficial velocity.

The turbulent viscosity obtained for this case with the Sato model or using the no BIT model is significantly higher than the obtained turbulent viscosity using the BIT modeling with source terms using the formulation of Rzehak and Krepper (2013b). Consequently, the liquid velocity profiles are less steep using the Sato model and using no BIT model compared to the BIT modeling with source terms. Compared to the experimental data the liquid velocity is underpredicted using the Sato model or the no BIT model, but predicted well by the modeling using source terms.

4.5 Conclusions

It was shown that for transient simulations with RANS-based turbulence modeling (URANS) an independent solution concerning simulation time, time step length and mesh size is reachable with the two fluid model. For this purpose, the defined convergence and a symmetry criterion give reliable information.

The resolved flow structures that are obtained due to the transient simulation give important contributions to the turbulence, indifferent of the used bubble induced turbulence (BIT) model. As expected, the resolved turbulence is very low for the low gas volume flow rate; here the turbulence might be dominated by the BIT. Thus, the URANS simulations are capable to reproduce bubbly flows dominated by large-scale structures and dominated by BIT.

Moreover, it was found that the virtual mass force is not negligible, especially for the higher gas volume flow rate in which the resolved turbulence is significant. Despite the simulation results reproduce the experiments better without the virtual mass force, the force has to be included towards a reliable modelling.

The baseline model gives very good results, especially with the baseline BIT model the turbulent kinetic energy for both volume flow rates can be reproduced. The baseline

BIT model was also compared to other BIT models for the present experimental setup in (Ziegenhein et al. 2013); regarding to the root mean square of the normal Reynolds stress tensor component the baseline model gives the best results.

The further studies will be performed with the here developed method. From the findings above, it is justified to identify two leading turbulence scales: The scales that are in the size of the apparatus and the small scales, which might be dominated by the bubble, induced turbulence. For the here investigated experimental setup these scales are both present for the 13 mm/s superficial velocity case. In contrast, for the 3 mm/s superficial velocity case large scales might not be present. In the following section, the capability of the shown URANS approach with the baseline model is investigated to reproduce the large-scale flow structures in a bubble column.

5 Prediction of the large liquid structures of bubbly flows with the URANS equations

In this section, especially the fluid dynamics on the large scale is of interest, which is often generated due to a partial aeration or a heterogeneous bubbly flow regime. Such partial aeration is often obtained with common spargers like the ring or spider sparger (Kulkarni et al. 2009). Moreover, the heterogeneous flow regime produced by large bubbles created at the inlet or due to coalescence might be also a common flow regime. Thus, this topic is of general interest.

The local high gas void fraction generated by a partial aeration is in general called bubble plume. Besides the bubble plumes in bubble columns this effect is found for a wide variety of applications. In the field of bioengineering partial aeration is used to drive the flow inside different vessels (Wang et al. 2014) (Bitog et al. 2011) and wastewater pools (Garcia & Garcia 2006). Without confining walls bubble plumes are used to mix complete lakes (Wuest et al. 1992) (Boegman & Sleep 2012), helps to build barriers for oil on water (McClimans et al. 2012) or even fishing (Grimaldo et al. 2011). Moreover, bubble plumes are naturally found in oceans (Schmale et al. 2015) (Nauw et al. 2015) or occur due to mining processes or pipe ruptures under water (Cloete et al. 2009).

In the following, the simulations are focused on bubble columns for chemical or biological engineering since here comprehensive experimental data exist. Notwithstanding the large amount of experiments and simulations conducted in the recent years on this topic, the research is ongoing experimental (Besbes et al. 2015) as well as theoretically (Masood & Delgado 2014).

Such large-scale structures that are generated by a bubble plume dominate the flow field in the vessel, thus the prediction of the correct transient behavior of such is essential. This is studied with the above-discussed URANS approach. Often a distinct bubble plume frequency can be determined from the experiment which is easily compared to simulations; many studies regarding this topic exist, e.g. (Rensen & Roig 2001) (Buwa & Ranade 2004) (Juliá et al. 2007).

Three experiments dominated by bubble plumes with different operating conditions are chosen from the literature. Namely, the experiment by Becker et al. (1994) with an asymmetric gas aeration, the experiment by Pfleger et al. (1999) with a central gas aeration and the experiments by Julia et al. (2007) using different aeration widths and different gas volume flow rates.

The experiments of Becker et al. (1994) and Pfleger et al. (1999) are well known and often simulated. The experiment of Becker et al. (1994) might be one of the most simulated bubble plume experiments ranging from Euler-Euler two fluid model methods (Sokolichin & Eigenberger 1999) (Mudde & Simonin 1999) to Euler-Lagrange methods (Delnoij et al. 1997) (Hu & Celik 2008). The experiment of Pfleger et al. (1999) is also used for many different model validation e.g. by (Bech 2005) or (Ma et al. 2015). These two experiments are standard experiments and are used to show that the here used simulation methods are capable to give the same good results as other methods. The experiments of Julia et al. (2007) are more complex since different sparger conditions

and high superficial velocities are realized. Simulations for these experiments are not published yet.

5.1 Simulation setup and experimental data

The experimental setups of the three investigated cases of Becker et al. (1994), Pfleger et al. (1999) and Julia et al. (2007) are shown in Figure 5-1. All setups are narrow bubble columns of different sizes and operate in water with air supply. The largest bubble column is used by Becker et al. with a water level of 1.5 m a width of 0.5 m and a deep of 0.08 m. The gas is aerated with 1.6 l/min through a porous frit at the left side 0.15 m away from the wall. The liquid velocity was measured with laser Doppler anemometry (LDA) at the points A and B as well over the width 0.75 m above the ground plate. The bubble size was measured using a photoelectrical suction probe and was determined to 3 mm.

The bubble column used by Pfleger et al. (1999) is smaller and is centrally aerated with 0.8 l/min through eight holes. The liquid velocity was measured using LDA as well. The bubble size were not measured explicitly but are given by Pfleger et al. between 1 and 5 mm; however, here a bubble size of 2 mm is used, which is also used by Pfleger et al. for their own simulations. The velocity profile is measured 0.13 m, 0.25 m and 0.37 m above the ground plate. In addition, the velocity is measured over time in the center of the column 0.25 m above the ground plate.

By Julia et al. (2007) a flat bubble column is used with a variable needle sparger consisting up to 137 needles. The bubbles are uniformly aerated over the 0.031 m column depth with different aeration width. The liquid velocities are determined with LDA on different heights. The bubble plume dynamics are measured mainly on a line 0.3 m above the ground plate. The used experiments for comparison with simulations are summarized in Table 5-1. Three different aeration pattern aerating 59 % to 18 % of the ground plate are used for the simulations from the experiments. The bubble sizes are determined with digital imaging from extra experiments in which only a single needle is operating. The holdup is determined by measuring the bed expansion for the smallest and the lowest gas volume flow rate.

The bubble columns are discretized to a regular grid. The grid size was determined after conducting a mesh study using a minimum of three different grid sizes. All simulations are conducted with the baseline model as described in the previous section and in Section 2.5. In particular, the column of Becker et al. is discretized with 100x150x16 (width x height x depth) rectangular cells. The column of Pfleger et al. is discretized with 40x90x16 cells. Finally, a rectangular mesh composed of 50x300x6 was found to be sufficient for the bubble column of Julia et al. The total simulation time varies from case to case; nevertheless, the convergence criteria defined in the previous section is fulfilled every time.

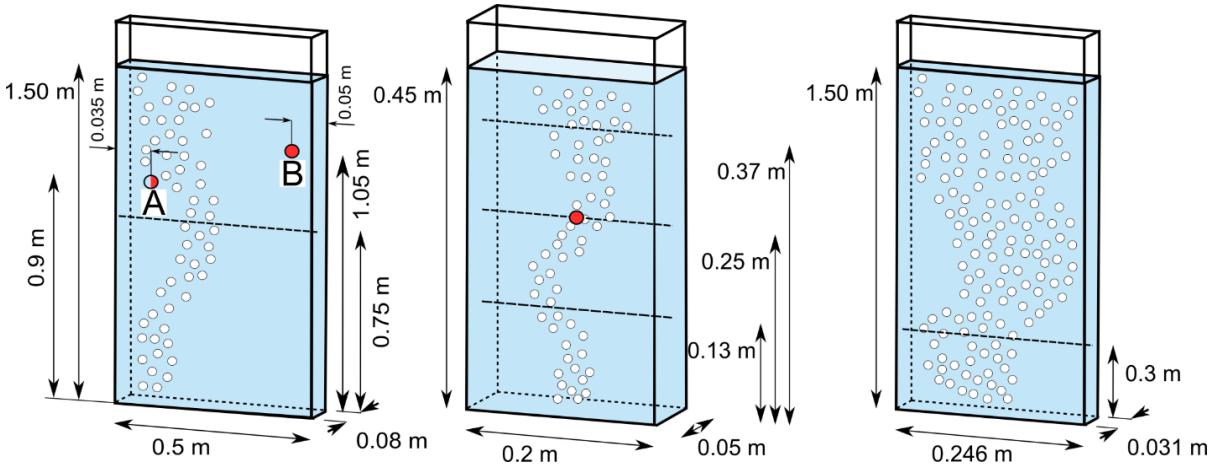

Figure 5-1 Setup of the experiments by Becker et al. (1994) (left), Pfleger et al. (1999) (middle) and Julia et al. (2007) (right). The measurement planes are dotted and points with measurements over time are marked red.

Flow pattern (Aerated area/ Used needles)	Superficial velocity [mm/s]	Bubble size [mm]	Holdup [%]
F8 (59 % / 81)	16 29 40 49	3.78 4.20 4.56 4.85	4.7 17.1
F11 (44 % / 59)	12 16 24 29 36	3.79 3.97 4.33 4.56 4.87	2.5 11
F16 (18 % / 25)	5 12 16 29	3.78 4.52 4.94 6.31	0.9 7.6

Table 5-1 Setups of the experiments by Julia et al. (2007) used for simulations.

5.2 Results

At first, the simulation results regarding the experiments of Becker et al. (1994) and Pfleger et al. (1999) are compared to the experimental observations. These two experiments were executed at relatively low gas volume flow rates with small bubbles. After that, the simulation results regarding to the experiments of Julia et al. (2007), which are summarized in Table 5-1, are compared to the experimental results. In contrast to the other two experiments, the experiments by Julia et al. are conducted over a wide range of bubble sizes and volume flow rates.

5.2.1 Experiments of Becker et al. (1994)

In the experiments of Becker et al. (1994) a large vortex is built near the wall due to asymmetric aeration. The vortex is wandering from the top to the bottom as can be seen in Figure 5-2. Another vortex is built on the other side pressing the bubble plume to the

wall in the bottom section. This behavior is very good reproduced by the simulations. In addition, the frequency of the meandering vortex is very good reproduced.

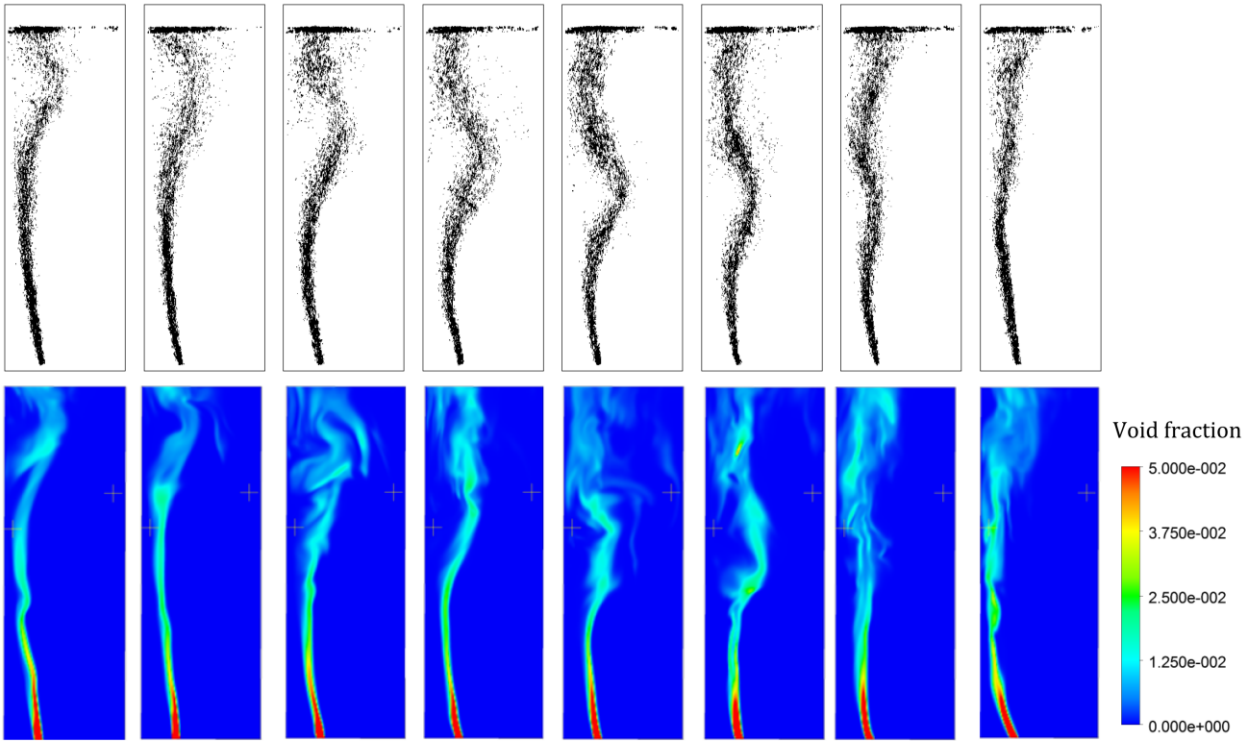

Figure 5-2 Qualitatively results of the experiments (top) of Becker et al. (1994) and the simulations (bottom). Pictures are taken every 5 seconds; the crosses in the simulation pictures mark the measuring points Point A and Point B, respectively.

Looking at the velocity at Point A and Point B over time shown in Figure 5-3 the frequency of the vortex is very well seen. The meandering of the bubble plume is more regular in the experiments than in the simulations. The first three passages of the vortex structures, however, are very similar to the experiments. The simulated meandering bubble plume tends sometimes to stay at one position as is seen at the last two passages. The absolute velocity peaks obtained by the LDA measurements are a little bit higher compared to the simulations; this is explained because the URANS modeling is not resolving the large velocity peaks.

The averaged results of the simulation are compared to the experiments in Figure 5-4, the experimental results are taken from (Deen 2001) since they are not given by Becker et al. in their published work. The vertical liquid velocity profile is reproduced qualitatively and quantitatively by the simulations. The root mean square of the normal components of the Reynolds stress tensor $v'v'$ and $u'u'$ ($RMS(u'u'), RMS(v'v')$ (u the horizontal and v the vertical velocity) are under predicted. Nevertheless, simulations qualitatively reproduce the experiments. A maximum in the $RMS(v'v')$ graphs at the wall is observed, they are falling below the $RMS(u'u')$ graph to a minimum around $X/d = 0.4$ to rise again above the $RMS(u'u')$ graph towards the right wall. The $RMS(u'u')$ graphs, in contrast, show a maximum around $X/d = 0.4$. Moreover, the unresolved part of the liquid velocity fluctuations in both directions is negligible with the baseline model.

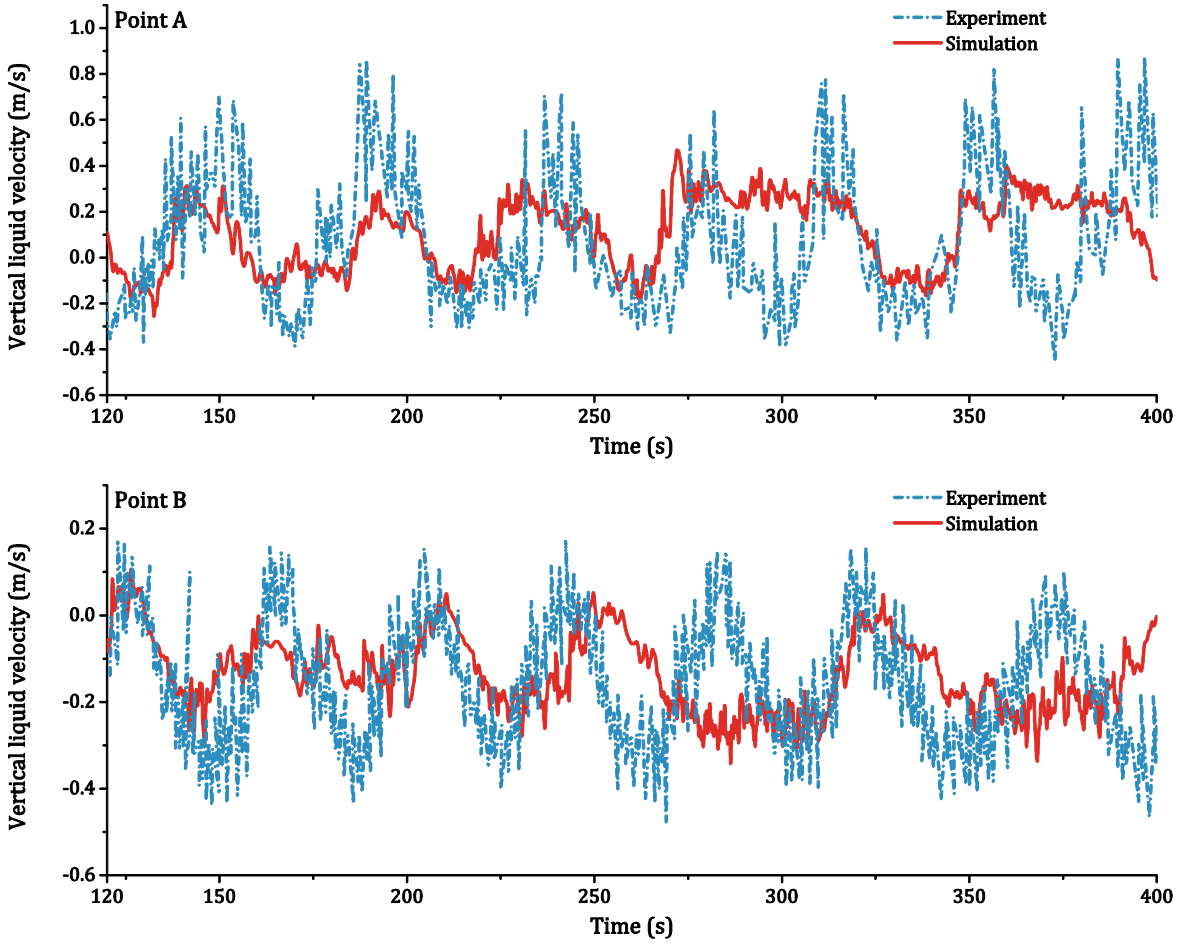

Figure 5-3 Liquid upward velocity at two different points obtained from experiments of Becker et al. (1994) and simulations.

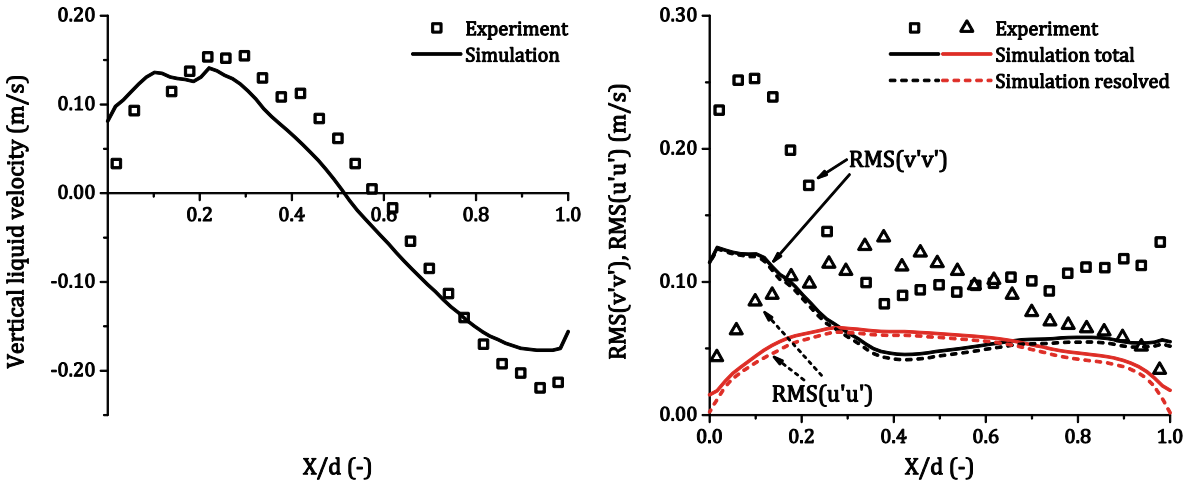

Figure 5-4 Comparison of the averaged results with the experiment at 0.75 m above the ground plate.

5.2.2 Experiments of Pfleger et al. (1999)

In contrast to the above-discussed bubble column, the bubble column of Pfleger et al. (1999) is aerated symmetric in the center. Here, also large vortexes near the wall are observed but symmetrical at both sides. Thus, a symmetrical swinging motion of the bubble plume is observed.

This swinging motion is seen at the sideward velocities determined with LDA in Figure 5-5 which can be reproduced by the simulations with nearly the same frequency. In contrast to the above discussed experiment, here the bubble plume obtained in the experiment tend to swing uneven and the bubble plume obtained from the simulations has a more regular motion. The absolute value of the measured velocity in Figure 5-5 is not comparable to the simulations since the experiments are moving averaged over time with an unknown filter length.

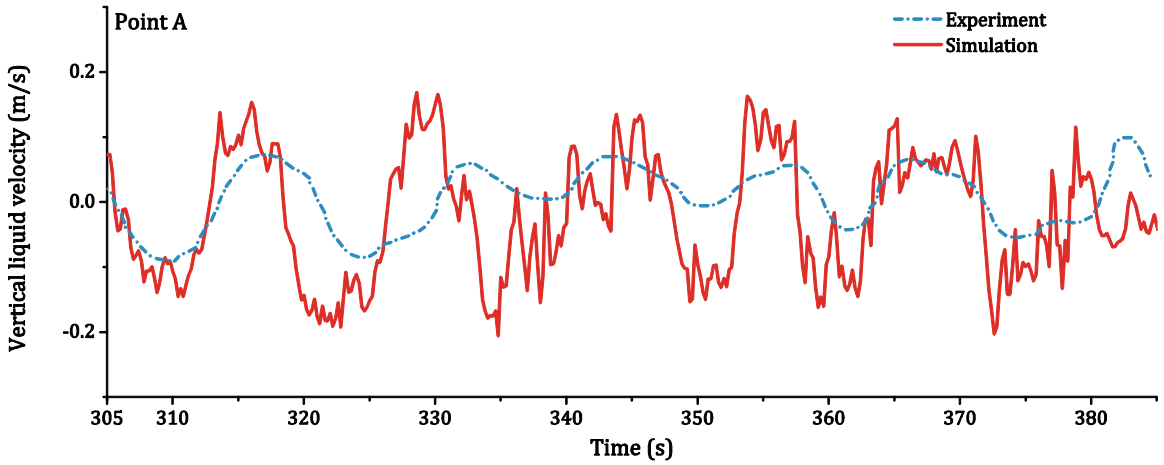

Figure 5-5 Liquid velocity in sideward direction at 0.25 m above the ground plate.

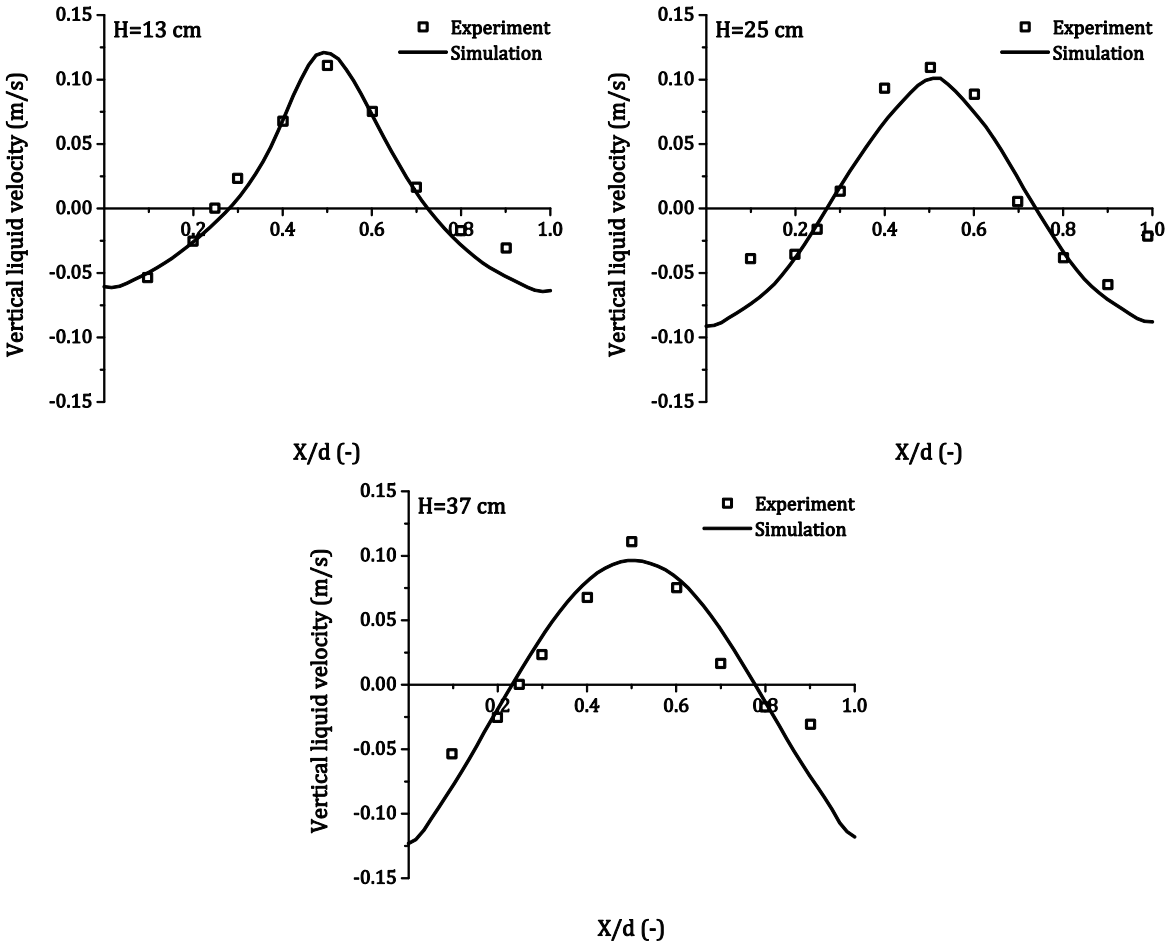

Figure 5-6 Liquid upward velocity profiles at three different heights.

Nevertheless, the vertical velocity profiles are also measured for three different heights, which are compared to the simulation results in Figure 5-6. The simulation results are in good agreement with the experimental data. Overall, the simulations can reproduce the qualitatively observed swinging bubble plume with nearly the same frequency as well as the quantitatively measured velocity profiles on three different heights.

5.2.3 Experiments of Julia et al. (2007)

Julia et al. (2007) conducted experiments over a wide range of gas volume flow rates and for three different aeration pattern as given in Table 5-1. In contrast to the previous experiments, the bubble plume is spreading after a certain height over the complete area of the bubble column.

The spreading is seen for most aeration pattern as shown in Figure 5-7. The vortex structures for pattern F11 and F8 are vanishing towards the top of the column, whereas the vortex structures of F16 are propagating until the top. For F8 and F11, the gas clusters detached from the bubble plume in the bottom are spreading over the column cross section and rise up as a front. At the bottom, the bubbles pulled downward in the large vortexes or even retained by them.

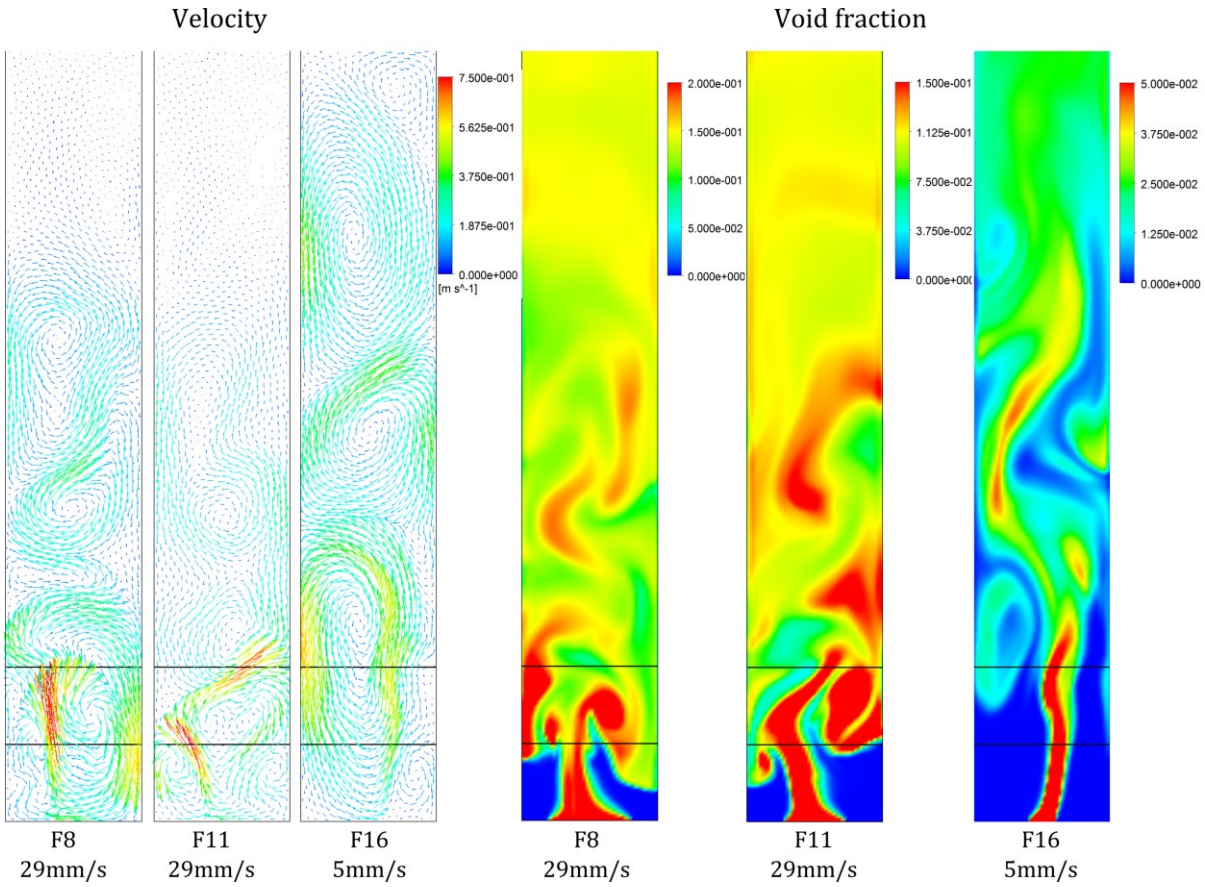

Figure 5-7 Simulation results for three different cases velocity vectors and void fraction profiles at the center plane. The measuring lines at 0.15 m and 0.3 m height are marked black.

Before looking at the transient behavior of the bubble plume, the averaged simulation results are compared to the experiments in Figure 5-8 for pattern F8 and F11 at four

different heights with 29 mm/s superficial velocity. For pattern F8 at a height of 0.15 m, the simulations clearly over predict the vertical velocity in the center and the downward velocity near the sidewalls. Due to the very high velocities in the simulations near the wall, more bubbles might be pulled downwards at the wall compared to the experiments. The experimental results at 0.15 m and 0.3 m are almost equal; in contrast, a flat velocity profile is obtained by the simulations at 0.3 m. In fact, the velocity fluctuations obtained by the simulations at 0.3 m have an amplitude of around 0.2 m/s but are symmetric leading to the flat velocity profile. Looking at the profiles at 0.6 m and 1.125 m, the measured velocity profiles show a wall peak while the simulations show a center peak. The velocity wall peaks might be indicating a coalescence process for the F8 pattern in the experiments since the small bubbles, which are obtained from the single needle experiments and used in the simulations, would migrate away from velocity peaks due to the lift force and a flat velocity profile would be obtained. Consequently, a wall peak in the velocity profile cannot be seen in the simulations since the bubble size distribution is fixed and the used lift force model forbids such peaks at the wall.

F8 - 29mm/s F11 - 29 mm/s

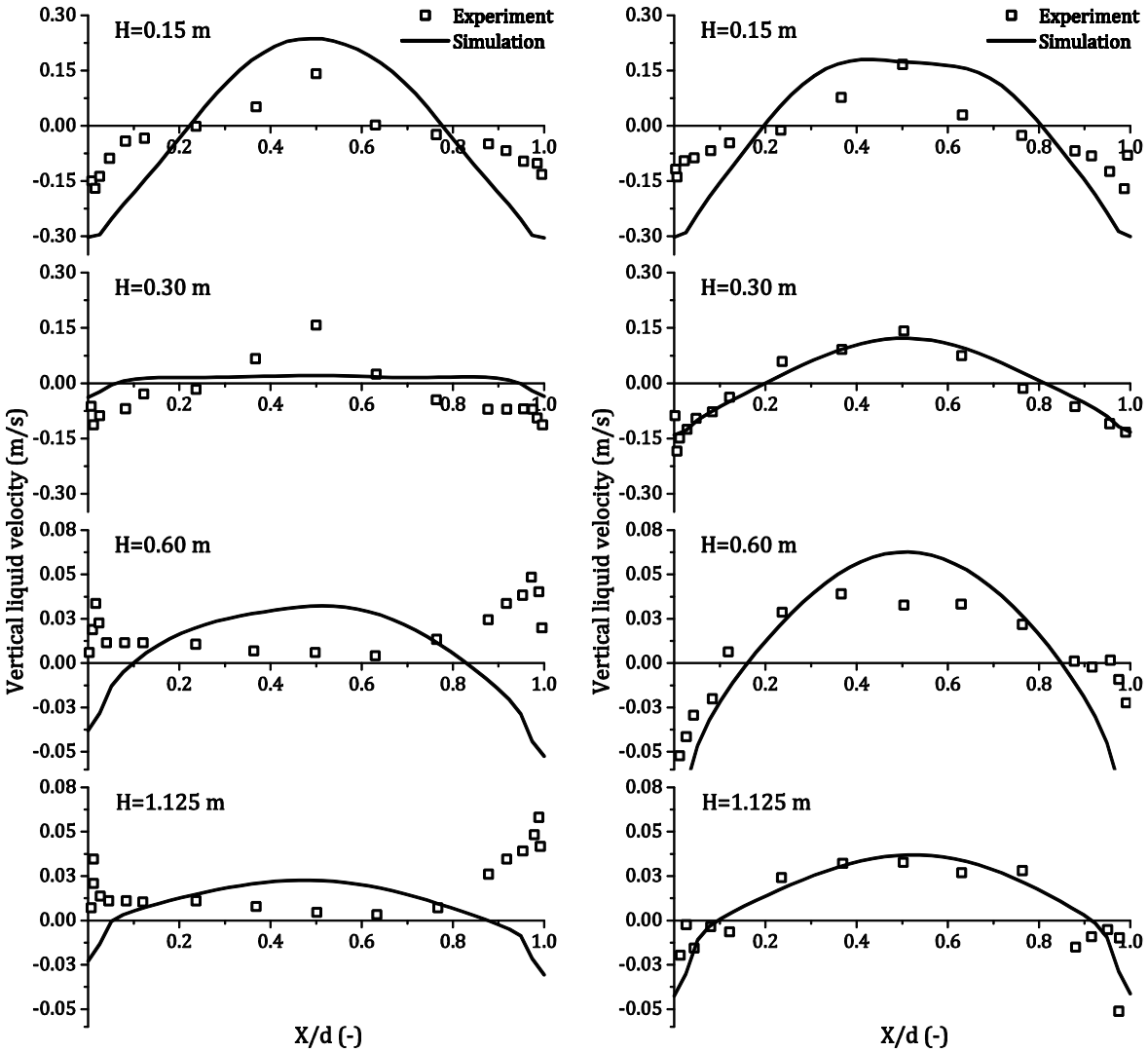

Figure 5-8 Velocity profiles at four different heights for pattern F8 and F11 with 29 mm/s superficial velocity compared with the experiments.

The F11 pattern at 29 mm/s superficial velocity, in contrast, is well reproduced by the simulations shown in Figure 5-8. Nevertheless, at 0.15 m the simulations also overpredict the downward velocity near the walls and the upward velocity at the center. At the next measurement line at 0.3 m, the simulations are in agreement with the experimental data. The discrepancy between the simulations and the measurements are also small for the other two heights at 0.6 m and 1.125 m. However, the measured velocity profiles tend to have a more flat profile in the center than the profiles obtained from the simulation, in general.

The trend from pattern F11 to F8 is different for the simulations. First, the velocity profiles measured at 0.15 m are nearly the same; in contrast, the profiles obtained from the simulations are flatter for the F11 pattern. It would be expected that the center peak for the broader aeration pattern is also broader. Vortex structures that compress the bubble plume at the bottom, which is seen in Figure 5-7, however, lead to a narrow velocity center peak. The vortex structures in the experiments for both patterns might have the same influence on the bubble plume since the velocity profiles are almost equal, which might also explain the same bubble plume swinging frequency as discussed below. Nevertheless, at a height of 0.3 m this trend of a flatter velocity profile obtained with the narrower aeration patter F11 is also seen in the experiments. The wall peaks in the measured velocity profiles at 0.6 m and 1.125 m for F8, which might indicate a bubble coalescence, are not present for F11.

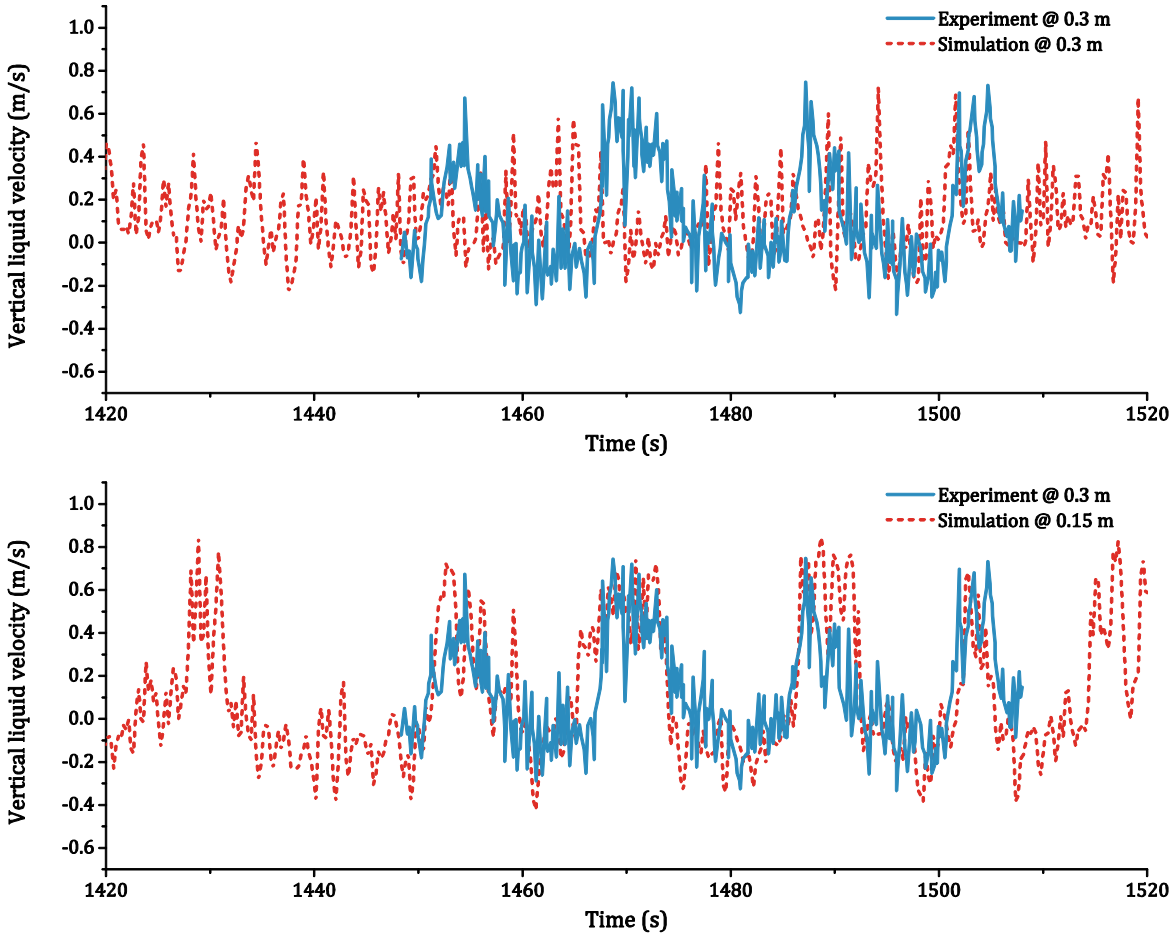

Figure 5-9 Vertical velocity over time in the center of the column for pattern F11 at a superficial velocity of 29 mm/s. Simulation results are shown at two heights.

Despite the good agreement between the simulations and the experiments for the F11 pattern at 29 mm/s superficial velocity, distinct differences occur looking at the velocities over time at the center at a height of 0.3 m as shown in Figure 5-9. Clearly, the simulation results at 0.3 m height do not coincide with the experiments whereas the simulation results at 0.15 m height are perfectly matching in frequency and amplitude. This might be explained by an earlier spreading bubble plume than in the experiments.

Indeed, the void fraction profiles obtained from the simulations are at 0.3 m already homogenized and a distinct plume is not remaining visible as indicated in Figure 5-7. A transition of the flow regime is obtained by the simulation shown in Figure 5-10. From the void fraction profiles at 0.15 m, a transition is seen from 16 mm/s to 24 mm/s. At 24 mm/s, more bubbles are pulled downwards at the walls than are found above the sparger. This effect significantly changes the velocity profiles at 0.3 m. The downward movement of the bubbles near the wall requires a strong downward flow; however, as seen in Figure 5-8 the averaged absolute vertical velocities near the wall from the experiments are distinctly smaller than in the simulations. Therefore, the downward movement of the bubbles could be different in the experiments; this might explain the differences in the transient behavior seen in Figure 5-9.

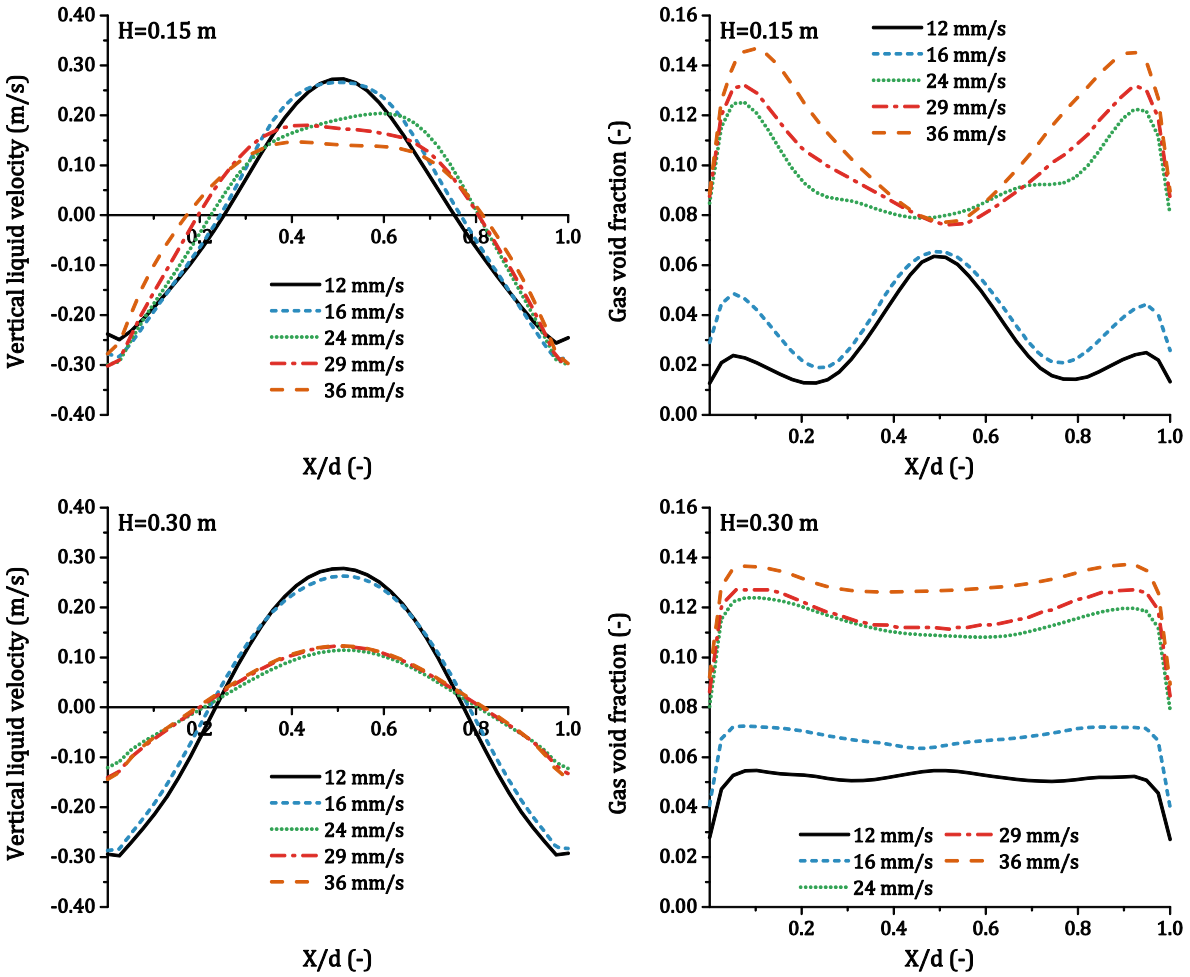

Figure 5-10 Velocity and gas void fraction profiles for pattern F11 for different superficial velocities at two different heights.

The bubble plume frequency is determined from the simulations by analyzing the vertical velocities at 0.15 m and not at 0.3 m as in the experiments. The plume frequency is changing over time in the simulations; in Figure 5-9 simulation and measurement are compared at a time at which the accordance between them is good. Time sections are found in which the simulations are not matching the experimental data. Therefore, the frequency was determined with the windowed Fourier transformation. The windows have the same length as the measurement time, namely 60 s and are overlapping 50 percentage; the obtained frequencies were averaged over time. The real time of the simulations is between 1000 and 2000 s.

Despite the differences between simulations and experiments discussed above, for pattern F8 and F11 the agreement regarding the bubble plume frequencies is very good as shown in Figure 5-11. The almost linear increase of the measured frequencies for the F8 and F11 pattern is reproduced by the simulations. The accuracy of the determined frequencies, especially for the experiments, is $1/60\ s = 0.016\overline{6}\ s$ (60 s measuring time).

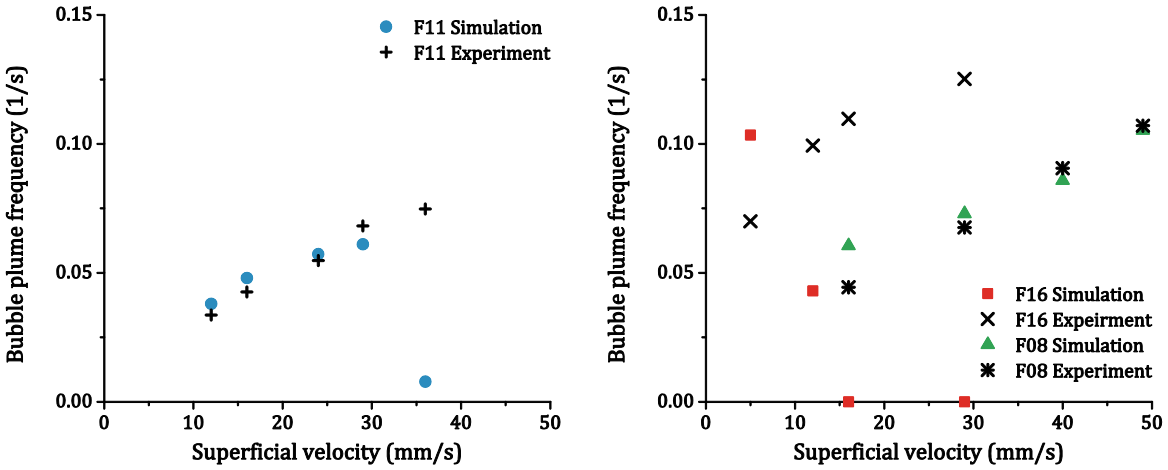

Figure 5-11 Comparison of the bubble plume frequency obtained by experiments and simulations. Left the Frequencies for the F11 pattern; right the frequencies for the F16 and F8 pattern.

Large differences are obtained for the F16 pattern in general and for the F11 pattern at 36 mm/s superficial velocity. The bubble plume tends to stabilize and is not moving anymore. The stabilized bubble plume for F11 at 36 mm/s superficial velocity and F16 at 16 mm/s superficial velocity is demonstrated in Figure 5-12. The averaging time was around 2000 seconds for the F11 pattern and around 1000 seconds for the F16 pattern. The bubble plume is meandering at the beginning but slowly stabilize after several minutes. Then, the vortex zones that would move downwards and dissipate at the bottom are stabilizing as is seen from the vector plots.

Such stabilized bubble plumes were also observed in previous simulations (Lucas et al. 2007b) in which the lift force stabilizes or destabilizes the plume (Lucas et al. 2005). The influence of the lift force on the present setup is demonstrated in Figure 5-13 for pattern F11 with a superficial velocity of 29 mm/s. Since the lift force model of Tomiyama et al. (2002) is used with a bubble diameter of 4.56 mm (see Table 5-1), the lift force coefficient is positive with a value of 0.25 in the original setup. Thus, the bubbles are moving towards the walls of the bubble column and away from positive vertical velocity peaks. These stabilizing effect leads to a homogenizing towards the top. Without the lift force, the bubble plume stands on one side, after approximately 400 seconds the plume

swings to the other side. This leads to a wall-peaked velocity profile near the sparger as seen in Figure 5-13. Moreover, towards the top of the column an inhomogeneous flow pattern is observed with a distinct upward flow in the center and downward flow at the walls.

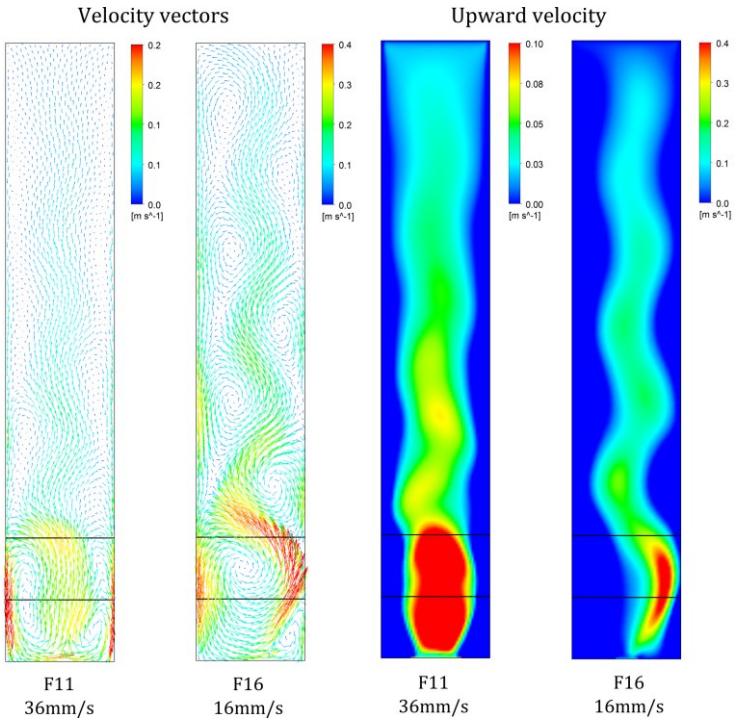

Figure 5-12 Averaged upward velocities and vector plots for pattern F11 at 36 mm/s superficial velocity and F16 at 16 mm/s superficial velocity.

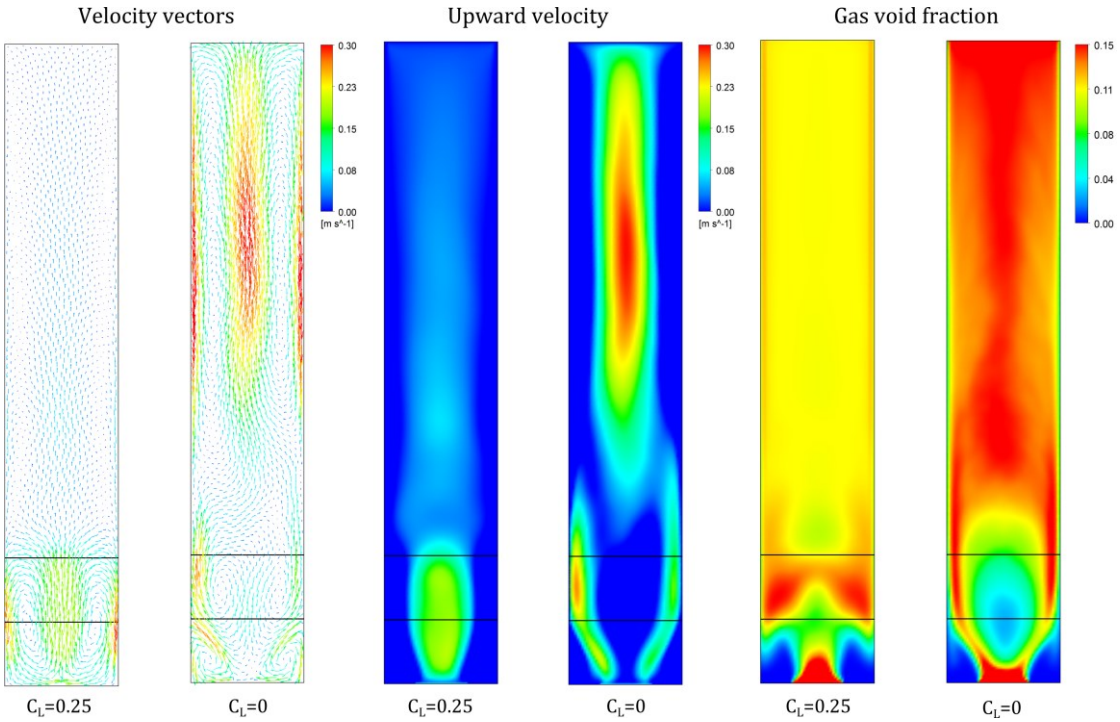

Figure 5-13 Sensitivity regarding lift force for pattern F11, superficial velocity 29 mm/s.

Since the bubble sizes in the experiment are determined from single needle experiments, another bubble size in the fully aerated bubble column is possible. Since the flow is stabilized for smaller bubbles due to the lift force (Lucas et al. 2005), the bubble size is decreased to 4 mm; among other effects, the lift force coefficient is increased to in $C_l = 0.288$. The influence of the bubble size is shown in Figure 5-14. The cases F11 – 36 mm/s and F16 – 29 mm/s do not show a swinging motion with the original setup (see Figure 5-11). A different behavior is seen for F11 with reduced bubble size, the stabilized vortex structures are broken up and the plume shows a swinging motion, occasionally. Nevertheless, the standing bubble plume persists for F16. However, the flow is homogenizing towards the center as is expected due to the lateral motion of the small bubbles away from the center, which is induced by the lift force.

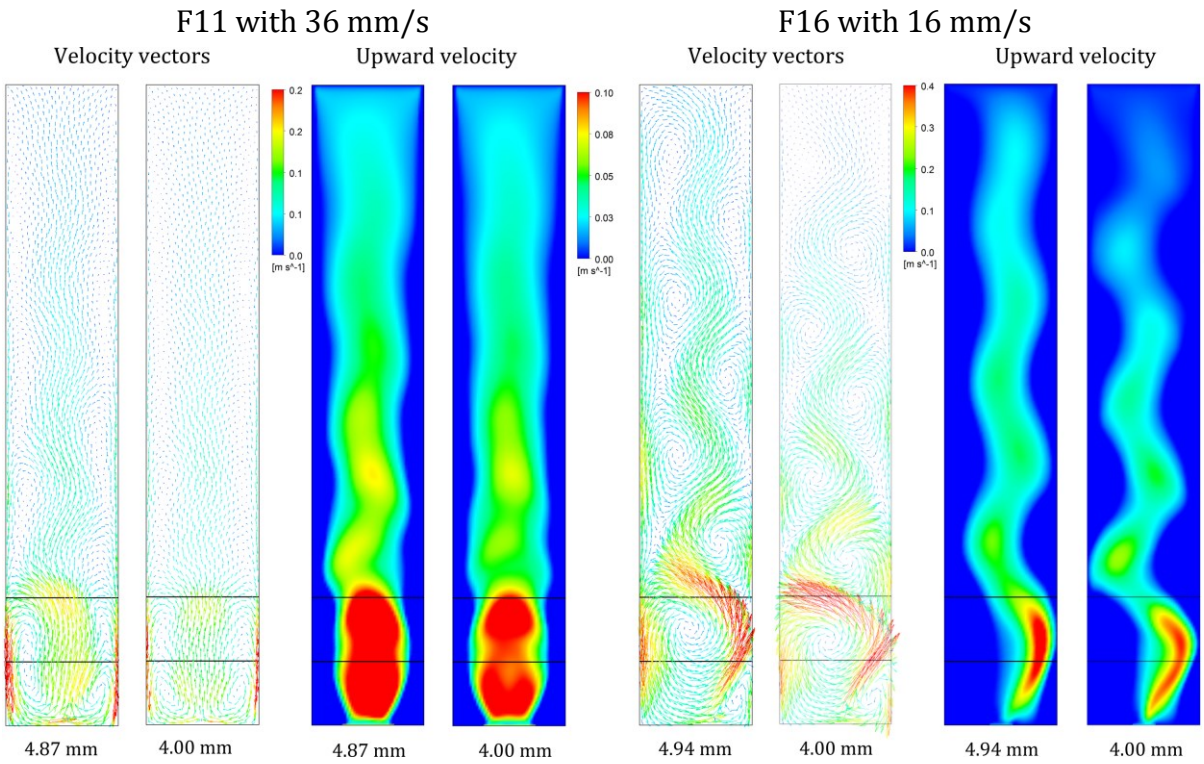

Figure 5-14 Influence of the bubble size for two different flow patterns.

From experience, also the bubble induced turbulence model influences the swinging motion of the bubble plume. This is demonstrated in Figure 5-15 for pattern F16 with 16 mm/s superficial velocity by comparing the baseline BIT model with the Sato model (Sato et al. 1981) described in Section 2.4.4. The stabilized vortex structures are not found with the Sato model, but the bubble plume is swinging slower compared to the experiments. The velocity profiles are symmetric as would be expected. These effects are due to the higher eddy viscosity shown on the right hand side of Figure 5-15. The highest eddy viscosity is found at the position where the bubbles are redirected and occasionally pulled downward. Nevertheless, using the Sato model leads to a non-swinging motion of the bubble plume for the lower superficial velocities (not shown).

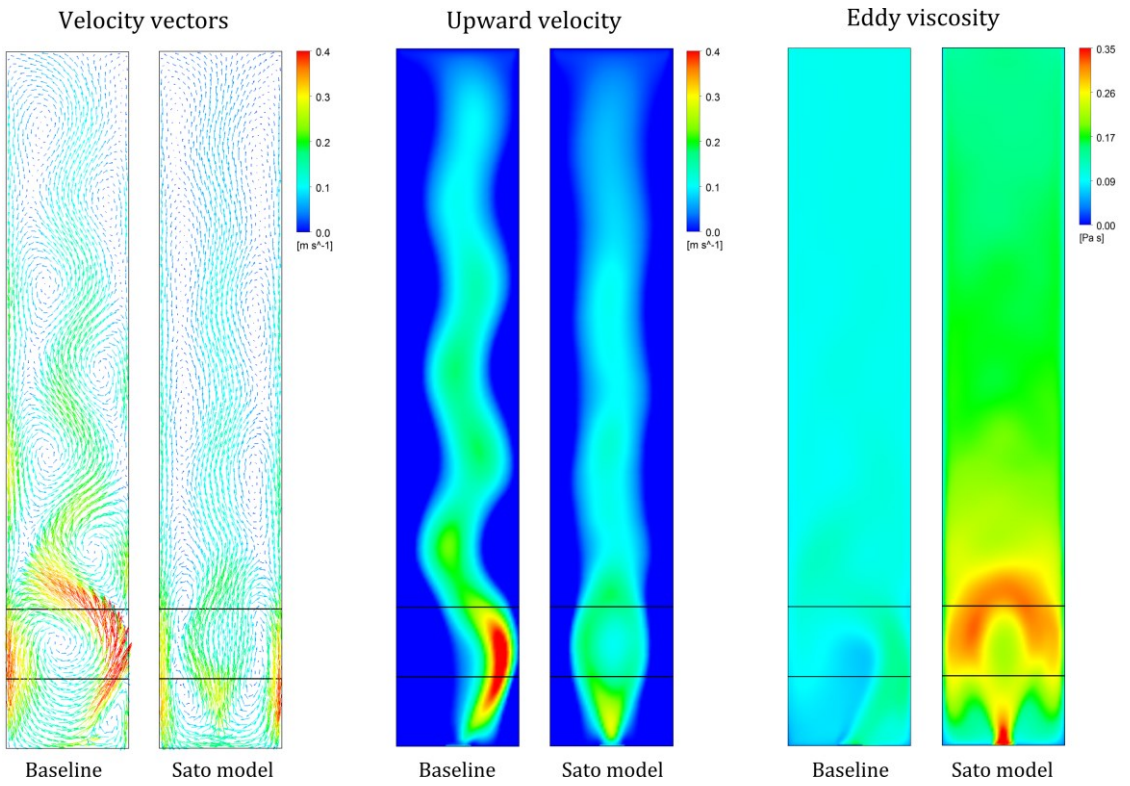

Figure 5-15 Influence of the turbulence model for flow pattern F16 and a superficial velocity of 16 mm/s.

5.3 Conclusions

The swinging bubble plumes are reproduced by the simulations in general. For the Becker and Pfleger cases, the experiments were reproduced qualitatively and quantitatively for the time-averaged results as well as for the transient results. For the Julia cases several deviations occur. The time averaged results are well reproduced for some cases; however, for some other cases the experiments could not be reproduced qualitatively as well as quantitatively.

Surprisingly, the bubble plume frequencies are similar to the experiments for most of the cases for the F8 and F11 flow pattern. Nevertheless, for the highest gas volume flow rate of the F11 pattern and for almost all cases of the F16 pattern the bubble plumes obtained from the simulations are more or less swinging asymmetrically; asymmetric time averaged velocity profiles were obtained as well.

The influence of the lift force, bubble size and turbulence model on the asymmetric swinging bubble plumes is significantly depending on the gas volume flow rate and aeration pattern. Changing these properties improve some cases but also has no effect on or worsen the result for other cases. Changing the lift force or bubble sizes in a way that the stability criterion by Lucas et al. (2005) is fulfilled, the asymmetric plumes are mostly maintained but are homogenizing faster towards the top of the column. Using the Sato BIT model, which is resulting in a significant higher turbulent viscosity, the asymmetric plumes tend to be symmetric, but the swinging motion is suppressed and for lower gas volume flow rates even no swinging motion is obtained.

The asymmetric bubble plume position is a stable or meta-stable state in the simulations. The comparison with experiments, however, is difficult especially since the

precise bubble size for the Julia experiments is not known. Nevertheless, from own experimental experience a bubble plume tends occasionally to stay at one side of the bubble column for an apparently arbitrary long time, especially if the bubble column is not exactly in absolute straight alignment. Since it might be difficult to align large facilities exactly straight, the effect of an asymmetric bubble plume is important for practical use, especially if flow situations exists that amplify such asymmetric behaviors.

It should be noted, that locally very high void fractions occur in the bubble plume. Swarm effects, however, are not minded in the present baseline model, but might be significant.

Nevertheless, the URANS approach with the present baseline model is capable to reproduce the large-scale structures in a bubble column at least for lower void fraction. The frequency of the bubble plume is reproduced for these cases as well as the time-averaged values.

6 Turbulence in bubbly flows using the URANS equations with separation in large and small turbulence structures

In bubbly flows, two flow regimes with different characteristics might be identified, especially in bubble columns. In one of them, there is a uniform flow pattern with a uniform distribution of the gas content over the cross section. The other flow regime is characterized by large-scale flow structures with a non-uniform flow pattern, which arise from partially distributed gas content and/or because of bubble coalescence and break-up processes (Mudde et al. 2009). Therefore, the bubble sizes in this regime are often ranging from very small to very large bubbles. In the uniform flow regime in contrast coalescence and breakup is absent. In this context, they are also refereed as heterogeneous and homogeneous regimes, respectively. Because of the different flow patterns, the dominant turbulent structures in heterogeneous and homogenous regimes might be different.

Partially aerated bubble columns like that of Becker et al. (1994), Pfleger et al., (1999) or Deen et al. (2001) are frequently used to validate simulation models for flows with a non-uniform pattern. The outcome of such studies is in general that the hydrodynamics can be well predicted even by neglecting the bubble induced turbulence (Sokolichin et al. 2004) or bubble forces like the lift force (Diaz et al. 2009). More recently, Ojima et al. (2014) concluded that even without any turbulence modeling non-uniform bubbly flows with large vortex structures could be well described.

Whereas in the previous section the ability of the URANS to reproduce the transient behavior in the heterogeneous regime in general was discussed, in the present it is shown that by using the URANS baseline model, both regimes, non-uniform and uniform bubbly flows, can be reproduced. An approach that is capable to model both regimes is essential for reliable CFD calculations since geometrical changes of the facilities can lead to a regime transition or just bubble coalescence and break up (Lucas et al. 2007b).

The heterogeneous regime is investigated by using the experimental data of Deen et al. (2001), the homogenous regime by using the experimental data of Julia et al. (2007) . At this point, the heterogeneous regime is simplified by using a partially aerated bubble column with a fixed bubble size distribution, which bypasses the additional complexity and uncertainty of modeling bubble coalescence and breakup.

6.1 Simulation Setup and experimental data

A sketch of both experimental setups, Deen et al. (2001) and Julia et al. (2007), is shown in Figure 6-1. The gas volume flow rates and bubble sizes are summarized in Table 6-1. The bubble column used by Deen et al. has a quadratic ground plate and an initial water level of 0.45 m. The sparger consists of an array of 7 by 7 holes. The mean and fluctuation of the liquid velocity were measured using LDA and PIV on a line 0.25 m above the ground plate. The bubble sizes were estimated as 4 mm by not further specified visual observations. Water was used in which 0.04 weight % of kitchen salt were added to suppress coalescence.

The bubble column used by Julia et al. (2007) is a flat bubble column with a homogenous distributed needle sparger that consists of 137 needles. The liquid velocities

and turbulence properties were measured with LDA on a line 0.6 m above the ground plate. The bubble sizes were obtained by single needle experiments using video cameras.

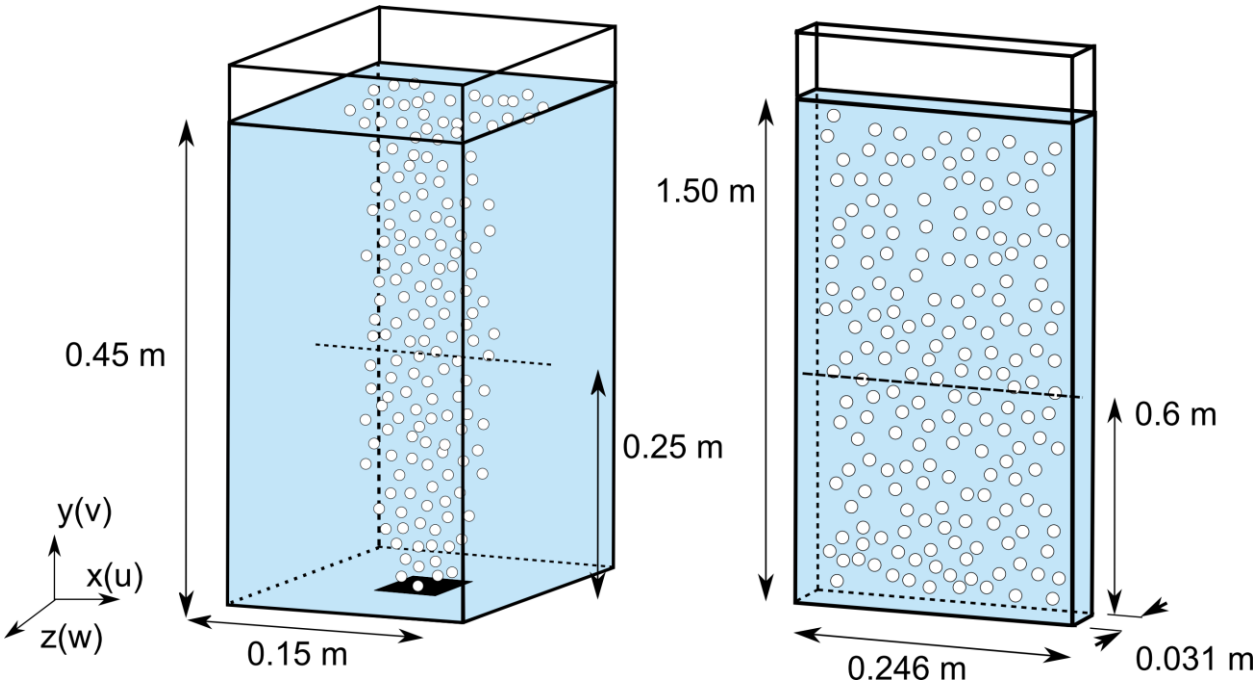

Figure 6-1 Sketch of the experimental setups. Right the setup of Julia et al. (2007); left the setup of Deen et al. (2001). The measurement positions are shown as dotted lines.

Author	Superficial velocity	Bubble size
Deen et al. (2001)	4.9 mm/s	4 mm
Julia et al. (2007)	21 mm/s	3.66 mm
	29 mm/s	3.82 mm
	43 mm/s	4.09 mm
	58 mm/s	5.6 mm

Table 6-1 The superficial velocities and bubbles sizes.

For both cases, grid studies were conducted. The bubble column of Deen et al. (2001) is discretized using a uniform cubic mesh of 5 mm cell size consisting of 81 000 cells. The bubble column of Julia et al. (2007) is, likewise, discretized using a uniform rectangular mesh of $\Delta x = 5\text{mm}$, $\Delta y = 8.2$ mm, $\Delta z = 5.1\bar{6}$ size, consisting of 90 000 cells.

For the Deen column, the inlet is modeled as a region of size of 0.03 x 0.03 m in the center of the column bottom as in the original work (Deen et al 2001). For the Julia column, the inlet corresponds with the full column bottom. Otherwise, the setup and methods are used as defined in Section 2.5 and Section 4.

6.2 Simulation results for both regimes

6.3 Heterogeneous regime

The flow in the bubble column of Deen et al. (2001) is characterized by large-scale flow structures. The liquid velocities were measured using particle image velocimetry (PIV) and laser Doppler anemometry (LDA). In the following, the PIV results are plotted with the LDA results as error bars to indicate the uncertainty of the experimental data. The measurement technique to determine the bubble size is not described by Deen et al., so the reported value may not be reliable.

Therefore three different bubble sizes 3, 4, and 5 mm were tested. The results are shown in Figure 6-2. The vertical liquid velocity varies strongly with the bubble size; the simulation with 4 mm gives here the best results compared to experiments. In contrast, the root mean square of the normal Reynolds stress tensor components v′v′ and $u'u'$ (RMS(v′v′) and RMS(u′u′), respectively) are not as much influenced by the bubble size as the vertical liquid velocity. Nevertheless, the RMS(v′v′) and RMS(u′u′) results shown in Figure 6-2 are the summation of the unresolved and resolved turbulence modeling, both contributions are varying with the bubble sizes but the total amount is nearly the same. Since the results for 4 mm bubble size are in fact closest to the experimental data, this value will be used from hereon.

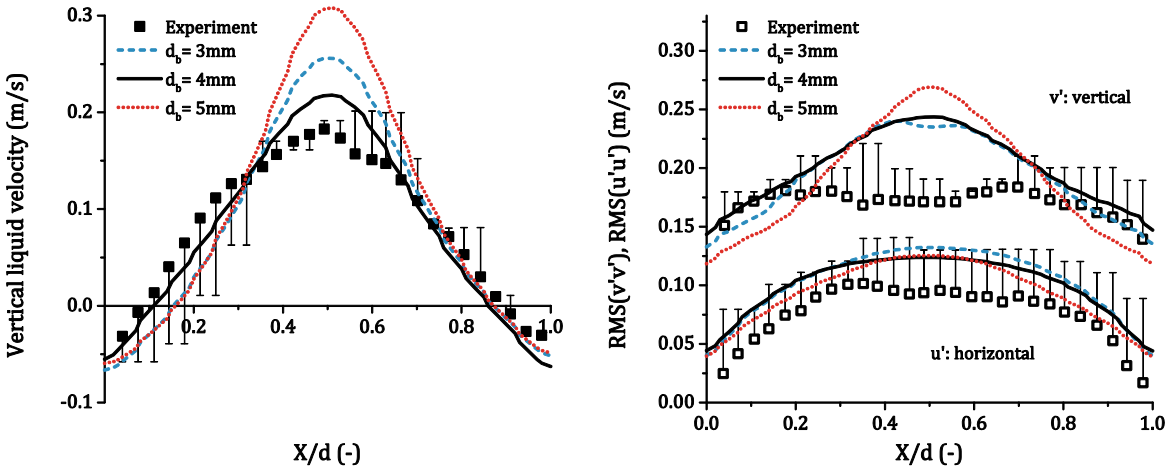

Figure 6-2 Simulation results using different bubble sizes compared to experiments (Deen et al. 2001). Left the vertical liquid velocity is shown; right the root mean square of the normal components of the Reynolds shear stress tensor (v vertical, u horizontal).

The contribution of the unresolved as well as the resolved parts of RMS(v′v′) and RMS(u′u′), both with and without BIT modeling are shown in Figure 6-3. For the mean liquid velocity, there is no significant difference whether BIT is included or not, therefore no additional figure is shown. Considering the measurement uncertainty, the total values of both RMS(v′v′) and RMS(u′u′) obtained by the simulations both with and without BIT are in reasonable agreement with the data. The most prominent difference between the models with and without BIT is the shape of the total RMS(v′v′) profiles. With BIT, a profile with a single center-peak is obtained with a trend to overpredict the measured values in the center of the column. Without BIT, a double-peaked profile is found which is somewhat closer to the data. The nature of these differences is situated in

the resolved contribution. For both models, the predicted variations are too pronounced compared with the experimental profiles, which have a rather flat shape. For the total RMS(u′u′), both models give similar results.

Such double peaked RMS(v′v′) profiles that are obtained without the BIT modeling have been observed in flat bubble columns with partial aeration (Simiano et al. 2006)(Section 3.4 and Section 7). The experimental data of Deen et al. in the square shaped bubble column might indicate also such profile shape; however, due to the measurement uncertainty this is speculative.

RMS(v′v′) is dominated by the resolved contribution for both models with and without BIT. In contrast, for RMS(u′u′) the resolved and unresolved contributions have similar values for the model with BIT whereas for the model without BIT the modeled contribution is much larger than the resolved contribution.

The resolved contribution to the Reynolds stresses is higher with BIT model than without a BIT model in general. This is caused by the eight times lower eddy viscosity obtained with the BIT model. Accordingly, the eddy dissipation rate is distinctly higher with the BIT model. Nevertheless, the liquid velocity profiles (not shown) obtained with BIT und without BIT modeling are nearly the same.

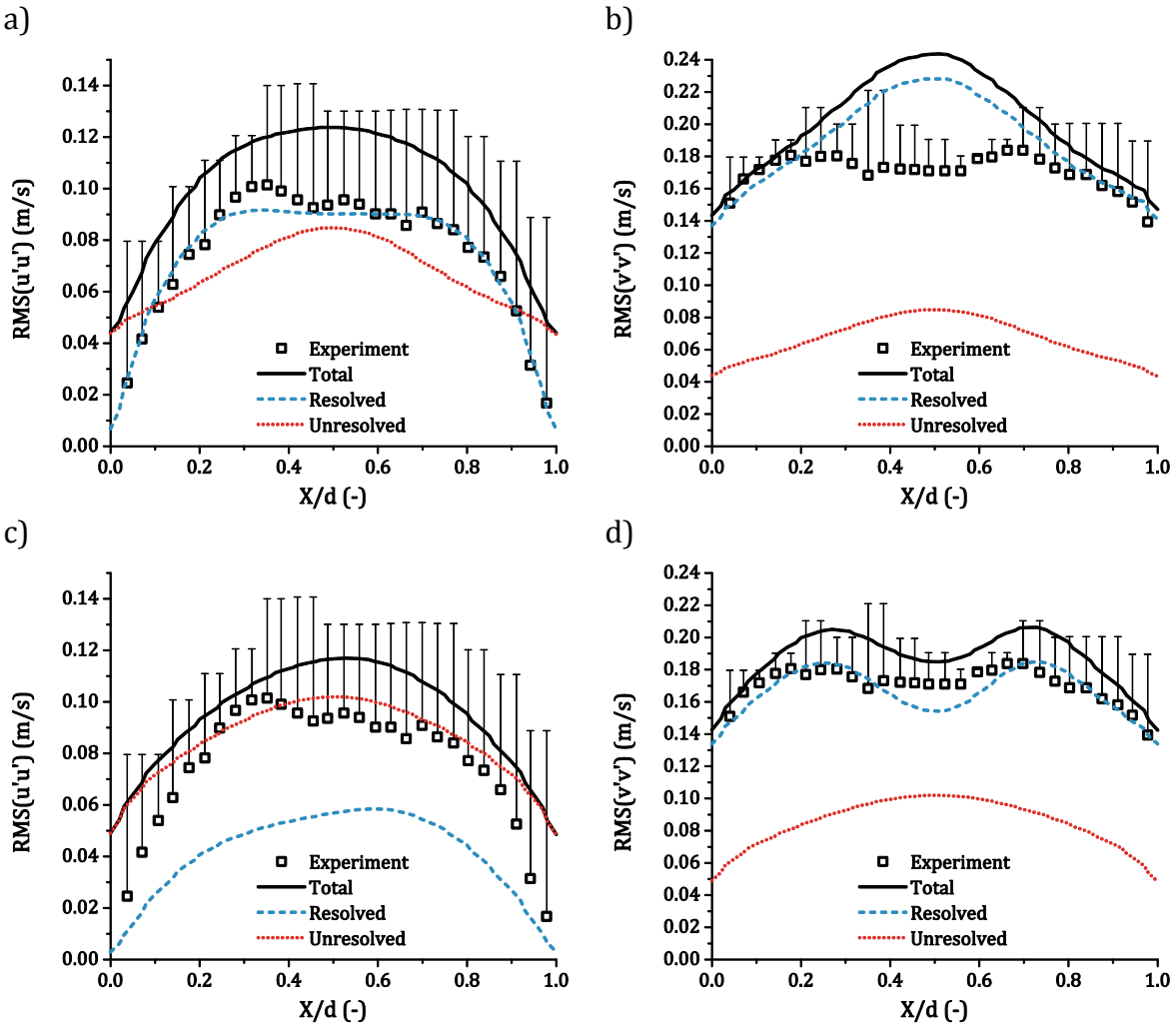

Figure 6-3 Resolved and unresolved parts of RMS(v′v′) and RMS(u′u′) with and without BIT at 0.25 m above sparger compared to experimental data by Deen et al. (2001). a) And b) using BIT; c) and d) without a BIT model.

Summarizing, the non-uniform regime represented here by the experiments of Deen et al. (2001) using a monodisperse bubble size distribution in a partially aerated bubble column can be reproduced satisfactorily using a two equation turbulence model either with or without BIT source terms. Moreover, the URANS modeling gives nearly the same results as large eddy simulations and scale adaptive simulations (Ma et al. 2015) or Reynolds stress models (Masood et al. 2014).

6.4 Homogenous regime

The uniform regime is characterized by a uniform distribution of the bubbles over the cross section of the column. When the bubbles are small enough this situation is stabilized by the lift force as discussed by Lucas et al. (2005) (2007b). Hence, no larger vorticities are expected in this regime as well as the turbulence is dominated by the BIT part. As discussed above, the experiments of Julia et al. (2007) are chosen for the investigation of this regime.

Profiles of the liquid velocity, which were measured with LDA for the cases with gas superficial velocities of 29 mm/s and 43 mm/s, are compared with the URANS modeling in Figure 6-4 a), b) and c), d) respectively. Simulation results obtained both with and without BIT modeling are shown. As expected, the resolved part of the fluctuations in both directions RMS(v′v′) and RMS(u′u′) turns out to be zero in the simulations for both model variants, thus only the modeled part is shown which equals the total fluctuations. As a consequence the calculated values for RMS(v′v′) and RMS(u′u′) are equal since the modeled fluctuations are isotropic.

In comparison to the non-uniform regime the liquid velocity profiles are much more plug flow like with the liquid flowing downwards only much closer to the sidewalls. Similarly the profiles of RMS(v′v′) and RMS(u′u′) here are almost constant over the column width and drop to zero steeply near the walls.

Comparing experiment and simulations, the vertical liquid velocity is underpredicted in the simulations for both values of the superficial velocity. As seen from the comparison of LDA and PIV data by Deen et al. (2001) a possible systematic error of the LDA method, which gives consistently higher values than obtained by PIV, may contribute to this deviation. From the modeling, the neglect of swarm effects and the use of a drag correlation for contaminated rather than clean systems are likely to play a role. The data show characteristic peaks near the walls, which are in principle also indicated in the simulations. Simulations with and without BIT modeling give quite similar results for the vertical liquid velocity.

Concerning the fluctuations the RMS(v′v′) and RMS(u′u′) which have both been measured for the lower superficial velocity of 29 mm/s a certain anisotropy is seen that is not covered by the present two-equation turbulence model. A Reynolds stress model is needed to capture this effect. Without a BIT model the turbulence is underpredicted by a factor of 4 or more whereas with BIT model it is overpredicted by a factor of approximately 2. The profile shape with BIT model shows peculiar peaks at the wall which are absent in the data. For the higher superficial velocity of 43 mm/s only data for

RMS(v′v′) are available which show slightly higher values than for 29 mm/s. This trend is also seen in the simulations with BIT model but not in those without BIT model.

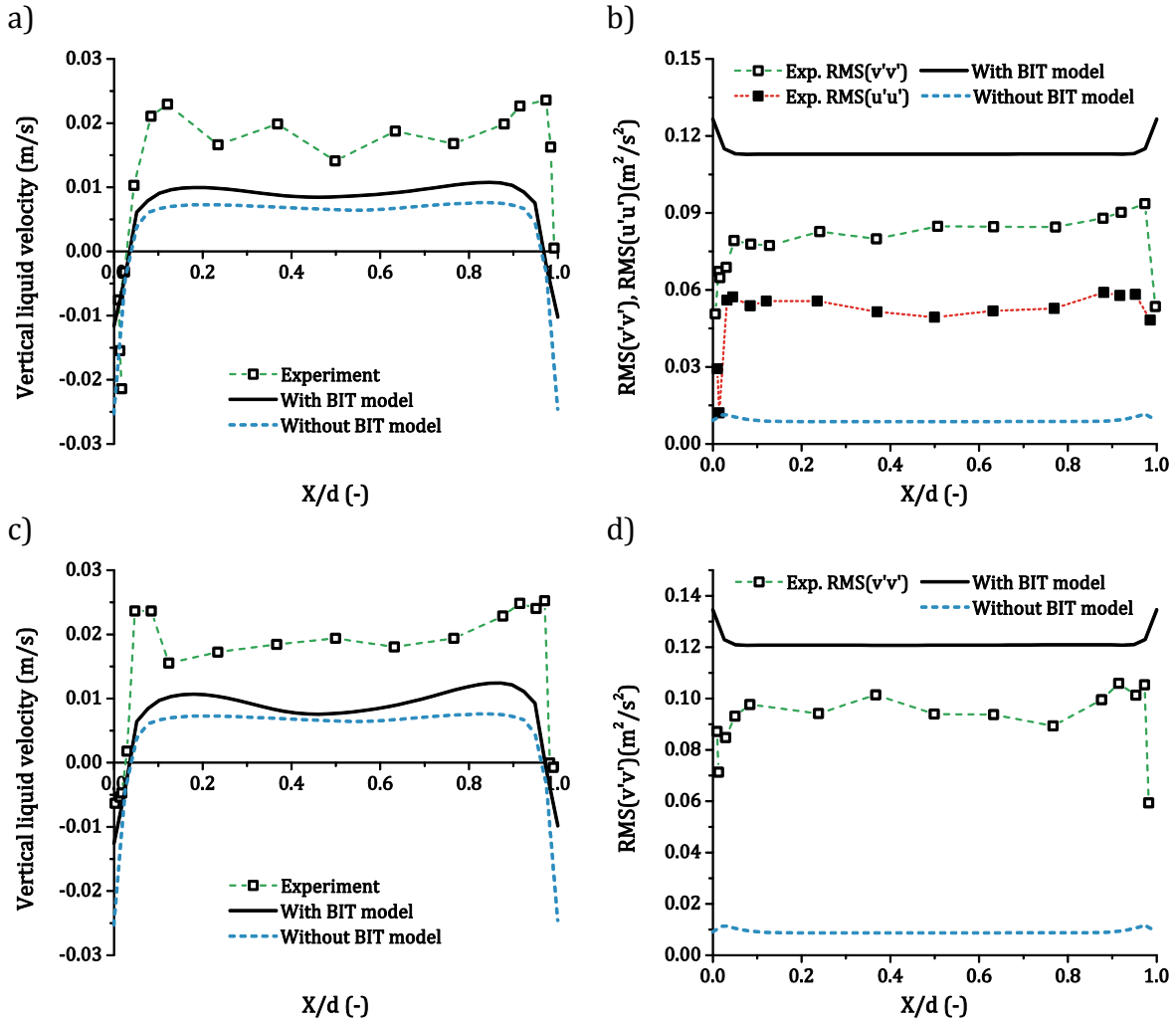

Figure 6-4 Vertical liquid velocity and RMS values of the normal Reynolds stress components obtained with the URANS modeling compared to experiment (Juliá et al. 2007). a) and b) superficial velocity of 29 mm/s. c) And d) superficial velocity of 43 mm/s.

For all four superficial velocities, averages of the RMS(v′v′) and RMS(u′u′) values along the measurement line have been reported by Julia et al. (2007) (without the near wall region). These are shown in Figure 6-5 together with the corresponding simulation results for the model with BIT. As can be seen, the overprediction of the values by the simulations is present for all superficial velocities with the deviations increasing with decreasing superficial velocity.

In addition, the data from another experiment for uniform flow in a bubble column by bin Mohd Akbar et al. (2012) and corresponding URANS simulations from Section 4 using the same modeling as in the present study with BIT is included. The results obtained with the URANS simulations for the latter case are in good agreement with the measured RMS(v′v′).

Since the data of Julia et al. (2007) and bin Mohd Akbar et al. (2012) do not fall on a single curve, it appears that besides the superficial velocity some other relevant parameter must exist. The bubble sizes in both experiments are about 4 mm and both have been conducted in an air/water system. Also the geometries are rather similar, the column of bin Mohd Akbar et al. (2012) being about twice as thick as that of Julia et al. (2007) or in other words almost twenty and ten times the bubble diameter respectively. The integral gas hold up differs strongly between the two experiments, for the experiments of bin Mohd Akbar et al. (2012) is about 1.5 % while for the experiments by and Julia et al. (2007) ranges from 5.4 % to 20.2 %. However, this difference corresponds with the different superficial velocity. Therefore, it is not clear where the mismatch between both experiments comes from.

In Julia et al. (2007) it is mentioned that a turbulence model for bubbly flows based on the pseudo turbulence obtained from potential flow (de Bertodano et al. 1990) with a dependency on the void fraction as $\alpha^{2/3}$ (Lance et al. 1991) can reproduce their experimental data. Additional simulations performed using this model, however, have shown heavy underprediction for the experiments by bin Mohd Akbar et al. (2012). Hence, such a model adaptation is not useful in general. Moreover, introducing a similar void fraction dependence in the prefactor $C_{\epsilon B}$ of the present BIT model would also worsen the agreement for the experiments by bin Mohd Akbar et al. (2012) and probably also for the pipe flow tests by Rzehak & Krepper (2013b) (2015) and Rzehak & Kriebitzsch (2014).

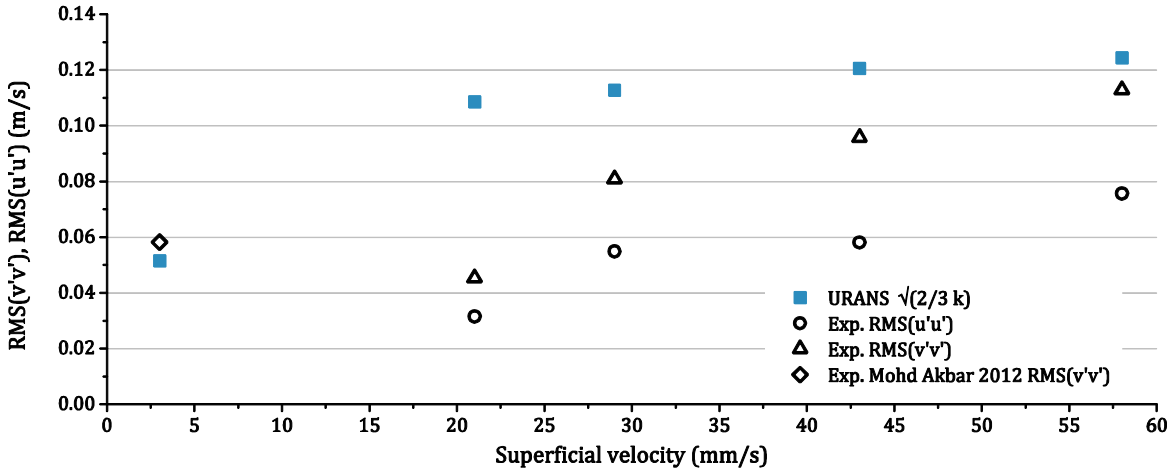

Figure 6-5 Reynolds stresses in homogenous bubble columns for different superficial velocities. The four superficial velocities from the present study (Juliá et al. 2007) and the experiments by bin Mohd Akbar et al. (2012) with the corresponding URANS simulations by Ziegenhein et al. (2015) are shown.

Summarizing, the uniform regime represented by the experiments of Julia et al. (2007) can be roughly reproduced by the URANS approach. The resolved part of the turbulence modeling is zero as would be expected and the simulated RMS values of the normal Reynolds stress components are completely dominated by the used BIT model.

6.5 Comparison with Large Eddy simulation

Besides the URANS approach also large eddy simulations (LES) were performed in corporation with the group of Prof. Jochen Fröhlich from TU-Dresden. The LES were executed by Dipl.-Ing. Tian Ma (HZDR/TU-Dresden), the results are described in several publications (Ma et al. 2015) (Ma et al. 2015) (Ma et al. 2015). At this point, the results are shortly compared to the URANS results by using the results of the last two mentioned papers. The results from the LES are reproduced with permission of Dipl.-Ing. Tian Ma, which is not repeated in the following. The results are taken from the LES with the Smagorinsky model using $C_s = 0.12$ and the Sato BIT model (see Section 2.4.3). Further, the same force model set was taken as used for the baseline URANS except the turbulent dispersion force since these turbulence structures are resolved in the LES.

For the experiment of Deen et al. (2001) which is investigated in the previous section, the LES from Ma et al. and URANS simulations are compared in Figure 6-6. The vertical liquid velocity is stronger over-predicted than by the URANS simulations compared to the experiments. The obtained root mean square of the normal components of the Reynolds stress tensor $u'u'$ and $v'v'$ are similar for both approaches. The $RMS(v'v')$ obtained from the LES, however, shows a very strong peak in the center. Likewise as the liquid velocity, the void fraction is higher in the center compared to the URANS simulations. The eddy viscosity obtained from the LES is distinctly smaller compared to that obtained from the URANS simulations, as would be expected. For comparison, the eddy viscosity obtained from the URANS simulations without a BIT model is shown. The lower the modeled eddy viscosity the higher the resolved part of the turbulence.

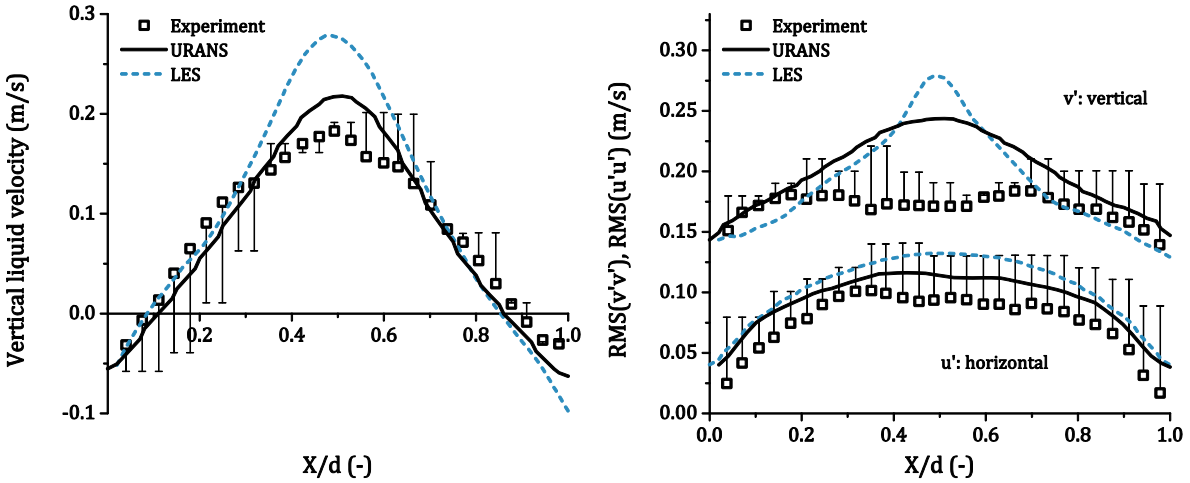

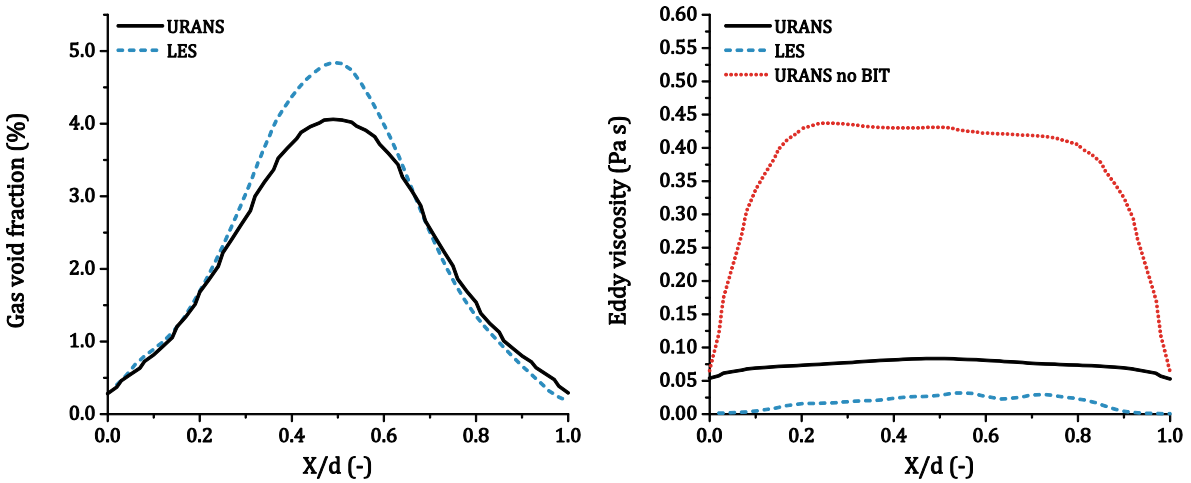

Figure 6-6 LES compared with the URANS simulations for experiments of Deen et al. (2001).

It should be noted, the LES result obtained without the Sato BIT model, which is leading to a lower eddy viscosity, fits better to the experiment. Therefore, LES are capable to reproduce the bubbly flow for this experiment in general.

For homogenous regimes that might be dominated by the BIT, the LES, however, cannot represent the turbulence as shown in Figure 6-7. Here, the experiments of Mohd bin Akbar et al. (2012), which are discussed in Section 4, are compared to LES and URANS simulations. For the 3 mm/s superficial velocity it was previously found that the resolved turbulence scales obtained from the URANS simulations are almost zero. The same result is obtained from the LES resulting in a strong underprediction of the $RMS(w'w')$ (w is the upward velocity to stay in the notation of the experiments) values shown in Figure 6-7 d). Nevertheless, vertical liquid velocity and gas volume fraction are similar to the URANS simulations.

The results of the LES for the 13 mm/s case are similar to the URANS results. Looking at the $RMS(w'w')$ profiles an improvement is obtained compared to the experiments; the distinct near wall peak is better reproduced by the LES.

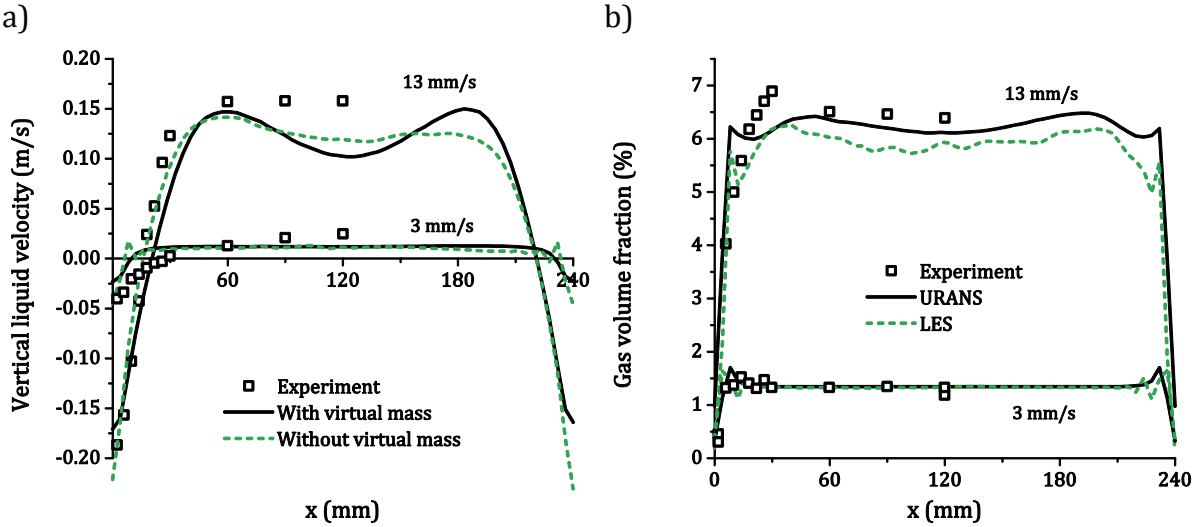

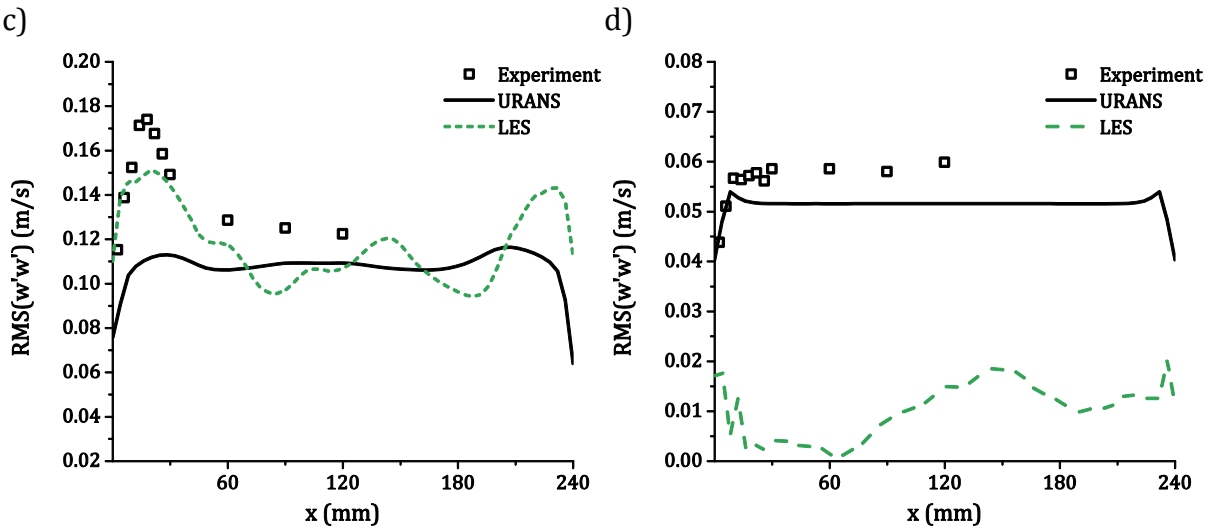

Figure 6-7 LES compared with the URANS simulations for the experiments of bin Mohd Akbar et al. (2012) (cf. Section 4). a) and b) vertical liquid velocity and gas volume fraction for 3 mm/s and 13 mm/s superficial velocity, c) $RMS(w'w')$ for 13 mm/s superficial velocity (w is the upward velocity), d) $RMS(w'w')$ for 3 mm/s superficial velocity.

Summarizing, the baseline URANS model approach and the LES give similar results in the inhomogeneous, large-scale flow dominated bubbly flow regime. Therefore, the URANS simulations are capable to reproduce such structures in general. The URANS approach is capable to reproduce the homogenous, BIT dominated regime, which is not possible with the present BIT modeling for the LES. Therefore, towards a general approach to model bubbly flows the URANS approach is advantageous.

6.6 Conclusions

The resolved structures obtained from the simulations give an important contribution to the turbulence in general. Further, the anisotropic character of the turbulence in this regime is reproduced in this way. Comparing the URANS results to other turbulence model approaches like LES (Section 6.5) or a Reynolds stress model (RSM) (Masood et al. 2014) similar results are obtained. Therefore, in the heterogeneous bubbly flow regime the URANS approach is capable to reproduce the large-scale flow structures in the same way as approaches that are more sophisticated.

The total turbulent kinetic energy is similar with and without BIT modeling; the unresolved and resolved parts, however, are different. Since also the LES with and without BIT and the RSM simulations give almost the same results for the Deen experiments, it is reasonable to assume that the BIT modelling has a minor influence in the heterogeneous regime. Differences between the approaches are small and are in the range of the experimental uncertainty; especially the not measured bubble size distribution is problematic.

A different situation is found in the homogeneous regime. The liquid velocity is small and no large-scale flow structures are expected. This expectation is consistent with the results obtained from the URANS simulations since the resolved turbulence part is nearly zero. Therefore, the turbulence is completely characterized by the unresolved turbulence model. Simulations without BIT modeling heavily underpredict the turbulence in this regime. The results obtained from the simulations with BIT in contrast overpredict the

experimental data to somewhat lesser degree with deviations increasing with decreasing superficial velocity. Despite the necessity to improve the modeling further, the URANS approach with the BIT model used here is capable to describe the uniform bubbly flow regime as well.

Therefore, the present URANS approach with a BIT modeling using source terms for k and ϵ/ω is able to reproduce both regimes. To improve the Eulerian LES it might be necessary to define at least a one-equation turbulence transport with a filter width addicted to the bubble size and not to the mesh size. To cover isotropic turbulence in the unresolved part, especially in the BIT modeling, a RSM approach might be the only reasonable approach.

The nature of the bubble-induced turbulence remains an issue of active research and up to now, no model is sufficient for a general formulation. Besides fundamental investigations to this topic, also reliable experimental data for a validation is needed. For this purpose, a comprehensive set of locally measured values is needed in different flow conditions. Indeed, the above discussed experiments, except of the one used in Section 4, do not provide such data since often information about the gas phase (gas void fraction) or liquid velocity field (basic turbulence parameters) are missing. In particular, the bubble sizes are insufficient determined since the measuring method is often not given or the bubble sizes are estimated from simplified flow conditions. Furthermore, the bubble size distribution at different positions is needed to evaluate if coalescence and break up processes are negligible or not. Unfortunately, such comprehensive experimental data that can be used for CFD validation are rare in the literature. Thus, an own experimental study is performed in the next section covering all the needs of a CFD validation.

In parallel, the modeling of the different closure models in the momentum equation (see Section 2.3) has to be evolved. From the discussion from the last sections it appears that the lift force plays an important role. Reliable measurements, however, were only performed under high Morton numbers and low Reynolds numbers, which are far away from the here used conditions. Moreover, the significance of the lift force in turbulent air/water bubbly flows is an open discussion in the community. Therefore, new methods are developed to measure the lift force in the after next section.

7 A complex validation case for CFD simulations: Airlift reactor

In the bubble columns that are discussed in the previous sections the gas bubbles drive the flow and usually the liquid is rising in the center and falling near the wall. The up- and downward flow are next to each other and can interact. Alternatively, internal walls can be placed in bubble columns to separate the up and downward flow; these reactors are called internal airlift reactors.

For many applications that use airlift reactors it is desired to know the exact fluid dynamics. For example, the light exposure of microorganisms in airlift photo bioreactors can be optimized by knowing the fluid dynamics (Fernandes et al. 2010). Moreover, the shear rate and turbulence parameters are important for all process with microorganisms (Liu & Tay 2002) (Miron et al. 200) (Oliver-Salvador et al. 2013) and for mass transfer modelling (Korpijarvi et al. 1999) (Lu et al. 2000). Nevertheless, such detailed information of the fluid dynamics are rarely accessible by the use of experiments.

A better understanding of the fluid dynamics is gained by using the methods of the computational fluid dynamics (CFD). A lot of work was done simulating airlift reactors in the past with the Eulerian two-fluid approach. However, in general the bubble sizes were not known (Huang et al. 2010) or only known in the downcomer (Luo & Al-Dahhan 2011). Further, often only integral measured values were available (Simcik 2011) (Ghasemi & Hosseini 2012). Hence, a validation of the closure models in airlift reactors is limited with the existing experimental data.

In the present section, an internal airlift reactor is experimental studied to provide a comprehensive set of locally measured data for CFD validation. To the best of the author's knowledge, those measurements were not published in the past and are urgently needed. Moreover, the measured data provide a complete picture of the flow in an internal airlift reactor.

7.1 Setup

The bubble column that is described in Section 3.1 is used with internal walls as shown in Figure 7-1. The 5 mm thick internal walls separate the 0.12 m wide riser from the downcomers. Each downcomer has a width of 0.06 m so that the riser and the sum of both downcomers have the same cross section. The distance from the ground plate to the beginning of the internal walls is 0.06 m, which is equal to the width of a downcomer. In addition, the distance from the top of the internal walls to the water surface (the top clearance) is held constant to 0.06 m for all gas volume flow rates. Thus, the liquid level is at 0.72 m above the ground plate for all setups.

Liquid velocity, turbulent kinetic energy, available Reynolds stress tensor components and bubble sizes are determined at a height of 0.2 m and 0.6 m in the riser and the downcomer, which is indicated with red lines in Figure 7-1. The void fraction is measured at a height of 0.6 m in the riser. In addition, the bubble size distribution and the void fraction are determined along the downcomer.

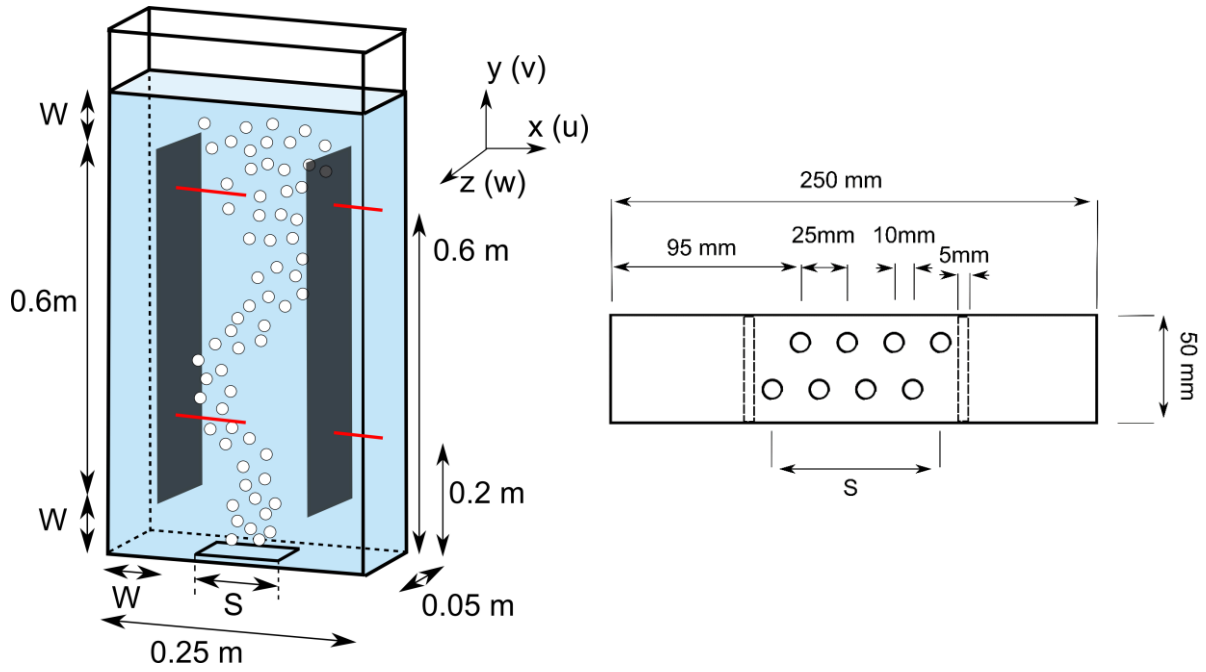

Figure 7-1 Experimental setup and the used ground plate setup. The red lines label the measuring positions.

Rubber seals that are attached at the side of the internal walls hold them in place. Therefore, no interaction between the riser and the downcomer is possible and no flow disturbing installations are needed to hold the walls in place. The Gas is injected through the ground plate, which is shown in Figure 7-1 on the right hand side, by using up to eight needles with an inner diameter of 0.6 mm. The volume flow rate per needle is held constant for all cases to get a similar bubble size distribution. The total gas volume flow rate is regulated by changing the needle count. A summary of the important parameters is given in Table 7-1.

case cumber	Volume flow	Sparger needle	Needle count	Volume flow rate per needle	S	W (gas on)
4	3 l/min	0.6 mm	4	0.75 l/min	35 mm	60 mm
6	4.5 l/min	0.6 mm	6	0.75 l/min	60 mm	60 mm
8	6 l/min	0.6 mm	8	0.75 l/min	85 mm	60 mm

Table 7-1 Experimental parameters at standard conditions.

7.2 Results

The bubble size distribution is determined with videography at several positions as discussed in Section 3.2. The volume fraction in the riser is measured with a conductivity needle probe as described in Section 3.3.1. In contrast, the volume fraction in the downcomer is determined by the use of videography as described in Section 3.3.2. The

liquid velocity and the turbulent kinetic energy are measured with particle-tracking velocimetry using micro bubbles (BTV), which is discussed in Section 3.4.

7.2.1 Bubble size distribution

The bubble size distributions in the riser for the different volume flow rates are shown in Figure 7-2. Bubbles that are smaller than 1.5 mm are not evaluated in order to reduce the measuring effort since the count of the small bubbles is large whereas such small bubbles are not significant for the Sauter diameter, which is used for CFD calculations. In the riser, the bubble sizes are determined at a height of 0.2 m and 0.6 m to evaluate possible break-up and coalescence effects. The number density function is identical at both heights for case 6 and case 4 (case 4 is not shown). For case 8, the number density function is shifted slightly towards smaller bubbles. Nevertheless, comparing the area density and volume density function of case 8 with the results of case 6 and case 4 no large differences are seen so that coalescence and break up might be negligible.

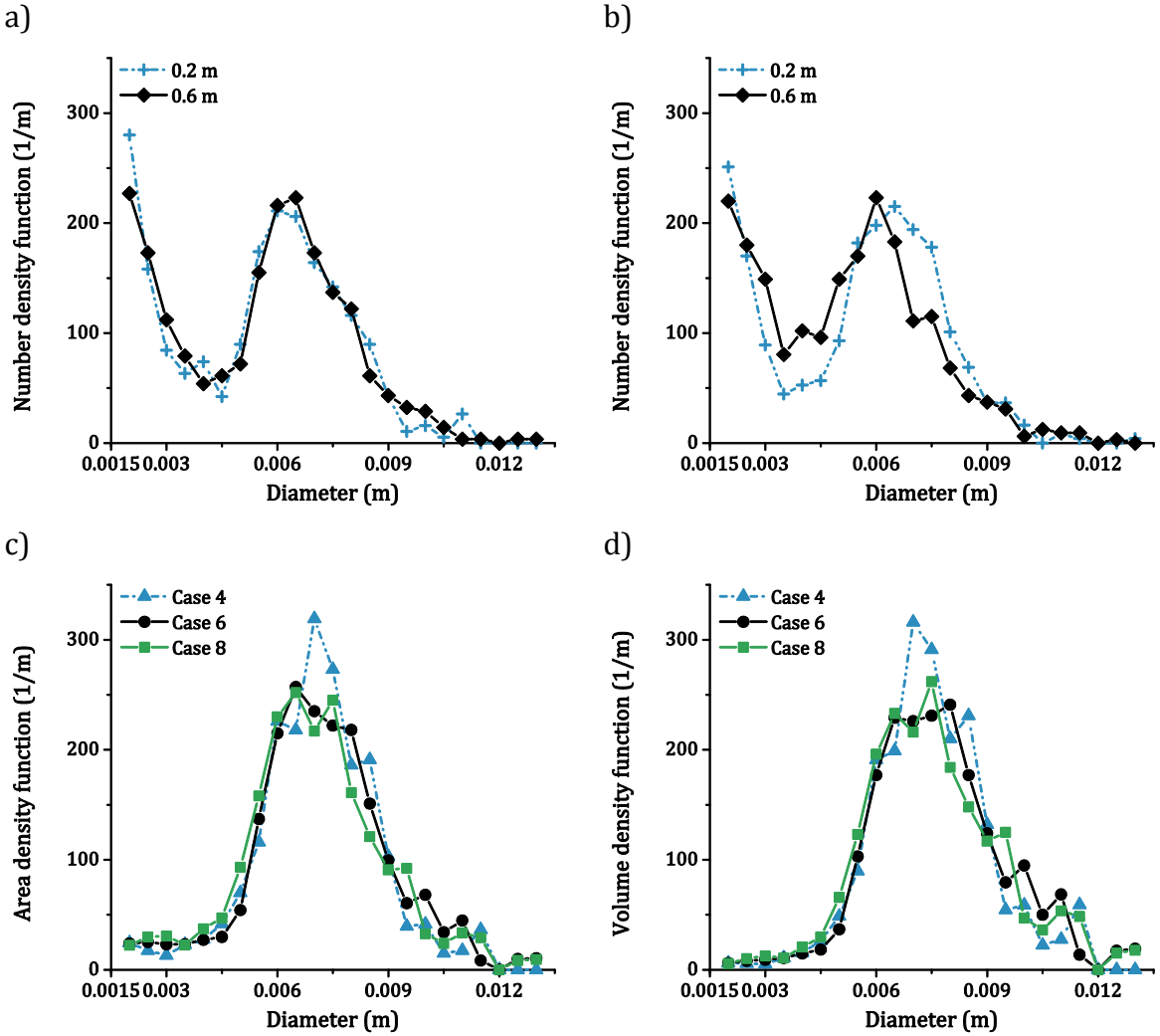

Figure 7-2 Bubble size distributions in the riser. a) Number density for case 6 at two different heights b) number density for case 8 at two different heights; c) averaged area density function at 0.2 m and 0.6 m; d) averaged volume density function at 0.2 m and 0.6 m.

The bubbles in the riser are shown in Figure 7-3. Bubble cluster are seen clearly for all volume flow rates. The bubbles inside the clusters are identified by chasing the bubble clusters over several images until the bubbles are seen distinctly as described in Section 3.2.3.

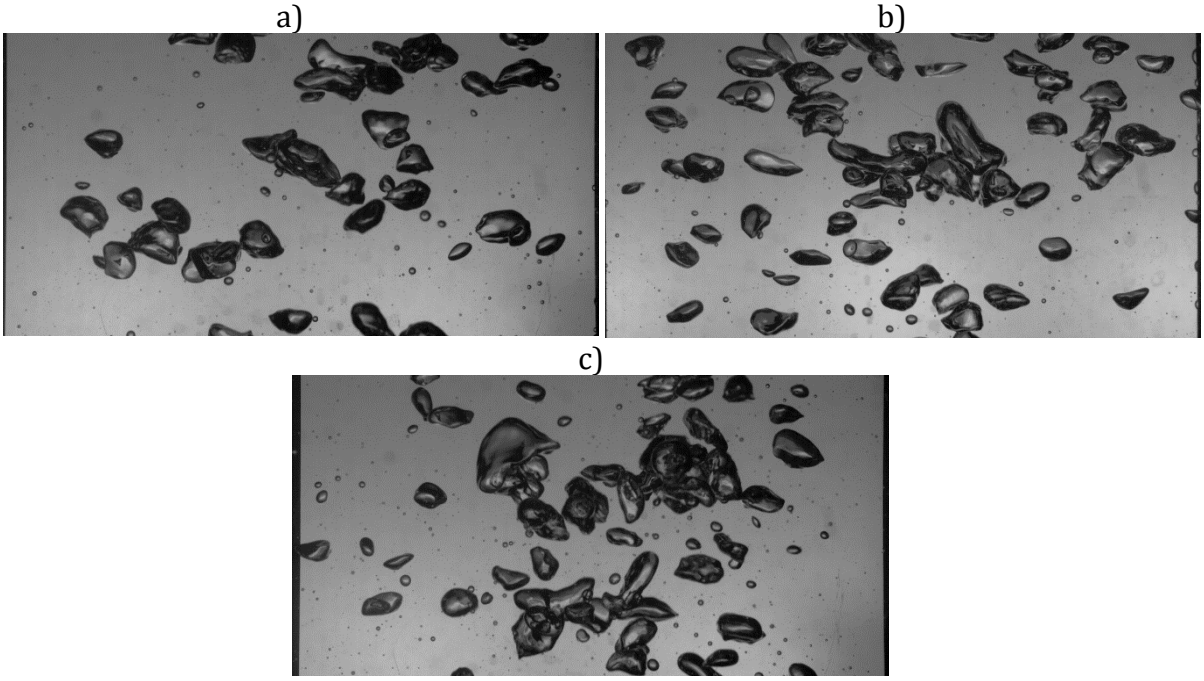

Figure 7-3 Pictures of the bubbly flow in the riser at a height of $y = 0.2$ m. a) case 4; b) case 6; c) case 8.

The automatically determined bubble sizes along the downcomer are shown in Figure 7-4 picture a). The bubble sizes are averaged over the cross section of the downcomer. The bubble size at the top of the downcomer for case 6 and case 8 are determined by hand because the void fraction is too high for an automated evaluation. A separation of the bubble sizes along the downcomer occurs.

Besides a separation over the height, also a separation of the bubble sizes over the width of the downcomer is seen as demonstrated in Figure 7-4 picture b) for case 8. The bubble sizes are averaged over height from $y = 0.3$ m to $y = 0.4$ m and are plotted against the horizontal coordinate from the airlift reactor wall at $x = 0$ m to the internal wall at $x = 0.06$ m. Near the reactor wall, larger bubbles are situated compared to the bubbles that are found near the internal walls. As will be discussed below, the liquid velocity near the reactor wall is higher than near the internal walls so that this separation occurs.

The situation in the downcomer is shown in Figure 7-5 for the three flow rates. The bubble count for case 4 is very low, although the size of the bubbles might be comparable to case 6. Many large bubbles are seen for case 8, which might be the reason for the larger Sauter diameter.

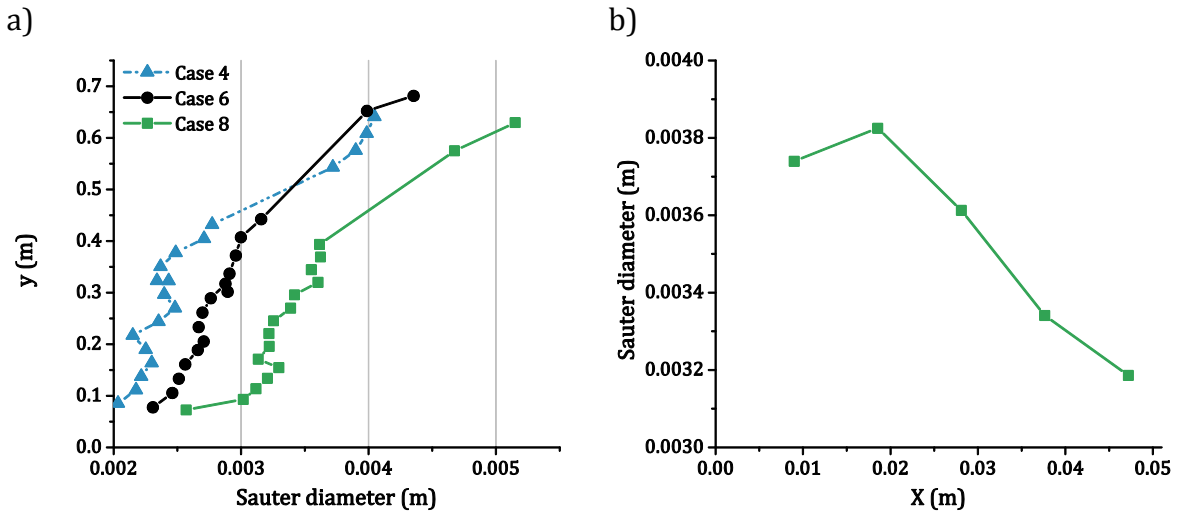

Figure 7-4 Bubble sizes in the downcomer. a) Bubble sizes along the downcomer. b) Bubble sizes over the width of the downcomer for case 8 averaged over height from y = 0.3 m to y = 0.4 m

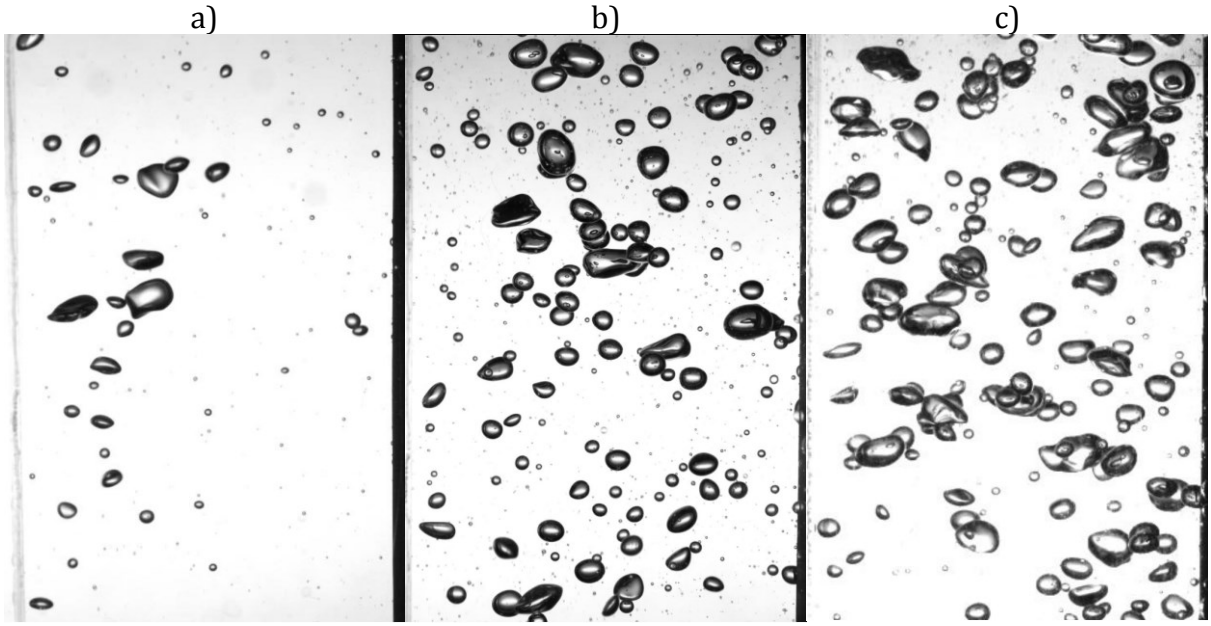

Figure 7-5 Situation in the downcomer, a) case 4 b) case 6 c) case 8.

7.2.2 Liquid velocity and turbulence

The described sampling bias for BTV is also present in the airlift reactor as demonstrated in Figure 7-6. The count of the trajectories is plotted with the velocity over time; a moving average over 2 s is used to show the sampling bias clearly. The count of the trajectories is low when the velocity is high and vice versa over 80 s. Therefore, the count of the tracked micro bubbles is correlated to the velocity, which is leading to a sampling bias. To overcome the bias the hold processor derived in Section 3.4.3 is used as described in Section 3.4.4.

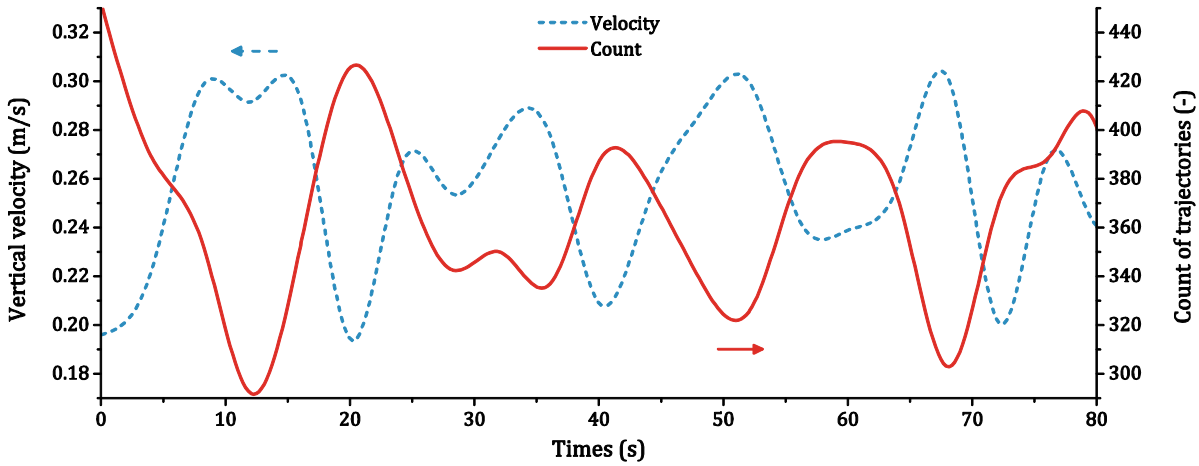

Figure 7-6 Sampling bias in the center of the riser for case 8 at y = 0.2 m.

The liquid velocity profiles in the riser are obtained from four single measurements with a distinct time between them. In total, 48 000 bursts, equivalent to eight minutes measuring time, are evaluated in the riser at a height of 0.2 and 0.6 m. In the upper part of the downcomer at a height of 0.6 m 36 000 bursts are recorded and in the lower part 24 000 bursts. The long measuring time is necessary because a bubble plume with a very long time scale occurs; especially in the lower part of the riser, this effect is noticeable.

The liquid velocities at two different heights in the riser and the downcomer for the investigated volume flow rates are shown in Figure 7-7. At a height of 0.2 m, the velocity profiles in the downcomer are flat and are nearly the same for all three flow-rates. Surprisingly, the integral averaged velocity for case 6 and case 8 along this measuring line are both almost exactly -0.2 m/s; this is nearly the exact value obtained for both cases at the height of 0.6 m in the downcomer. For case 4 a slightly lower averaged velocity of -0.18 m/s at y=0.2 m and y=0.6 m is obtained.

The similar results obtained in the riser at y = 0.2 m for all cases are due to a distinct bubble plume created by the circulating liquid that constricts the bubbles developed at the sparger. This bubble plume swings from one side to the other. An occasionally asymmetric stabilization at the internal walls of the bubble plume was observed.

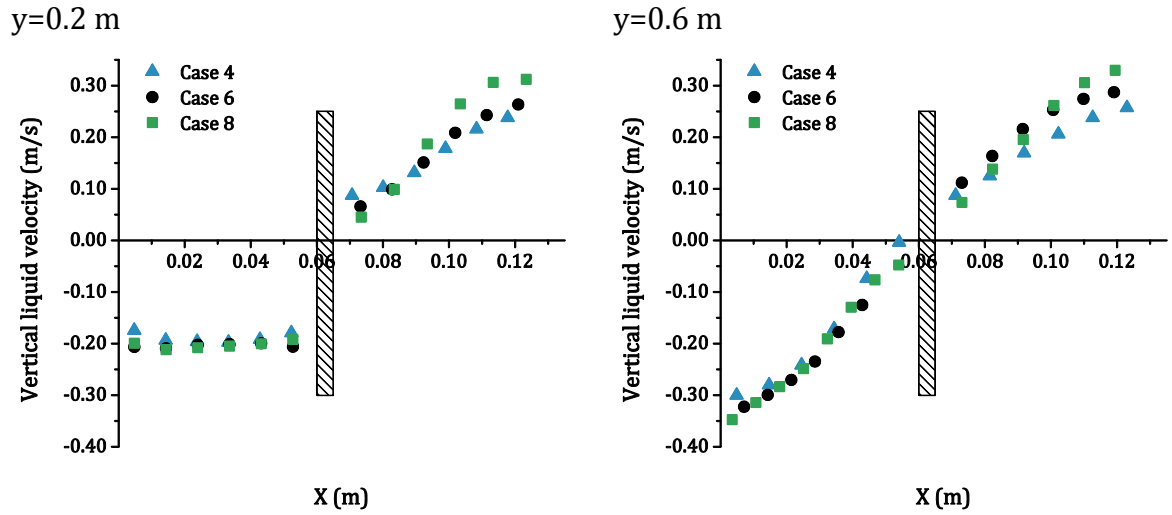

Figure 7-7 Liquid velocity profiles measured at two different heights.

The transient liquid velocity results in Figure 7-8 demonstrate the occasionally stabilization of the bubble plume at one side. From the transient results in the riser at a height y=0.2 m in the left quarter at x=0.09 m (upper plot), it is seen that the bubble plume is standing 40 seconds at the left wall before going to the right wall. However, between 60 s and 110 s a steady bubble plume swinging motion is not seen as well. Nevertheless, a steady swinging motion was dominant during the experiments. This motion is observed in all areas of the reactor as demonstrated in the lower transient vertical velocity plot, which was recorded in the downcomer, in Figure 7-8. Here, a more or less steady frequency over 120 s is observed.

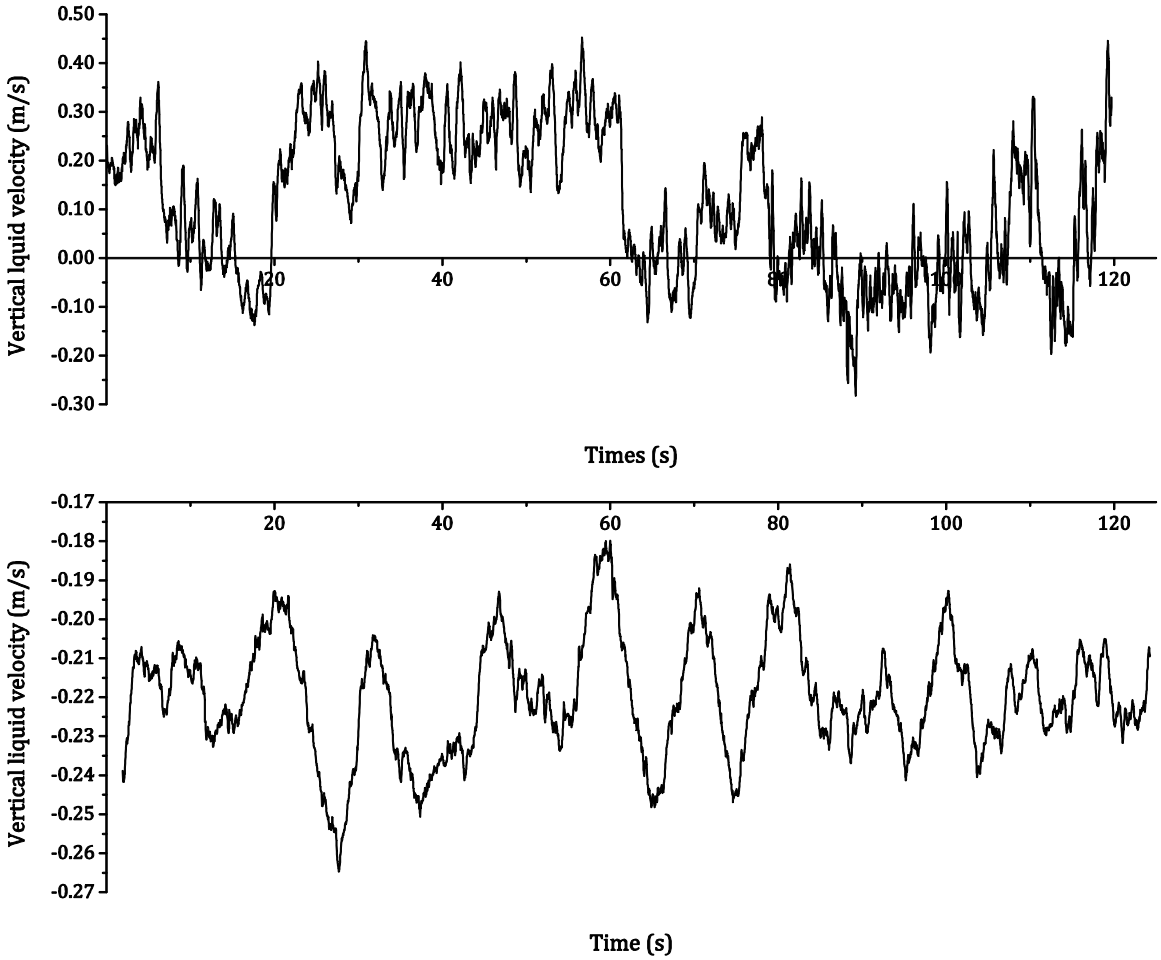

Figure 7-8 Vertical velocity over time at two different positions for case 6, the time scale is arbitrarily set to zero for both and is not synchronized. Top: The vertical velocity over time in the left quarter of the riser at $x = 0.095$ m and $y = 0.2$ m; every measuring point is moving averaged over 0.08 s. Bottom: The vertical velocity over time in the center of the left downcomer at $x = 0.03$ m and $y = 0.6$ m; every measuring point is moving averaged over 2 s.

The behavior of a standing bubble plume at one side of the riser for a distinct quantity of time was observed for every case. The time that the bubble plume stood at one side seemed to be arbitrary in the range of several seconds to minutes. In addition, the switching between the situations of a permanently swinging motion to a standing one at one wall seemed to be arbitrary. Deviations between the four consecutively conducted

liquid velocity measurements, as discussed in the method section, were observed, particularly, in the bottom part of the riser.

A more continuous situation is obtained in the upper part of the column. The bubble plume is spreading towards the top. The results that are obtained from the single measurements are not deviating much. The same is found in the downcomer.

Noteworthy, the vertical liquid velocity in the downcomer at a height of $y = 0.6$ m is zero near the internal walls and distinctly negative towards the reactor walls. Consequently, a large standing vortex in this region is observed; the liquid in the top clearance is forced to the side because of the driving force of the bubbles in the riser. Reaching the reactor wall the liquid is pulled downward in the downcomer. From visual observations, bubbles are dragged in the downcomer by the same mechanism. However, many bubbles that are pulled in the downcomer at the reactor walls migrate to the internal walls and rise up at them because of a lower vertical liquid velocity there. This lower vertical liquid velocity at the internal walls was observed along the complete downcomer and can be still observed at y=0.2 m for all volume flow rates.

Despite the averaged liquid velocities are similar for all investigated cases, the normal components of the Reynolds stress tensor $u'u'$ and $v'v'$ shown in Figure 7-9 are very different among the volume flow rates. In general, an increasing of $u'u'$ and $v'v'$ with increasing gas volume flow rate is seen. Looking at the bottom of the riser at a height of $y = 0.2$ m, the v'v' graphs show clear maxima located beside the center for all cases. Such maxima are consistent to previous measurements in the bubble plume regime (Section 3.4) (Simiano et al. 2006) (Mudde et al. 1997). In contrast, the $u'u'$ graphs show maxima in the center, which is also observed in the previously mentioned work.

Averaged over the cross section of the riser at $y = 0.2$ m, the $v'v'$ values are for all cases almost exactly twice as high as the $u'u'$ values. The averaged normal components of the Reynolds stress tensor along the centerline seem to increase linearly with the volume flow rate, for example for v'v' 0.01 m^2/s^2 from case 4 to case 6 and 0.011 m^2/s^2 from case 6 to case 8.

With increasing height $u'u'$ and $v'v'$ are decreasing in the riser as shown in Figure 7-9. The averaged $v'v'$ values, however, are remaining twice as high as the $u'u'$ values. Looking at the results obtained for case 8 distinct maxima are seen in the $u'u'$ and $v'v'$ graphs at $x = 0.095$ m. These maxima can be found in every measurement and are, therefore, no outlier. The origin of this effect is unknown.

Along the downcomer, $u'u'$ and $v'v'$ are decreasing, compared to the riser, the values in the downcomer are low. At a height of $y = 0.6$ m, the obtained profiles for case 4 and case 6 are, surprisingly, very similar. In contrast, for case 8 the values are distinctly higher. Nevertheless, the ratio between $u'u'$ and $v'v'$ is 1.5 for all cases, compared to a ratio of two in the riser. The turbulence intensity is almost zero at the bottom.

The cross component of the Reynolds stress tensor $u'v'$ is shown in Figure 7-10. Similar to the normal components, large values are obtained at a height of $y = 0.2$ m in the riser that are decreasing with increasing height. Although, the $u'v'$ values are similar for case 4 and case 6 at $y = 0.2$ m in the riser, the values for case 8 are distinctly larger.

In the downcomer at $y = 0.6$ m $u'v'$ is very similar for all cases. Parallel to the normal components, the $u'v'$ values are decreasing along the downcomer to almost zero.

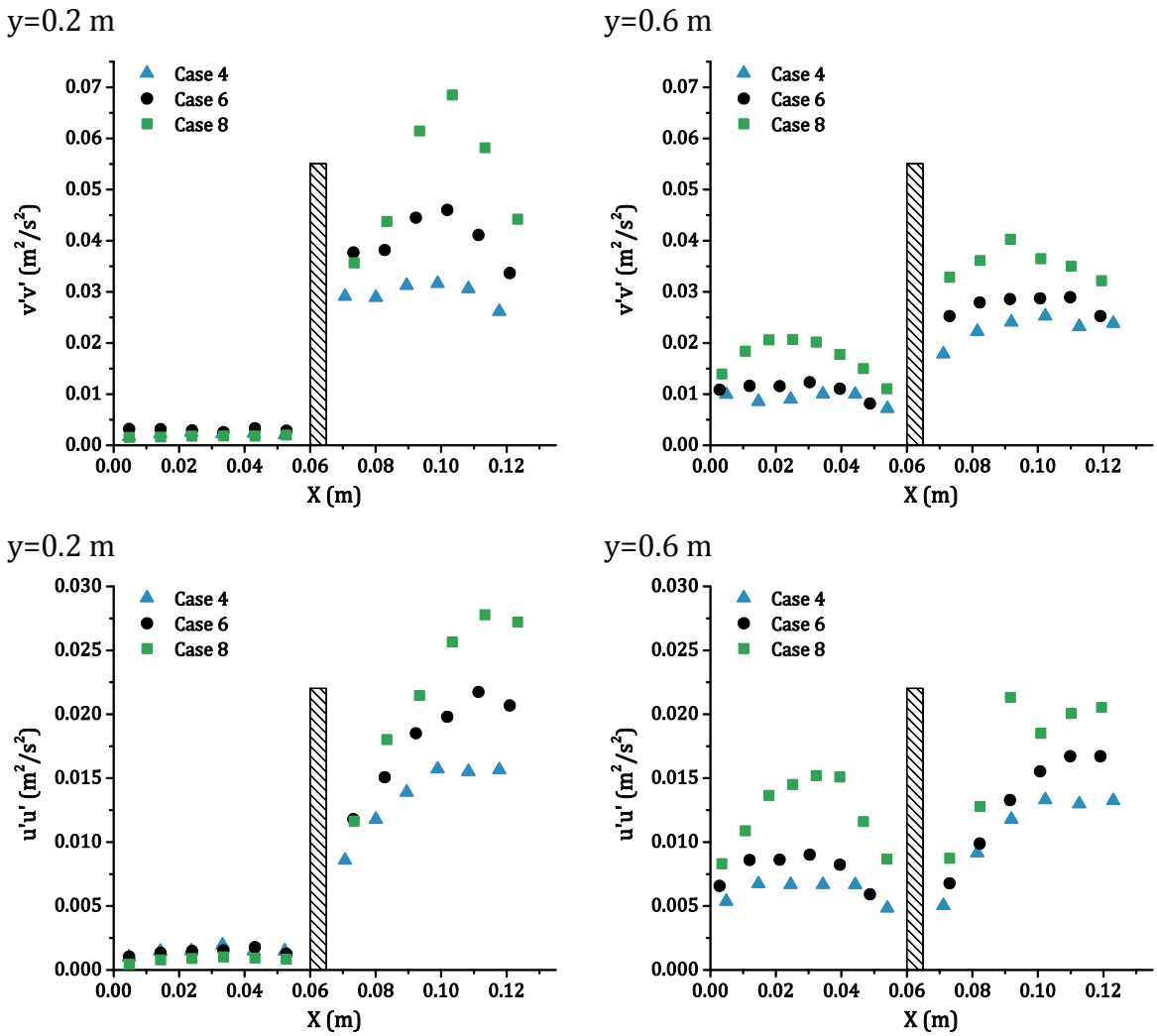

Figure 7-9 Normal Reynolds stresses in the vertical (v'v') and horizontal (u'u') direction at two different heights.

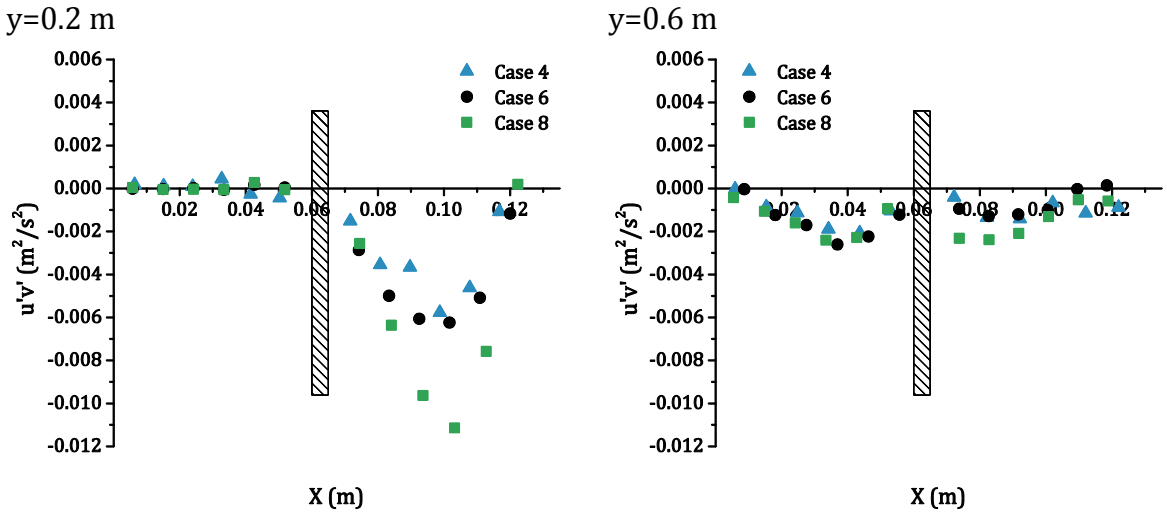

Figure 7-10 Cross Reynolds stress u'v' at two different heights.

7.2.3 Void fraction

The void fraction was determined inside the riser with a needle probe and along the downcomer by using videography. The void fraction that is measured with a needle probe is a local value. In contrast, the values that are obtained in the downcomer by using videography are the quantity of gas inside a specific measuring volume. The measuring volume is composed of the cross section of the downcomer (0.06 m width and 0.05 m depth) and a height of $\Delta y = 0.025$ m. The given values are placed in the middle of these volumes.

The void fraction results for the upper region of the riser and along the lower region of the downcomer are shown in Figure 7-11. The void fraction is measured only in the upper region of the riser in order not to disturb the bubble plume at the bottom. The void fraction inside the downcomer is determined only up to a height of 0.45 m because a flange is blocking the view. Above the flange the void fraction inside the vortex structure at the top of the internal walls, which is described above, was too high for reliable measurements with the videography method.

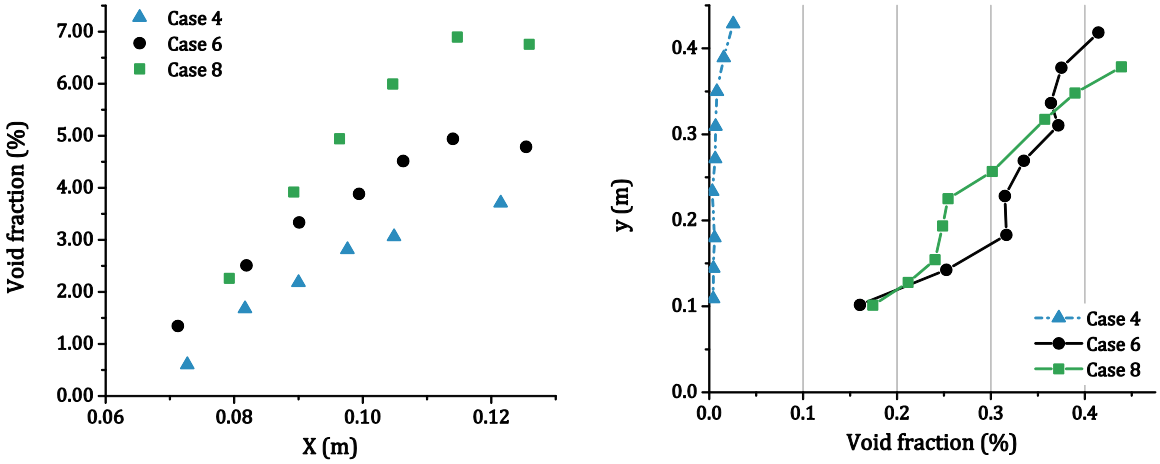

Figure 7-11 Void fraction in the riser at y = 0.6 m (left) and along the downcomer (right).

The void fraction inside the riser is increasing with the volume flow rate. A center peak is observed for all cases, with a maximum void fraction of around 7 % for case 8 at the center.

Along the downcomer, surprisingly, the profiles obtained for case 6 and case 8 are very similar. The void fraction is steadily decreasing with decreasing height in general. Moreover near the end of the internal walls (the bottom edge of the internal walls is at $y = 0.06\ m$) the void fraction is rapidly decreasing due to an increasing liquid velocity at this point. The rising bubbles in the riser pull the liquid from the downcomer into the riser and, therefore, also the bubbles from the downcomer.

The steadily decreasing void fraction along the downcomer in general is explained by the liquid velocity field. As a strong downward flow at the reactor wall is observed, a positive horizontal liquid velocity in the downcomer towards the internal walls occurs, as shown in Figure 7-12 a). Naturally, this horizontal velocity is decreasing along the downcomer, surprisingly, in the bottom region the strongest horizontal velocity is seen for case 4 whereas it is for case 8 almost zero. This behavior might be due to the higher void fraction and/or larger bubble sizes for case 6 and case 8. Nevertheless, a liquid

velocity that pushes the bubbles towards the internal walls is observed in the downcomer in general.

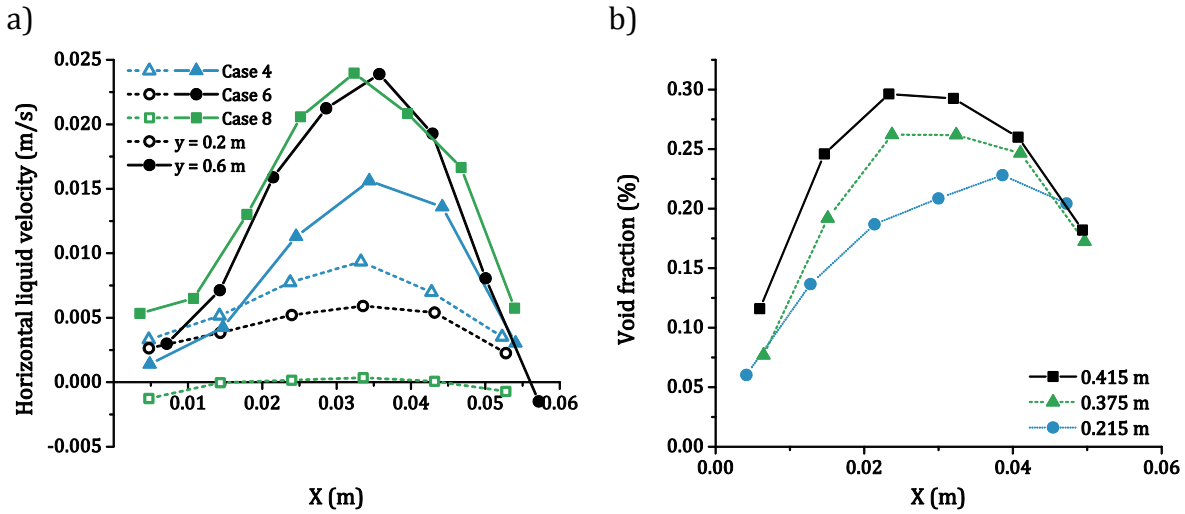

Figure 7-12 Flow situation in the downcomer. a) Horizontal liquid velocity at two different heights, b) void fraction profiles for case 6 at three different heights.

The bubbles are pulled into the downcomer near the reactor wall so that the void fraction profile in the upper part of the downcomer at y = 0.415 m has a peak near the reactor walls at x = 0.02 m, as shown in Figure 7-12 b). Below this measuring position at y = 0.375 m the void fraction near the reactor wall is distinctly smaller but towards the internal walls almost the same. This indicates a migration of the bubbles away from the reactor wall to the internal walls where a lower downward liquid velocity is observed so that the bubbles rise up (see Figure 7-7). Nevertheless, the peak is still near x = 0.02 m. Looking at the void fraction profile further downstream at y = 0.215 m, the gas void fraction at the internal walls is still at the same level, further the maximum gas fraction is seen near the internal walls at x = 0.04 m. Thus, more and more bubbles had moved to the internal walls and risen up.

7.3 CFD Simulations

The URANS baseline setup as discussed in Section 2.5 and in Section 4 is used to simulate the hydrodynamics in the investigated airlift reactor. For this purpose, four bubble size classes with their own velocity field were used. The volume weighted bubble size distribution was used to distribute the gas volume on the single bubbles classes at the inlet. Since coalescence and break up might be negligible, the bubble size distribution is fixed. The inlet conditions are summarized in Table 7-2.

The gas volume flow rate of the bubble classes 1 and 2 is very small at the inlet, thus they are negligible in the riser but are important in the downcomer. The bubble class 1 contains all bubbles $d_B < 3\ mm$, bubble class 2: $3\ mm \leq d_B < 4.5\ mm$. These two bubble classes are chosen somewhat arbitrary by evaluating the occurring bubble sizes in the downcomer from the experiment. Bubble class 3 was chosen to cover the remaining bubble diameters up to 5.83 mm, which is the zero of the Tomiyama lift force coefficient. Bubble class 4 includes the remaining from that diameter.

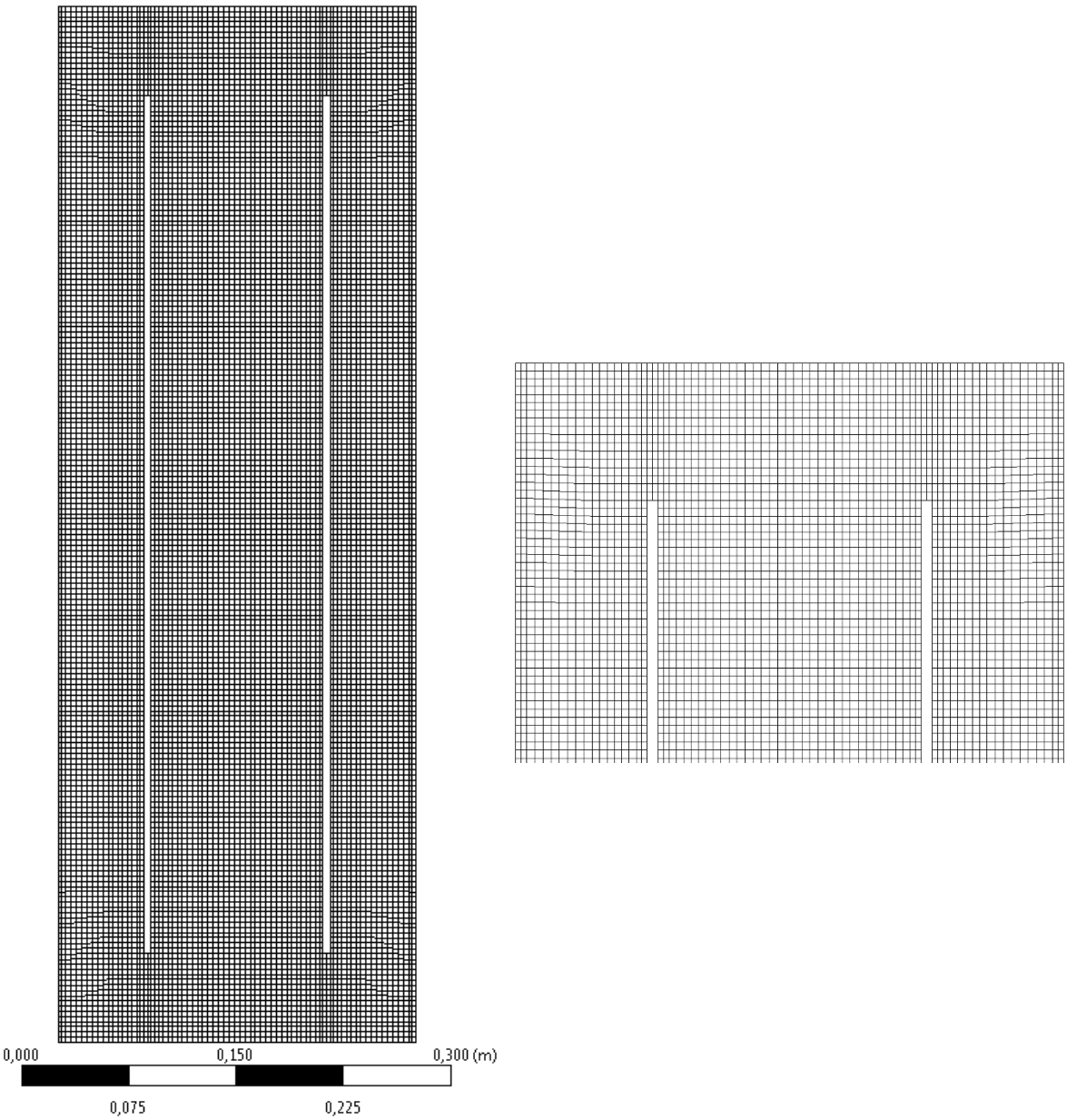

Figure 7-13 The complete computational mesh and a magnification of the top region.

	Bubble class	Sauter diameter [mm]	Void fraction [-]
Case 4	1	2.15	0.0085
	2	3.85	0.0263
	3	5.37	0.1321
	4	7.50	0.8331
Case 6	1	2.24	0.0120
	2	3.79	0.0226
	3	5.38	0.1325
	4	7.63	0.8329
Case 8	1	2.30	0.0145
	2	3.87	0.0312
	3	5.32	0.1623
	4	7.59	0.7920

Table 7-2 Inlet conditions.

The computational domain is the complete airlift reactor in three dimensions as shown in Figure 7-1. A structured mesh was used as shown in Figure 7-13. After a mesh study, the base mesh size was chosen to 3.75 mm, cells at the wall were refined to 1.875 mm. In addition, above and below the internal walls the mesh was locally refined to cover large gradients at these points. Since the top clearance was held constant in the experiments, the same mesh was used for all cases. The internal walls are treated in the same way as the reactor wall, namely, no-slip condition for the liquid phase and slip condition for the gas phase are applied.

7.3.1 Results

After a problem time of 400 seconds the simulations had converged by using the local integral convergence criteria described in Section 4.1, although the symmetric convergence criteria is not fulfilled. Thus, an asymmetric flow behavior for all cases is obtained, which is demonstrated in Figure 7-14. The shown averaged vertical liquid velocity tends to the right-hand side internal wall for case 4 and case 6 and to the left-hand side internal wall for case 8. Indeed, this behavior of an asymmetric bubble plume was also observed in the experiments as described above.

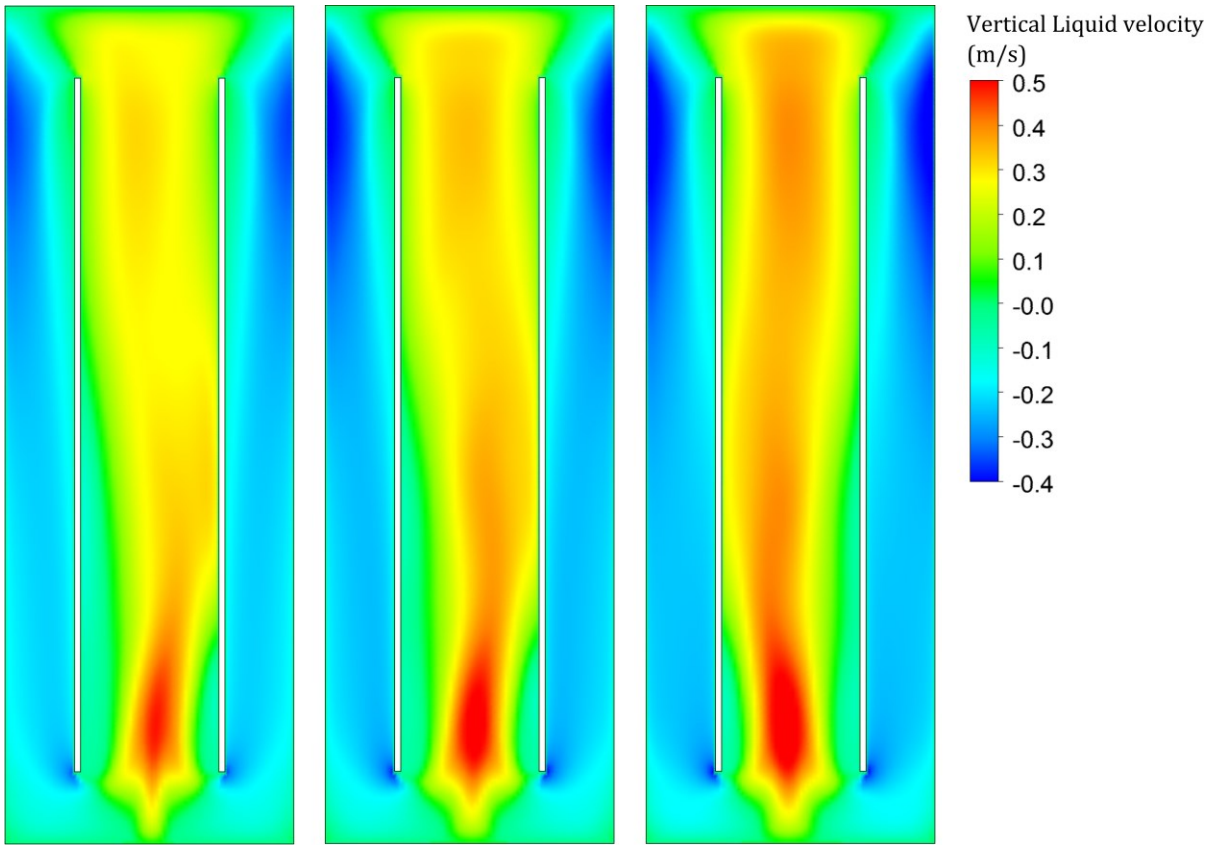

Figure 7-14 Asymmetric flow behavior in the airlift reactor. From left to right: Case 4, case 6, case 8.

If the bubble plume in the experiments shows a symmetric state, it is still swinging asymmetric rather than standing at one wall. In addition, the bubble plume often tends to restore a symmetric swinging motion, but the time of the asymmetric behavior was sometimes distinctly long; the liquid velocity measurements during these times were discarded. During the experiments, it was assumed that this asymmetric behavior was

due to not exactly placed internal walls or not exactly equal mass flow controllers; two mass flow controllers were used to control the gas volume flow rate of four needles of the eight used needles each. However, since the simulations show an equal behavior, at least three metastable conditions that contain the asymmetric bubble plume at each side and the symmetric bubble plume swinging might exist. A systematic error in the simulations is unlikely because a perfectly symmetrical regular mesh was used and the position where the plume stands is different for case 8 compared to case 4 and case 6. In addition, this behavior was seen in all cases of the mesh study. The bubble plume in the simulations is asymmetric swinging at one side and not steady standing, which is the same behavior as observed in the experiments.

Since the state when the bubble plume swings asymmetric was discarded in the experiments, a sampling bias might be the result because the symmetric state was actively chosen, especially in the lower part of the riser. Nevertheless, a comparison of the simulations with the experiments is meaningful because towards the top of the riser all quantities are more or less homogenized over the cross section. Moreover, the simulation results in the left and the right downcomer are almost equal, for all cases.

In Figure 7-15 the void fraction profiles are compared to the experimental data in the riser at y = 0.6 m. Still, an asymmetrical void fraction profile from the simulations is seen. Considering this, the simulation results are in agreement with the experimental results. However, for case 8 the void fraction profile is underpredicted in the center in general.

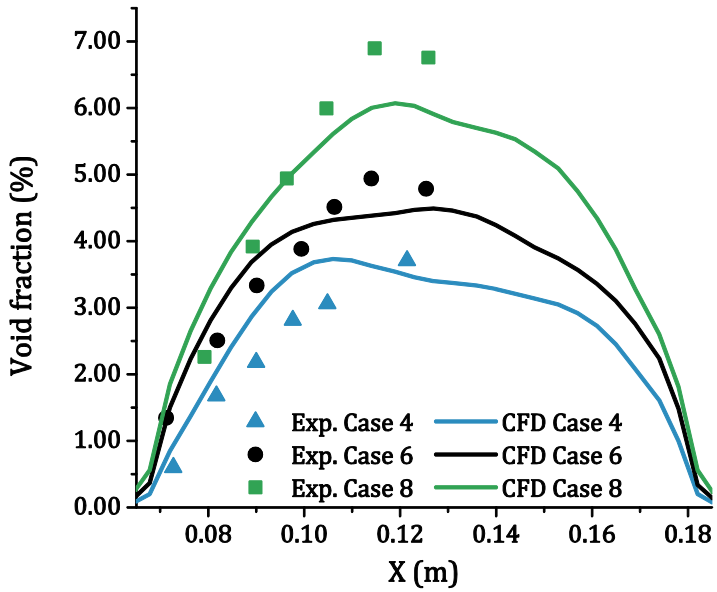

Figure 7-15 Void fraction at y = 0.6 m in the riser.

In Figure 7-16 the obtained liquid velocity and the normal components of the Reynolds stress tensor $u'u'$ and $v'v'$ are compared with the experiments. As expected, at the bottom of the riser at y = 0.2 m the liquid velocity profiles are asymmetrical, so a comparison with the experiments is difficult. At y = 0.6 m, the liquid velocity profiles are becoming symmetrical but all simulations over-predict the liquid velocity.

The obtained $v'v'$ profiles are more or less symmetrical in the riser at y = 0.2 m. For case 6 and case 8, the $v'v'$ profiles are in good agreement with the experimental data. The minima in the center as well as the maxima towards the inner walls are reproduced; the

heights of the maxima are almost equal compared to the experimental data whereas the positions of the maxima are slightly displaced. The $v'v'$ profile for case 4 is asymmetrical, so this result might be difficult to compare with the experiment; nevertheless, the quantity of the results is similar to the experiments in general. In the top region of the riser at y = 0.6 m, the simulations for case 6 and case 8 over-predict the $v'v'$ profiles. Case 4 is better reproduced quantitatively. Nevertheless, all simulation results show a distinct peak towards the internal walls that is only seen for case 8 in the experiments.

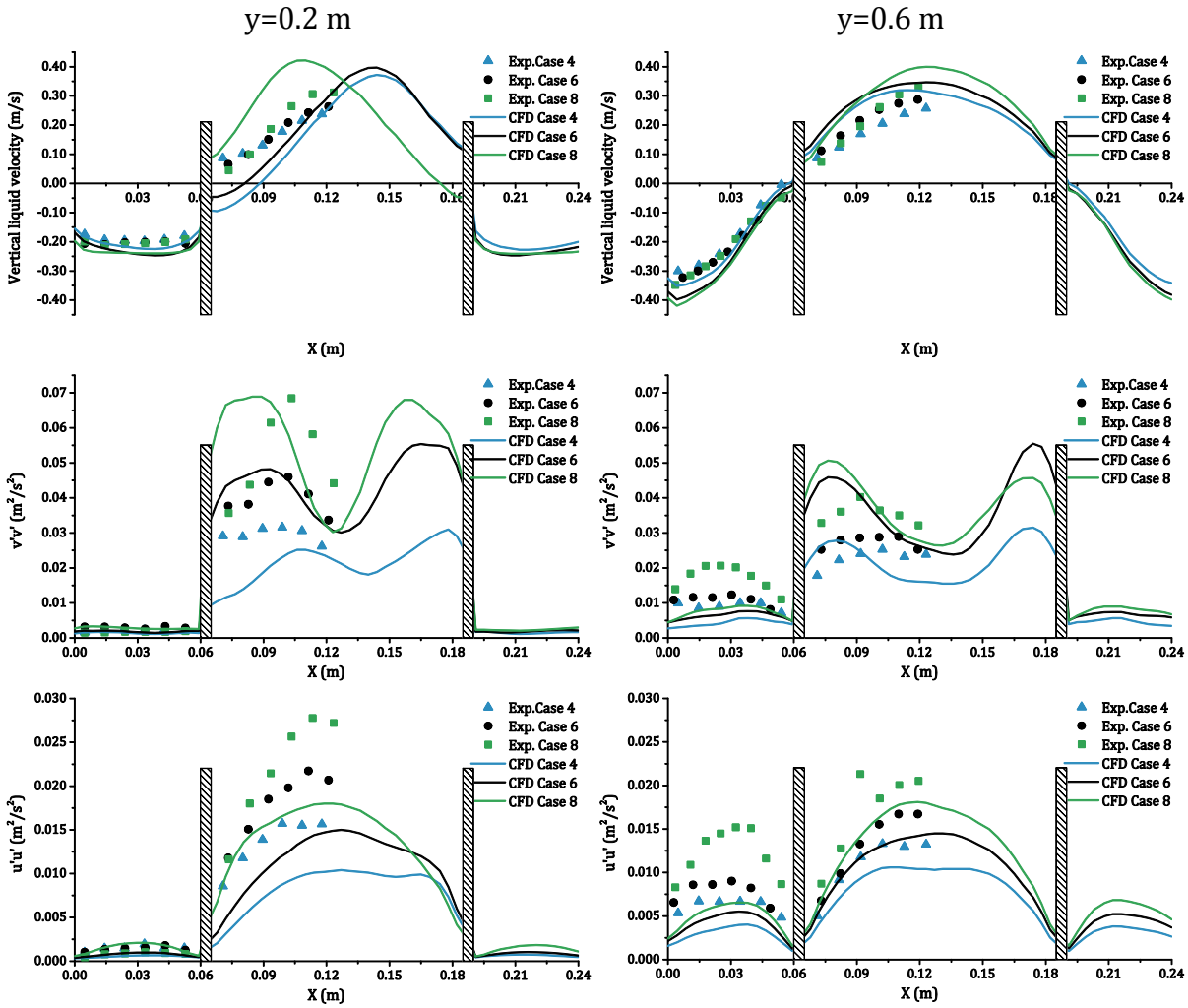

Figure 7-16 Liquid velocity and normal components of the Reynolds stress tensor v′v′ and u′u′ (u is the horizontal liquid velocity) at y = 0.2 m (left) and y = 0.6 m (right) with delineated internal walls.

The obtained u′u′ values at y = 0.2 m are consistently too small in the riser compared to the experiments for all cases. At y = 0.6 m, however, the simulations are, despite a slight underprediction, in agreement with the experimental data. In contrast to the experiments, the obtained u′u′ values are almost equal at y = 0.2 m and y = 0.6 m.

In the downcomer at y = 0.6 m, the u′u′ and v′v′ profiles are underpredicted in general. The decreasing turbulence intensity to almost zero at y = 0.2 m, however, is reproduced in the simulations.

The vertical liquid velocity is overpredicted in the downcomer at y = 0.6 m for case 6 and case 8. However, at y = 0.2 m the velocity obtained from the simulation is in agreement with the experiments and for all cases almost equal as in the experiment.

The resolved and unresolved contribution of the turbulence modelling to u′u′ and v′v′ are shown in Figure 7-17. In this context, the summation of the contributions gives the total value. In the riser, the double-peaked v′v′ profiles are produced by the resolved part at both heights; further, the resolved part is distinctly larger than the unresolved part. In contrast, the influence of the resolved part is minor for the u′u′ profiles at both heights. The same trend is found in the downcomer at y = 0.6 m, whereas the resolved and unresolved part for v′v′ are similar.

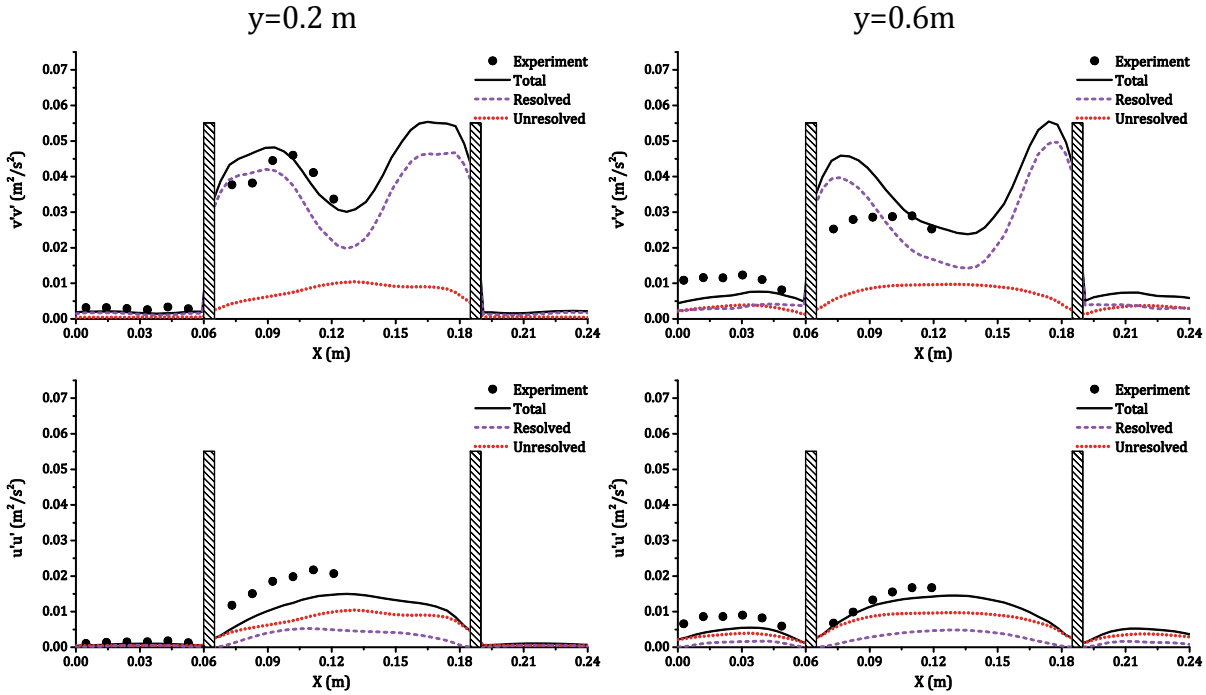

Figure 7-17 Resolved and unresolved normal components of the Reynolds stress tensor v′v′ and u′u′ (u is the horizontal liquid velocity) for case 6 at y = 0.2 m (left) and y = 0.6 m (right) with delineated internal walls.

The obtained gas void fraction along the downcomer is compared to the experiments in Figure 7-18. Despite of case 4, the qualitative behavior is not well reproduced by the simulations. In the experiments, the void fraction is slowly decreasing over the height, in the simulations the void fraction is rapidly falling from very large values to almost zero at the bottom of the downcomer. In addition, the void fraction profiles for case 6 and case 8 are not similar as observed in the experiments.

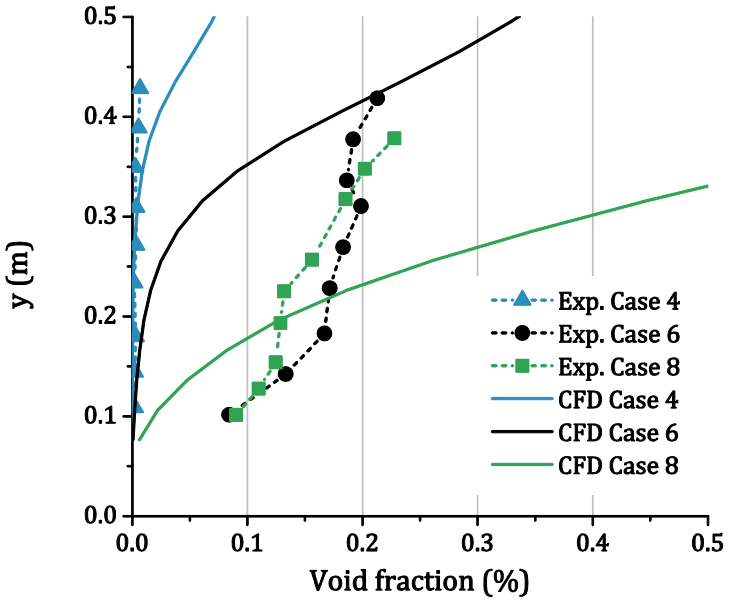

Figure 7-18 Void fraction along the downcomer.

The Sauter diameters are compared to the experiments in Figure 7-19. The Sauter diameters are determined by averaging the (fixed) bubble sizes of the four bubble classes with their void fraction by weight. Thus, the separation of the bubble classes along the downcomer is seen. For case 4, the simulation underpredicts the Sauter diameter in the upper region of the downcomer, since the void fraction becomes zero towards the bottom region no bubble size could be calculated for the simulation here. The experimental determined Sauter diameters for case 6 are well reproduced by the simulation; again, the void fraction becomes zero towards the bottom region. For case 8, the bubble sizes are distinctly underpredicted over the complete downcomer.

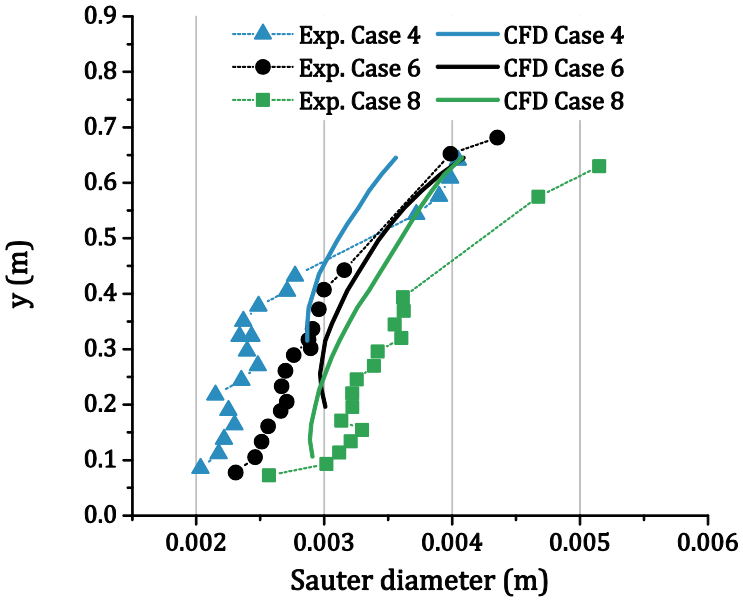

Figure 7-19 Bubble size seperation along the downcomer.

Despite the acceptable agreement of the Sauter diameter especially for case 6, the void fraction obtained from the simulations are distinctly different. Several reason can be identified; on the one hand, the discretization of the bubble size distribution might be too coarse, on the other hand horizontal liquid velocity in the downcomer over-predicted as shown in Figure 7-20. This higher velocity pushes the bubbles towards the internal walls where they can rise up in the downcomer as discussed below (as well as discussed above in the experimental section). Consequently, a rapid decrease of the void fraction along the downcomer occurs as shown in Figure 7-20 on the right hand side.

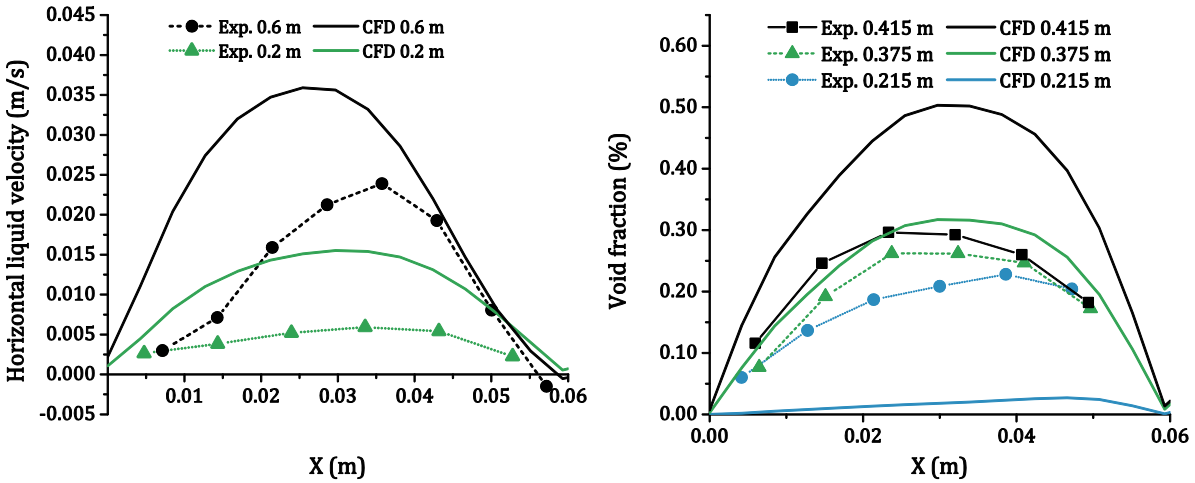

Figure 7-20 Horizontal liquid velocity and gas void fraction in the downcomer compared to experiments for case 6.

The Situation of the gas phase in the downcomer is shown in Figure 7-21 for case 6. A strong vortex at the top of the downcomer is observed in the simulations as is seen from the two dimensional gas fraction profile. In this, the bubbles are pulled deeper into the downcomer but a majority is already rising up and leaving the downcomer, which is also observed in the experiments. The positions where bubbles rise up are seen in the gas velocity profile, the red color indicate a positive (upward) gas velocity. The bubbles clearly rise up at the internal walls of the downcomer where they are pushed by the liquid velocity. The liquid velocity at $y = 0.415$ m is shown in the vector plot in which a large vortex structure directed towards the internal walls is seen. This structure is propelled by the bubbles themselves as seen in the horizontal slip velocity plot. The positive (directed to the internal walls) horizontal slip velocity means that a positive bubble force acts. From the baseline model, this force is the summation of the lift and turbulent dispersion force, in which the lift force might be dominating.

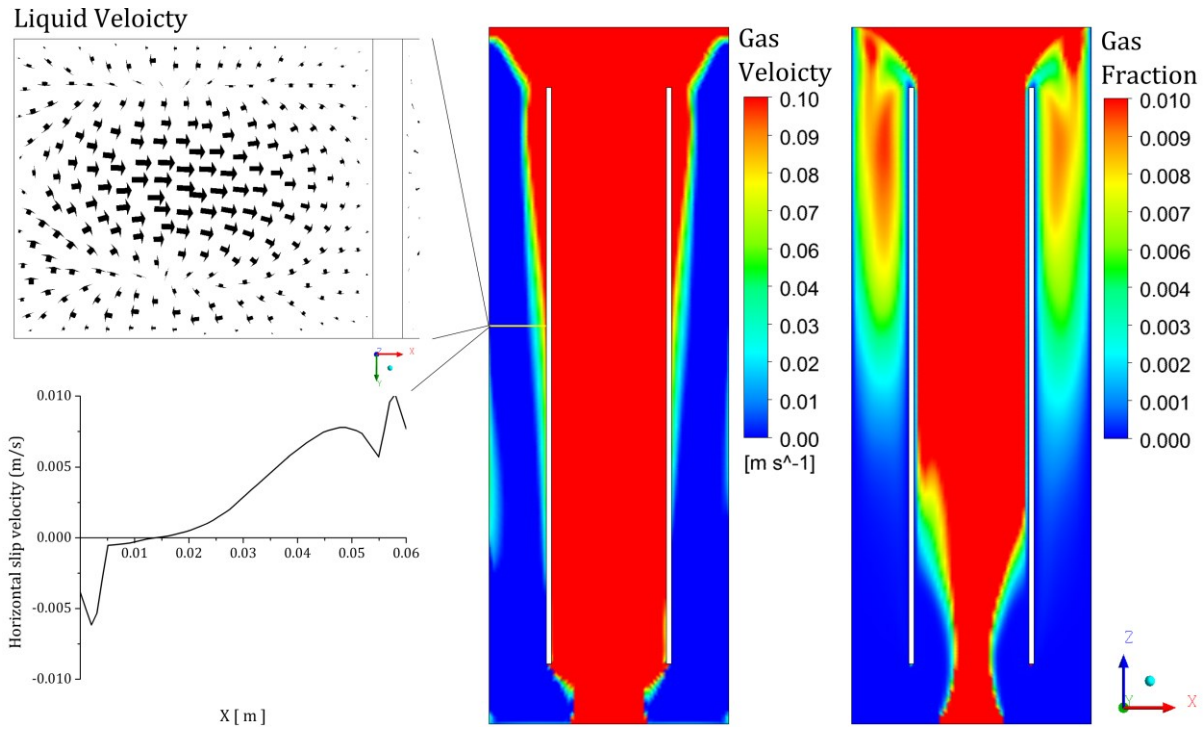

Figure 7-21 Flow situation of the gas phase in the downcomer for case 6. From right to left: The gas void fraction and the gas velocity in the center plane; the liquid velocity vectors from the aerial view in the downcomer at $y = 0.415$ m, the horizontal slip velocity in the downcomer at $y = 0.415$ m. All shown values are time averaged.

Consequently, the situation in the downcomer is very complex and not only the drag force regulate the void fraction in the downcomer. The void fraction here might be very sensitive to the bubble size since the coefficient of the lift force, which propels the horizontal flow in the downcomer, strongly depends on it. Moreover, the turbulent dispersion force might be important since bubbles that rise up lead to a gradient in the void fraction profile that the dispersion counteracts.

7.4 Conclusion

The experiments are situated in the regime of a constant velocity in the downcomer as described e.g. by van Benthum et al. (1999) or Law et al. (2013). Indeed, for case 6 and case 8 the mean velocity in the downcomer along the centerline is 0.2 m/s and for case 4 around 0.18 m/s. Therefore, case 4 might be at the beginning of this regime. The velocity profiles in the riser are similar for all cases.

Although similar velocity profiles obtained for the different flow rates, distinct differences are found for the normal and cross components of the Reynolds stress tensor, especially in the riser. The turbulence parameters might be a summation of larger scale structures induced by the swinging bubble plume and bubble induced turbulence phenomena. The CFD simulations reproduce the similar velocity profiles for the different flow rates as well as the different normal components of the Reynolds stress tensor. Although the vertical normal components are dominated by the resolved large-scale structures, the horizontal normal component is dominated by the unresolved part. Moreover, the influence of the resolved large-scale structures is smaller towards the top

region of the riser. In the downcomer, however, both parts are almost equal for both directions. The resolved structures as well as the unresolved part, which might be dominated by BIT, are important for the present setup. As discussed above, a steady state RANS model as well as a LES or RSM model without a proper BIT modeling might not be able to reproduce the experiments.

For all used sparger setups a distinct bubble plume is build up at the bottom of the riser so that a distinct swinging motion is observed. In the experiments, the bubble plume swings asymmetric on one side occasionally for an arbitrary time, but the swinging motion is restored in general. In the CFD simulations, however, this metastable state of an asymmetric bubble plume is overrated so that asymmetric time averaged results are obtained, especially in the bottom of the riser. The origin of this effect is unclear, as already discussed in Section 5. Moreover, asymmetric time averaged profiles can be observed in many work dealing with CFD simulations of bubble plumes, e.g. (Masood & Delgado 2014) and (Pourtousi et al. 2015).

A large vortex structure is seen at the top of the downcomer so that bubbles are pulled in the downcomer at the reactor wall. Due to a horizontal liquid velocity, these bubbles move to the internal wall where they can rise up because the vertical velocity is smaller there. Both effects are well reproduced by the CFD simulations; from the simulations, the horizontal liquid velocity is accelerated by the lateral bubble movement due to lift and turbulent dispersion force. However, the resulting bubble movement to the internal walls might be overpredicted in the simulations, because the void fraction is rapidly decreasing along the downcomer, in contrast to a slow decreasing in the experiments. Since it is a complex phenomenon, the reasons for this deviation are manifold. One likely reason is a too coarse discretization of the bubble size distribution. In general, discrete bubble classes might be critical for such cases in which a bubble size separation takes place since locally very different bubble size distributions are seen in the experiment. At least, besides a mesh size and time step study, a study for the discretization of the bubble size distribution is needed. Another reason might be the missing consistency regarding clean and contaminated systems in the bubble forces. Indeed, the water used in the present experiment is reliably pure by using the naturally occurring micro bubbles as tracer for particle tracking instead of additional tracer particles.

8 Lift force measurements in very low Morton number systems and high bubble Reynolds number flows

Measuring the lift force on bubbles in a shear field is a very challenging task. Up to now, the only working measurement concept that allows the direct measurement of the lift force consists of a submerged rotating belt confined by walls (Kariyasaki 1987). The rotating belt drives the flow and produces a shear field between the belt and a wall. Tomiyama et al. (2002) used this experimental setup to measure the lift force on bubbles in water/glycerin systems. With these experiments, it was shown that the lift force coefficient changes it sign with increasing bubble diameter, also a well-known empirical lift force correlation was obtained. Moreover, such experiments were repeated by Dijkhuizen et al. (2010b) for polluted systems, in which a distinctly shear rate dependency of the lift force was observed. Nevertheless, all experiments are conducted in fluids with a large Morton number of around $Mo > 10^{-5}$, which results in a very low bubble Reynolds number in the rage of 10^1 and laminar flow conditions. In contrast, bubbly flows are often investigated in air/water like systems having a very low Morton number of $Mo = 2.63 \times 10^{-11}$ with bubble Reynolds numbers in the range of 10^3 and, additionally, with a turbulent background flow. Therefore, determining the lift force in such systems is highly desirable. Nevertheless, the change of sign of the lift force for large bubbles in air/water systems was already shown by Lucas & Tomiyama (2011) by using a large database of bubbly pipe flow experiments.

In the following section, a measuring concept is developed for measuring the lift force in systems with a very low Morton number. The focus during the present work was on the development of the new techniques and assembling the experimental setup. Nevertheless, preliminary results are shown at which the measurement concept is demonstrated.

8.1 Experimental setup

Measuring the lift force in low viscosity systems like water under turbulent conditions poses some problems. Moreover, using a belt to produce a shear field is connected to several extra problems. In the first place, the moving of the belt generates abrasion debris that pollutes the measurement system (Dijkhuizen et al. 2010b). Furthermore, producing a linear shear field with a moving belt in low viscosity systems over a necessary wide channel under turbulent conditions might be hardly possible.

Another serious problem is that bubbles in turbulent low Morton number systems rise in a non-straight motion so that a clear direction of movement cannot be seen. In addition, the turbulent background distributes the bubbles over the channel, which has to be separated from the migration induced by a lift force.

In the present work, a suitable shear flow is produced with an uneven aerated bubbly flow, as shown in Figure 8-1, to overcome the problems that arise by using belts in low viscosity systems. A circulation flow is induced by aerating the bubble column at one side with large bubbles. Particularly, a linear shear field in a large vortex over a wider range is obtained in the center. The lift force is determined for single bubbles generated at the other side of the bubble column. They are pulled into the vortex where they experience

the shear field. Here, the lift force is determined by investigating the movement of the single bubbles in the vortex structure.

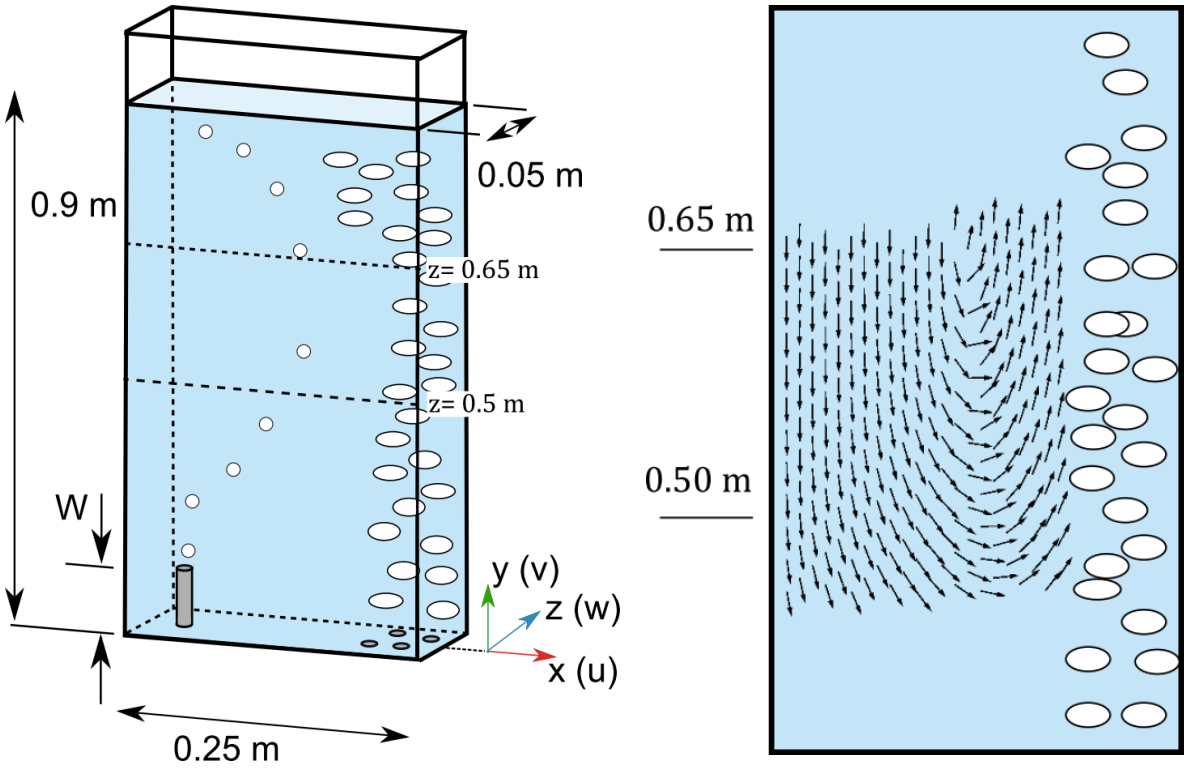

Figure 8-1 Setup to determine the lift force coefficient with the measuring area delineated form $z = 0.5\,m$ to $z = 0.65\,m$ (left) and the flow structure from PIV measurements (right).

Nevertheless, the bubbles still rise up in an arbitrary swinging motion overlaying the lateral migration. To determine this migration clearly, time averaged three dimensional void fraction distributions are determined. For this purpose, the rising bubbles are photographed from the front and the side view. The three dimensional shape and position of the bubbles are calculated from these two projections. Afterwards, the reconstructed bubble is transferred to a grid discretizing the used bubble column. A representative gas void fraction at one grid point is obtained by counting the times when gas is present at this point. Assuming that the swinging rising motion of the bubbles is truly random, the time averaged bubble trace is calculated by connecting the maxima of the void fraction in the horizontal planes along the vertical Axis.

Furthermore, assuming that the turbulent dispersion force is symmetrical along the obtained bubble trace, in particular that no turbophoresis effects occur, the bubble force balance along the trace reads

$$0 = \overline{\boldsymbol{F}}_{Buoyancy} + \overline{\boldsymbol{F}}_{VirtualMass} + \overline{\boldsymbol{F}}_{Drag} + \overline{\boldsymbol{F}}_{Lift} \ . \tag{8-1}$$

The wall force in the x and z direction is neglected, moreover, the wall force is assumed to be symmetrical in the y direction along the trace. The bar over the forces indicates that the time-averaged forces fulfill this balance.

The time average of the buoyancy force and virtual mass force are trivial since all quantities are constant for the present setup over time and statistically independent,

respectively. Nevertheless, to calculate the time average values of the other forces some assumptions have to be made. The time average is calculated by using the ensemble average $\langle\cdot\rangle$

$$\begin{aligned}\overline{\boldsymbol{F}}_{Drag} = \langle \boldsymbol{F}_{Drag} \rangle &= \frac{3}{4d_B}\rho_l \langle C_D |\vec{u}_G - \vec{u}_L|(\vec{u}_G - \vec{u}_L)\rangle \\ &= \frac{3}{4d_B}\rho_l C_D \, |\langle\vec{u}_G\rangle - \langle\vec{u}_L\rangle| \, (\langle\vec{u}_G\rangle - \langle\vec{u}_L\rangle) \, .\end{aligned} \tag{8-2}$$

The last equal sign is only valid if C_D , $|\vec{u}_G - \vec{u}_L|$ and $(\vec{u}_G - \vec{u}_L)_i$ are statistically independent. In particular, this can be interpreted that the drag force is statistically independent of the flow condition. During the further procedure, this will be assumed.

Looking at the averaged lift force similar problems arise

$$\begin{aligned}\overline{\boldsymbol{F}}_{Lift} = \langle \boldsymbol{F}_{Lift} \rangle &= -\rho_l \langle C_L(\vec{u}_G - \vec{u}_L) \times rot(\vec{u}_L)\rangle \\ &= -\rho_l C_L(\langle\vec{u}_G\rangle - \langle\vec{u}_L\rangle) \times rot(\langle\vec{u}_L\rangle) \, .\end{aligned} \tag{8-3}$$

Again, it is assumed that C_L and $(\vec{u}_G - \vec{u}_L) \times rot(\vec{u}_L)$ are statistically independent during one measurement. This might be fulfilled since the flow conditions are less changing during the same experiment due to a low turbulence level as will be discussed below. In addition, it is assumed that the slip velocity of the bubble is independent from the liquid velocity shear field ($(\vec{u}_G - \vec{u}_L)$ and $rot(\vec{u}_L)$), which was shown valid by Dijkhuizen et al. (2010b) using DNS.

From these simplifications, the velocity field of the liquid and gas phase can be determined separately. In addition, since only single bubbles are generated at the left side of the bubble column (Figure 8-1) it is assumed that these single bubbles do not influence the time averaged liquid velocity field. This assumption was found to be valid by comparing velocity profiles obtained with and without the generated small bubbles. Therefore, the liquid velocity is measured only once without the single bubbles in the test section.

As will be discussed below the liquid velocity is measured with particle image velocimetry (PIV), therefore the separation of the liquid and gas velocity is necessary because the lift force experiments cannot be executed with PIV tracer particles since they contaminate the bubble surface. This, in turn, implies the assumption that the generated flow by the large bubbles on the right hand side is not influenced by the tracer particles.

After the liquid and gas velocity fields are determined, the lift force can be directly calculated by using the force balance in Equation (8-1). In particular, only the horizontal vector component is used for the calculation because the vertical direction is superimposed with the relatively strong buoyancy force.

The direct calculation is an improvement compared to the method that is usually used estimating the bubble velocity by calculating the derivation of the bubble trajectory in vertical direction (Tomiyama 2002) (Bothe et al. 2006) (Dijkhuizen et al. 2010b). The disadvantageous of such a method is that a bubble trajectory has to be smoothly reconstructed to obtain a reliable derivation. Especially if an arbitrary movement is superimposed on the rising bubble, this reconstruction is difficult and not well defined.

The entire bubble column is divided in five measuring areas in which the three-dimensional void fraction is determined and three areas in which the velocity is measured with PIV. However, only the results from a height of 0.5 m to 0.65 m including

two void measuring areas and one PIV area will be used for the lift force calculations. Three different gas volume flow rates for the large bubbles, which drive the flow, are used to generate different shear fields. The lift force is evaluated for several bubble sizes that are generated by using eight different single needles. The experimental inlet conditions are summarized in Table 8-1. The used drilled out needle is different compared to the other needles, which are described in Section 3.1. A flat needle with 1.5 mm inner diameter is drilled out to a cone that flares to 3 mm diameter.

Needle inner diameter	Volume flow rate Bubble diameter	Driving volume flow rate
0.2 mm	1 ml/min 2.22 mm	800 ml/min - -
0.3 mm	3 ml/min 2.25 mm	800 ml/min 1000 ml/min -
0.5 mm	6 ml/min 2.76 mm	800 ml/min - -
0.6 mm	10 ml/min 2.95 mm	800 ml/min 1000 ml/min -
0.7 mm	10 ml/min 3.16 mm	800 ml/min - -
0.9 mm	10 ml/min 3.77 mm	800 ml/min 1000 ml/min 1200 ml/min
1.5 mm	13 ml/min 6.17 mm	- 1000 ml/min -
Drilled out 3 mm	10 ml/min 4.34 mm	800 ml/min 1000 ml/min -

Table 8-1 Experimental conditions of the lift force experiments.

8.2 Methods

8.2.1 3D-Videometry

Approaches to determine the three dimensional void fraction with videometry are well known and are used in various fields ranging from 3D particle tracking (Pereira et al. 2006) to 3D bubble identification with stereo cameras (Murai et al. 2001). Two synchronized cameras are used and the bubble is reconstructed from the projected front view of the bubble. The side view is used to position the recorded bubbles on the y-axis. The bubble is reconstructed to three dimensions by defining an ellipse with the major and minor axis from the front view of the bubble.

For the present setup, the identification of the bubbles in the side view is problematic because the bubbles from the driving bubble plume interfere the view on the single bubbles. To overcome this problem the driving bubble plume is not illuminated by the backlight as shown in Figure 8-2.

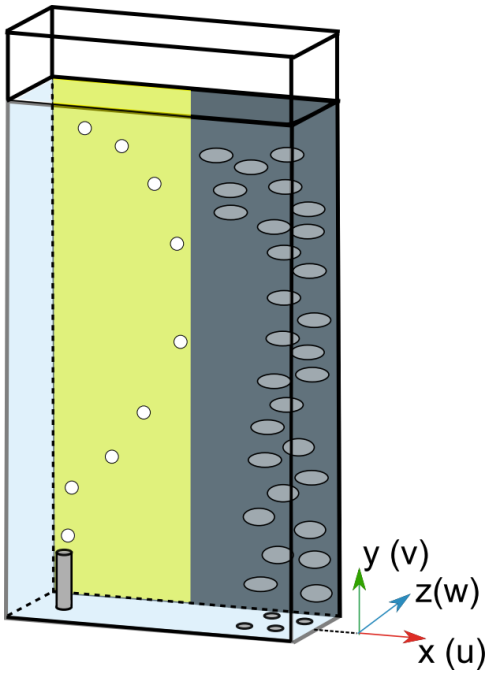

Figure 8-2 Back illumination (yellow) of the experimental setup.

Nevertheless, the driving bubble plume is not completely dark since at least one side is always open and scattered light illuminates the bubbles. The single bubbles that are directly illuminated by the backlight, however, are reflecting the light very bright on the backlight facing bubble tip as shown in Figure 8-3. This reflection is used to identify the bubbles in the side view.

The position of the bubble in the side view is not directly accessible since only the left tip is seen. Here, the position is determined by adding half the length of the major axis (d_M in Figure 8-4), which is determined from the front view, to the left illuminated tip as shown in Figure 8-4. This procedure is reasonable since the obtained void fraction profiles in y-direction are symmetrical with a peak in the center (not shown).

After determining the position of the bubble, an ellipse defined by the minor and major axis from the front view is discretized to a three dimensional grid of the measuring area. If a grid point is inside the ellipse, the value of the grid point is increased by one. This is repeated for every bubble. Over time, a three dimensional representation of the void fraction in the bubble column is obtained. The recording time for every measuring area for all used needle sizes was 15 minutes, resulting in 100 000 up to 400 000 recorded bubbles for the 1.5 mm and the 0.3 mm inner diameter needle, respectively. The gird size on which the bubbles are discretized is chosen to 0.1 mm.

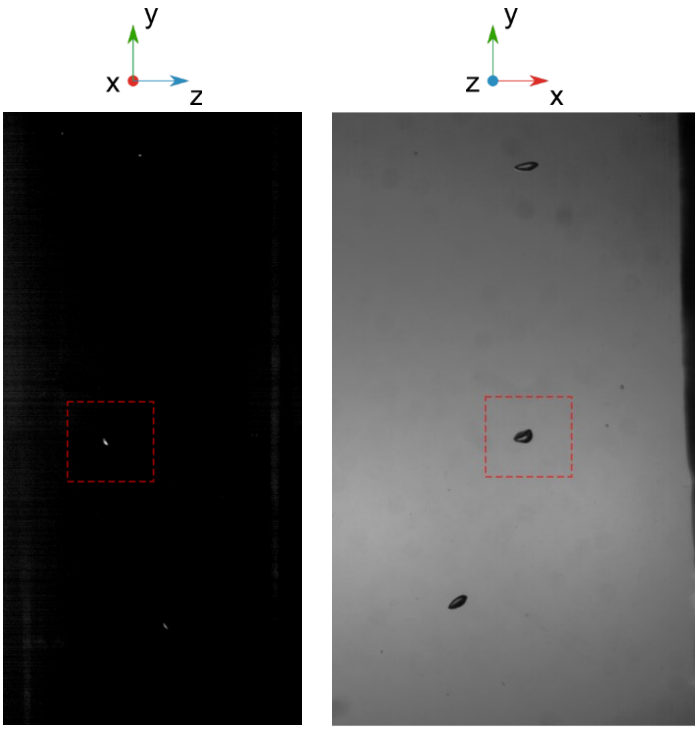

Figure 8-3 Side view (left), which is illuminated from left, and front view (right), which is illuminated from the back. The red rectangles mark the same bubble and edge the pictures used in Figure 8-4.

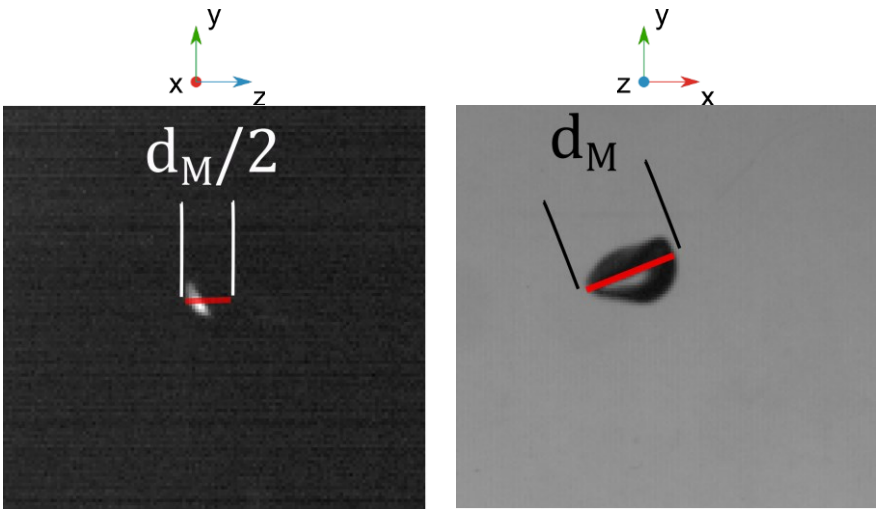

Figure 8-4 Determining the position of the bubble in the side view (left) by adding half of the major axis d_M determined from the front view (right) to the left tip.

8.2.2 Averaged bubble trace and spline interpolation

After a representative three dimensional void fraction function on a grid is determined, the averaged bubble trace is calculated. For this purpose, the maximum of the representative void fraction function for every horizontal plane on the grid is calculated by determining the local minima of the absolute value of the derivative. To find the correct local minima of the derivation, the neighborhood is defined as a region with a sufficient count of bubbles. Particularly, if not enough bubbles are in the neighborhood of a grid point, the derivation is not calculated. Moreover, the void fraction function is smoothed for this purpose by using a constant convolution function with a size

of 3x3x3 mm. The determined maxima in the void fraction function are shown in Figure 8-5 on the left hand side. Indeed, a simplification was done for further calculation by reducing the calculation area to a two dimensional cut through the center as shown in Figure 8-5. This simplification reduced the amount of used grid points from 10^9 to 10^6. This, however, implies the assumption that the bubble path is situated in the center of the bubble column which was found to be reasonable.

As mentioned above, the experimental setup was divided in five measuring sections and only two sections were used to evaluate the lift force coefficient. The border of the sections is at $y = 0.6\ m$; the void fraction function is averaged in the overlapping region. In Figure 8-5 the 0.6 m line is delineated with a straight dashed line and the overlapping region is marked with a red arrow.

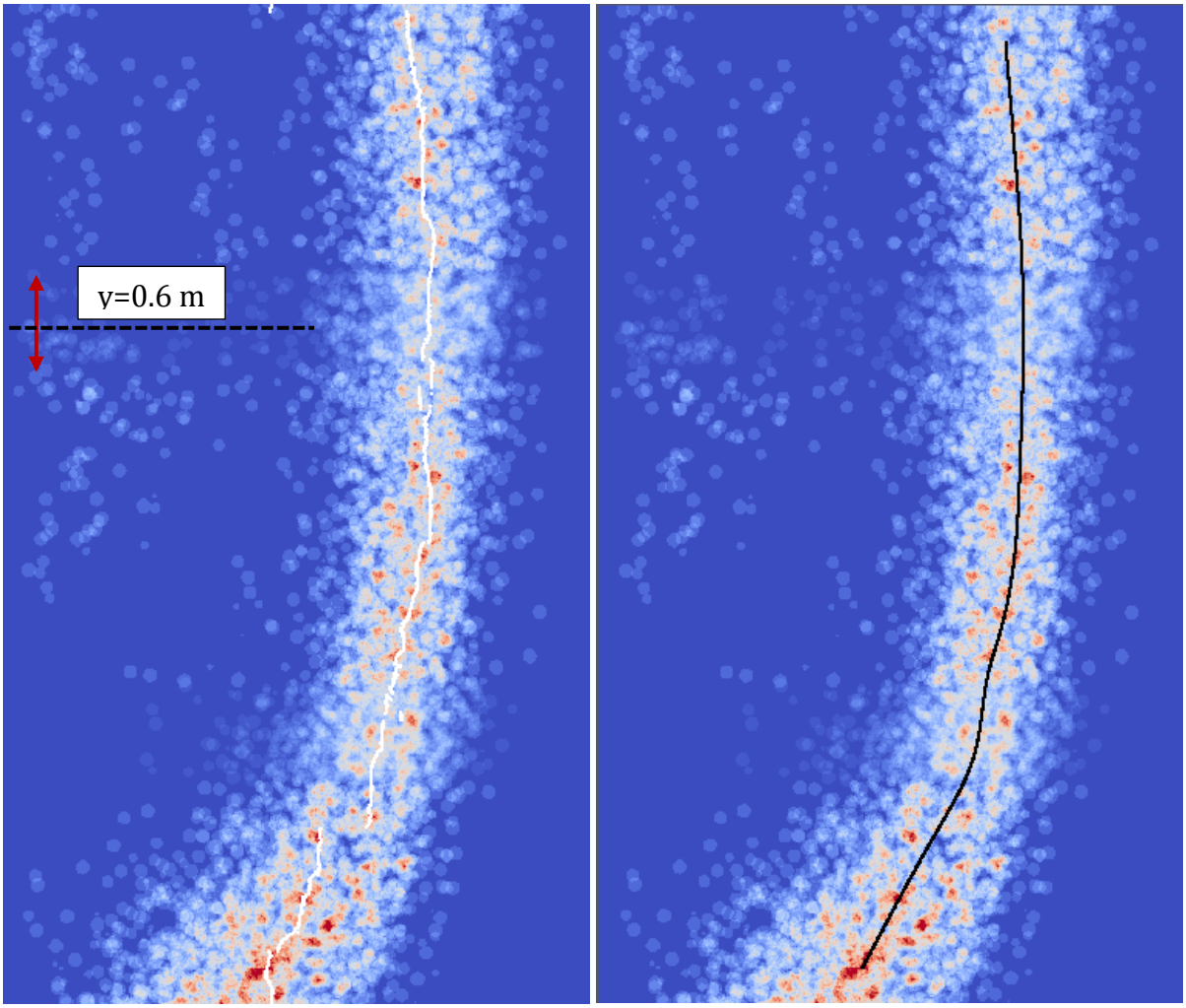

Figure 8-5 The void fraction function on a two dimensional cut in the center between z = 0.4 m and z = 0.7 m for the drilled out needle and 800 ml/min driving volume flow rate. The color from red to blue indicates the void fraction function from high to low values, respectively. The left picture shows the determined local maxima and the right picture the spline that is taken as bubble trace.

In general, a discontinuous trace is obtained if the determined maxima in the void fraction function are connected along the vertical axis. To get a continuous and sufficiently smooth trace, a B-Spline curve is determined with the algorithm proposed by Liu et al. (2005). The algorithm is simplified by introducing a minimum energy criterion,

in which the second order derivation of the B-Spline is minimized. The performance of the B-Spline approximation is demonstrated in Figure 8-5 on the right hand side.

It should be noted that in fact a great effort was done to reconstruct the bubble trace with B-Spline functions in a way that the first derivation is meaningful to compare the present method with the method used in previous work. Promisingly, by minimizing the energy represented by the second derivation of the B-Spline, very good results were obtained. Nevertheless, calculating the lift force directly with the velocity of the gas phase is much more reliable compared to using the angle of the bubble trace as done in previous work for single bubble trajectories. Especially, the horizontal bubble velocity is very small compared to the vertical velocity so that small deviations or uncertainties have a big effect on the first derivation. In addition, the method that uses the first derivation includes the assumption of a simple shear flow without a gradient in vertical direction, which is not fulfilled in the present setup satisfactorily.

8.2.3 Liquid phase velocity

The liquid velocity is determined with PIV. The velocity is measured once using only the driving flow. The different generated shear rates $\partial v_z/\partial x$ are around 2.45 1/s for 800 ml/min, around 2.65 1/s for 1000 ml/min and around 2.9 1/s for 1200 ml/min.

The averaged velocity field that is generated by the 800 ml/min flow is shown simplified in Figure 8-6. Clearly, the shear field ranging from the left wall at x = 0 m to the driving flow at the right wall, which is situated between x = 0.2 m and x = 0.25 m, is seen. The measuring window shows the lower part of the vortex created along the bubble column. The size of the vortex can be adjusted by the water level of the bubble column, which was preliminary optimized with CFD simulations.

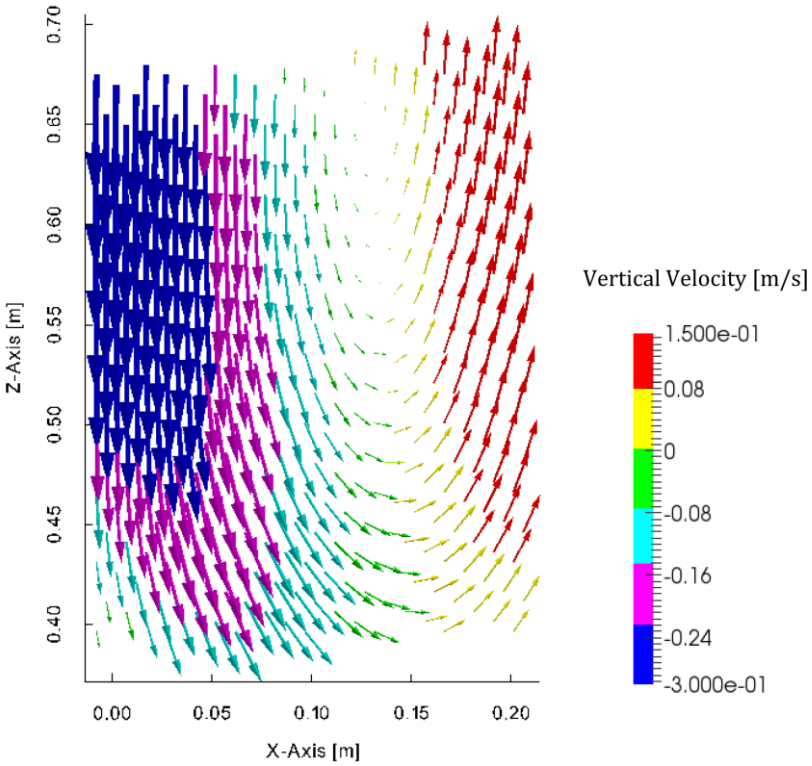

Figure 8-6 Liquid velocity field determined with PIV for 800 ml/min. The left reactor wall is at x = 0 m, the driving flow at the right wall is between x = 0.2 m and x = 0.25 m.

The normal components of the Reynolds stress tensor $u'u'$ and $v'v'$ are shown in Figure 8-7. From the two dimensional distribution for 800 ml/min gas volume flow rate it is seen that larger values are present in the downflow region. Moreover, the $v'v'$ values are high at the left wall and near the driving bubble plume on the right-hand side; in these regions, however, no bubble trajectories are obtained. The values are increasing with increasing gas volume flow rate, which drives the flow.

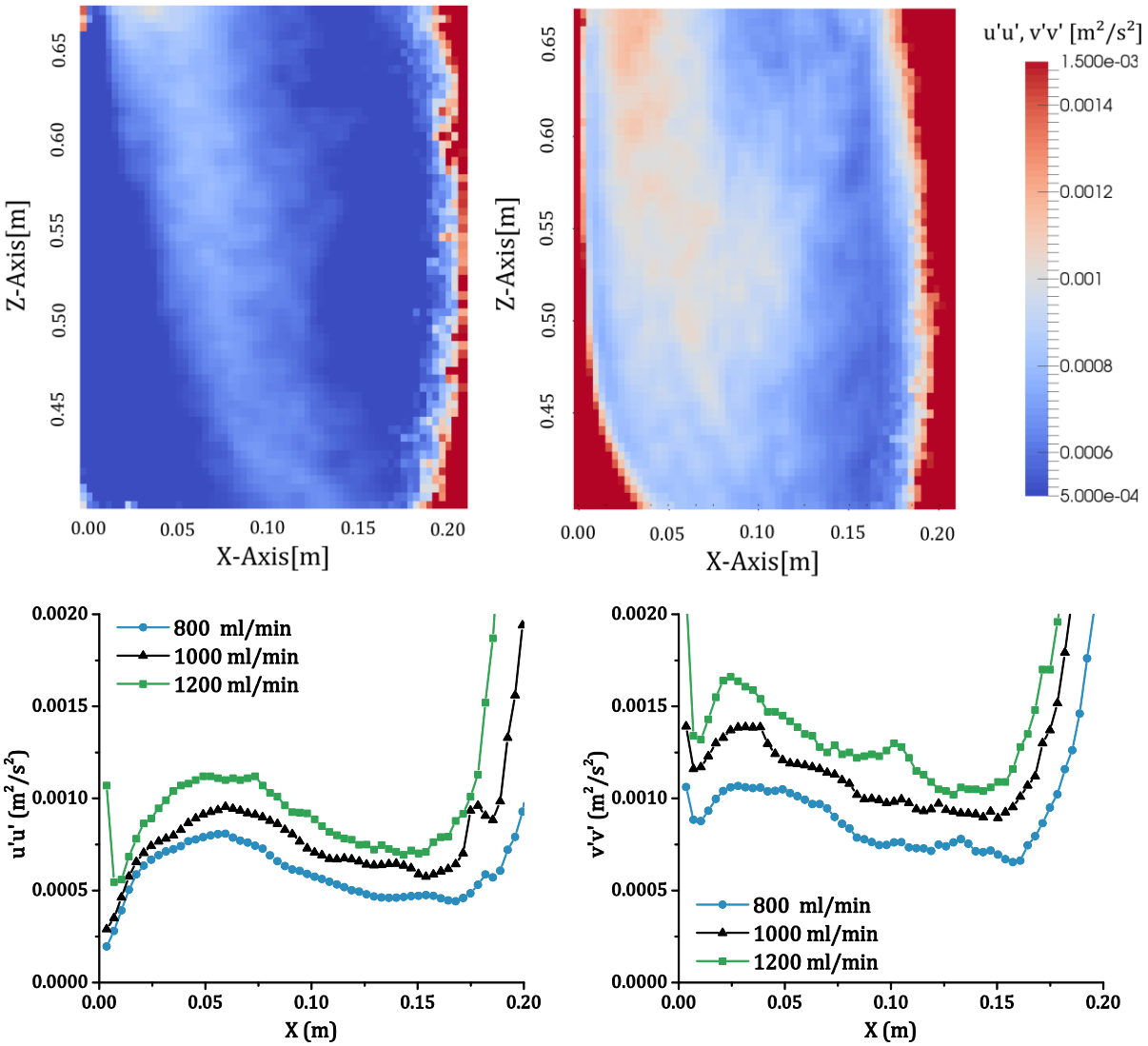

Figure 8-7 Normal components of the Reynolds stress tensor u′u′ and v′v′. Top: Two dimensional distribution of u′u′ (left) and v′v′ (right) for 800 ml/min gas volume flow rate. Bottom: Profile at y=0.6 m for all gas volume flow rates.

In the vortex, the vertical velocity is almost constant over height as demonstrated in Figure 8-8 on the left-hand side for the 800 ml/min case. The shear rate $\partial v_z/\partial x$ is also almost constant over height in the measuring section between x = 0.1 m and x = 0.15 m. The horizontal velocity, however, is changing over height because of the round shape of the generated vortex, which is not avoidable.

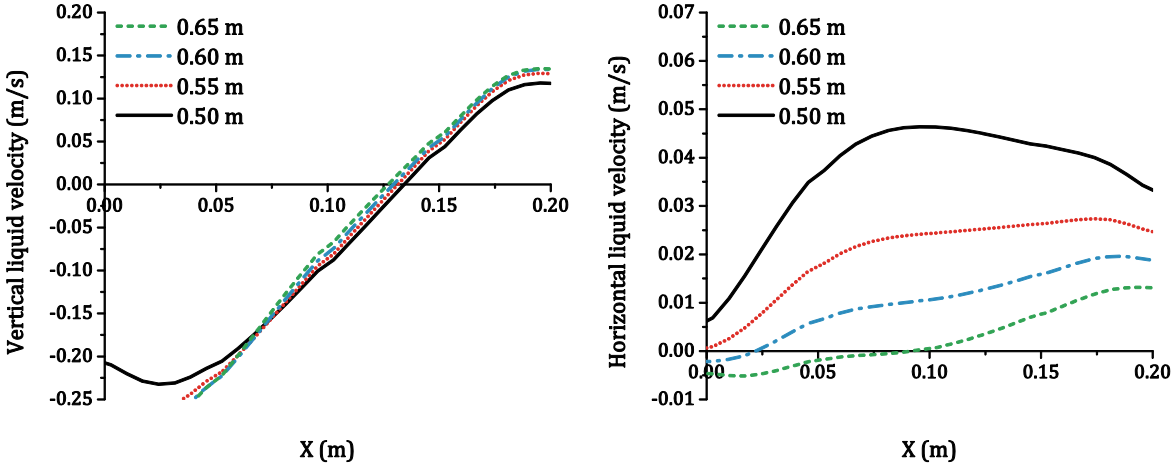

Figure 8-8 Vertical and horizontal liquid velocity along the x-axis for different heights generated by the 800 ml/min driving flow. Left the vertical velocity and right the horizontal velocity.

The bubble traces for the different bubble sizes are not the same. Thus, the different bubble sizes run through the vortex on different paths and, therefore, experience a slightly other flow field of the vortex each. The velocities and shear rates along the traces over height for the 0.3 mm inner diameter needle (2.25 mm bubble size) and the drilled out needle (4.13 mm bubbles size) are shown in Figure 8-9.

Looking at the vertical velocity, the smaller bubbles experience a higher negative velocity compared to the larger bubbles because the smaller bubbles are situated more left in the vortex. Indeed, the bubble trace has a parabolic shape as indicated in Figure 8-5 so the vertical velocity is for both bubble sizes not constant over height. Furthermore, the vortex is slightly inclined what is seen by the shifting of the zero of the vertical velocity with increasing height in Figure 8-8. The experienced shear rate $\partial v/\partial x$ is slightly different for the different bubble sizes as shown in Figure 8-9. The shear rate $\partial v/\partial z$ (not shown) is very small for both traces and constant over height.

Looking at the horizontal velocity, the experienced velocity and largest shear rate $\partial v/\partial x$ component is almost equal for both traces as well as the shear rate $\partial u/\partial z$ (not shown).

8.2.4 Bubble Size and gas phase velocity

The bubble sizes as well as the major and minor axis are determined from the front view by using edge-detecting algorithms as described in Section 3.2. Tomiyama et al. (2002) formulated an empirical lift force coefficient as a function of the maximum axis of the bubble perpendicular to the flow, in the following this is stated as major axis or is denoted with $\perp$. This axis, however, is in general not known, so the empirical correlation by Wellek et al. (1966) is used

$$\frac{d_{Major}}{d_{Minor}} = 1 + 0.163Eo^{0.757} \quad , \tag{8-4}$$

$$d_{Major} = d_B \sqrt[3]{1 + 0.163Eo^{0.757}} \quad , \tag{8-5}$$

with d_B the spherical equivalent diameter.

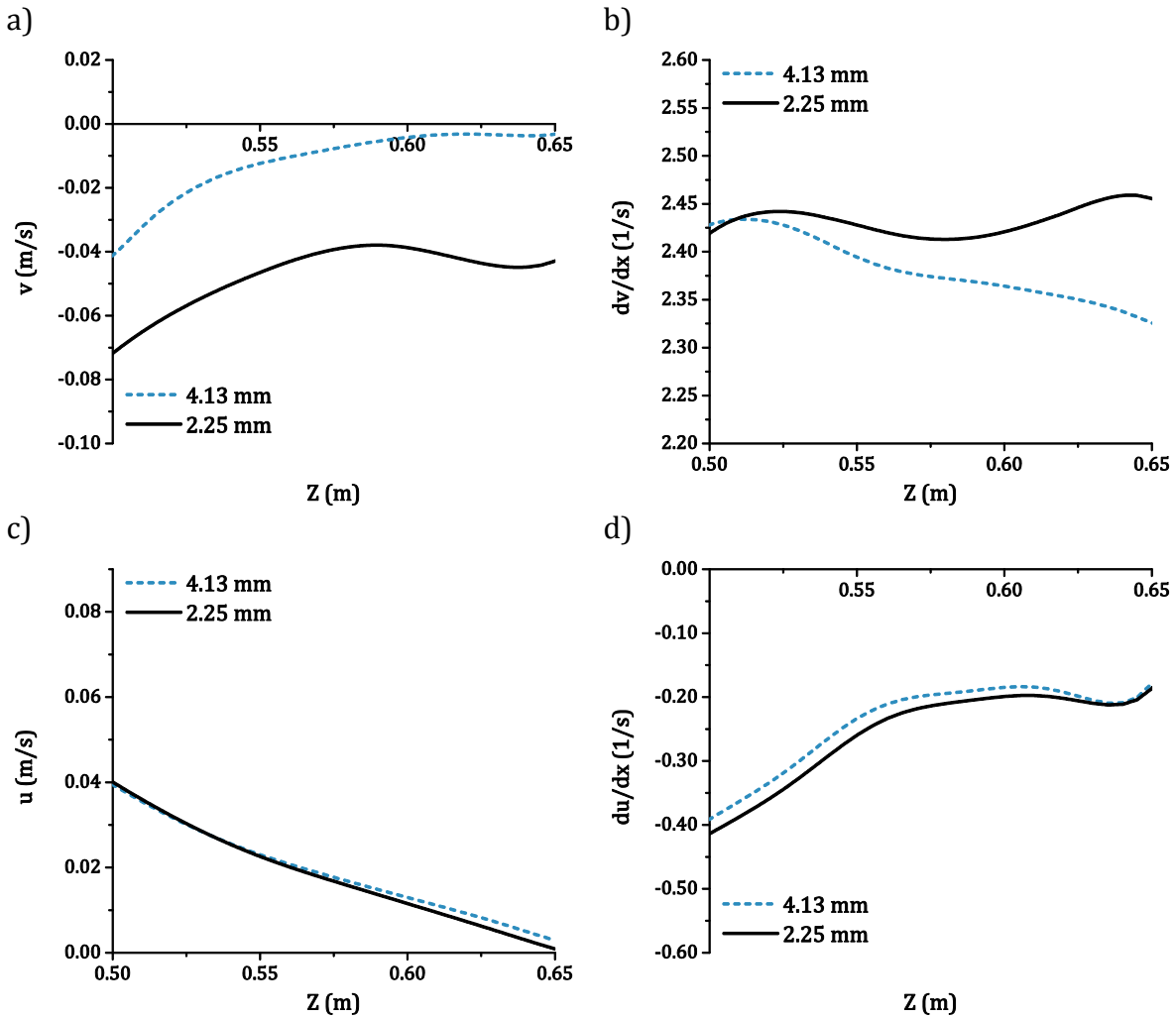

Figure 8-9 Fluid velocities along two bubble traces over height for 800 ml/min driving flow.

The empirical Wellek correlation, however, is derived for fully contaminated flow without a turbulent background flow. The results from the lift force experiments are compared to the Wellek correlation in Figure 8-10. The ratio of major to minor axis is clearly underpredicted by the correlation; the bubbles have a stronger ellipsoid shape.

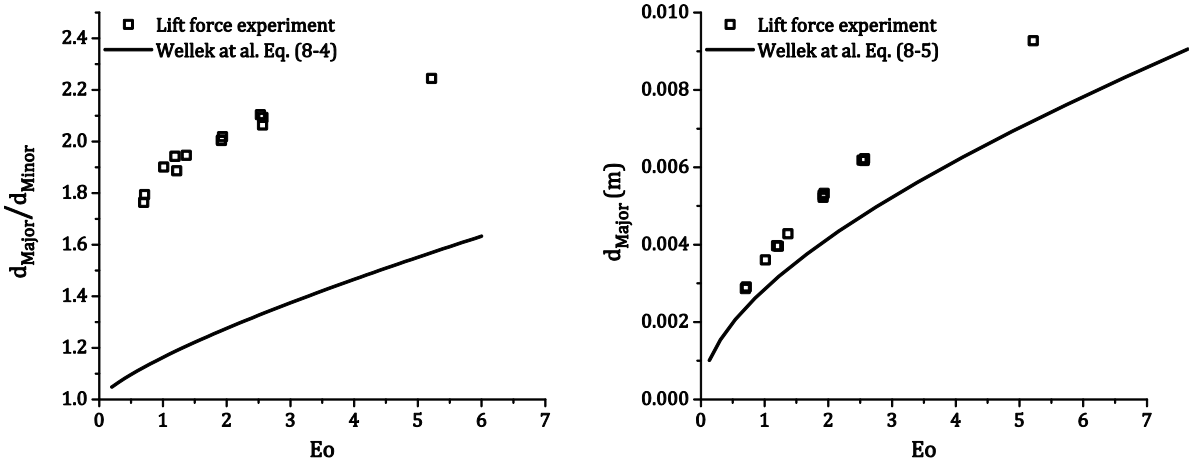

Figure 8-10 Comparison of the empirical Wellek correlation with the results in air/water with turbulent background flow.

The bubbles from different experiments are shown in Figure 8-11. The shape of small bubbles is clearly ellipsoidal in contrast to the Wellek correlation, which predicts an almost spherical shape with $d_{Major} \approx d_{Minor}$. A significant difference among the different driving gas volume flow rates was not observed.

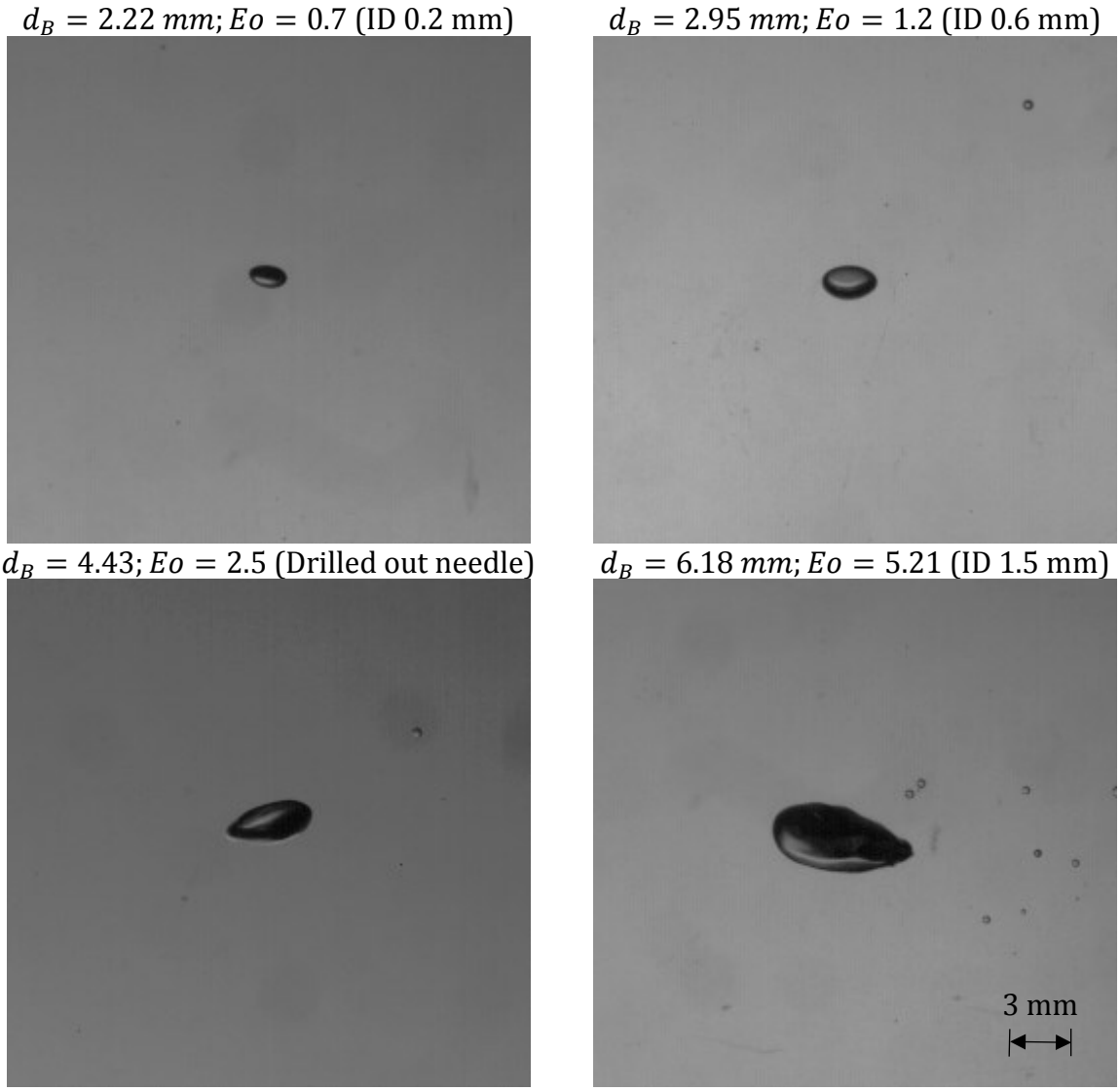

Figure 8-11 Different bubble sizes in the lift force experiment (All pictures have the same scale).

The number density functions of the determined spherical equivalent bubble diameter and the major axis are plotted in Figure 8-12 for 0.8 l/min driving gas flow rate. The used bubble sizes are averaged along the single bubble tracks. The density functions are discretized with 0.25 mm. Except for the 1.5 mm needle, the generated bubbles have a low variance in the range of 0.25 mm.

The density function of the large 6.18 mm bubbles generated by the 1.5 mm needle is clearly asymmetric for both values. In the experiments, it was observed that the bubbles

sometimes break up in the shear field and sometimes the bubble generation at the needle was instable.

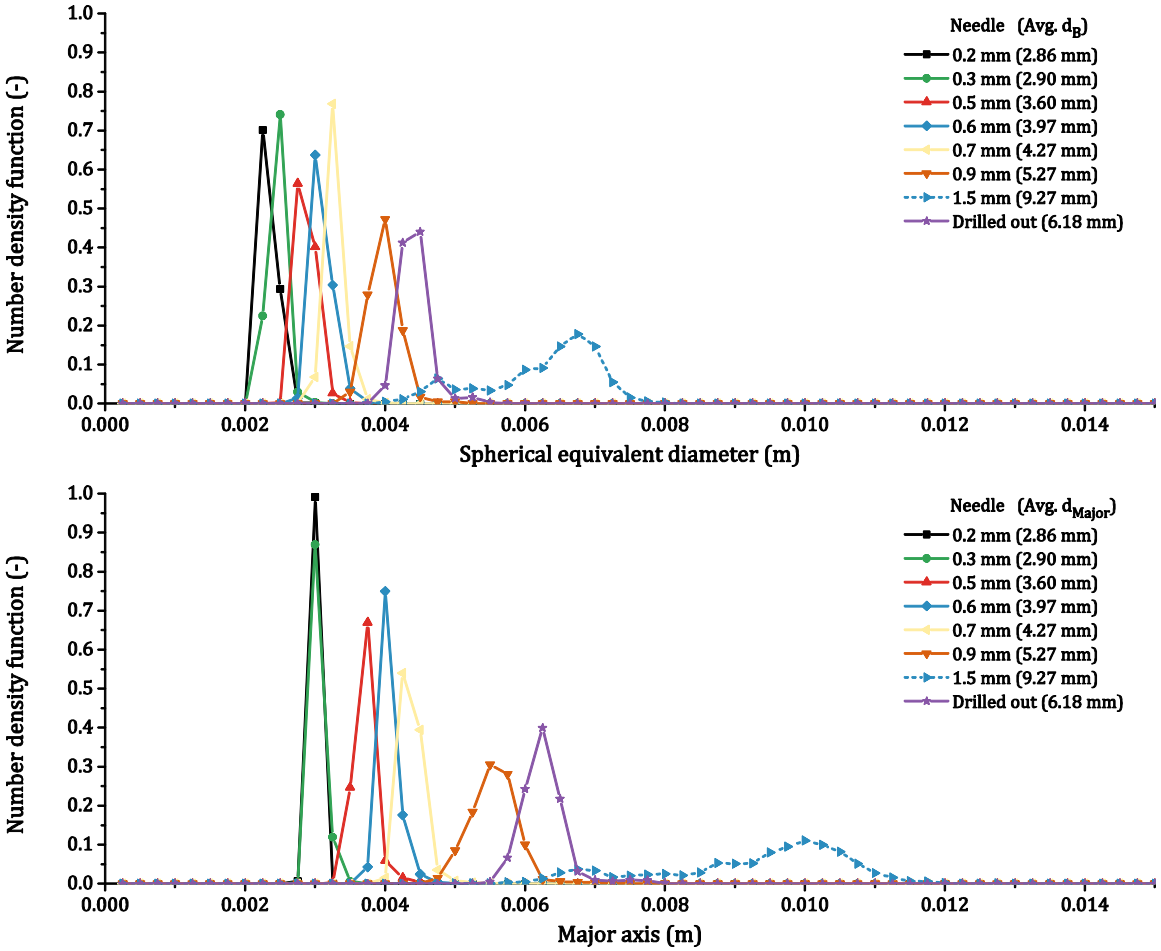

Figure 8-12 Number density function of the spherical equivalent diameter and major axis for 0.8 l/min driving flow, except for the 1.5 mm needle 1.0 l/min is plotted.

The velocity of the gas phase is calculated by tracking the bubbles in the same way as described in Section 3.4.2. The used measuring frequency was 25 Hz. The calculated relative velocities are compared to results from literature in Figure 8-13.

The relative velocities that are determined from experiments are situated between the terminal velocities obtained from the drag force model of Bozzano & Dente (2001) and Tomiyama et al. (1998) for pure systems. Therefore, it is reasonable to assume that the used water is pure. The drag force coefficient, which is needed to solve the force balance equation, is calculated by the experimental determined relative velocity. For the use in the force balance, it is assumed that these obtained drag coefficients are isotropic as also assumed in previous work, e.g. by Tomiyama et al. (2002).

Furthermore, the velocity field of the gas phase has to be determined. Indeed, the gas velocity used for calculating the lift force coefficient is only calculated along the determined averaged bubble traces with a round averaging area. The results for the determined (absolute) gas phase velocity field on a rectangular mesh, however, are demonstrated in Figure 8-14 for the 0.3 mm needle and the drilled out needle at a driving flow of 800 ml/min.

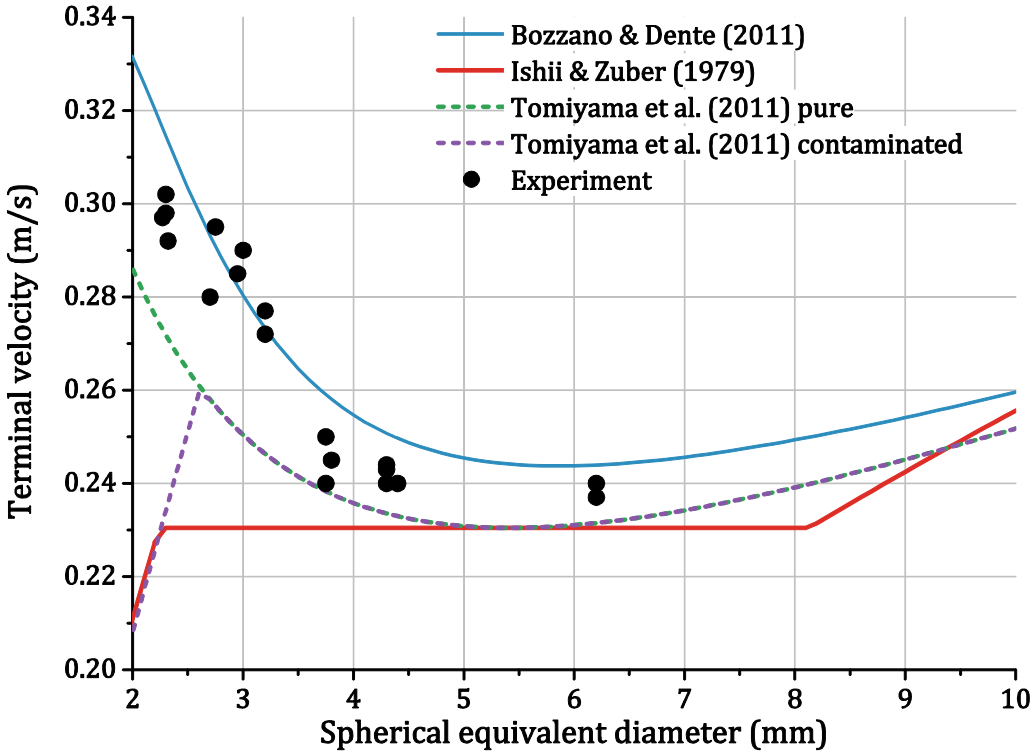

Figure 8-13 Determined terminal velocity.

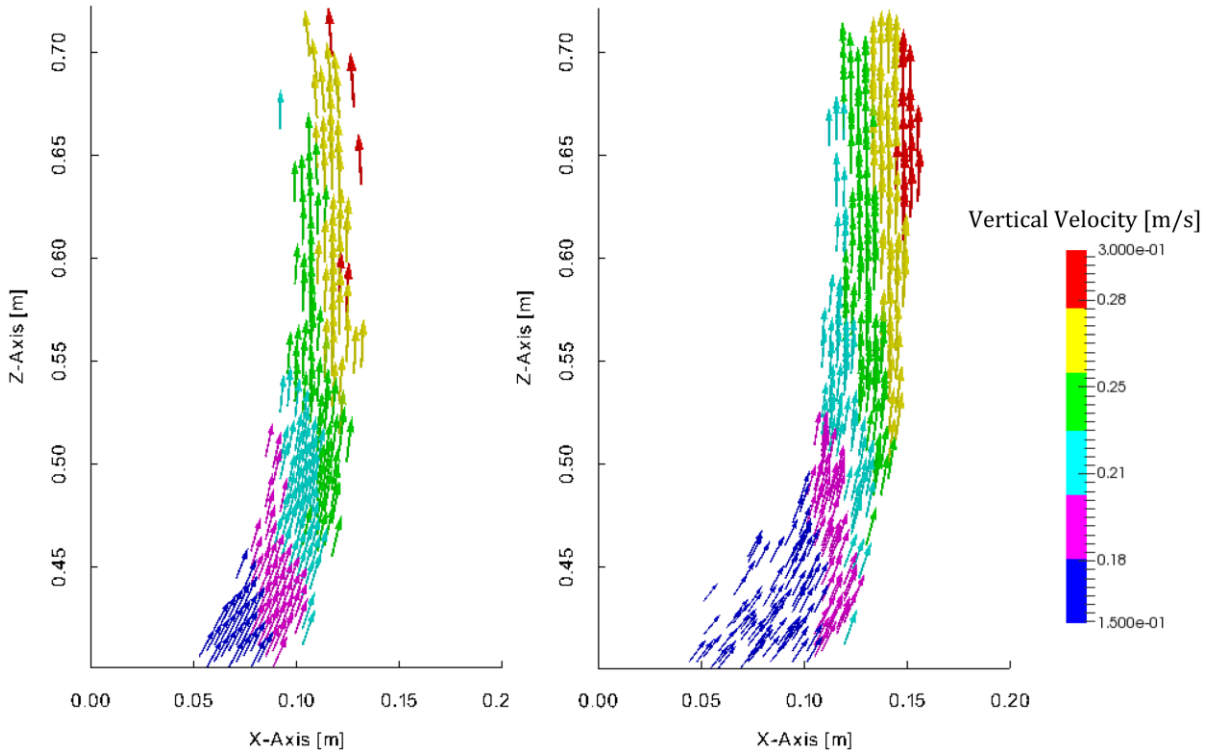

Figure 8-14 Absolute gas phase velocity field with vertical velocity as color for 800 ml/min driving flow. The left reactor wall is at x = 0 m, the driving flow at the right wall is between x = 0.2 m and x = 0.25 m. Left: The velocity field obtained with the 0.3 mm inner diameter needle generating 2.27 mm bubbles. Right: The velocity field obtained with the drilled out needle generating 4.13 mm bubbles.

In Figure 8-14 only the velocity vectors that are calculated by a sufficient amount of tracked bubbles are shown. Clearly, the shear field of the underlying liquid velocity is seen. The bubbles follow the velocity field shown in Figure 8-6. However, comparing the velocity field of the small bubbles (2.25 mm) generated by the 0.3 mm needle and the large bubbles (4.3 mm) generated by the drilled out needle, some differences are seen. At first, the large bubbles are dragged further towards the right wall. Moreover, the small bubbles move towards the left wall (towards x = 0 m) whereas the large bubbles are rising straight up. Nevertheless, since along both traces a positive liquid velocity is recorded (see Figure 8-9) the relative horizontal gas velocity is negative (in the direction of $x = 0\ m$) for both traces. This horizontal velocity of the gas phase, which is directed opposite to the positive liquid velocity, is the result of a lateral force that is assumed the lift force. The distinctly higher negative horizontal velocity of the smaller bubbles, which is indicated by the velocity vectors pointing towards the negative x-axis, might be the result from a higher lift force. In contrast, plotting the (absolute) gas phase velocity field of the largest bubbles (6.17 mm) (not shown) the velocity vectors point towards the positive x-axis.

8.3 Results for air/water

The lift force coefficient is calculated with the velocity data of the liquid and gas phase along the averaged traces, as discussed in the previous section. Using the force balance given in Equation (8-1) the lift force coefficient is the only unknown remaining. The lift force coefficient is calculated by using the horizontal component of the force balance.

The lift force coefficients are averaged between a height of $y = 0.5\ m$ and $y = 0.65\ m$. In this area, the bubbles are less accelerated due to small liquid velocity gradients $dv_{l,i}/dx_i$. In the lower and upper sections, these are large; the lift force coefficients obtained in these sections might not be comparable to the lift force coefficients obtained in other work with a not accelerated bubbles motion due to the flow. The results are shown in Figure 8-15. Clearly, the lift force coefficient is not constant along the bubble traces, which might indicate an insufficient amount of tracked bubbles in general.

The available data do not allow an obvious statement regarding the dependency of the lift force coefficient of the shear rate strength as shown in Figure 8-16. The lift force coefficient is plotted against the modified Eötvös number

$$Eo_\perp = \frac{\Delta\rho g d_\perp}{\sigma} \quad , \tag{8-6}$$

with $d_\perp$ the axis perpendicular to the flow, which is assumed equal with the major axis. The amount of experiments is too small in general so that the lift force coefficients are scattered and no clear trend is found. From previous findings in high Morton number systems under laminar conditions (Tomiyama et al. 2002) (Dijkhuizen et al. 2010b), however, also no dependency is found. Nevertheless, a high shear rate is connected to a high turbulence intensity in the present setup. Thus, no clear dependency of the lift force regarding the turbulence intensity is seen as well, or possible effects cancel each other out.

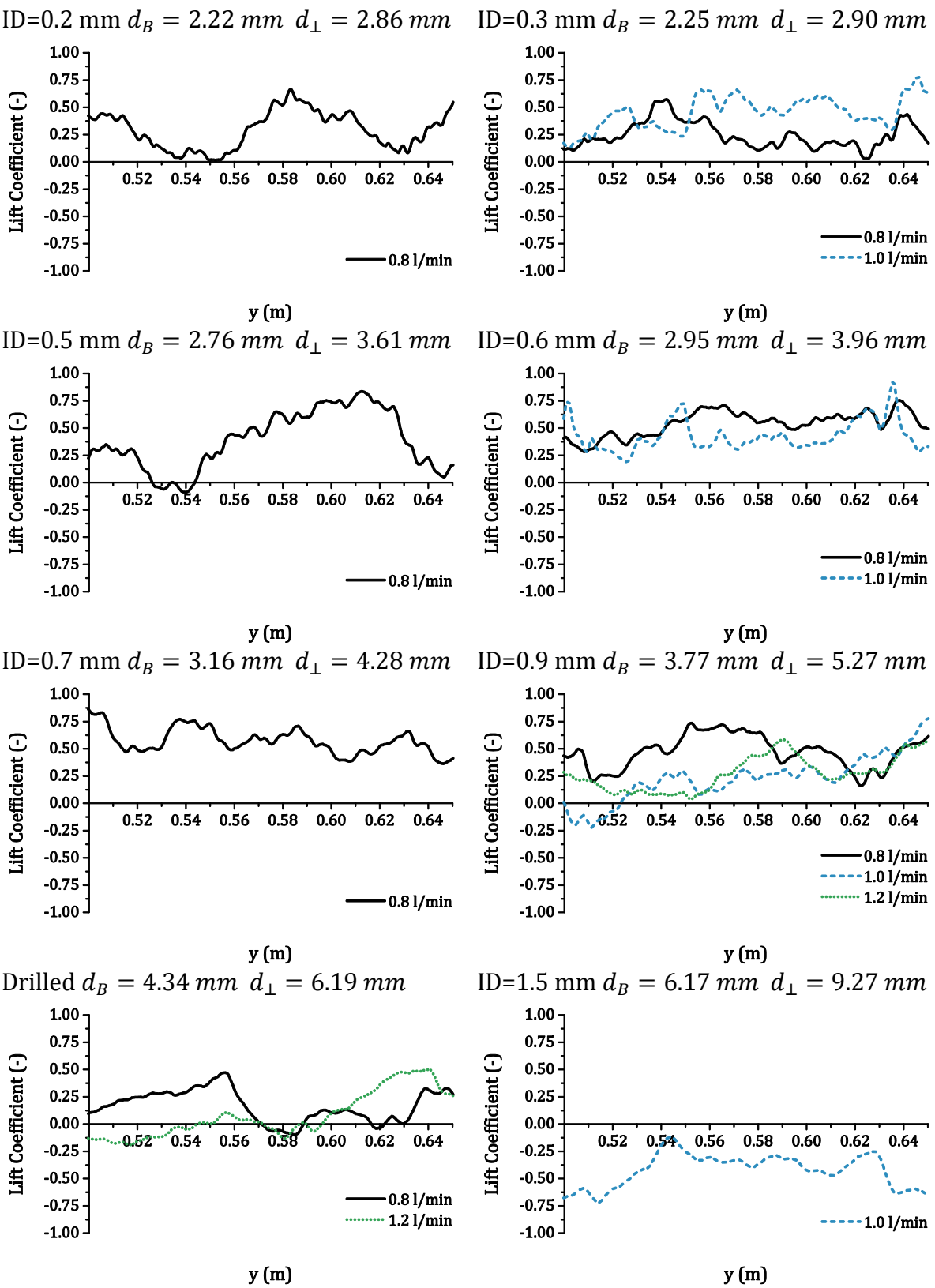

Figure 8-15 Lift force coefficient along the averaged traces.

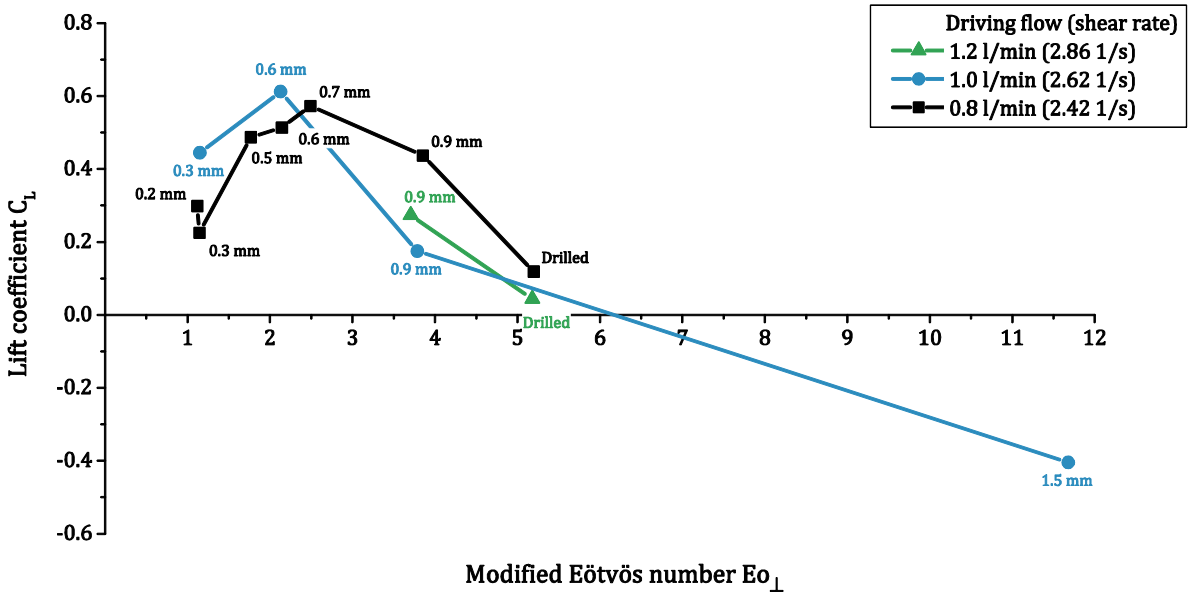

Figure 8-16 Averaged lift force coefficients along the averaged bubble traces for different shear rates. The needle diameter is written at the points.

The results are compared to results from literature (Tomiyama et al. 2002) (Dijkhuizen et al. 2010b) in Figure 8-17 for the Eötvös number calculated with the spherical equivalent diameter and with the perpendicular flow axis. The lift force coefficients obtained from the present experiments are falling to negative values with rising Eötvös numbers. This falling is consistent to the results obtained in the other work. Apparently, from the actual measurements a peak is seen at an Eötvös number of around 1.2, after the peak the lift force is tending to smaller values with decreasing Eötvös numbers.

Comparing the results of the present study with the results of the well-known Tomiyama lift force model, distinct differences are observed for the Eötvös number graph but similarities for the modified Eötvös number graph. In contrast, the present experiments fit the DNS of Dijkhuizen et al. (2010b) very well for both, the normal and modified Eötvös number. Overall, the DNS, the present experiments and the empirical Tomiyama lift force model agree for the modified Eötvös number.

Whereas the graph for the normal Eötvös number was obtained for the present experiments and the DNS from directly measured variables, the correlation of Wellek et al. (1966) was used by Tomiyama et al. (2002) to calculate the spherical equivalent diameter from the (measured) perpendicular flow axis. In Section 8.2.4 it was shown that the Wellek correlation might not be applicable to pure and/or turbulent air/water flows. Thus, it is reasonable that such large deviations regarding the lift force coefficient occur for the normal Eötvös number. Moreover, since the present experiments agree well with the DNS of Dijkhuizen et al., which were also done for pure systems, for both Eötvös numbers it is reasonable to assume that the Wellek correlation is incorrect. The rotating belt generating the shear field in the experiments of Tomiyama et al. might create abrasion that lead to a contamination of the liquid as pointed out by Dijkhuizen et al. (2010b). Speculatively, this contamination might be the reason why Tomiyama et al. used the Wellek correlation formulated for contaminated flows (Tomiyama et al. 2002).

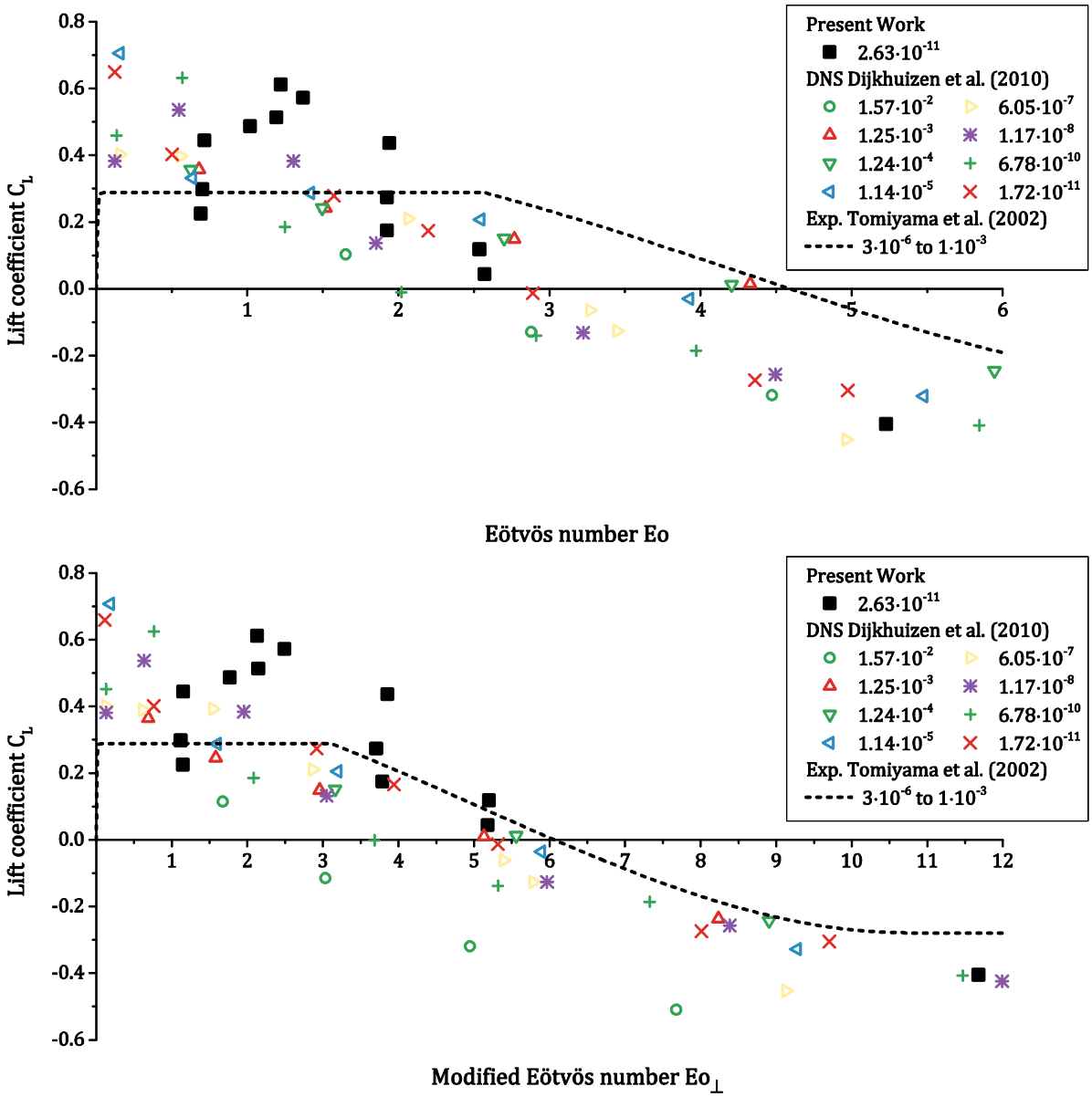

Figure 8-17 Results of the present lift force measurements in turbulent air/water flow (Morton number of around $2.63 \cdot 10^{-11}$) compared to results from the literature for different Morton numbers. The DNS by Dijkhuizen et al. (2010b) and the experiments of Tomiyama et al. (2002) are conducted under laminar conditions.

Nevertheless, the agreement regarding the modified Eötvös number of the present experiment, the DNS and the empirical Tomiyama model is suprisingly good considering the very different flow conditions. In the first place, the Morton numbers used in the Tomiyama experiment are distinctly higher (in the range of 10^{-3} to 10^{-6}) compared to the present experiment in air/water ($Mo = 2.63 \cdot 10^{-11}$). In addition, the experiments of Tomiyama et al. (2002) are conducted under laminar flow conditions with bubble Reynolds numbers below 10^2 whereas turbulent flow conditions with bubble Reynolds numbers ranging from 680 to 1500. The shear rates used in the present study are comparable with the shear rates used by Tomiyama et al.

The used bubble Reynolds numbers for the DNS of Dijkhuizen et al. (2010b) are in the range of 10 to 1609 (1609 only for very large bubbles, which are not shown here) and

comparable to the present experiment. In addition, the used Morton numbers are in the range of an air/water system. The background flow, however, was laminar. The amount of DNS is limited, especially in the distorted regime in which the bubbles are wobbling. This leads to a poor statistic since the wobbling motion is random. Therefore, the DNS lift force coefficients are scattering because many DNS are needed for reliable results (Bothe et al. 2006).

8.4 Discussion and Conclusions

With the developed measuring concept, the lift force was successfully determined in a system with a very low Morton number under turbulent conditions by using long-term measurements. This is the first time that the lift force is direct measureable in such systems. In contrast to other measuring concepts, the here presented concept do not have any moving parts like moving belts that tend to contaminate the measuring system. Therefore, it is a very simple and reliable method and, further, can be applied to every chemical system.

Comparing to results from the literature (Tomiyama et al. 2002) (Dijkhuizen et al. 2010b) a very good agreement is reached. From the present measurements, it is confirmed that the lift force coefficient is significant and is likely changing its sign in turbulent flow and in very low Morton number systems.

Nevertheless, more experiments are needed to confirm the findings quantitatively, especially the gap between $Eo = 2.5$ and $Eo = 5.2$ has to be filled up. In addition, the measuring effort has to be decreased; now, the complete bubble column is investigated, which results in a measuring time of around 80 hours. Focusing only on one measuring area might be sufficient. Moreover, the scattering of the determined lift force coefficients has to be decreased, which is caused by a poor statistic on the gas phase side. This is a general problem because the lift force can only be evaluated on the center plane since the liquid velocity is only known there. As a result, the bubbles not situated in this plane cannot be taken into account. Assuming an equal velocity, an extension to a narrow three-dimensional region around the center plane might be justified to increase the bubble count. Nonetheless, the measuring time has to be increased in general to get accurate data.

9 Summary

The complex nature of bubbly flows limits by now the predictive capabilities of two-fluid CFD approaches. Applying such CFD simulations to bubbly flows for unknown experimental setups, however, is highly preferable for process design. Since the physical phenomena are independent of the application, an important step toward predictive CFD simulations are baseline models in which all closure models and all constants are fixed. Such models have to reflect the underlying physics. Based on this idea, a baseline model developed at the Helmholtz-Zentrum Dresden-Rossendorf mainly basing on experimental data for bubbly pipe flows is validated to bubble columns, bubble plumes and airlift reactors that are relevant in chemical and biological engineering applications.

Such applications comprise buoyancy driven bubbly flows that often show dynamics on the scale of the used facility. It was shown that this large-scale flow phenomena can be well described with the baseline model in combination with the unsteady Reynolds-averaged Navier–Stokes equations (URANS) approach. The advantage of the URANS approach is that problems in which such large scales appear (mainly heterogeneous bubbly flows and partial aerated reactors) as well as problems that are dominated by the small scales (mainly homogenous bubbly flows) can be well predicted. This was shown by validating a large variety of experimental setups with respect to time averaged but also transient experimental results. However, in literature there is a lack of experimental data that are suitable for comprehensive CFD validation, in particular the bubble size distribution and reliable liquid velocity measurements in higher void fractions are missing.

In order to conduct own CFD-grade experiments measuring techniques were developed to determine the bubble size distribution in bubble clusters and to measure the liquid velocities without contaminating the flow by tracer particles for high void fractions. The main idea for the bubble size measurements is to follow the bubbles over a distinct period so that bubbles that are overlapped by others can be clearly seen in one of the images since the shape of a bubble cluster is steadily changing. In combination with an edge detector, this method gave reproducible and reliable results in complex bubbly flows.

Measuring the liquid velocity in bubbly flows is very difficult in general. Independent of the used measuring technique a sampling bias that had not been yet published is described in the present work. In particular, the sampling bias was shown to be distinct in bubbly flows for particle image and particle tracking velocimetry. Using the developed hold processor, very similar averaged liquid velocities and Reynolds-stresses could be obtained with both measuring methods. Moreover, common tracer particles, which are necessary for measuring the liquid velocities, contaminate the bubble interface. Contaminated bubbles can show a different behavior compared to clean bubbles so that a modeling of such is problematic since the grade of contamination due to the presence of tracer particles is not known. In order to obtain experimental data in reliable clean systems, micro bubbles that are naturally occurring in bubbly flows were used as tracer particles. It was shown that micro bubbles up to 300 µm are feasible for liquid velocity measurements for the setups used in the present work.

A CFD-grade airlift experiment was conducted, for which the bubble size, void fraction, liquid velocities and normal Reynolds-stress components were determined at two different heights in the riser and the downcomer as well as along the downcomer. In addition, the transient behavior of the airlift was studied since a distinct bubble plume was observed. The complexity of the experiments is intentional reduced by using gas volume flow rates and a sparger with which break-up and coalescence processes can be neglected. The URANS CFD-simulations gave good results in the riser; however, the void fraction in the downcomer does not fit the experimental observations. The reason for that might be a too strong predicted migration of the bubbles toward the internal walls at which the bubbles can rise up and escape the downcomer.

Besides a validation of closure models, a new measuring concept to determine the lift force on bubbles in systems with a very low Morton number and under turbulent conditions was developed. In particular, the new concept does not have any moving parts, which other measuring concepts usually have, that causes some problems with contamination due to abbreviation reported in the literature. Preliminary studies with the new concept in air/water confirmed that the lift force changes its sign for larger bubbles and the lift force coefficient is in the range of experiments conducted in high Morton number systems under laminar conditions. In comparison with DNS results from the literature a good agreement was reached.

References

Adoua, R., Legendre, D. & Magnaudet, J., 2009. Reversal of the lift force on an oblate bubble in a weakly viscous linear shear flow. *J. Fluid Mech.,* Volume 628, p. 23.

Ansys, 2013. *CFX 14.5 Manual: CFX-Solver Modeling Guide..* Canonsburg: Ansys, Inc..

Aris, R., 1962. *Vectors, Tensors and the Basic Equations of Fluid Mechanics.* Englewood Cliffs: Prentice-Hall.

Auton, T. R., 1987. The lift force on a spherical body in a rotational flow. *J. Fluid Mech.,* Volume 183, p. 199.

Badreddine, H., Sato, Y., Niceno, B. & Prasser, H.-M., 2015. Finite size Lagrangian particle tracking approach to simulate dispersed bubbly flows. *Chemical Engineering Science ,* 122(0), pp. 321-335.

Bech, K., 2005. Dynamic simulation of a 2D bubble column. *Chemical Engineering Science,* 60(19), pp. 5294-5304.

Becker, S., Sokolichin, A. & Eigenberger, G., 1994. Gas-liquid flow in bubble columns and loop reactors: Part II. Comparison of detailed experiments and flow simulations. *Chemical Engineering Science,* 49(24, Part 2), pp. 5747-5762.

Besbes, S. et al., 2015. PIV measurements and Eulerian-agrangian simulations of the unsteady gas-liquid flow in a needle sparger rectangular bubble column. *Chemical Engineering Science,* 126(0), pp. 560-572.

bin Mohd Akbar , M. H., Hayashi , K., Hosokawa , S. & Tomiyama, A., 2012. Bubble tracking simulation of bubble-induced pseudoturbulence. *Multiphase Science and Technology,* 24(3), pp. 197-222.

Bitog, J. et al., 2011. Application of computational fluid dynamics for modeling and designing photobioreactors for microalgae production: A review. *Computers and Electronics in Agriculture ,* 76(2), pp. 131-147.

Boegman, L. & Sleep, S., 2012. Feasibility of Bubble Plume Destratification of Central Lake Erie. *Journal of Hydraulic Engineering,* 138(11), pp. 985-989.

Bolotnov, I. A. et al., 2011. Detached direct numerical simulations of turbulent two-phase bubbly channel flow. *International Journal of Multiphase Flow ,* 37(6), pp. 647-659.

Bothe, D., Schmidtke, M. & Warnecke, H.-J., 2006. VOF-Simulation of the Lift Force for Single Bubbles in a Simple Shear Flow. *Chem. Eng. Technol.,* Volume 29, p. 1048.

Bourgoin, M. et al., 2011. Turbulent transport of finite sized material particles. *Journal of Physics: Conference Series,* Volume 318.

Bozzano, G. & Dente, M., 2001. Shape and terminal velocity of single bubble motion: a novel approach. *Computers and Chemical Engineering,* Volume 25, p. 571–576.

Bröder, D. & Sommerfeld, M., 2007. Planar shadow image velocimetry for the analysis of the hydrodynamics in bubbly flows. *Meas. Sci. Technol.,* Volume 18, p. 2513–2528.

Brücker, C., 2000. PIV IN TWO-PHASE FLOWS. *Von Karman Institute for Fluid Lecture Series 2000-01*, 17-21 January.

Buckingham, E., 1914. On Physically Similar Systems; Illustrations of the Use of Dimensional Equations. *Phys. Rev.,* Volume 4, p. 345–376.

Burns, A., Frank, T., Hamill, I. & Shi, J.-M., 2004. *The Favre Averaged Drag Model for Turbulent Dispersion in Eulerian Multi-Phase Flows.* Yokohama, Japan,, 5th International Conference on Multiphase Flow.

Buwa, V. V. & Ranade, V. V., 2004. Characterization of dynamics of gas-liquid flows in rectangular bubble columns. *AIChE Journal,* 50(10), pp. 2394-2407.

Calzavarini, E., Cencini, M., Lohse, D. & Toschi, F., 2008. Quantifying Turbulence-Induced Segregation of Inertial Particles. *Phys. Rev. Lett.,* Aug, Volume 101, pp. 1-5.

Calzavarini, E. et al., 2011. Impact of trailing wake drag on the statistical properties and dynamics of finite-sized particle in turbulence. *Physica D: Nonlinear Phenomena,* 241(3), pp. 237-244.

Canny, J., 1986. A Computational Approach To Edge Detection. *IEEE Trans. Pattern Analysis and Machine Intelligence,* 8(6), p. 679–698.

Cloete, S., Olsen, J. E. & Skjetne, P., 2009. CFDmodeling of plume and free surface behavior resulting from a sub-sea gas release. *Applied Ocean Research,* 31(3), pp. 220-225.

da Silva, M. J., 2008. *Impedance Sensors for Fast Multiphase Flow.* Technische Universität Dresden: Fakultät Elektrotechnik und Informationstechnik der Technischen Universität Dresden .

Da Silva, M., Schleicher, E. & Hampel, U., 2007. A Novel Needle Probe Based on High-Speed Complex Permittivity Measurements for Investigation of Dynamic Fluid Flows. *Instrumentation and Measurement, IEEE Transactions on,* Aug, 56(4), pp. 1249-1256.

Dabiri, S., Lu, J. & Tryggvason, G., 2013. Transition between regimes of a vertical channel bubbly upflow due to bubble. *Physics of Fluids,* Volume 25.

de Bertodano, M. L., Lahey, R. T. & Jones, O. C., 1994. Development of a k-epsilon Model for Bubbly Two-Phase Flow. *Journal of Fluids Engineering,* Volume 116, p. 128.

de Bertodano, M. L., Lee, S.-J., R. T. Lahey, J. & Drew, D. A., 1990. The Prediction of Two-Phase Turbulence and Phase Distribution Phenomena Using a Reynolds Stress Model. *J. Fluids Eng.,* Volume 112, p. 107.

Deen, N., 2001. *PHD thesis: An Experimental and Computational Study of Fluid Dynamics in Gas-Liquid Chemical Reactors.* Esbjerg, Denmark: The Faculty of Engineering and Science, Aalborg University.

Deen, N. G., Solberg, T. & Hjertager, B., 2001. Large eddy simulation of the Gas–Liquid flow in a square cross-sectioned bubble column. *Chemical Engineering Science,* 56(21-22), p. 6341–6349.

Deen, N. G., Westerweel, J. & Delnoij, E., 2002. Two-Phase PIV in Bubbly Flows: Status and Trends. *Chem. Eng. Technol. ,* Volume 25.

Deen, N., Solberg, T. & Hjertager, B., 2001. Large eddy simulation of the Gas-Liquid flow in a square cross-sectioned bubble column. *Chemical Engineering Science,* Volume 56, pp. 6341-6349.

Delhaye, J. M., 1974. Jump conditions and entropy sources in two-phase systems. Local instant formulation. *International Journal of Multiphase Flow,* 1(3), pp. 395-409.

Delnoij, E., Kuipers, J. A. M., van Swaaij, W. P. M. & Westerweel, J., 2000. Measurement of gas-liquid two-phase flow in bubble columns using ensemble correlation PIV. *Chemical Engineering Science ,* Volume 55, pp. 3385 - 3395.

Delnoij, E., Lammers, F., Kuipers, J. & van Swaaij, W., 1997. Dynamic simulation of dispersed gas-liquid two-phase flow using a discrete bubble model. *Chemical Engineering Science ,* 52(9), pp. 1429-1458.

Diaz, M., Montes, F. & Galan, M., 2009. Influence of the lift force closures on the numerical simulation of bubble plumes in a rectangular bubble column. *Chemical Engineering Science,* Volume 64, pp. 930-944.

Dijkhuizen, W., Roghair, I., Van Sint Annaland, M. & Kuipers, J. A., 2010a. DNS of gas bubbles behaviour using an improved 3D front tracking. *Chemical Engineering Science,* Volume 65, p. 1415–1426.

Dijkhuizen, W., van Sint Annaland, M. & Kuipers, J. A., 2010b. Numerical and experimental investigation of the lift force on single bubbles. *Chemical Engineering Science,* Volume 65, p. 1274–1287.

Dimotakis, P., Debussy, F. D. & Koochesfahani, M. H., 1981. Particle streak velocity field measurements in a two-dimensional mixing layer. pp. 995-999.

Edwards, R. V., 1987. Report of the Special Panel on Statistical Particle Bias Problems in Laser Anemometry. *J. Fluids Eng.,* 109(2), pp. 89-93.

Ervin, E. A. & Tryggvason, G., 1997. The Rise of Bubbles in a Vertical Shear Flow. *J. Fluids Eng.,* Volume 119, p. 443.

Feng, Y., Goree, J. & Liu, B., 2007. Accurate particle position measurement from images. *Review of Scientific Instruments,* 78(5).

Feng, Y., Goree, J. & Liu, B., 2011. Errors in particle tracking velocimetry with high-speed cameras. *Rev. Sci. Instrum.,* Volume 82.

Fernandes, B. D., Dragone, G. M., Teixeira, J. A. & Vicente, A. A., 2010. Light Regime Characterization in an Airlift Photobioreactor for Production of Microalgae with High Starch Content. *Appl Biochem Biotechnol,* pp. 218-226.

Ferziger, J. H. & Peric, M., 2002. *Computational Methods for Fluid Dynamics.* 3rd ed. Berlin Heidelberg New York: Springer-Verlag.

Fish, F. E., Legac, P., Williams, T. M. & Wei, T., 2014. Measurement of hydrodynamic force generation by swimming dolphins using bubble DPIV. *The Journal of Experimental Biology,* 217(2), pp. 252-260.

Frank, T. et al., 2008. Validation of CFD models for mono- and polydisperse air–water two-phase flows in pipes. *Nuclear Engineering and Design,* Volume 238, pp. 647-659.

Fujiwara, A., Minato, D. & Hishida, K., 2004. Effect of bubble diameter on modification of turbulence in an upward pipe flow. *International Journal of Heat and Fluid Flow,* 25(3), p. 481–488.

Fukuta, M., Takagi, S. & Matsumoto, Y., 2008. Numerical study on the shear-induced lift force acting on a spherical bubble in aqueous surfactant solutions. *Phys. Fluids,* Volume 20, p. 040704.

Garcia, C. & Garcia, M., 2006. Characterization of flow turbulence in large-scale bubble-plume experiments. *Experiments in Fluids,* 41(1), pp. 91-101.

Ghasemi, H. & Hosseini, S. H., 2012. Investigation of hydrodynamics and transition regime in an internal loop airlift reactor using CFD. *Brazilian Journal of Chemical Engineering,* 12, Volume 29, pp. 821-833.

Grace, J. R., Wairegi, T. & Nguyen, T. H., 1976. Shapes and Velocities of Single Drops and Bubbles Moving Freely Through Immiscible Liquids. *Transactions of the Institute of the Chemical Engineers,* Volume 54, p. 167.

Graff, E. C., Pereira, F. & Gharib, M., 2008. *Defocusing Digital Particle Image Velocimetry: A Volumetric DPIV Technique for Dual and Single Phase Flows.* Lisbon, Portugal, 14th Int Symp on Applications of Laser Techniques to Fluid Mechanics, pp. 1-12.

Grimaldo, E. et al., 2011. Field demonstration of a novel towed, area bubble-plume zooplankton (Calanus sp.) harvester. *Fisheries Research,* 107(13), pp. 147-158.

Gruber, M., Radl, S. & Khinast, J., 2013. Coalescence and Break-Up in Bubble Columns: Euler-Lagrange Simulations Using a Stochastic Approach. *Chemie Ingenieur Technik,* 85(7), pp. 1118-1130.

Haberman, W. L. & Morton, R. K., 1953. *An experimental investigation of the drag and shape of air bubbles rising in various liquids,* Bethesda, MD.: David W. Taylor Model Basin.

Hadamard, J. S., 1911. Mouvement permanent lent d'une sphere liquide et visqueuse dans un liquide visqueux". *CR Acad. Sci. (in French),* Volume 152, p. 1735–1738.

Hampel, U. et al., 2012. Multiphase flow investigations with ultrafast electron beam X-ray tomography. *AIP Conference Proceedings,* Volume 1428, pp. 167-174.

Hänsch, S., Lucas, D., Krepper, E. & Höhne, T., 2012. A multi-field two-fluid concept for transitions between different scales of interfacial structures. *International Journal of Multiphase Flow ,* Volume 47, pp. 171-182.

Hoesel, W. & Rodi, W., 1977. New biasing elimination method for laser-Doppler velocimeter counter. *Rev. Sci. Instrum.,* Volume 48, pp. 910-919.

Hosokawa, S. & Tomiyama, A., 2004. Turbulence modification in gas-liquid and solid-liquid dispersed two-phase pipe flows. *Int. J. Heat and Fluid Flow,* Volume 25, p. 489.

Hosokawa, S. & Tomiyama, A., 2013. Bubble-induced pseudo turbulence in laminar pipe flows. *Int. J. Heat Fluid Flow,* Volume 40, pp. 97-105.

Hosokawa, S., Tomiyama, A., Misaki, S. & Hamada, T., 2002. *Lateral Migration of Single Bubbles Due to the Presence of Wall.* Montreal, Quebec, ASME 2002 Joint U.S.-European Fluids Engineering Division Conference, p. 855.

Hua, J., 2015. CFDsimulations of the effects of small dispersed bubbles on the rising of a single large bubble in 2D vertical channels. *Chemical Engineering Science,* 123(0), pp. 99-115.

Huang, Q., Yang, C., Yu, G. & Mao, Z.-S., 2010. CFD simulation of hydrodynamics and mass transfer in an internal airlift loop reactor using a steady two-fluid model. *Chemical Engineering Science ,* 65(20), pp. 5527-5536.

Hu, G. & Celik, I., 2008. Eulerian-Lagrangian based large-eddy simulation of a partially aerated flat bubble column. *Chemical Engineering Science,* 63(1), pp. 253-271.

Ishii, M. & Hibiki, T., 2006. *THERMO-FLUID DYNAMICS OF TWO-PHASE FLOW.* 2nd ed. New York: Springer Science+Business Media, Inc..

Ishii, M. & Zuber, N., 1979. Drag Coefficient and Relative Velocity in Bubbly, Droplet or Particulate Flows. *AlChE Journal,* Volume 25, p. 843.

Ishikawa, M., Irabu, K., Teruya, I. & Nitta, M., 2009. PIV Measurement of a Contraction Flow using Micro-Bubble Tracer. *Journal of Physics: Conference Series,* Volume 147, p. 012010.

Jain, D., Kuipers, J. & Deen, N. G., 2014. Numerical study of coalescence and breakup in a bubble column using a hybrid volume of fluid and discrete bubble model approach. *Chemical Engineering Science ,* 119(0), pp. 134-146.

Jain, D., Lau, Y. M., Kuipers, J. & Deen, N. G., 2013. Discrete bubble modeling for a micro-structured bubble column. *Chemical Engineering Science ,* 100(0), pp. 496-505.

Jakobsen, M. L., Easson, W. J., Greated, C. A. & Glass, D. H., 1996. Particle image velocimetry: simultaneous two-phase flow measurements. *Meas. Sci. Technol. ,* Volume 7, p. 1270–1280.

Jay Sanyal, ., Marchisio, D. L., Fox, R. O. & Dhanasekharana , K., 2005. On the Comparison between Population Balance Models for CFD Simulation of Bubble Columns. *Industrial & Engineering Chemistry Research,* 44(14), pp. 5063-5072.

Jones, W. P. & Launder, B. E., 1972. The Predicition of Laminarization with a two-equation model of turbulence. *Int. J. Heat Mass Transfer,* Volume 15, pp. 301-334.

Juliá, J. E., Hernandez, L., Chiva, S. & Vela, A., 2007. Hydrodynamic characterization of a needle sparger rectangular bubble column: Homogeneous flow, static bubble plume and oscillating bubble plume. *Chemical Engineering Science ,* 62(22), pp. 6361-6377.

Kariyasaki, A., 1987. *Behavior of a single gas bubble in a liquid flow with a linear velocity profile.* , Proceedings of the 1987 ASME/JSME Thermal Engineering Conference. No. 384.

Kataoka, I. & Serizawa, A., 1989. Basic equations of turbulence in gas-liquid two-phase flow. *International Journal of Multiphase Flow,* Volume 15, p. 843.

Kitagawa, A., Murai, Y. & Yamamoto, F., 2001. Two-way coupling of Eulerian-Lagrangian model for dispersed multiphase flows using filtering functions. *International Journal of Multiphase Flow,* 27(12), pp. 2129-2153.

Korpijarvi, J., Oinas, P. & Reunanen, J., 1999. Hydrodynamics and mass transfer in an airlift reactor. *Chemical Engineering Science,* Volume 54, pp. 2255-2262.

Krepper, E. et al., 2008. The inhomogeneous MUSIG model for the simulation of polydispersed flows. *Nuclear Engineering and Design,* Volume 238, p. 1690–1702.

Krepper, E., Lucas, D. & Prasser, H.-M., 2005. On the modelling of bubbly flow in vertical pipes. *Nuclear Engineering and Design,* Volume 235, p. 597.

Kulkarni, A. A., 2008. Lift force on bubbles in a bubble column reactor: Experimental analysis. *Chemical Engineering Science,* Volume 63, pp. 1710-1723.

Kulkarni, A. V., Badgandi, S. V. & Joshi, J. B., 2009. Design of ring and spider type spargers for bubble column reactor: Experimental measurements and \{CFD\} simulation of flow and weeping. *Chemical Engineering Research and Design ,* 87(12), pp. 1612-1630.

Lakshmanan, P. & Ehrhard, P., 2010. Marangoni effects caused by contaminants adsorbed on bubble surfaces. *Journal of Fluid Mechanics,* 3, Volume 647, pp. 143-161.

Lance, M. & de Bertodano, M. L., 1994. Phase Distribution Phenomena and Wall Effects in Bubbly Two-phase Flows. *Multiphase Scuience and Technology,* Volume 8, p. 69.

Lance, M., Mariè, J. & Bataille, J., 1991. Homogeneous turbulence in bubbly flows. *Journal of Fluids Engineering,* Volume 113, p. 295.

Lau, Y., Bai, W., Deen, N. & Kuipers, J., 2014. Numerical study of bubble break-up in bubbly flows using a deterministic Euler-Lagrange framework. *Chemical Engineering Science,* 108(0), pp. 9-22.

Lau, Y. et al., 2013. Experimental study of the bubble size distribution in a pseudo-2D bubble column. *Chemical Engineering Science ,* 98(0), pp. 203-211.

Law, D. & Battaglia, F., 2013. Numerical Simulations for Hydrodynamics of Air-Water External Loop Airlift Reactor Flows With Bubble Break-Up and Coalescence Effects. *Journal of Fluids Engineering,* Volume 135, pp. 081302-1 - 081302-8.

Lawler, M. T., 1971. The role of lift in the radial migration of particles in a pipe flow. *Advances in Solid–Liquid Flow in Pipes and Its Application,* pp. 39-57.

Legendre, D. & Magnaudet, J., 1997. A note on the lift force on a spherical bubble or drop in a low-Reynolds-number shear flow. *Phys. Fluids,* Volume 9, p. 3572.

Legendre, D. & Magnaudet, J., 1998. The lift-force on a spherical bubble in a viscous linear shear flow. *J. Fluid Mech.,* Volume 368, p. 81.

Lesieur, M., Métais, O. & Comte, P., 2005. *Large-Eddy Simulations of Turbulence.* 1st ed. Cambridge: Cambridge University Press.

Liao, Y. & Lucas, D., 2009. A literature review of theoretical models for drop and bubble breakup in turbulent dispersions. *Chemical Engineering Science,* Volume 64, p. 3389.

Lindken, R., Gui, L. & Merzkirch, W., 1999. Velocity Measurements in Multiphase Flow by Means of Particle Image Velocimetry. *Chem. Eng. Technol. ,* 22(3).

Lindken, R. & Merzkirch, W., 2002. A novel PIV technique for measurements in multiphase flows and its application to two-phase bubbly flows. *Experiments in Fluids,* Volume 33, pp. 814-825.

Liu, Y. & Tay, J.-H., 2002. The essential role of hydrodynamic shear force in the formation of biofilm and granular sludge. *Water research,* Issue 1653-1665.

Liu, Y., Yang, H. & Wang, W., 2005. *Reconstructing B-spline Curves from Point Clouds--A Tangential Flow Approach Using Least Squares Minimization.* Cambridge, MA, Shape Modeling and Applications, 2005 International Conference, pp. 4-12.

Loth, E., 2008. Quasi-steady shape and drag of deformable bubbles and drops. *International Journal of Multiphase Flow,* 34(6), p. 523–546.

Lucas, D., Krepper, E. & Prasser, H.-M., 2007a. Use of models for lift,wall and turbulent dispersion forces acting on bubbles for poly-disperse flows. *Chemical Engineering Science,* Volume 62, p. 4146.

Lucas, D., Krepper, E., Prasser, H.-M. & Manera, A., 2007b. *Stability effect of the lateral lift force in bubbly flows.* Leipzig, Germany, 6th International Conference on Multiphase Flow, ICMF 2007, p. S1_Mon_C_9.

Lucas, D., Prasser, H.-M. & Manera, A., 2005. Influence of the lift force on the stability of a bubble column. *Chemical Engineering Science,* Volume 60, p. 3609 – 3619.

Lucas, D. & Tomiyama, A., 2011. On the role of the lateral lift force in poly-dispersed bubbly flows. *International Journal of Multiphase Flow,* Volume 37, p. 1178.

Luo, H.-P. & Al-Dahhan, M. H., 2008. Local characteristics of hydrodynamics in draft tube airlift bioreactor. *Chemical Engineering Science ,* 63(11), pp. 3057-3068.

Luo, H.-P. & Al-Dahhan, M. H., 2011. Verification and validation of CFD simulations for local flow dynamics in a draft tube airlift bioreactors. *Chemical Engineering Science,* 66(5), pp. 907-923.

Lu, X., Ding, J., Wang, Y. & Shi, J., 2000. Comparison of the hydrodynamics and mass transfer characteristics of a modified square airlift reactor with common airlift reactors. *Chemical Engineering Science,* Volume 55, pp. 2257-2263.

Manera, A. et al., 2009. Comparison between wire-mesh sensors and conductive needle-probes for measurements of two-phase flow parameters. *Nuclear Engineering and Design ,* 239(9), pp. 1718-1724.

Maric, T., Marschall, H. & Bother, D., 2015. lentFoam – A hybrid Level Set/Front Tracking method on unstructured. *Computers & Fluids,* Volume 113, pp. 20-31.

Masood, R. & Delgado, A., 2014. Numerical investigation of the interphase forces and turbulence closure in 3D square bubble columns. *Chemical Engineering Science ,* Issue 0, pp. - .

Masood, R., Rauh, C. & Delgado, A., 2014. CFD simulation of bubble column flows: An explicit algebraic Reynolds stress model approach. *International Journal of Multiphase Flow,* 66(0), pp. 11-25.

Ma, T. et al., 2015. Scale-Adaptive Simulation of a square cross-sectional bubble column. *Chem. Eng. Sci.,* Volume 131, p. 101–108.

Ma, T., Ziegenhein, T., Lucas, D. & Fröhlich, J., 2015. Large eddy simulations of the gas-liquid flow in a rectangular bubble column. *Nuclear Engineering and Design ,* pp. - .

Ma, T. et al., 2015. Euler-Euler large eddy simulations for dispersed turbulent bubbly flows. *International Journal of Heat and Fluid Flow ,* Volume 56, pp. 51-59.

Maxey, M. R., 1987. The gravitational settling of aerosol particles in homogeneous turbulence and random flow fields. *Journal of Fluid Mechanics,* Volume 174, pp. 441-465.

McClimans, T. et al., 2012. Pneumatic oil barriers: The promise of area bubble plumes. *Journal of Engineering for the maritime enviroment,* 0(0), pp. 1-17.

Mei, R. & Klausner, J., 1994. Shear lift force on spherical bubbles. *International Journal of Heat and Fluid Flow,* Volume 15, p. 62.

Menter, F. R., Kuntz, M. & Langtry, R., 2003. Ten Years of Industrial Experience with the SST Turbulence Model. *Turbulence, Heat and Mass Transfer,* Volume 4.

Mercado, J. M. et al., 2012. Lagrangian statistics of light particles in turbulence. *Physics of Fluids (1994-present),* 24(5).

Miron, A. S. et al., 200. Bubble-Column and Airlift Photobioreactors for Algal Culture. *AIChE Journal,* 49(9), pp. 1872-1887.

Morel, C., 1997. *Turbulence modeling and first numerical simulations in turbulent two-phase flows,* Grenoble, France: SMTH/LDMS/97-023.

Mougin, G. & Magnaudet, J., 2002. The generalized Kirchhoff equations and their application to the interaction between a rigid body and an arbitrary time-dependent viscous flow. *International Journal of Multiphase Flow,* Volume 28, p. 1837.

Mudde, R. F., 2005. Gravity-driven Bubbly Flows. *Annual Review of Fluid Mechanics,* 37(1), pp. 393-423.

Mudde, R. F., Harteveld, W. K. & van den Akker, H. E. A., 2009. Uniform Flow in bubble-Columns. *Ind. Eng. Chem. Res.,* Volume 48, p. 148–158.

Mudde, R. F., Lee, D. J., Reese, J. & Fan, L.-S., 1997. Role of Coherent Structures on Reynolds Stresses in a 2-D Bubble Column. *Particle Technology and Fluidization,* 43(4), pp. 913-926.

Mudde, R. F. & Simonin, O., 1999. Two- and three-dimensional simulations of a bubble plume using a two-fluid model. *Chemical Engineering Science ,* 54(21), pp. 5061-5069.

Muñoz-Cobo, J. L., Chiva, S., El Aziz Essa, M. A. A. & Mendes, S., 2012. Tracking of bubble trajectories in vertical pipes in bubbly flow regime by coupling lagrangian, eulerian and 3D random walks models: Validation with experimental data. *Journal of Computational Multiphase Flows,* 4(3), p. 309.

Murai, Y., Matsumoto, Y. & Yamamoto, F., 2001. Three-dimensional measurement of void fraction in a bubble plume using statistic stereoscopic image processing. *Experiments in Fluids,* 30(1), pp. 11-21.

Murai, Y., Oshi, Y., Takeda, Y. & Yammamoto, F., 2006. Turbulent shear stress profiles in a bubbly channel flow assessed by particle tracking velocimetry. *Experiments in Fluids,* Issue 41, pp. 343-352.

Naciri, A., 1992. *Contribution `a l´´etude des forces exerc´ees par un liquide sur une bulle de gaz: portance, masse ajout´ee et interactions hydrodynamiques.* Ec. Centrale Lyon, France.: These de Doctorat.

Nauw, J., Linke, P. & Leifer, I., 2015. Bubble momentum plume as a possible mechanism for an early breakdown of the seasonal stratification in the northern North Sea. *Marine and Petroleum Geology ,* Issue 0, pp. - .

Oakley, T. R., Loth, E. & Adrian, R. J., 1997. A Two-Phase Cinematic PIV Method for Bubbly Flows. *J. Fluids Eng.,* 119(3), pp. 707-712.

Ojima, S., Hayashi, K., Hosokawa, S. & Tomiyama, A., 2014. Distributions of void fraction and liquid velocity in air–water bubble column. *International Journal of Multiphase Flow,* Volume 67, pp. 111-121.

Oliver-Salvador, M. d. C. et al., 2013. Shear rate and microturbulence effects on the synthesis of proteases by Jacaratia mexicana cells cultured in a bubble column, airlift, and stirred tank bioreactors. *Biotechnology and Bioprocess Engineering,* pp. 808-818.

Pang, M. & Wei, J., 2013. Experimental investigation on the turbulence channel flow laden with small bubbles by PIV. *Chemical Engineering Science,* Volume 94, pp. 302-315.

Parker, J. R., 2010. *Algorithms for Image Processing and Computer Vision.* Second ed. Indianapolis: John Wiley & Sons.

Pereira, F., Stüer, H., Graff, E. C. & Gharib, M., 2006. Two-frame 3D particle tracking. *Measurement Science and Technology,* 17(7), p. 1680.

Petrou, M. & Petrou, C., 2010. *Image Processing: The Fundamentals.* Second ed. Chichester: John Wiley & Sons.

Pfleger, D., Gomes, S., Gilbert, N. & Wagner, H.-G., 1999. Hydrodynamic simulations of laboratory scale bubble columns fundamental studies of the Eulerian-Eulerian modelling approach. *Chemical Engineering Science,* 54(21), pp. 5091-5099.

Politano, M., Carrica, P. & Converti, J., 2003. A model for turbulent polydisperse two-phase flow in vertical channels. *International Journal of Multiphase Flow,* Volume 29, p. 1153.

Pope, S. B., 2000. *Turbulent Flows.* 1st ed. Cambridge: Cambridge University Press.

Pourtousi, M., Zeinali, M., Ganesan, P. & SAHU, P. J. N., 2015. Prediction of multiphase flow pattern inside a 3D bubble column reactor using a combination of CFD and ANFIS. *RSC Adv.*

Prakash, V. N., 2013. *PHD thesis : LIGHT PARTICLES IN TURBULENCE.* Twente: Universiteit Twente.

Prandtl, L., 1961. *Ludwig Prandtl Gesammelte Abhandlungen.* Berlin: Springer Berlin Heidelberg.

Rabha, S. & Buwa, V. V., 2009. *Lift Force Acting on Mono-dispersed Bubbles Rising in Sheared Liquids.* Montreal, Canada , GLS-9/8th World Congress of Chemical Engineering.

Raffel, M., Willert, C. E., Wereley, S. & Kompenhans, J., 2007. *Particle Image Velocimetry.* 2nd ed. Berlin Heidelberg: Springer-Verlag.

Rensen, J. & Roig, V., 2001. Experimental study of the unsteady structure of a confined bubble plume. *International Journal of Multiphase Flow ,* 27(8), pp. 1431-1449.

Riboux, G., Risso, F. & Legendre, D., 2010. Experimental characterization of the agitation generated by bubbles rising at high Reynolds number. *Journal of Fluid Mechanics,* Volume 643, p. 509.

Risso, F. et al., 2008. Wake attenuation in large Reynolds number dispersed two-phase flows. *Phil. Trans. R. Soc. A,* Volume 366, p. 2177.

Roghair, I., M.W.Baltussen, M.VanSintAnnaland & J.A.M.Kuipers, 2013. Direct Numerical Simulations of the drag force of bi-disperse bubble swarms. *Chemical Engineering Science,* Volume 95, p. 48–53.

Rosenberg, B., 1950. *The drag and shape of air bubbles moving in,* Bethesda, MD: David W. Taylor Model Basin.

Ryu, Y., Chang, K.-A. & Lim, H.-J., 2005. Use of bubble image velocimetry for measurement of plunging wave impinging on structure and associated greenwater. *Meas. Sci. Technol.,* Volume 16, p. 1945–1953.

Rzehak, R. & Krepper, E., 2012. Bubble-induced Turbulence: Comparison of CFD Models. *Nuclear Engineering and Desig,* Volume 13, pp. 57-65.

Rzehak, R. & Krepper, E., 2013a. CFD modeling of bubble-induced turbulence. *International Journal of Multiphase Flow,* Volume 55, p. 138–155.

Rzehak, R. & Krepper, E., 2013b. Closure models for turbulent bubbly flows: A {CFD} study. *Nuclear Engineering and Design,* Volume 265, pp. 701-711.

Rzehak, R. & Krepper, E., 2015. Bubbly flows with fixed polydispersity: Validation of a baseline closure model. *Nuclear Engineering and Design,* Volume 287, pp. 108-118.

Rzehak, R., Krepper, E. & Lifante, C., 2012. Comparative study of wall-force models for the simulation of bubbly flows. *Nuclear Engineering and Design,* Volume 253, pp. 41-49.

Rzehak, R. & Kriebitzsch, S., 2014. Multiphase CFD-simulation of Bubbly Pipe Flow: A Code Comparison. *Int J Multiphase Flow.*

Saffman, P. G., 1965. The lift on a smalll sphere in a slow shear flow. *J. Fluid Mech.,* Volume 22, pp. 385-400.

Santarelli, C. & Fröhlich, J., 2012. Simulation of bubbly flow in a vertical turbulent channel. *PAMM,* 12(1), pp. 503-504.

Sathe, M. J., Thaker, I. H., Strand, T. E. & Joshi, J. B., 2010. Advanced PIV/LIF and shadowgraphy system to visualize flow structure in two-phase bubbly flows. *Chemical Engineering Science,* Volume 65, p. 2431–2442.

Sato, Y., Sadatomi, M. & Sekoguchi, K., 1981. Momentum and heat transfer in two-phase bubble flow I: Theory. *Int. J. Multiphase Flow,* Volume 7, p. 167.

Saunter, C. D., 2010. Quantifying Subpixel Accuracy: An Experimental Method for Measuring Accuracy in Image-Correlation-Based, Single-Particle Tracking. *Biophysical Journal,* Volume 98, pp. 1566-1570.

Schleicher, E., Da Silva, M. & Hampel, U., 2008. Enhanced Local Void and Temperature Measurements for Highly Transient Multiphase Flows. *Instrumentation and Measurement, IEEE Transactions on,* Feb, 57(2), pp. 401-405.

Schmale, O. et al., 2015. Bubble Transport Mechanism: Indications for a gas bubble-mediated inoculation of benthic methanotrophs into the water column. *Continental Shelf Research ,* 103(0), pp. 70-78.

Schmidt, E., 1934. Ähnlichkeitstheorie der Bewegung von Flüssigkeitsgasgemischen. *Forschungsheft,* 365(VDI, Berlin, 1–3).

Serizawa, A. & Kataoka, I., 1990. Turbulence suppression in bubbly two-phase flow. *Nuclear Engineering and Design,* Volume 122, p. 1.

Serizawa, A., Kataoka, I. & Michiyoshi, I., 1975. Turbulence structure of air-water bubbly flow - II. local properties. *Int. J. Multiphase flow,* Volume 2, pp. 235-246.

Simcik, M., 2011. CFD simulationandexperimentalmeasurementofgasholdupandliquid interstitialvelocityininternalloopairliftreactor. *Chemical EngineeringScience,* Volume 66, p. 3268–3279.

Simiano, M. et al., 2006. Comprehensive experimental investigation of the hydrodynamics of large-scale, 3D, oscillating bubble plumes. *International Journal of Multiphase Flow,* Volume 32, pp. 1160-1181.

Sokolichin, A. & Eigenberger, G., 1999. Applicability of the standard k epsilon turbulence model to the dynamic simulation of bubble columns: Part I. Detailed numerical simulations. *Chemical Engineering Science,* 54(13-14), pp. 2273-2284.

Sokolichin, A., Eigenberger, G. & Lapin, A., 2004. Simulation of Buoyancy Driven Bubbly Flow: Established Simplifications and Open Questions. *Fluid Mechanics and Transport Phenomena,* Volume 50, pp. 24-45.

Spalart, P., 2000. Strategies for turbulence modelling and simulations. *International Journal of Heat and Fluid Flow,* 21(3), pp. 252-263.

Squires , K. D., 1990. Particle response and turbulence modification in isotropic turbulence. *Physics of Fluids A: Fluid Dynamics,* Volume 2, pp. 1191-1203.

Sugioka, K. & Tsukada, T., 2015. Direct numerical simulations of drag and lift forces acting on a spherical. *International Journal of Multiphase Flow,* Volume 71, pp. 32-37.

Tabib, M. V., Roy, A. & Joshi, J., 2008. CFD simulation of bubble column - An analysis of interphase forces and turbulence models. *Chemical Engineering Journal,* Volume 139, pp. 589-614.

Tennekes, H. & Lumley, J. L., 1972. *A First Course in Turbulence.* 1st ed. Cambride, MA: The MIT Press.

Tomiyama, A., 2002. *Single Bubbles in Stagnant Liquids and in Linear Shear Flows.* Dresden, Germany, Workshop on Measurement Technology (MTWS5).

Tomiyama, A., 2004. *Drag, lift and virtual mass forces acting on a single bubble.* Lyon, France, 3rd International Symposium on Two-Phase Flow.

Tomiyama, A., Kataoka, I., Zun, I. & Sakaguchi, T., 1998. Drag Coefficients of single bubbles under normal and micro gravity conditions. *JSME International Journal Series B ,* 41(2), p. 472.

Tomiyama, A. et al., 1995. Effects of Eötvös number and dimensionless liquid volumetric flux on lateral motion of a bubble in a laminar duct flow. In: A. Serizawa, T. Fukano & J. Bataille, eds. *Advances in multiphase flow.* : Elsevier, pp. 3-15.

Tomiyama, A., Tamai, H., Zun, I. & Hosokawa, S., 1999. *Measurement of Transverse Migration of Single Bubbles in a Couette Flow.* Pisa, 2nd Int. Symposium on Two-Phase Flow Modelling and Experimentation, p. 941.

Tomiyama, A., Tamai, H., Zun, I. & Hosokawa, S., 2002. Transverse migration of single bubbles in simple shear flows. *Chemical Engineering Science ,* 57(11), pp. 1849-1858.

Tripathi, M. K., Sahu, K. C. & Govindarajan, R., 2015. Dynamics of an initially spherical bubble rising in quiescent liquid. *NATURE COMMUNICATIONS,* Volume 6.

Troshko, A. A. & Hassan, Y. A., 2001. A two-equation turbulence model of turbulent bubbly flows. *International Journal of Multiphase Flow,* Volume 27, p. 1965.

Tryggvason, G., Dabiri, S., Aboulhasanzadeh, B. & Lu, J., 2013. Multiscale considerations in direct numerical simulations of multiphase flows. *PHYSICS OF FLUIDS,* Volume 25.

Tryggvason, G., Esmaeeli, A., Lu, J. & Biswas, S., 2006. Direct numerical simulations of gas/liquid multiphase flows. *Fluid Dyn. Res.,* Volume 38, p. 660.

van Benthum, W., van der Lans, R., van Loosdrecht, M. & Heijnen, J., 1999. Bubble recirculation regimes in an internal-loop airlift reactor. *Chemical Engineering Science ,* 54(18), pp. 3995-4006.

Volk, R. et al., 2008. Acceleration of heavy and light particles in turbulence: comparison between experiments and direct numerical simulations. *Physica D: Nonlinear Phenomena,* 237(14-17), p. 2084–2089.

Wang, A., Marashdeh, Q. & Fan, L.-S., 2014. ECVT imaging of 3D spiral bubble plume structures in gas-liquid bubble columns. *The Canadian Journal of Chemical Engineering,* 92(12), pp. 2078-2087.

Wellek, R. M., Agrawal, A. K. & Skelland, A. H. P., 1966. Shape of Liquid Drops Moving in Liquid Media. *AlChE Journal,* Volume 12, p. 854.

Wilcox, D. C., 1994. *Turbulence Modeling for CFD.* 2nd ed. La Canada, California: DCW Industries, Inc..

Wuest, A., Brooks, N. H. & Imboden, D. M., 1992. Bubble plume modeling for lake restoration. *Water Resources Research,* 28(12), pp. 3235-3250.

Xu, H. & Bodenschatz, E., 2008. Motion of inertial particles with size larger than Kolmogorov scale in turbulent flows. *Physica D: Nonlinear Phenomena,* 237(14-17), pp. 2095-2100.

Zhongchuna, L., Xiaoming, S. & Jiyang, Y., 2014. Numerical investigation on lateral migration and lift force of single. *Nuclear Engineering and Design,* Volume 274, p. 154–163.

Ziegenhein, T., Lucas, D., Rzehak, R. & Krepper, E., 2013. *Closure relations for CFD simulation of bubble columns.* Jeju, Korea, ICMF 2013.

Ziegenhein, T., Rzehak, R. & Lucas, D., 2015. Transient simulation for large scale flow in bubble columns. *Chemical Engineering Science ,* 122(0), pp. 1-13.

Zun, I., 1980. The transverse migration of bubbles influenced by walls in vertical bubbly flow. *International Journal of Multiphase Flow,* Volume 6, p. 583.

HZDR
HELMHOLTZ
ZENTRUM DRESDEN
ROSSENDORF

Bautzner Landstraße 400
01328 Dresden, Germany
Tel. +49 351 260-2530
Fax +49 351 260-12503
t.ziegenhein@hzdr.de
http://www.hzdr.de